Stochastic thermodynamics : driving of micro-oscillators applied to the study and the optimisation of information processing

Salambô Dago

Numéro National de Thèse : 2022LYSEN019

THÈSE DE DOCTORAT DE L'UNIVERSITÉ DE LYON

opérée par

l'École Normale Supérieure de Lyon

École doctorale N° 52 :
Physique et Astrophysique de Lyon (PHAST)

Discipline : Physique

Soutenue publiquement le 9 Juin 2022, par :

Salambô Dago

Stochastic thermodynamics: driving of micro-oscillators applied to the study and the optimisation of information processing

---

Thermodynamique stochastique: pilotage de micro-oscillateurs et application à l'étude et l'optimisation du traitement de l'information

---

Devant le jury composé de :

Bechhoefer,	John	Professeur	*Simon Fraser University*	Rapporteur
Pekola,	Jukka	Professeur	*Aalto University*	Rapporteur
Auffèves,	Alexia	DR	*Institut Néel (CNRS)*	Examinatrice
Jarzynski,	Christopher	Professeur	*University of Maryland*	Examinateur
Bellon,	Ludovic	CR	*ENS de Lyon (CNRS)*	Directeur de thèse

Remerciements

Ce manuscrit est le fruit de 3 années de travail (et de télétravail), même si "travail" semble un mot un peu trop sévère pour retranscrire correctement tout le plaisir que j'ai eu à mener mon activité de recherche. Je voudrais remercier ici toutes les personnes qui ont rendu mon quotidien si agréable et m'ont permis de découvrir le monde de la recherche sous son meilleur jour.

En premier lieu je souhaite remercier mon directeur de thèse, Ludovic, qui est l'ingrédient principal de la réussite de cette thèse et qui m'a permis de pleinement m'épanouir professionnellement et humainement. Merci de m'avoir toujours encouragée dans mes initiatives (je ne compte plus les lettres de recommandations) et de m'avoir ouvert de nombreuses opportunités: conférences, événements de vulgarisation scientifique, participation à la vie du laboratoire, jusqu'à tenter des sauts de 4m en canyoning. Merci pour la générosité, l'humour et l'enthousiasme qui m'ont nourri pendant ces trois belles années. Je suis reconnaissante d'avoir bénéficié de son excellence scientifique qui m'a orientée dans les périodes d'errances expérimentales ou théoriques pour mener ma barque à bon port. Dans le même registre je souhaiterais remercier tout particulièrement Sergio qui a co-encadré ma thèse et suivi mes travaux de manière constante. Merci Sergio pour ton aide précieuse, sans laquelle je me serai sûrement noyée dans les circuits électroniques et les nombreux écueils expérimentaux de ma thèse, merci pour ton enthousiasme et tes idées, merci pour nos discussions et tes travaux théoriques qui répondront à nos interrogations, merci pour ta compagnie au laboratoire ou aux conférences, et enfin merci pour la relecture attentive de ce manuscrit. Dans la continuité des remerciements dédiés aux membres du laboratoire je tiens à remercier tous mes collaborateurs, Artyom qui m'a tant aidé dans ma première année de thèse, Benjamin pour son aide aussi et nos discussions devant les pinces optiques, Nicolas pour avoir été mon premier stagiaire et avoir fait tellement plus que le café et les photocopies, et Jorge pour son énergie et sa générosité. Un grand merci à l'équipe au grand complet, en particulier Richard, Alex, Basile, Aubin, Baptiste et Caroline. Merci également aux membres éminents de ce laboratoire sans qui tout s'effondrerait: Fatiha et Nadine pour votre aide patiente et bienveillante dans ce territoire opaque des demandes de mission et des commandes de matériel, et Thierry puis Jean-Christophe à la barre de ce joli navire. Enfin, que serait la vie au laboratoire sans les collègues: je tiens à remercier tout particulièrement Nicolas pour nos séances de sports et nos sorties, son soutien et son amitié; et Freddy pour son engagement écologique et nos discussions. Et bien sûr la joyeuse bande de thésards qui ont mis des paillettes dans ma vie: j'ai nommé Lucas, immense partenaire de cordée et d'activités en tout genre (surtout les jeux de sociétés sa passion secrète), Saskia qui aurait dû arriver avant pour son amitié et la livraison à domicile de galette des rois en temps de COVID, Hubert pour sa fraîcheur sa curiosité sans limite et son bon esprit sportif, les co-bureaux : Stéphane mon phare dans la nuit toujours là et presque toujours allumé pour les Ricards et la bonne ambiance (et les conseils photoshop pour mes slides), Eric pour les sorties culturelles/sportives/culinaires, Jeremy qui a essuyé les plâtres avant moi pour son humour en toutes circonstances, et en vrac Léa, David, les deux François, Théophile, Corentin, Hariette, Nicolas.

Mais heureusement je n'ai pas passé ces 3 années uniquement au laboratoire (malgré la fausse impression que peut donner la maturité scientifique de ce manuscript), et il est temps de rendre à César ce qui appartient un peu à César quand même: Papa, Maman il y a une grande partie de vos cerveaux géniaux à l'ironie démoniaque dans cette thèse. Bravo d'avoir tenu bon (avec le sourire, beaucoup d'amour et un zeste

de ricannement) pendant toutes ces années remplies de Moi: Moi au téléphone, Moi par email, Moi qui écris des mails, Moi en vacance, Moi qui pédale, Moi qui cuisine, Moi dans le train, encore Moi dans le train parce qu'il a du retard... À défaut d'une piscine je vous offre en retour 200 pages de science de haut vol et un paragraphe de remerciement: ça vaut non ? Maman, merci pour ton énergie ton enthousiasme et ton soutien, merci pour les bonnes adresses (ne pas hésiter à lui demander, comme elle le dit si bien une bonne adresse est une adresse partagée), les bon plans, les livres, les vacances, le tennis, la recette secrète des chouquettes et les brunchs. Merci d'être mon agent carrière, de relire mes CV, mes emails, d'écouter mes présentations, de me dire que mes choix sont les bons, et de continuer de m'éduquer à la vie. Papa, merci d'avoir été 'l'appel à un ami' de ma thèse en cas de blocage scientifique, de panne de vélo, ou d'ordinateur inondé, de ton interêt sincère pour toutes mes initiatives (artistiques, sportives, sociales, écologiques...), de partager mes sujets de discussion de prédilection (même si tu as souvent tort sans que j'arrive à le démontrer), de ton humour bête et de ta sagesse millénaire. Et j'ajoute un remerciement officiel d'une thésarde à son rapporteur officieux. Merci à mon petit frère Roman qui rend notre famille complète et sur lequel je peux toujours compter pour faire équipe contre la puissance de frappe parentale. Et bien sûr, un grand merci à toute ma famille au grand complet !

Merci à mon amoureux Jean-Lynce, pour le ménage, les courses, le pain, et les cheesecakes au kiwi... Plus sérieusement, merci d'être comme tu es, merci pour ton amour et ton soutien dans toutes mes entreprises (avec un enthousiasme plus sincère que celui que Papa et Maman soyons honnêtes), merci de me faire découvrir tellement de choses, et merci pour toutes les petites choses qui rendent la vie plus belle.

Enfin il me faut remercier la deuxième famille: les copains. Commençons par les Parisiens, ces pauvres gens perdus dans une ville de l'enfer, qui méritent bien de passer en premier dans ces remerciements. Alice, merci d'être là dans toutes les étapes de ma vie et d'y être avec tant de style; Manon, merci de tout ce que tu me donnes, de ta motivation sans faille à faire partie de ma vie et de ta drôlerie acerbe; Lara pour tous ces moments partagés et la simplicité de notre amitié; Aude pour ta joie de vivre communicative et ton enthousiasme sans faille et Lorène mon ange gardien pour la loyauté et la présence. Il faut aussi remercier tout mes amis qui sont chacun un petit soleil: Perrine et son +1 si sportif, Hugo, Luc, Héloïse, Aurélian, Lucie, Mathias, Flavien, Inés et Léo, Emilie et Pascal, Shirley et Mathieu (seul Toulousain revenu aux sources). Et viennent enfin les amis de Lyon avec qui j'ai partagé de si nombreuses activités, de si nombreuses fêtes et de si nombreux confinements. Il y a Thomas que je remercie de m'avoir suivi depuis Toulouse pour m'initier à la montagne et pour surveiller la bonne tenue de mes résolutions; Aurélien le tazgentleman au grand coeur qui prend toujours soin de ses proches et que j'ai la chance de compter comme ami; Gabriel le voisin envahissant que tout le monde rêverait d'avoir: merci pour les rires et les chèques culture; Bastien, cet humain incroyable qui pourrait éclairer toute la métropole avec son énergie et l'assourdir avec son rire; Mathieu pour les blagues de bon goût et les discussions, et sa binôme Clara pour la danse et l'énergie; Morgane pour la musique et la joie; Cécile pour la générosité et la gentillesse; Clara pour les rires et les discussions; Elodie pour la pêche à toute épreuve; Johann pour les bons moments; Hugo pour la présence les week-ends, les volleys sauvages et les balades marseillaises; et Simon pour le tennis mais pas que. Il y a aussi Aline, Simon, Gaëtan, Marianne, Laurane, Halima, Souleyman et Aurélie, et Naomie. Et c'est tout ? Probablement pas, mais les grands oubliés de ce paragraphe sont invités à faire une réclamation par écrit avec lettre de motivation tout ça tout ça.

Contents

Résumé substantiel

Résumé substantiel

Thermodynamique stochastique: pilotage de micro-oscillateurs et application à l'étude et l'optimisation du traitement de l'information.

En 1832, le botaniste Robert Brown observa au microscope des graines de pollen en suspension dans l'eau et remarqua la présence de très petites particules s'agitant dans tous les sens [1]. Cette marche aléatoire de petits objets, appelé "mouvement brownien" demeura inexpliquée pendant quatre-vingt ans avant qu'Albert Einstein ne modélise le mouvement des particules comme un déplacement induit par l'action des molécules d'eau voisines [2], confirmant indirectement au passage l'existence des atomes et des molécules. En effet, même si un fluide ou un gaz est au repos du point de vue macroscopique, ses molécules microscopiques sont en permanence en mouvement dans des directions aléatoires. C'est pourquoi tout objet immergé dedans est poussé aléatoirement, donnant ainsi lieu à un mouvement brownien de l'objet quand ce dernier est suffisamment petit pour être déplacé par les collisions. Le terme de bruit thermique ou de fluctuation thermique est souvent utilisé pour décrire cette agitation de la matière, car son amplitude croît avec la temperature.

Que ce soit en biologie, chimie, mécanique ou électronique, les avancées technologiques tendent vers des dispositifs de plus en plus petits ou des échelles de mesure atteignant le royaume microscopique, gouverné par les fluctuations thermiques. En effet, ces systèmes évoluent à des échelles d'énergie si petites que les conséquences du bruit thermique ne peuvent plus être négligées. Il devient alors crucial de contrôler le bruit thermique pour pouvoir piloter des micro-systèmes browniens dans le cadre de la physique statistique hors équilibre, et les utiliser pour des applications pratiques. Dans cette perspective, le contrôle des systèmes browniens abordés dans cette thèse est appliqué au traitement de l'information dans le but de créer des micro-dispositifs rapides et économes en énergie.

Pour atteindre cet objectif, il est indispensable d'explorer le lien entre la Thermodynamique et l'Information. Une des pierres fondatrices de ce sujet de recherche a été posée par Ralf Landauer en 1961 lorsqu'il a borné le coût du traitement de l'information par une limite basse fondamentale. Il prédit que l'effacement d'1-bit d'information nécessite au minimum une énergie $k_B T_0 \ln 2$, T_0 étant la température de la mémoire à 1-bit, et k_B la constante de Boltzmann. Cette limite représentant une très petite quantité d'énergie (seulement 3×10^{-21} J à temperature ambiante) est complètement générale et ne dépend pas du type de mémoire utilisée ou de la procédure d'effacement. En d'autres termes, l'information est physique et cela doit être pris en compte lors de la conception d'ordinateurs. Si les avancées technologiques continuent de suivre la croissance actuelle, ce minimum fondamental sera atteint par les micro-processeurs d'ici 40 ans.

Dans ce contexte, nous étudions expérimentalement et théoriquement le coût énergétique du traitement de l'information, dans le but d'optimiser la consommation énergétique et la rapidité d'une porte logique à 1-bit. Cette dernière est construite grâce à une méthode de contrôle innovante permettant de piloter un micro-système obéissant à une dynamique stochastique sous-amortie, utilisé comme mémoire à 1-bit. Nous quantifions et modélisons la consommation énergétique de la porte logique dans le cadre de la thermodynamique stochastique, ce qui ouvre la voie à de nouvelles stratégies d'optimisation basées sur la connaissance fine des échanges d'énergie.

Dans le premier chapitre de la thèse, nous introduisons le cadre expérimental et théorique nécessaire à la bonne compréhension. Nous rappelons les bases de la physique

statistique et en particulier les équations qui régissent l'évolution des systèmes browniens dans tous les régimes d'amortissement, ansi que l'équipartition de l'énergie. Pour décrire proprement la mémoire à 1-bit utilisée dans la suite, nous exprimons également le taux de commutation d'un système sous-amorti évoluant dans un double puit de potentiel quelque soit la hauteur de la barrière énergétique, en combinant la description de Kramer valide pour les hautes barrières, avec un modèle plus adapté aux petites barrières. Ensuite, nous présentons les deux systèmes expérimentaux (sous-amorti et sur-amorti) utilisés dans la thèse ainsi que leurs méthodes de piégeage respectives. Enfin, nous utilisons le formalisme de la thermodynamique stochastique pour définir et donner une expression simplifiée de quantités thermodynamiques utiles lorsque les fluctuations thermiques dominent (chaleur et travail stochastique, température cinétique...). Nous revenons aussi rapidement sur l'état de l'art de la limite de Landauer qui borne l'énergie nécessaire au traitement de l'information. Nous concluons en introduisant des notations adimensionnées utilisées dans tout le manuscrit.

Dans le deuxième chapitre, nous abordons des procédures de raccourci à l'équilibre, appelées 'Engineered Swift Equilibration' (ESE), représentant une piste prometteuse pour réduire le temps de traitement des opérations effectuées sur des micro-dispositifs. L'objectif de ces nouvelles méthodes est en effet de réduire les transitoires et de faire relaxer les systèmes browniens plus rapidement vers le nouvel équilibre après le changement d'un paramètre de contrôle. À cet effet, le potentiel dans lequel évolue le système est piloté entre sa valeur initiale et finale selon un profil spécifique. Les profils ESE peuvent être calculés à l'aide d'outils théoriques de physique statistique hors équilibre, puis testés sur des systèmes réels tels des particules colloïdales uniques sur-amorties, piégées et contrôlées par des pinces optiques. Nous ajoutons ici un nouveau degré de liberté (DOF), que ce soit en introduisant un couplage hydrodynamique avec une seconde particule, ou en travaillant dans le régime sous-amorti qui introduit le DOF de vitesse. Ces systèmes plus complexes nécessitent des procédures de raccourci adaptées, c'est pourquoi nous construisons de nouvelles familles de protocoles ESE. Enfin, nous relevons le défi expérimental de commander la raideur du potentiel dans laquelle évolue un micro-résonateur sous-amorti à l'aide d'une boucle de rétroaction. Des résultats encourageants sont obtenus, ouvrant la voie à la validation expérimentale de protocoles ESE sous-amortis.

Fort de la démonstration expérimentale du contrôle par rétroaction de l'oscillateur sous-amorti, nous nous attaquons dans le troisième chapitre à la construction d'un double puit de potentiel virtuel. Nous étudions et modélisons le comportement du système en réponse à la rétroaction afin d'identifier les contraintes expérimentales nécessaires à la création d'un potentiel virtuel approprié. Nous proposons ensuite deux boucles de rétroaction pour commander l'oscillateur sous-amorti sans biais : une boucle analogique adaptée à un amortissement modéré, et une boucle numérique (utilisant un dispositif FPGA) adaptée au régime hautement sous-amorti.

Utilisant un oscillateur micro-mécanique sous-amorti confiné dans le double puit virtuel comme mémoire à 1 bit, nous explorons au quatrième chapitre le lien entre information et thermodynamique en mesurant le travail et la chaleur stochastiques d'un effacement (opération [RESET]). Nous étudions en particulier l'effet de l'inertie sur le coût de l'effacement et démontrons expérimentalement que la limite de Landauer est atteinte avec des protocoles aussi courts que 100 ms, c'est-à-dire plusieurs ordres de grandeur plus vite que les mémoires sur-amorties de l'état de l'art. Supprimer la dissipation pour réduire le prix énergétique des opérations rapides semble donc être une stratégie gagnante, mais nous montrons qu'à faible amortissement, un autre mécanisme

couteux en énergie apparaît: le réchauffement du système. Nous étudions alors les échanges d'énergie lors des processus d'effacement et prédisons quantitativement le coût des opérations rapides : pour la première fois, l'écart à la limite de Landauer lorsque la vitesse du pilotage augmente est entièrement modélisé, en accord avec les résultats expérimentaux et de simulation. Enfin, afin d'ouvrir la voie à une utilisation concrète de la mémoire à 1 bit, nous proposons quelques nouvelles stratégies d'optimisation, avant d'étudier sa réponse à des opérations successives.

Dans le cinquième chapitre, nous examinons de plus près le lien entre information et thermodynamique en cherchant comment cette dernière est affectée lorsque la connaissance de la position passée du système est utilisée par le contrôle de rétroaction. Nous étudions en particulier les conséquences d'une hystérésis dans la rétroaction sur la température d'équilibre du système dans le double puit de potentiel virtuel. Enfin, nous démontrons que la limite fondamentale à la manipulation d'information trouvée par Landauer peut être battue en présence d'hystérésis créant un bain thermique hors équilibre.

Dans le dernier et sixième chapitre, nous traitons l'opération logique réversible [NOT] (bit-flip) pour compléter l'étude de l'ensemble des opérations à 1 bit effectuées sur la porte logique sous-amortie. Nous discutons de la faisabilité du bit-flip en fonction du régime d'amortissement et proposons un protocole de bit-flip réversible (dans le sens de la réversibilité physique) spécialement conçu pour les mémoires sous-amorties. Ce dernier tire parti du degré de liberté de vitesse pour effectuer le bit-flip en un temps très court, seulement la moitié de la période du micro-oscillateur, pour un coût énergétique très faible provenant de l'amortissement résiduel. Enfin, nous proposons un modèle correspondant parfaitement aux observations, et offrant de nouvelles stratégies d'optimisation adaptées aux exigences de l'opérateur.

Dans une dernière section, nous concluons en résumant les résultats obtenus et en présentant quelques ouvertures. Nous discutons en particulier de la façon dont de nouvelles formes de mémoire, différentes des double puits quadratiques, ainsi que des protocoles de raccourci à l'équilibre pourraient conduire à une optimisation du traitement de l'information. En outre, nous soulevons des directions à explorer concernant le possible compromis entre énergie et information dans la boucle de rétroaction de la porte logique.

References

[1] R. Brown, "A brief account of microscopical observations made in the months of june, july, and august, 1827 on the particles contained in the pollen of plants, and on the general existence of active molecules in organic and inorganic bodies", The miscellaneous botanical works of Robert Brown, vol. 1 (1828).

[2] A. Einstein, Annalen der Physik **322**, 549 (1905).

Abstract/Résumé

Abstract

Stochastic thermodynamics: driving of micro-oscillators applied to the study and the optimisation of information processing.

This thesis extends by theoretical and experimental studies our understanding of the dynamics of systems ruled by thermal fluctuations in order to better control them and, in particular, use them as 1-bit logic gates. This work falls within the framework of out-of-equilibrium statistical physics and of thermodynamics of information based on stochastic thermodynamics. In this respect, we study the minimal work required to perform irreversible operations on 1-bit of information ([RESET] to 0 or 1), or reversible ones ([NOT] operation), and we aim to optimise the energetic cost and the speed of these processes. Our strategy to enhance the processing efficiency and speed consists in using as 1-bit memory a low dissipation micro-mechanical oscillator, therefore evolving at much smaller time-scales than the over-damped test systems used to date (colloidal particles in solution). The feedback control designed to create a virtual energy potential in which evolves the micro-resonator is a major step forward in coding and handling the 1-bit information: it represents the fastest and most energy-efficient device among those which perform logic operations at the thermal energy scale. We furthermore provide a solid theoretical basis, validated by experimental and numerical simulation results, to model energy exchanges. Taken as a whole, this work results in the theoretical prediction of the energetic cost of any logical operation and opens perspectives for information processing optimisation in term of reliability, speed and energy saving.

Résumé

Thermodynamique stochastique: pilotage de micro-oscillateurs et application à l'étude et l'optimisation du traitement de l'information.

Cette thèse approfondit par des études expérimentales et théoriques les connaissances sur la dynamique de systèmes soumis au bruit thermique afin de mieux les manipuler et notamment de les utiliser comme porte logique à 1-bit. Ces travaux relèvent de la physique statistique hors équilibre et de la thermodynamique stochastique appliquée à la théorie de l'information. Nous étudions ainsi l'énergie minimale qu'un opérateur doit fournir pour manipuler 1 bit d'information de manière irréversible (opération [RESET] à 0 ou 1), ou réversible (opération [NOT]), et cherchons à optimiser le coût et la durée de ces opérations. Notre stratégie pour gagner en efficacité et en rapidité est d'utiliser comme mémoire un micro levier à faible dissipation, évoluant à des échelles de temps bien plus rapides que les systèmes modèles sur-amortis utilisés jusqu'ici (colloïdes en solution). La conception d'une rétroaction pour créer un potential d'énergie virtuel dans lequel évolue le micro-oscillateur constitue une avancée expérimentale majeure, permettant de coder et manipuler le bit d'information: il s'agit de la porte logique classique la plus économe et la plus rapide démontrée à ce jour. Nous déployons par ailleurs une base théorique solide, validée par les résultats d'expériences et de simulations numériques, pour modéliser les échanges énergétiques. Ces travaux dans leur ensemble permettent de prédire théoriquement le coût de toute opération logique, et ouvrent de nombreuses perspectives d'optimisation du traitement de l'information en terme de fiabilité, rapidité et coût énergétique.

Introduction

In 1828, the botanist Robert Brown observed with a microscope that tiny particles in pollen grains suspended in water have a surprising random motion [1]. This random walk of small objects, called "brownian motion" remained unexplained for eighty years until Albert Einstein's proposal to model the motion of the particles as being moved by water molecules [2], hence indirectly confirming the existence of atoms and molecules. Indeed even if a fluid or a gas is at rest from the macroscopic point of view, its microscopic molecules are constantly moving in random directions, so that any object immersed in it is randomly hit, leading to the brownian behavior when the latter is small enough to be moved by the collisions. The terms thermal noise or thermal fluctuations are often used to describe this agitation as its amplitude grows with the temperature.

Whether it is in biology, chemistry, mechanics or electronics, technological advances result in smaller and smaller devices or measurement scales reaching the microscopic realm, ruled by thermal fluctuations. Indeed, those systems evolve at energy scales so small that the consequences of the thermal noise prevail on their behavior. It is consequently crucial to harness the thermal noise within the framework of out of equilibrium statistical physics in order to drive brownian micro-objects and use them for concrete applications. In this respect, the control of brownian systems addressed in this thesis is applied to information processing for the purposes of creating fast and energy-efficient micro-devices.

This goal requires to explore the link between thermodynamics and information. One of the foundation of this topic of research was laid by Ralf Landauer in 1961 when he predicted a fundamental lower limit to the cost of information processing. He stated that the erasure of 1-bit of information requires an energy of at least $k_B T_0 \ln 2$, T_0 being the 1-bit memory temperature, k_B the Boltzmann constant. This lower bound, representing only a tiny amount of energy (3×10^{-21}J at room temperature) is completely general and doesn't depend on the type of memory used, neither on the erasure procedure. In other words, information is physical and it has to be taken into account when conceiving computers. If the technological advances keep following the current trend, this fundamental minimum will be reached by micro-processors within 40 years.

In this context, we study experimentally and theoretically the energetic cost of information processing, in order to optimise the frugality and the speed of a 1-bit logic gate. Indeed these two challenges are complementary in so far as optimizing the energetic consumption at very low operating speed is of little interest. The logic gate is based on innovative control methods allowing the precise driving of a micro-system governed by underdamped stochastic dynamics and used as 1-bit memory. We quantify and model the logic gate energetic consumption within the stochastic thermodynamics framework, paving the way to new optimisation strategies based on the thorough understanding of the energy exchanges.

The manuscript is organized as follow:

1. In the first chapter, we introduce some useful theoretical and experimental background. We recall the basics of statistical physics, in particular the evolution equations of brownian systems in all damping regimes and the energy equipartition. To properly describe the 1-bit memory in the next chapters, we also express the switching time of an underdamped system evolving in a double-well for all barrier heights, combining for the first time Kramer's description, valid at high barriers, with an adjusted model for lower ones. Then we present the two complementary experimental test systems (over-damped and under-damped) used in

the thesis, and their respective trapping methods. Finally we use the stochastic thermodynamics formalism to define and give simplified expressions of useful thermodynamic quantities in the thermal fluctuation realm (stochastic heat and work, kinetic temperature...). The state-of-the-art on the Landauer's limit that bounds the energetic cost of information processing is also quickly reviewed. We conclude by introducing dimensionless notations used in all the manuscript.

2. In the second chapter, we address shortcut procedures, called Engineered Swift Equilibration (ESE), representing a very promising path to cut the processing time of operations conducted on micro-devices. The point of these emerging methods is indeed to reduce the transients of systems and make them relax faster to equilibrium after a change of a control parameter. For this purpose, the potential energy is controlled between its initial and final values according to specific profiles. The ESE profiles can be computed using theoretical out-of-equilibrium statistical physics tools and then tested in actual over-damped systems of single colloidal particles trapped by optical tweezers. We add a new degree of freedom (DOF), whether it is by introducing hydrodynamic coupling with a second particle, or by working in the underdamped regime with the velocity DOF. These more complex systems need adapted shortcut procedures, and that is why we build new families of ESE protocols. Finally, we take up the experimental challenge of driving the potential energy stiffness in which evolves an underdamped micro-oscillator using a feedback loop. Encouraging results are obtained, paving the way for experimental implementations of underdamped ESE procedures.

3. Strong of the experimental demonstration of the underdamped resonator feedback control, we tackle in the third chapter the construction of a virtual double-well potential. We study and model the behavior of the system in response to a feedback in order to identify the experimental contraints necessary to create a proper virtual potential. Then we propose two feedback loops to drive the underdamped oscillator without bias: an analogical one at moderate damping and a digital one, using a FPGA device, in the highly underdamped regime.

4. Using as a 1-bit memory an underdamped micro-mechanical oscillator confined in the virtual double-well potential, we explore in the fourth chapter the link between information and thermodynamics by measuring the stochastic work and heat of an erasure ([RESET] operation). We study in particular the effect of inertia on the erasure cost and demonstrate experimentally that the Landauer's bound (LB) is reached with protocols as short as 100 ms, that is to say several order of magnitude faster than the state-of-the-art over-damped memories. Removing dissipation to cut energy expenses for fast operations hence seems a winning strategy but we show that, at low damping, another limiting mechanism occurs: the warming of the system. In this context, we study the energy exchanges during erasure processes and predict quantitatively the cost of fast operations: for the first time, the divergence from Landauer's bound when the driving speed increases is fully modeled in agreement with experimental and simulation results. Finally, in order to pave the way to a practical use of the 1-bit memory we propose some new optimisation strategies before studying its response to repeated operations.

5. In the fifth chapter, we examine further the link between information and thermodynamics by investigating how the latter is impacted when the knowledge of the system past position is used by the feedback control. In particular we investigate

the consequences of feedback hysteresis on the system equilibrium temperature in the virtual double-well potential. Ultimately we demonstrate that the fundamental lower limit to information irreversible manipulation found by Landauer can be beaten in the presence of hysteresis, using an out-of-equilibrium thermal bath.

6. In the last and sixth chapter, we handle the logically reversible [NOT] operation (bit-flip) to complete the study of all 1-bit operations conducted on the underdamped logic gate. We discuss the feasibility of the bit-flip depending on the damping regime and propose a physically reversible bit-flip protocol designed for underdamped memories. The latter takes advantage of the speed degree of freedom of the underdamped system to perform the bit-flip in a very small amount of time, half the micro-oscillator period, for a very small energetic price originating from the residual damping. Finally, we propose a model that perfectly matches the observations and paves the way to optimisation strategies adapted to operator requirements.

In the conclusion, we summarize the results and presenting some perspectives opened by this wok. We discuss in particular how new memory shapes different from the quadratic wells and shortcut procedures could be promising steps forward in terms of information processing optimisation. Besides, we raise directions to explore regarding the possible trade off between energy and information in the logic-gate feedback loop.

References

[1] R. Brown, "A brief account of microscopical observations made in the months of june, july, and august, 1827 on the particles contained in the pollen of plants, and on the general existence of active molecules in organic and inorganic bodies", The miscellaneous botanical works of Robert Brown, vol. 1 (1828).

[2] A. Einstein, Annalen der Physik **322**, 549 (1905).

Chapter 1:

State of the art

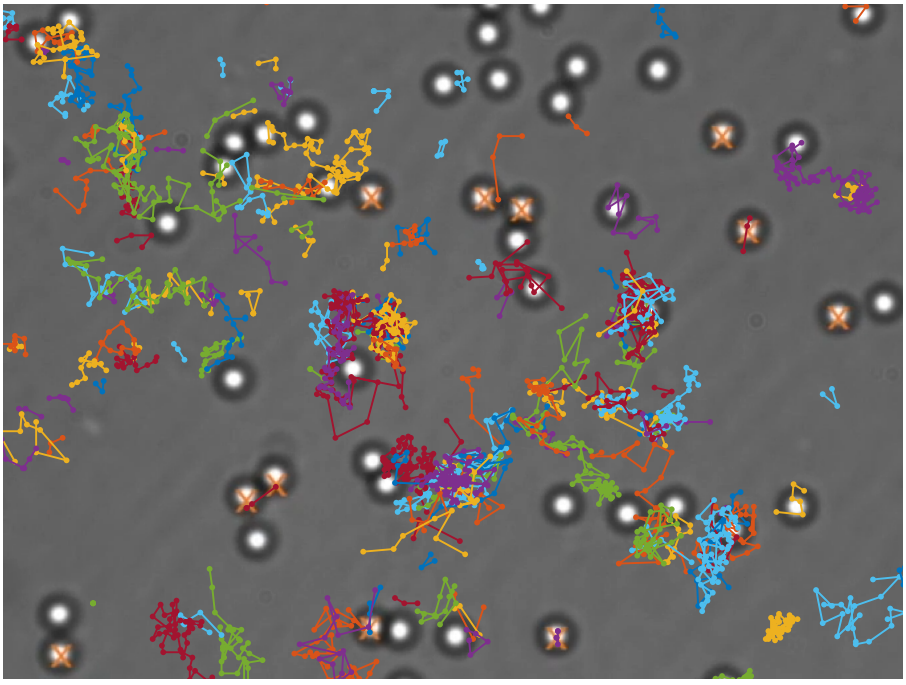

Brownian motion of colloids in water

1.1 Statistical Physics Tool Box

Classical dynamical systems can be described from different perspectives. At the more detailed level stands the Hamiltonian dynamics predicting the evolution of all the degrees of freedom of the system in a deterministic approach. On the other hand the macroscopic level uses the thermodynamics formalism [1]. The intermediate level between them would be the stochastic dynamics, not deterministic because of the introduction of an external random force of which only the probability distribution is known. The latter leads us to consider the possibility of describing the dynamics of the system in a direct probabilistic way so that we have a stochastic differential equation for the path [2]. We feature in the following the stochastic dynamic framework used to describe micro-systems behaviors.

1.1.1 Langevin equation and damping regimes

We consider a Brownian system of mass m in a bath at temperature T_0 characterized by its position $\vec{x}$ and speed $\vec{v}$. Its dynamic into a potential energy $U(\vec{x})$ is described by the 3-dimension Langevin equation [3],

$$m\frac{d\vec{v}}{dt} = -\vec{\nabla}U(\vec{x}) - \gamma\vec{v} + \gamma\sqrt{D}\vec{\xi}(t). \tag{1.1}$$

In the following, we restrict the description to one dimension: position x and speed $v = \dot{x}$, so that the Langevin equation in 1D is given by:

$$m\ddot{x} + \gamma\dot{x} = -\frac{dU}{dx} + \gamma\sqrt{D}\xi(t). \tag{1.2}$$

The friction coefficient γ of the environnement, the bath temperature T_0 and Boltzmann's constant k_B define the diffusion constant through the Einstein relation: $D = k_B T_0/\gamma$. The thermal noise, $\xi(t)$, is a δ-correlated white Gaussian noise:

$$\langle \xi(t)\xi(t+t')\rangle = 2\delta(t'). \tag{1.3}$$

For clarity purposes we introduce the thermal force F_ξ defined by:

$$F_\xi = \gamma\sqrt{D}\xi. \tag{1.4}$$

Langevin's equation is a stochastic differential equation: each solution represents a different random trajectory.

If the potential is harmonic, $U(x) = \frac{1}{2}kx^2$, the Langevin equation (1.2) simplifies into:

$$\ddot{x} + \frac{\gamma}{m}\dot{x} + \frac{k}{m}x = \frac{F_\xi(t)}{m}, \tag{1.5}$$

$$\ddot{x} + \frac{\omega_0}{Q}\dot{x} + \omega_0^2 x = \frac{F_\xi(t)}{m}, \tag{1.6}$$

with $Q = \omega_0 m/\gamma$ the quality factor and $\omega_0 = \sqrt{k/m}$ the angular resonance frequency.

In practice depending on the system mass and the bath viscosity, the corresponding over-damped or underdamped description leads to different dynamics. We distinguish two regimes: the over-damped regime where the damping force exceeds the inertia ($Q \ll 1$) and the under-damped one where it is the contrary ($Q > 1$).

In the over-damped regime, the inertial term $m\ddot{x}$ is neglected and the Langevin equation reads:

$$\gamma\dot{x} = -\frac{dU}{dx} + F_\xi(t). \tag{1.7}$$

In the harmonic potential case, it simplifies into

$$\dot{x} = -\frac{k}{\gamma}x + \sqrt{D}\xi(t). \tag{1.8}$$

1.1.2 Ito's Calculus

The Langevin equation most often studied is the over-damped one, Eq. (1.7), that can be written in the general form:

$$\dot{x} = a(x,t) + b(x,t)\xi(t). \tag{1.9}$$

The corresponding integral equation is therefore:

$$x(t) - x(0) = \int_0^t a(x(s),s)ds + \int_0^t b(x(s),s)\xi(s)ds. \tag{1.10}$$

We introduce the integral of the thermal noise $\xi(t)$ interpreted as the Wiener process $W(t)$:

$$W(t) = \sqrt{2}\frac{1}{\sqrt{2}}\int_0^t \xi(t')dt', \tag{1.11}$$

so that the second integral in Eq. (1.10) becomes:

$$\int_0^t b(x(s),s)dW(s). \tag{1.12}$$

The above demonstrates the importance of building a proper formalism to address the manipulation of stochastic quantities (integral, derivation...). In particular, to carry out such a stochastic integral, one has to be cautious regarding the discretization. In all the manuscript we will stick to the Ito stochastic integral [4] that prescribes for a function $G(t)$:

$$\int_{t_0}^t G(s)dW(s) = \lim_{n\to\infty}\sum_{i=1}^{n} G(t_{i-1}) \times [W(t_i) - W(t_{i-1})]. \tag{1.13}$$

with the t_i the subdivision of the interval $[t_0, t]$ into n subintervals.

The general differentiation rule for any function $f(W(t),t)$ stems from the Ito stochastic integral (Eq. (1.13)):

$$df[W(t),t] = (\partial_t f + \frac{1}{2}\frac{\partial^2 f}{\partial W^2})dt + \frac{\partial f}{\partial W}dW(t) \tag{1.14}$$

Let us also point out here the two following properties:

$$dW(t)^2 = dt, \tag{1.15}$$

and for nonanticipating function $G(t)$ (for example $x(t)$ or $v(t)$), in the Ito framework:

$$\langle\int_{t_0}^t G(s)dW(s)\rangle = 0 \tag{1.16}$$

We conclude this section by deriving the so called Ito's formula from a change of variable on Eq. (1.14). We expand the expression of the derivative of any stochastic function $f(x(t))$ of the trajectory $x(t)$ governed by the general over-damped Langevin equation in Eq. (1.9):

$$df(x(t)) = \{a(x,t)f' + \frac{1}{2}b(x,t)^2 f''\}dt + b(x,t)f'dW(t) \tag{1.17}$$

where spaces derivatives are denoted by a dash.

1.1.3 Fokker-Plank and Kramers Equation

If we introduce the probability density function $P(x,v,t)$ for finding the Brownian system in position x, and velocity v at time t, we can describe the dynamics through the Kramer's equation [5]:

$$\partial_t P + v\partial_x P - \frac{\partial_x U}{m}\partial_v P = \frac{\gamma}{m}\partial_v(vP) + \frac{\gamma^2}{m^2}D\partial_v^2 P, \tag{1.18}$$

The Langevin's equation (1.2) and Kramer's equation (1.18) are equivalent and both characterize the stochastic process. In fact the Kramer's equation derives from the Langevin's equation by considering the time development of an arbitrary function of $f(x(t))$, on average, using Ito's formula in Eq. (1.17).

At thermal equilibrium, the solution of Eq. (1.18) simply gives the Boltzmann law:

$$P_{eq}(x,v) = P_0 \exp\left\{-\frac{U(x)}{k_B T_0} - \frac{mv^2}{2k_B T_0}\right\} \tag{1.19}$$

In the over-damped regime, the velocity degree of freedom disappears and the whole dynamic is described by the probability density function $\rho(x,t) = \int P dv$. The Kramer's equation Eq. (1.18) then turns into the Fokker-Plank equation [6; 7] (noted FP equation) governing the time evolution:

$$\partial_t \rho = \frac{1}{\gamma}\partial_x(\rho\partial_x U) + D\partial_x^2\rho. \tag{1.20}$$

In a harmonic potential, the FP equation is:

$$\partial_t \rho = \frac{k}{\gamma}\partial_x(x\rho) + D\partial_x^2\rho. \tag{1.21}$$

The equilibrium solution of the FP equation again corresponds to the Boltzmann law:

$$\rho_{eq}(x) = \rho_0 \exp\left\{-\frac{U(x)}{k_B T_0}\right\} = \rho_0 \exp\left\{-\frac{kx^2}{2k_B T_0}\right\} \tag{1.22}$$

1.1.4 Equipartition theorem

The total energy of the system $E = U + K$ (with the kinetic energy $K = \frac{1}{2}mv^2$) is given at thermal equilibrium (at bath temperature T_0) by the very general equipartition formula :

$$\langle x_m \frac{\partial E}{\partial x_n}\rangle = \delta_{nm} k_B T_0, \tag{1.23}$$

where the x_n are the degrees of freedom of the system. In our 1D description we have only two degrees of freedom : the velocity $v = \dot{x}$ and the position x, and the potential $U(x)$ is considered to be independent of v. The equipartition theorem (1.23) applied to the first degree of freedom therefore results in:

$$\langle v\frac{\partial E}{\partial v}\rangle = k_B T_0, \tag{1.24}$$

$$\langle v\frac{\partial K}{\partial v}\rangle = k_B T_0, \tag{1.25}$$

$$\langle K\rangle = \frac{1}{2}k_B T_0. \tag{1.26}$$

For the second degree of freedom we derive :

$$\langle x\frac{\partial E}{\partial x}\rangle = k_B T_0, \tag{1.27}$$

$$\langle x\frac{\partial U}{\partial x}\rangle = k_B T_0. \tag{1.28}$$

Hence, in the case of an harmonic potential $U = \frac{1}{2}kx^2$, we have:

$$\langle U\rangle = \frac{1}{2}k_B T_0. \tag{1.29}$$

Eqs. (1.26) and (1.29) defines the equilibrium velocity and position variances:

$$\sigma_{v,0}^2 = \langle v^2\rangle = \frac{k_B T_0}{m}, \qquad \sigma_0^2 = \langle x^2\rangle = \frac{k_B T_0}{k}. \tag{1.30}$$

In the following, we will consider quadratic double well potentials defined by $U_1(x, x_1) = \frac{1}{2}k(|x| - x_1)^2$ with two wells centered in $-x_1$ and x_1. If we apply the equipartition theorem, the kinetic energy is unchanged, but the potential energy at equilibrium is not given by Eq. (1.29) anymore and depends on the distance $2x_1$ between the wells. Indeed, the equipartition for the position degree of freedom in Eq.(1.28) gives:

$$\langle x\frac{\partial U_1}{\partial x}\rangle = k\langle x^2 - |x|x_1\rangle = k_B T_0 \tag{1.31}$$

$$2\langle U_1\rangle + kx_1(\langle|x|\rangle - x_1) = k_B T_0 \tag{1.32}$$

The term $\langle|x|\rangle$ can be computed using the equilibrium probability distribution, as detailed in the Supplementary Materials of Ref. 8 reproduced in Appendix C:

$$\langle|x|\rangle = \sigma_0\sqrt{\frac{2}{\pi}}\frac{e^{-\frac{x_1^2}{2\sigma_0^2}}}{(1+\operatorname{erf}\frac{x_1}{\sqrt{2}\sigma_0})} + x_1 \tag{1.33}$$

Finally, plugging in the above expression into Eq. (1.32) gives the mean potential energy:

$$\langle U_1\rangle = k_B T_0\left(\frac{1}{2} - \frac{x_1}{\sigma_0}\frac{e^{-\frac{x_1^2}{2\sigma_0^2}}}{\sqrt{2\pi}(1+\operatorname{erf}\frac{x_1}{\sqrt{2}\sigma_0})}\right) \tag{1.34}$$

Eq. (1.34) is not intuitive because we are used to the equipartition result in the harmonic potential case: $\langle U\rangle = \frac{1}{2}k_B T_0$. Nevertheless for a double well quadratic potential the

equipartition theorem leads to this more complex expression. The equipartition in the double well is displayed in Fig. 4.6a) and b): the kinetic energy remains unchanged as the velocity degree of freedom conserves a quadratic contribution, meanwhile the potential energy has lower values depending on x_1 (following Eq. (1.34)) to satisfy the equipartition. Let us point out here that for $x_1 = 0$ and $x_1 \gg \sigma_0$, Eq. (1.34) tends to the harmonic result: we have either a single well ($x_1 = 0$) or two no overlapping ones ($x_1 \gg \sigma_0$).

1.1.5 Switching rate in a bi-quadratic potential

When the Brownian system of mass m evolves in a bi-quadratic potential of stiffness k, $U_1(x, x_1) = \frac{1}{2}k(|x| - x_1)^2$, it is worth wondering what is its switching rate between the two wells. In the following we are only interested in underdamped limit ($Q > 1$), as the systems trapped in double-well potentials tackled in this work will always be weakly damped with their environnement. Kramer's theory [5] prescribes the escape rate $\Gamma(t) = \frac{\omega_0}{2\pi} e^{-\mathcal{B}/k_B T_0}$ [9], with the potential barrier $\mathcal{B} = \frac{1}{2}kx_1^2$, and $\omega_0 = \sqrt{k/m}$ the resonance frequency in the initial quadratic well of stiffness k. Nevertheless, this expression doesn't hold for low barrier ($\mathcal{B} < k_B T_0$), as shown in Fig. 1.1. That is why we propose in the following an expression of the average switching rate in a double well potential valid in very good approximation for all barrier heights.

In the limit of weak damping, the total energy of the system $E = U + K$ is conserved, and its motion in the trapping potential U_1 is periodic in time. The period of oscillation $\mathcal{T}$ depends on the value of E with respect to the barrier height $\mathcal{B}$. If $E < \mathcal{B}$, then the motion is confined to a single well, there is no switch, and the period is $\mathcal{T}_0 = 1/f_0$. If $E > \mathcal{B}$, the system visits both wells every period, so there are 2 switches every period, with

$$\mathcal{T}(E, \mathcal{B}) = 2\int_{-x_M}^{x_M} \sqrt{\frac{m}{2(E - U(x, x_1))}}dx \tag{1.35}$$

$$= \frac{2}{\omega_0}\int_{-x_M}^{x_M} \frac{1}{\sqrt{(x_M - x_1)^2 - (|x| - x_1)^2}}dx \tag{1.36}$$

$$= \frac{2}{\omega_0}\left[\pi + 2\sin^{-1}\left(\sqrt{\frac{\mathcal{B}}{E}}\right)\right], \tag{1.37}$$

where $x_M = x_1 + \sqrt{2E/k}$ is the maximum excursion of the system. This period is twice $\mathcal{T}_0$ when $E \gtrsim \mathcal{B}$, and tends to $\mathcal{T}_0$ for $E \gg \mathcal{B}$.

In equilibrium, the statistics of the total energy E is ruled by the Boltzmann distribution: $P(E) = e^{-E/k_B T}/k_B T$. We deduce the average switching rate Γ by weighting the 2 switches per period for $E > \mathcal{B}$ by this probability:

$$\Gamma(\mathcal{B}, T) = \int_{\mathcal{B}}^{\infty} \frac{2}{\mathcal{T}(E, \mathcal{B})}\frac{\exp(-E/k_B T)}{k_B T}dE \tag{1.38}$$

$$= \omega_0 \frac{\mathcal{B}}{k_B T}\int_1^{\infty} \frac{\exp\left(-\epsilon\frac{\mathcal{B}}{k_B T}\right)}{\pi + 2\sin^{-1}(\epsilon^{-1/2})}d\epsilon \tag{1.39}$$

For finite damping, the energy is not conserved along single trajectories, but still is in average thanks to the equilibrium with the thermostat. Eq. (1.39) is therefore

a good approximation of the switching rate between the two wells for a given barrier height $\mathcal{B}$ and system temperature T. In Fig. 1.1, we superimpose the result of numerical simulation with both the Kramer's theory (dotted black) and our model. It highlights the fact that Kramer's simple formula doesn't work for low energy barriers and justifies the use of Eq. (1.39) in all the following.

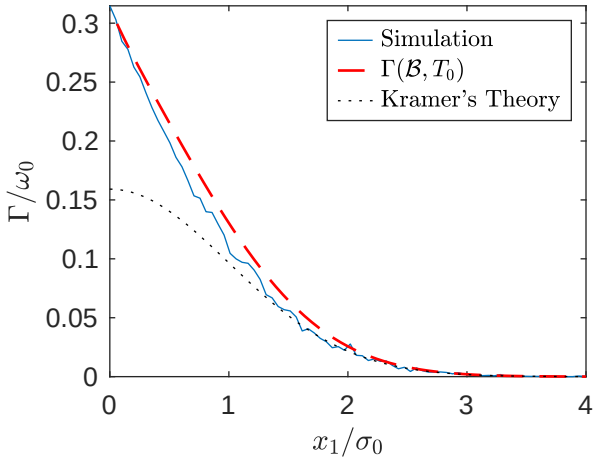

Figure 1.1 – **Switching rate** Γ as a function of the half distance x_1 between the wells: for high energy barriers $\mathcal{B} = \frac{1}{2}kx_1^2$, the simple Kramer's model in dashed black line holds and perfectly matches the simulation data from $N = 100$ iterations of $30\mathcal{T}_0$ long trajectories in blue line. However, for smaller barrier height the model $\Gamma(\mathcal{B}, T_0)$ of Eq. (1.38) in red dashed line provides a better prediction. The numerical simulation detailed in Appendix E is run here for an underdamped system ($Q = 10$). The numerical simulation gives the same result for a wide panel of damping regimes ($0.1 \leq Q \leq 1000$).

1.2 Brownian systems

Depending on the damping regime one wants to investigate, it is interesting to study different Brownian systems. We will present in the following the two ones tackled during my thesis: colloidal particles in water and a micro-cantilever.

1.2.1 Over-damped colloidal particles

Colloidal particules in solution are broadly used systems to explore statistical physics in the over-damped regime. As sketched in Fig. 1.2, let us consider a colloidal particle of position x (1D description) in a fluid at temperature T_0 trapped in an harmonic potential $U(x,t) = \frac{1}{2}kx^2$ by optical tweezers (as detailed later in paragraph 1.3.1). The usual stiffness for such optical traps is $0.5\,\mathrm{pN}/\mu\mathrm{m} < k < 50\,\mathrm{pN}/\mu\mathrm{m}$. We use in all the following silica beads of density $\mu = 3 \times 10^3\,\mathrm{kg\,m^{-3}}$ and radius $r \sim 1\,\mu\mathrm{m}$. The Stokes friction coefficient in the bath writes $\gamma = 6\pi\eta r$, with $\eta = 10^{-3}\,\mathrm{Pa\,s}$ the kinetic viscosity for usual fluids like water. The diffusion coefficient of the silica bead in the surrounding fluid is therefore $D = k_B T_0/(6\pi\eta r)$.

The influence of the inertia lasts on a characteristic time $\tau_{\mathrm{inertia}} = m/\gamma = 2\mu r^2/(9\eta)$. To evaluate the impact of inertia on the colloid's dynamics, we compare the latter to the time needed for a particle to diffuse on a distance equivalent to its diameter,

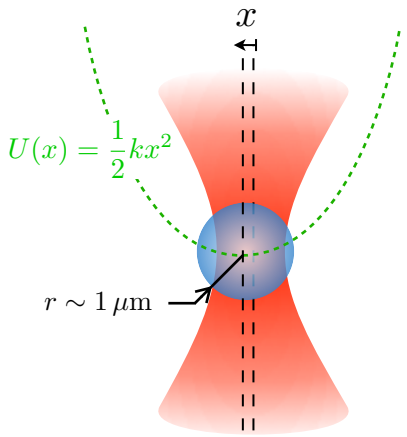

Figure 1.2 – **Schematic overview of an over-damped colloidal particle trapped by optical tweezers** creating an harmonic potential $U(x) = \frac{1}{2}kx^2$.

$\tau_{\text{diff}} = (2r)^2/D$. We compute that the region where $\tau_{\text{inertia}} \ll \tau_{\text{diff}}$ corresponds to $r \gg 0.01\,\text{pm}$. Hence, for the silica beads whose typical radius is $r = 1\,\mu$m, the inertia fades too fast compared to the other phenomena to be noticed and to the acquisition time: $\tau_{\text{inertia}} \sim 0.7\,\mu$s and $\tau_{\text{diff}} \sim 1\,$s. Moreover, the period of the harmonic oscillator $0.1\,\text{ms} < 2\pi/\omega_0 = 2\pi\sqrt{m/k} < 1\,\text{ms}$ is always smaller than the trap characteristic time $\tau_{\text{trap}} = 2\pi\gamma/k$, which is in the range $1\,\text{ms} < \tau_{\text{trap}} < 0.1\,\text{s}$. In other words, the time scales ratio corresponding to the quality factor is very small: $Q = k/(\gamma\omega_0) \sim 10^{-2} \ll 1$. Hence, the regime is strongly over-damped and its dynamic is described by the Langevin Equation (1.8). That is why colloidal particules are often used as proof of over-damped statistical physics principles, whether it concerns shortcuts to equilibrium [10] or information theory [11–14].

1.2.2 Under-damped micro cantilever

Since its invention by Binnig, Quate and Gerber [15] more than 35 years ago, Atomic Force Microscopy (AFM) has turned into a mature technique widely spread in many domains (material sciences, biology, nanotechnology...). The AFM tip is attached to a micro-cantilever which behaves as a micro-oscillator evolving at room temperature. The cantilever is therefore sensitive to thermal noise. Its deflection x can be measured with very high accuracy and signal-to-noise ratio by a differential interferometer [16]. That is why such cantilevers are relevant systems to explore stochastic dynamics.

We use conductive cantilevers to take advantage of the electrostatic force that can be easily applied to them: we approach a metallic surface a distance d from the cantilever's tip, and tune the force at will through the voltages applied, as sketched in Fig. 1.3. Indeed if a voltage V is applied to the cantilever while the facing electrode is kept at a voltage V_0, the voltage difference $V_0 - V$ creates an electrostatic attractive force, $F_{\text{el}} = \frac{1}{2}\partial_d C(d)(V_0 - V)^2$ [17], where $C(d)$ is the cantilever-electrode capacitance. The distance is chosen high enough compared to the characteristic fluctuations of the cantilever, $d \gg \sigma_0$, so that $\partial_d C(d)$ can be assumed constant. That is why we can introduce in the

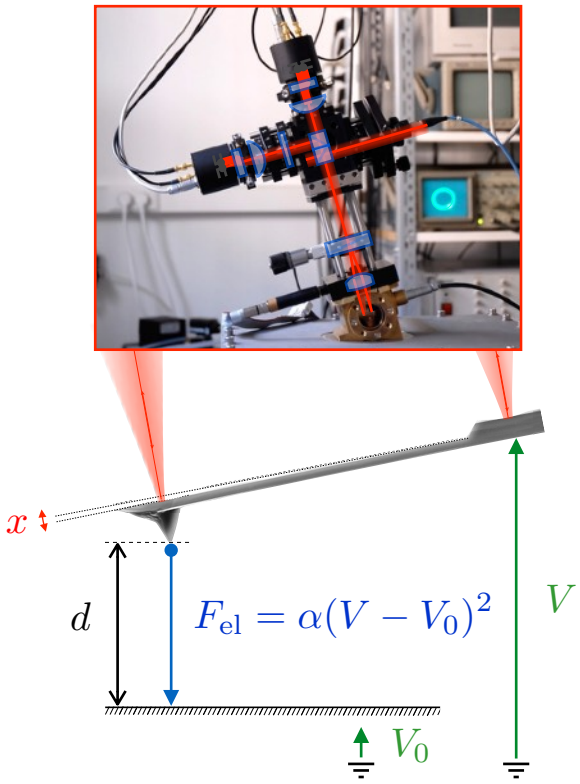

Figure 1.3 – **Schematic overview of an under-damped micro cantilever set-up.** The conductive cantilever at voltage V, whose deflection x is measured by a differential interferometer using two laser beams focused respectively on its base and in its tip, is at distance d from a conductive surface kept at voltage V_0. The voltage difference $V - V_0$ between the two electrodes creates an attractive electrostatic force $F_{\text{el}} = \alpha(V_0 - V)^2$.

following the parameter α:

$$F_{\text{el}} = \alpha(V_0 - V)^2, \text{ with } \alpha = \frac{1}{2}\partial_d C(d). \tag{1.40}$$

As shown by the fluctuation dissipation theorem (FDT) [18], the thermally induced fluctuations are linked to the mechanical response function of the system. Indeed, if we define in Fourier's space the mechanical response function linking the external force F and the deflection x as:

$$G(\omega) = \frac{F(\omega)}{x(\omega)}, \tag{1.41}$$

the FDT stands that the Power Spectral Density (PSD) S_ξ of thermal fluctuations of the force satisfies:

$$S_\xi(\omega) = \frac{2k_B T_0}{\pi\omega}\,\text{Im}(G(\omega)). \tag{1.42}$$

And as a consequence, the PSD S_x of the thermal fluctuations of x is:

$$S_x(\omega) = \frac{1}{|G(\omega)|^2} \times S_\xi(\omega) = \frac{2k_B T_0}{\pi\omega}\,\text{Im}(\frac{1}{G(\omega)}). \tag{1.43}$$

We experimentally illustrate the FDT in Fig. 1.4 by superimposing the imaginary part of the cantilever response function on its natural thermal deflexion PSD. The response function $G^{-1}(\omega)$ is obtained by measuring the response of the system to a white noise electrostatic force.

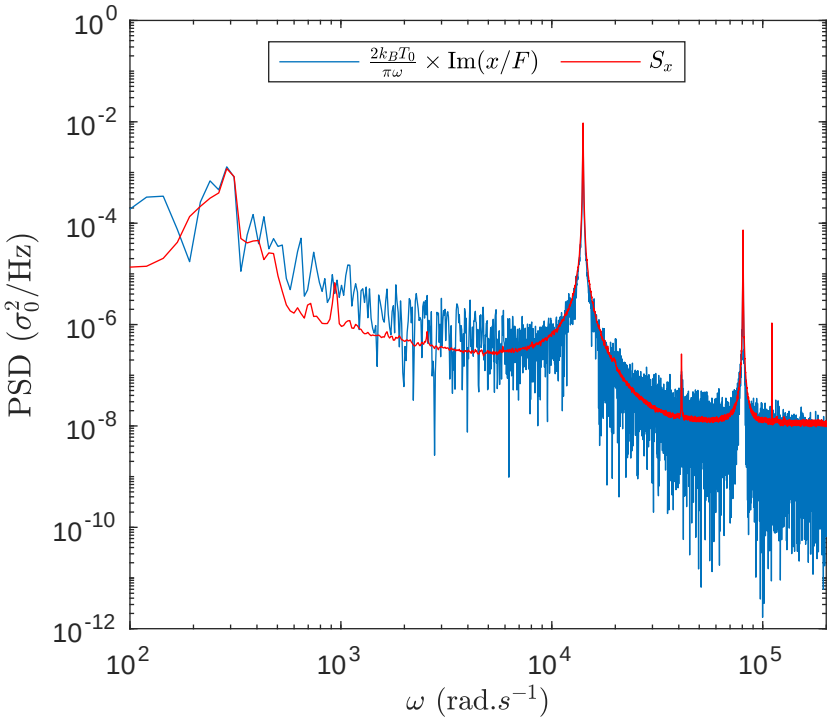

Figure 1.4 – **Fluctuation Dissipation experimental illustration**. $S_x(\omega)$ (red) is inferred from a 10s acquisition of the cantilever's deflexion fluctuation in response to the thermal noise at room temperature T_0, in air. As predicted by the FDT, it matches $\frac{2k_BT_0}{\pi\omega}\,\mathrm{Im}(G^{-1}(\omega))$ (blue). The latter is computed by imposing an intense white noise electrostatic force and measuring the system's response to obtain the transfer function $G^{-1}(\omega) = x(\omega)/F(\omega)$.

It remains to be seen what is the expression of the mechanical response function $G(\omega)$. Many models have been proposed to account for the numerous physical sources of dissipation [19], but in a first approximation the AFM cantilever can be modeled by a damped spring-mass system. The displacement of the punctual mass in the model will correspond to the deflexion x of the cantilever, the spring constant k to the response to the external force F acting on its tip, the mass m to the inertia of the mechanical beam, and the damping coefficient γ to the dissipation processes due to the surrounding atmosphere and internal losses. This Simple Harmonic Oscillator (SHO) responds to the following equation of motion, with $\omega_0 = \sqrt{k/m}$ and $Q = m\omega_0/\gamma$:

$$m\ddot{x} = -kx - \gamma\dot{x} + F \tag{1.44}$$

$$\ddot{x} + \frac{\omega_0}{Q}x + \omega_0^2 x = \frac{F}{m} \tag{1.45}$$

When the external force consists only in the thermal force F_ξ, Eq. (1.45) corresponds to the Langevin equation Eq. (1.6). Here, the regime is underdamped as the damping in the air leads to a viscous force comparable to the inertia. We deduce from Eq. (1.45)

the response function in the SHO model:

$$G^{\mathrm{SH0}}(\omega) = k(1 - u^2 + \frac{u}{Q}), \tag{1.46}$$

where $u = \omega/\omega_0$ is the reduced frequency. We can therefore express the PSD S_ξ when the force originates only from the thermal noise by applying the FDT in Eq. (1.42):

$$S_\xi^{\mathrm{SHO}}(\omega) = \frac{2k_BT_0}{\pi}\gamma. \tag{1.47}$$

Similarly, we obtain the PSD S_x of the thermal fluctuation in x by applying the FDT in Eq. (1.43):

$$S_x^{\mathrm{SHO}}(\omega) = \frac{2k_BT_0}{\pi\omega_0 k}\frac{1/Q}{(1-u^2)^2 + u^2/Q^2} \tag{1.48}$$

Let us point out that the Equipartition theorem prescribes (from Eq. (1.30)):

$$\int_0^\infty S_x(\omega)d\omega = \langle x^2\rangle = \sigma_0^2 = \frac{k_BT_0}{k}. \tag{1.49}$$

The SHO model applies for the fundamental deflexion mode of the cantilever to a very good approximation. If one wants to depict the various modes of oscillation [20] and other mechanical and coupling effects, some other theoretical models have been proposed, including Sader's model [21–23]. In particular the decomposition of the cantilever behavior in normal mode is derived by a clamped-free beam description in an Euler-Bernoulli framework [19; 20].

1.3 Trapping methods

As we are considering micro-size objects, the question of control arises: we will show in the following some trapping methods to control Brownian systems.

1.3.1 Optical tweezers

Optical traps (also called optical tweezers) as the one sketched on Fig. 1.2 allow for trapping and manipulating dielectric particles, with sizes from 10 nm to 10 μm, thanks to the radiation pressure exerted by light on matter. The first experimental realization was done by Ashkin in 1969 [24], using two counter-propagating laser beams to trap micron-sized particles. Then the technology evolved rapidly and successfully, and optical tweezers are nowadays widely used scientific tools, especially in fields like biology, colloids physics and microfluidic [25; 26]. Thanks to a highly focused beam (with a high numerical aperture microscope objective), the gradient force pushing toward the region of high intensity exceeds the scattering force and the particle ends up trapped in the laser beam [27]. All in all, near the center of the beam, the optical tweezer creates an harmonic potential $U(x) = \frac{1}{2}kx^2$. Typical siffnesses are in the range $0.5\,\mathrm{pN}/\mu\mathrm{m} < k < 50\,\mathrm{pN}/\mu\mathrm{m}$.

1.3.2 Virtual potentials

Feedback traps have been demonstrated to trap and manipulate Brownian particles in solution, and explore fundamental questions in non-equilibrium statistical mechanics of small systems [13; 28–30]. Indeed, by controlling an external force acting on a colloidal particle as a function of its measured position, one can create a virtual potential. This is a very powerful tool, more flexible [12; 14; 31] than its physical counterparts consisting of localized potential forces created by optical or magnetic tweezers [11; 14; 32–34].

Virtual potentials can also be used for underdamped systems but the implementation is not an easy task, especially within the stochastic thermodynamics framework that requires a high measurement precision to resolve the $k_B T_0$ scale. Indeed, at low damping, systems are resonant and very sensitive to perturbation, noise or drift. Furthermore, the characteristic time scale of underdamped systems being significantly lower, the feedback update delay can have strong consequences on the coupling between the system and the thermal bath [30; 35].

1.4 Information and thermodynamics

1.4.1 Context

Stochastic thermodynamics comes into play to extend traditional thermodynamic laws - the field of physics focused on how heat and energy move and transform - to account for small-scale fluctuations [36]. Indeed, thermodynamic quantities such as internal energy, applied work, exchanged heat or entropy production cannot be characterized only by their mean values, but their fluctuations and probability distributions become also relevant. The prominent relations providing general laws applicable to non-equilibrium systems, particularly relevant for Brownian systems are reviewed in Ref. 37.

In particular, for driven Brownian motion, Sekimoto gave birth in Refs. 1 and 38 to the stochastic energetics ruling the first law for fluctuating quantities. Ultimately, the definition of a stochastic entropy [39] paved the way for the "fluctuating" second law and the unifying perspective of these two developments has been called the stochastic thermodynamics [40].

Let us point out here that, in most experiments on stochastic thermodynamics, the conclusions about energetic costs (applied work, exchanged heat, kinetic temperature...) rely on precise modeling of the system and measurements of associated quantities, and not on direct calorimetric experiments. For example, in this thesis, we measure the system position x and deduce its velocity v. At the same time, we record the driving parameters of the potential U. From the precise description of the underdamped system, we can then compute the energetic quantities with the expressions given in the next paragraphs.

1.4.2 Stochastic thermodynamics

Over-damped stochastic thermodynamics

We consider an over-damped Langevin description in a potential $U(x)$:

$$\gamma \dot{x} = -\frac{dU}{dx} + \gamma\sqrt{D}\xi(t). \tag{1.50}$$

Following Refs 36–38; 41; 42, we multiply Eq. (1.50) by $\dot{x}$:

$$\frac{dU}{dx}\dot{x} = -\gamma(\dot{x} - \sqrt{D}\xi(t))\dot{x} \tag{1.51}$$

The term $\gamma(\dot{x} - \sqrt{D}\xi(t))\dot{x}$ corresponds to the force exerted by the heat bath on the system, so that Eq. (1.51) defines the first law of thermodynamics for stochastic dynamics:

$$\frac{dU}{dt} = -\frac{d\mathcal{Q}}{dt} \tag{1.52}$$

where $\dot{U}$ is the internal energy variation, and the stochastic dissipated heat $\mathcal{Q}$ into the surrounding environment is defined by:

$$\frac{d\mathcal{Q}}{dt} \equiv \gamma(\dot{x} - \sqrt{D}\xi(t))\dot{x}. \tag{1.53}$$

Now, if there is an external operator acting on the potential $U(x, \lambda)$ through a control parameter λ, we can similarly define the stochastic work performed by the operator. Indeed Eq. (1.51) is consequently amended:

$$\frac{\partial U}{\partial x}\dot{x} = \gamma(-\dot{x} + \sqrt{D}\xi(t))\dot{x} \tag{1.54}$$

$$\frac{dU(x,\lambda)}{dt} = -\gamma(\dot{x} - \sqrt{D}\xi(t))\dot{x} + \frac{\partial U}{\partial \lambda}\dot{\lambda} \tag{1.55}$$

$$\frac{dU(x,\lambda)}{dt} = -\frac{d\mathcal{Q}}{dt} + \frac{\partial U}{\partial \lambda}\dot{\lambda} \tag{1.56}$$

Therefore it is natural to define the work $\mathcal{W}$ done by the operator through the variations the external parameter λ as:

$$\frac{d\mathcal{W}}{dt} \equiv \frac{\partial U}{\partial \lambda}\dot{\lambda} \tag{1.57}$$

We recover a proper energy balance equation:

$$\frac{dU}{dt} = \frac{d\mathcal{W}}{dt} - \frac{d\mathcal{Q}}{dt}. \tag{1.58}$$

As $\dot{U} = \partial_x U\dot{x} + \partial_\lambda U\dot{\lambda}$, we can rewrite the stochastic heat as:

$$\frac{d\mathcal{Q}}{dt} \equiv -\frac{\partial U}{\partial x}\dot{x} \tag{1.59}$$

All in all, if the trajectory of the system $x(t)$ is described by the Langevin equation Eq. (1.50), the stochastic required work $\mathcal{W}$ and the stochastic dissipated heat $\mathcal{Q}$ are obtained by integrating Eqs. (1.57) and (1.59) on the duration of the experiment. As they are fluctuating quantities, depending on the stochastic trajectory x, the relevant quantities are often the probability distribution functions and the average values: $\langle\mathcal{W}\rangle$ and $\langle Q\rangle$, where $\langle.\rangle$ denotes the ensemble average over all possible trajectories.

General formulation

As we are tackling both over-damped and underdamped systems, the stochastic thermodynamics framework has to be extended to the underdamped regime. We follow the same steps than in the previous paragraph including this time the inertial terms and the kinetic energy $K = 1/2m\dot{x}^2$.

As the total energy is now worth $E = U + K$, the energy balance equation becomes:

$$\frac{dK}{dt} + \frac{dU}{dt} = \frac{d\mathcal{W}}{dt} - \frac{d\mathcal{Q}}{dt}, \tag{1.60}$$

with $\mathcal{W}$ still defined by Eq. (1.57) and,

$$\frac{d\mathcal{Q}}{dt} \equiv -\int \frac{\partial U}{\partial x}\dot{x} - \frac{dK}{dt}. \tag{1.61}$$

The computation of an explicit expression of the mean dissipated heat requires to write the general Langevin equation of an underdamped system in a potential U:

$$m\ddot{x} = -\frac{\partial U}{\partial x} - \frac{m\omega_0}{Q}\dot{x} + \gamma\sqrt{D}\xi(t) \tag{1.62}$$

We again multiply Eq.(1.62) by $\dot{x}$ and identify the stochastic heat defined in Eq. (1.61):

$$\frac{d\mathcal{Q}}{dt} = m\ddot{x}\dot{x} - \frac{dK}{dt} + \frac{m\omega_0}{Q}\dot{x}^2 - \gamma\sqrt{D}\xi(t)\dot{x} \tag{1.63}$$

$$= m\ddot{x}\dot{x} - \frac{dK}{dt} + \frac{2\omega_0}{Q}K^2 - \gamma\sqrt{D}\xi(t)\dot{x} \tag{1.64}$$

The term $m\ddot{x}\dot{x}$ involves a product of stochastic quantities, and in that respect cannot be identified with the derivative of K using the Ito derivation rules. Indeed some caution is required and we obtain after discretizing (when the dt tends to 0 limit), taking the average value (to remove all terms of the form of Eq. (1.16)):

$$\frac{d\langle K\rangle}{dt} = m\langle\ddot{x}\dot{x}\rangle + k_B T_0\frac{\omega_0}{Q} \tag{1.65}$$

Hence, Eq. (1.64) simplifies on average into:

$$\frac{d\langle\mathcal{Q}\rangle}{dt} = \frac{d\langle K\rangle}{dt} - k_B T_0\frac{\omega_0}{Q} - \frac{d\langle K\rangle}{dt} + \frac{2\omega_0}{Q}\langle K\rangle - 0 \tag{1.66}$$

$$= \frac{\omega_0}{Q}(2\langle K\rangle - k_B T_0) \tag{1.67}$$

This expression is completely general and doesn't depend on the potential shape or current transformations occurring in the system. It also highlights that for a large quality factor Q, the heat exchanges with the thermal bath are reduced. Finally, at equilibrium when the equipartition theorem prescribes $K_{eq} = \frac{1}{2}k_B T_0$, there are in average no heat exchanges, as expected.

1.4.3 Kinetic temperature

We define the kinetic temperature T of the first deflection mode of the system through the velocity variance $\sigma_v^2 = \langle v^2\rangle - \langle v\rangle^2$:

$$T = \frac{m}{k_B}\sigma_v^2. \tag{1.68}$$

Therefore, the average heat can be expressed from Eq. (1.67) as:

$$\frac{d\langle\mathcal{Q}\rangle}{dt} = \frac{\omega_0}{Q}\Big(m\langle v\rangle^2 + k_B(T - T_0)\Big). \tag{1.69}$$

At equilibrium in a potential that does not depends on the velocity, the kinetic temperature should match the bath temperature T_0 as prescribed by the equipartition (Eq. (1.30)). Besides, when the deterministic terms are negligible compared to the thermal ones, $\langle v \rangle^2 \ll \sigma_v$, the average kinetic energy is proportional to the kinetic temperature, $\langle K \rangle = \frac{1}{2} k_B T$, and the average heat simplifies into:

$$\frac{d\langle \mathcal{Q} \rangle}{dt} = \frac{\omega_0}{Q} k_B (T - T_0) \tag{1.70}$$

1.4.4 Cost of information

The thermodynamic energy cost of information processing is a widely studied subject both for its fundamental aspects and for its potential applications [43–51]. This energy cost has a lower bound, set by Landauer's principle [52]: at least $k_B T_0 \ln 2$ of work is required to erase one bit of information from a memory at temperature T_0, with k_B the Boltzmann constant. This is a tiny amount of energy, only $\sim 3 \times 10^{-21}$ J at room temperature (300 K), but it is a general lower bound, independent of the specific type of memory used. The Landauer bound (LB) has been measured in several classical experiments, using optical tweezers [11; 32], an electrical circuit [53], a feedback trap [12–14] and nanomagnets [33; 34] as well as in quantum experiments with a trapped ultracold ion [54] and a molecular nanomagnet [55]. The LB can be reached asymptotically in quasi-static erasure protocols whose duration is much longer than the relaxation time of the above mentioned systems used as one-bit memories.

1.5 Dimensionless notations

Quantity	Symbol	Dimensionless quantity
System's position	x	$z = x/\sigma_0$
Potential well position	x_1 (respectively X_1)	$z_1 = x/\sigma_0$ (respectively Z_1)
Bi-quadratic potential barrier position	x_0	$z_0 = x/\sigma_0$
Comparator hysteresis	h	$\mathbf{h} = h/\sigma_0$
System's velocity	$v = \dot{x}$	$\mathbf{v} = v/(\sigma_0\omega_0)$
Potential driving velocity	$v_1 = \dot{x}_1$	$\mathbf{v_1} = \dot{z}_1/\omega_0$
Total Energy	E	$\mathbf{E} = E/(k_B T_0)$
Kinetic Energy	K	$\mathbf{K} = K/(k_B T_0)$
Potential Energy	U	$\mathbf{U} = U/(k_B T_0)$
Barrier height Energy	$\mathcal{B}$	$\boldsymbol{\mathcal{B}} = \mathcal{B}/(k_B T_0)$
Work	$\mathcal{W}$	$\boldsymbol{\mathcal{W}} = \mathcal{W}/(k_B T_0)$
Heat	$\mathcal{Q}$	$\boldsymbol{\mathcal{Q}} = \mathcal{Q}/(k_B T_0)$
Temperature	$T = m\sigma_v^2/k_B$	$\theta = T/T_0 = \langle \sigma_{\mathbf{v}}^2 \rangle$

Table 1.1 – Dimensionless notations

In the following, it is sometimes easier to use σ_0 as length scale, ω_0^{-1} as time scale, T_0 as temperature scale, and $k_B T_0$ as energy scale. Let us point out that natural the velocity scale is therefore $\sigma_0 \omega_0$, matching the equilibrium velocity standard deviation $\sigma_{v,0}$ defined in Eq. (1.30).

For clarity purposes we list in Tab. 1.1 the matching between each quantity used in the following and its dimensionless counterpart, which is written using a bold font (except for $z = x/\sigma_0$).

1.6 References

[1] K. Sekimoto, Progress of Theoretical Physics Supplement **130**, 17 (1998).

[2] C. Gardiner, *Stochastic Methods: A Handbook for the Natural and Social Sciences*, Springer Series in Synergetics (Springer Berlin Heidelberg, 2010).

[3] D. S. Lemons and A. Gythiel, American Journal of Physics **65**, 1079 (1997).

[4] K. Itô, Proceedings of the Imperial Academy **20**, 519 (1944).

[5] H. Kramers, Physica **7**, 284 (1940).

[6] A. Fokker, Annalen Der Physik **43**, 810 (1914).

[7] M. Planck, Sitzungsberichte der Königlich Preussischen Akademie der Wissenschaften zu Berlin. **24**, 324 (1917).

[8] S. Dago, J. Pereda, N. Barros, S. Ciliberto, and L. Bellon, Phys. Rev. Lett. **126**, 170601 (2021).

[9] V. Mel'nikov, Physics Reports **209**, 1 (1991).

[10] I. A. Martínez, A. Petrosyan, D. Guéry-Odelin, E. Trizac, and S. Ciliberto, Nature Physics **12**, 843 (2016).

[11] A. Bérut, A. Arakelyan, A. Petrosyan, S. Ciliberto, R. Dillenschneider, and E. Lutz, Nature **483**, 187 (2012).

[12] Y. Jun, M. Gavrilov, and J. Bechhoefer, Phys. Rev. Lett. **113**, 190601 (2014).

[13] M. Gavrilov and J. Bechhoefer, EPL (Europhysics Letters) **114**, 50002 (2016).

[14] K. Proesmans, J. Ehrich, and J. Bechhoefer, Phys. Rev. Lett. **125**, 100602 (2020).

[15] G. Binnig, C. F. Quate, and C. Gerber, Phys. Rev. Lett. **56**, 930 (1986).

[16] P. Paolino, F. Aguilar Sandoval, and L. Bellon, Rev. Sci. Instrum. **84**, 095001 (2013).

[17] H.-J. Butt, B. Cappella, and M. Kappl, Surface Science Reports **59**, 1 (2005).

[18] H. B. Callen and R. F. Greene, Phys. Rev. **86**, 702 (1952).

[19] L. Bellon, *Exploring nano-mechanics through thermal fluctuations*, Habilitation à diriger des recherches, Ecole normale supérieure de lyon - ENS LYON (2010).

[20] H. J. Butt and M. Jaschke, Nanotechnology **6**, 1 (1995).

[21] C. P. Green and J. E. Sader, Journal of Applied Physics **98**, 114913 (2005).

[22] J. E. Sader, Journal of Applied Physics **84**, 64 (1998).

[23] C. A. Van Eysden and J. E. Sader, Journal of Applied Physics **101**, 044908 (2007).

[24] A. Ashkin, Phys. Rev. Lett. **24**, 156 (1970).

[25] D. G. Grier, Nature **424**, 810 (2003).

[26] M. Padgett, J. Molloy, and D. McGloin, *Optical Tweezers: Methods and Applications* (Chapman and Hall/CRC, 2010).

[27] A. Ashkin, J. M. Dziedzic, J. E. Bjorkholm, and S. Chu, Opt. Lett. **11**, 288 (1986).

[28] M. Gavrilov, Y. Jun, and J. Bechhoefer, Review of Scientific Instruments **85**, 095102 (2014).

[29] A. E. Cohen, Phys. Rev. Lett. **94**, 118102 (2005).

[30] Y. Jun and J. Bechhoefer, Phys. Rev. E **86**, 061106 (2012).

[31] J. A. C. Albay, P.-Y. Lai, and Y. Jun, Applied Physics Letters **116**, 103706 (2020).

[32] A. Bérut, A. Petrosyan, and S. Ciliberto, Journal of Statistical Mechanics: Theory and Experiment **2015**, P06015 (2015).

[33] J. Hong, B. Lambson, S. Dhuey, and J. Bokor, Sci. Adv. **2**, e1501492 (2016).

[34] L. Martini, M. Pancaldi, M. Madami, P. Vavassori, G. Gubbiotti, S. Tacchi, F. Hartmann, M. Emmerling, S. Höfling, L. Worschech, and G. Carlotti, Nano Energy **19**, 108 (2016).

[35] M. L. Rosinberg, T. Munakata, and G. Tarjus, Phys. Rev. E **91**, 042114 (2015).

[36] S. Ciliberto, Phys. Rev. X **7**, 021051 (2017).

[37] U. Seifert, Reports on Progress in Physics **75**, 126001 (2012).

[38] K. Sekimoto, *Stochastic Energetics*, Lecture Notes in Physics, Vol. 799 (Springer, 2010).

[39] U. Seifert, Phys. Rev. Lett. **95**, 040602 (2005).

[40] U. Seifert, The European Physical Journal B **64**, 423 (2008).

[41] K. Sekimoto and S. Sasa, Journal of the Physical Society of Japan **66**, 3326 (1997).

[42] C. Jarzynski, Annual Review of Condensed Matter Physics **2**, 329 (2011).

[43] H. Leff and A. Rex, *Maxwell's Demon: Entropy, Classical and Quantum Information, Computing* (Institute of Physics, Philadelphia, 2003).

[44] J. M. R. Parrondo, J. M. Horowitz, and T. Sagawa, Nature Physics **11**, 131 (2015).

[45] E. Lutz and S. Ciliberto, Physics Today **68**, 30 (2015).

[46] C. Lent, A. Orlov, W. Porod, and G. Snider, *Energy Limits in Computation* (Springer, 2018).

[47] M. López-Suárez, I. Neri, and L. Gammaitoni, Nat Commun. **7**, 12068 (2016).

[48] M. Konopik, T. Korten, E. Lutz, and H. Linke, Fundamental energy cost of finite-time computing (2021).

[49] S. Toyabe, T. Sagawa, M. Ueda, M. Muneyuki, and M. Sano, Nature Phys. **6**, 988 (2010).

[50] É. Roldán, I. A. Martínez, J. M. R. Parrondo, and D. Petrov, Nature Physics **10**, 457 (2014).

[51] J. V. Koski, V. F. Maisi, J. P. Pekola, and D. V. Averin, Proceedings of the National Academy of Sciences **111**, 13786 (2014).

[52] R. Landauer, IBM Journal of Research and Development **5**, 183 (1961).

[53] A. O. Orlov, C. S. Lent, C. C. Thorpe, G. P. Boechler, and G. L. Snider, Japanese Journal of Applied Physics **51**, 06FE10 (2012).

[54] L. L. Yan, T. P. Xiong, K. Rehan, F. Zhou, D. F. Liang, L. Chen, J. Q. Zhang, W. L. Yang, Z. H. Ma, and M. Feng, Phys. Rev. Lett. **120**, 210601 (2018).

[55] R. Gaudenzi, E. Burzuri, S. Maegawa, H. S. J. van der Zant, and F. Luis, Nature Physics **14**, 565 (2018).

Chapter 2:

Shortcuts to equilibrium

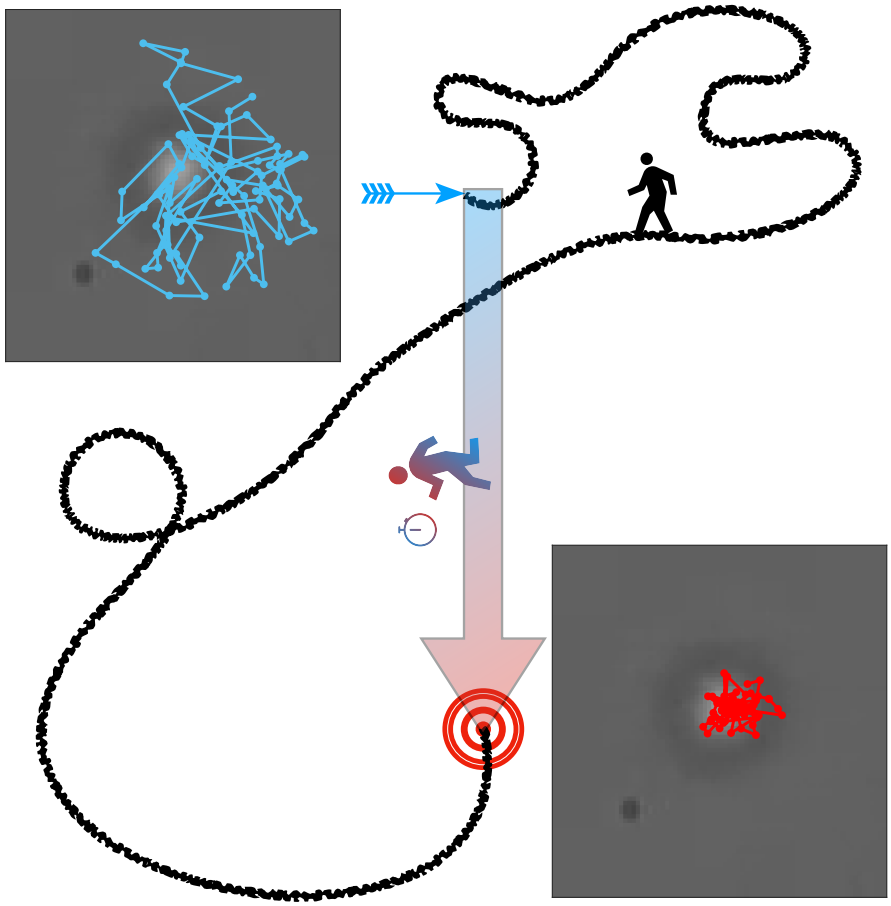

2.1 Engineered Swift Equilibration (ESE)

Speeding-up an equilibration process is a delicate task, because the relaxation time is an intrinsic property of a system which depends on parameters such as the dissipation, the potential strength, the inertia, or the number of degrees of freedom. Furthermore, when a control parameter is suddenly changed, the system may pass from states that widely differ from the target one. One way of speeding up a specific transformation between well defined equilibrium states is to apply complex protocols in which the time dependence of one or several control parameters is tuned in a highly specific fashion, to reach the final target in a selected short amount of time. This problem, related to optimal control theory, can be traced back to Boltzmann [1–3]. It has recently received sustained attention within the framework of the so-called "Shortcut To Adiabaticity" protocols, which study such complex procedures for specific transformations [4].

We are interested here in over-damped systems in contact with a thermostat, for which we can define protocols of Engineered Swift Equilibration (ESE) that shortcut time-consuming relaxations. We apply ESE to Brownian particles trapped by optical tweezers introduced in section 1.2.1 and sketched in Fig. 1.2. The optical trap properties can be controlled in time [5] using experimental set-ups similar to the one described in Appendix B. For example, one can perform the compression of a single particle trapped in an harmonic potential by increasing its stiffness k between an initial state in equilibrium at k_i and a final state in equilibrium at k_f. After a sudden change in k (STEP protocol) the bead will equilibrate with its natural relaxation time ($\tau_{\text{relax}} \sim 15\,\text{ms}$). Using an ESE protocol for the time evolution of $k(t)$, the same final equilibirum state can be reached several order of magnitude faster than STEP [5].

We consider as a benchmark the ESE protocol designed in Ref. 5 for a single particle trapped in the potential $U(t) = \frac{1}{2}k(t)x^2$ evolving in water at temperature T_0. Its over-damped dynamics is described by a the over-damped Langevin equation (1.8) (that can be recast into the Fokker-Planck equation (1.21) for the probability density $\rho(x,t)$). The single particle ESE consists in changing the stiffness over a period of time t_f to reach a new equilibrium at k_f. The corresponding stiffness profile, illustrated in Fig. 2.1a) is:

$$\kappa(s) = 1 + (\kappa_f - 1)(3 - 2s)s^2 - \frac{3\Gamma(\kappa_f - 1)(s-1)s}{1 + (\kappa_f - 1)(3-2s)s^2}, \tag{2.1}$$

using the dimensionless quantities $\kappa(t) = k(t)/k_i$ (in particular $\kappa_f = k_f/k_i$), $s = t/t_f$ and $\Gamma = \gamma/(k_i t_f)$ (ratio of relevant timescales). Indeed, plugging the quadratic potential stiffness driving of Eq. (2.1) into the Fokker-Plank equation (1.21) results into a gaussian probability distribution $\rho(x,t) = \sqrt{\frac{1}{2\pi\sigma(t)^2}}e^{-\frac{x^2}{2\sigma(t)^2}}$ of variance evolution:

$$\sigma(s)^2 = \frac{k_B T_0}{k_i}\frac{1}{1 + (\kappa_f - 1)(3s^2 - 2s^3)}. \tag{2.2}$$

Eq. (2.2) demonstrates that the Boltzmann equilibrium is reached in the initial and final states, as the variance satisfies $\sigma(0)^2 = k_B T_0/k_i$ and $\sigma(t_f)^2 = k_B T_0/k_f$, while keeping a smooth profile in between (in particular vanishing derivatives in 0 and t_f) as shown in Fig. 2.1c). Actually the ESE protocols are precisely computed by demanding a smooth evolution of the probability density between the two Boltzmann equilibrium states enforced by Eq. (2.2), and deducing the corresponding stiffness profile using Eq. (1.21). Different choices of variance profiles (always satisfying the boundary conditions) would lead to different ESE solutions.

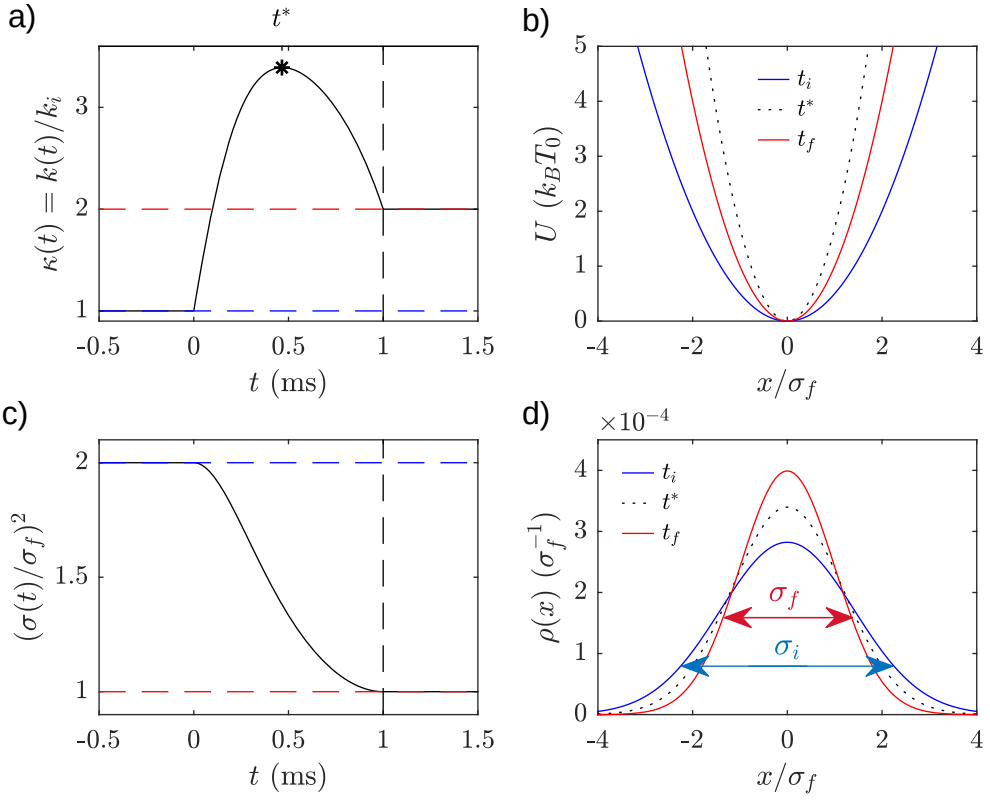

Figure 2.1 – **ESE compression of parameters $\kappa_f = 2$, $\Gamma = 3.8$ and $t_f = 1\,\text{ms}$. a) ESE stiffness driving** $\kappa(t) = k(t)/k_i$ for a compression aiming to double the stiffness ($\kappa_f = 2$) in a short time $t_f = 1\,\text{ms} \ll \tau_{\text{relax}} = 15\,\text{ms}$. The stiffness goes through a maximum in $t^* = 0.47\,\text{ms}$ before reaching the desired final value. **b) Driving potential** $U(x,t)$ at the initial (blue) and final (red) states, and at the transient state in which the stiffness is maximal: $t = t^*$. **c) Time evolution of the variance** $\sigma^2(t)$ of the probability distribution $\rho(x,t)$ in response to the ESE protocol in b). It corresponds to the simplest polynomial form (for $1/\sigma^2$) enforcing the two Boltzmann equilibriums (in dashed blue, and dashed red $\sigma_f^2 = \sigma_i^2/2$) and the constraint of the derivatives (null in 0 and t_f). **d) Probability density** $\rho(x,t)$ at the initial (blue) and final (red) states, and at the transient state in which the stiffness is maximal: $t = t^*$.

2.2 ESE for over-damped coupled particles

When designing these protocols, one of the key questions lies in the stability against external perturbations. In this context, we tackle the case of two particles trapped in different potentials but hydro-dynamically coupled all the more when their separation d decreases. On the first hand we study to what extent the equilibration dynamics imposed by the single particle ESE in Eq. (2.1) is modified by the hydrodynamic interactions with another bead. On the other hand we build and test experimentally a new family of ESE protocols specifically designed for such a more complex system. Our work in this context is extensively covered in Ref. 6 (reproduced in Appendix A), except for the details of the experimental set up that we present in Appendix B. We refer the reader to those two appendices for the complete study, and we only summarize below the main results of Ref. 6:

- The experimental set-up detailed in Appendix A and B allows the study of two hydro-dynamically coupled particles, and the driving of two independent trapping potentials.

- In very good agreement with the model, experiments prove the relative robustness of the single particle ESE of section 2.1 applied to the coupled system. The perturbation due to the coupling deviates the response of only around 10% from the 0-coupling case even when d is smaller than the bead radius r ($d = 0.8\,\mathrm{r}$).

- It is nevertheless possible to work out explicitly ESE solutions that take due account of the coupling, and are therefore immune to it.

- In particular, a protocol enforces independence between the particles is proposed and experimentally validated. It is very robust as it is independent on d.

- Other solutions can be investigated such as a symmetric protocol designed for coupled particles. The latter is more difficult to implement because it requires a precise knowledge of d.

2.3 ESE in the underdamped regime

The ESE protocols addressed in the previous sections are designed for over-damped confined Brownian object. It is desirable to study the generalization of the idea to underdamped situations, when inertial effects are no longer negligible (such as for the AFM cantilever). In the underdamped regime, one should include the velocity degree of freedom v in the description, and the probability density function $P(x, v, t)$ now obeys Kramer's equation (1.18). Many transformations can be addressed with ESE protocols, for example transport of an underdamped oscillator as been studied in Ref. 7. We focus here on protocols similar to those of previous section: compression of the trapping potential. For a compression in a time dependent harmonic potential the dynamics is entirely described by three moments [8], $\theta_x(t) = 1/(2\sigma_x^2)$, $\theta_v(t) = 1/(2\sigma_v^2)$ and $\theta_{xv}(t)$ defined by:

$$P(x, v, t) = P_0(t) \exp\Big\{-\theta_x(t)x^2 - \theta_y(t)v^2 - \theta_{xv}(t)xv\Big\} \tag{2.3}$$

In order to shortcut the relaxation to a stiffness change from k_i to k_f in a duration t_f, the boundary conditions on the moments are imposed according to the Boltzmann equilibrium:

$$\theta_x(0) = \frac{k_i}{k_B T_0} \qquad \theta_x(t_f) = \frac{k_f}{k_B T_0} \tag{2.4}$$

$$\theta_v(0) = \frac{m}{k_B T_0} \qquad \theta_v(t_f) = \frac{m}{k_B T_0} \tag{2.5}$$

$$\theta_{xv}(0) = 0 \qquad \theta_{xv}(t_f) = 0 \tag{2.6}$$

Following to the over-damped method, ESE protocols are obtain by reverse computation using Kramer's equation, but the resolution is much more complex. In Ref. 8 are proposed several families of explicit protocols, depending once again on the moments' chosen profile meeting the boundary conditions. M. Chupeau and coworkers manage to exhibit ESE protocols for which the only quantity that has to be driven is the trap stiffness $k(t)$. Depending on the system properties (damping, initial stiffness, mass...), the stiffness profile can be irregular and sometimes have negative values.

Let us compute an example of ESE protocol designed for a highly underdamped micro-mechanical oscillator, following step by step the method in Ref. 8. We choose parameters consistent with the micro cantilever used in the following: $f_0 = 12\,\mathrm{kHz}$, $k_i = 0.12\,\mathrm{N/m}$ and $Q = 53$. The characteristic relaxation time of the cantilever in the exponential decay is $\tau_r = 2Q/\omega_0 \sim 2\,\mathrm{ms}$. We propose in Fig. 2.2a) the ESE stiffness driving to compress the system by a factor 2 and shortcut the relaxation to $t_f = 0.7\,\mathrm{ms} \sim \tau_r/3$. We compare in Fig. 2.2b) c) and d) the moments evolution in response to the ESE, with the response to a STEP (sudden change in stiffness). Both were obtained by solving numerically Kramer's equation with the ESE stiffness driving of Fig. 2.2a). The system natural relaxation consists in decaying oscillations (at its resonance frequency), before reaching the new equilibrium after almost $3\tau_r \sim 9t_f$. On the contrary, the ESE protocol successfully shortcuts the relaxation to t_f and removes the transient oscillations, at the expense of a high stiffness maximum in the ESE profile. Of course, contrary to over-damped system the natural relaxation time of underdamped oscillators is already very small, so that the gain in time is less impressive. Larger accelerations could be computed, but it would require a control range for the stiffness beyond what would be reasonably accessible in experiments.

All in all, the ESE presented in Fig. 2.2 would be a concrete application of the extension of ESE to the underdamped regime, achievable for the our experimental underdamped system. In this perspective, we study in section 2.4 the feasibility of driving the potential stiffness in which evolves the AFM cantilever whose natural stiffness is fixed by its mechanical properties.

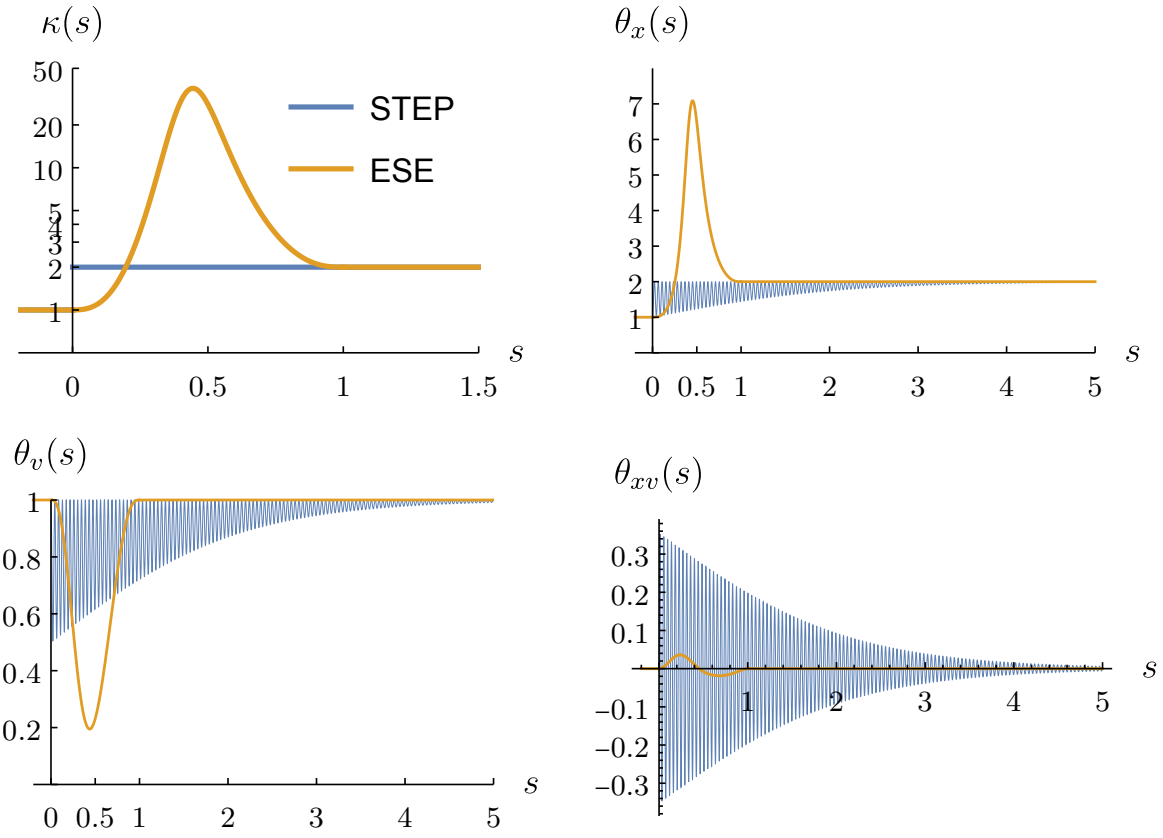

Figure 2.2 – **a) ESE protocol for the underdamped cantilever**. The ESE is designed to double the stiffness: $k_f = 2k_i$, in $t_f = 0.7\,\text{ms}$ (used to define the normalized time $s = t/t_f$). The systems parameters required to compute the ESE protocol are chosen to match the micro cantilever characteristics: $k_i = 0.12\,\text{N/m}$, $\omega_0 = \sqrt{k_i/m} = 7.5 \times 10^4\,\text{rad}\,\text{s}^{-1}$, and $Q = m\omega_0/\gamma = 53$ so that $\Gamma = \gamma/(k_i t_f) = 3.6 \times 10^{-4}$. The ESE normalized stiffness $\kappa(s) = k(s)/k_i$ goes through a maximum $\kappa = 35$ before reaching $k(t_f) = 2$. **b) c) and d) Evolution of the moments in response to an ESE, and a STEP,** inferred from the numerical resolution of the Kramer's equation with the stiffness profiles in a). As expected the ESE responses are shortcut to t_f, while on the contrary the relaxation oscillations the STEP decays exponentially with a time constant of $\tau_r = 3t_f$.

2.4 Prototype of experimental demonstration

2.4.1 Underdamped micro-mechanical oscillator

The underdamped oscillator is a conductive cantilever[1] which is weakly damped by the surrounding air. Its deflection x is measured with very high accuracy and signal-to-noise ratio by a differential interferometer [9]. The Power Spectral Density (PSD) of the thermal fluctuations of x is plotted in Fig. 2.3(a). The fit with the thermal noise spectrum of a Simple Harmonic Oscillator (SHO) (Eq. (1.48)) gives the system's resonance frequency $f_0 = \omega_0/2\pi = 11.76\,\mathrm{kHz}$, and quality factor $Q = 65$. From the PSD we also compute the variance $\sigma_0^2 = \langle x^2 \rangle = (0.14\,\mathrm{nm})^2$ used to normalize measured quantities and deduce the stiffness $k = k_B T_0/\sigma_0^2 = 0.22\,\mathrm{N/m}$. A voltage V is applied to the cantilever, and the facing electrode at a distance d is kept at a voltage V_0. Since $d \gg \sigma_0$ the resulting electrostatic force is given by Eq. (1.40): $F_{\mathrm{el}} = \alpha(V_0 - V)^2$.

2.4.2 How to drive the potential stiffness using a feedback-loop

In the following sections we detail the creation of a virtual harmonic potential whose stiffness can be tuned at will. The principle of the feedback-loop is displayed on Fig. 2.3b): a voltage proportional to the measured position is applied to the conductive cantilever, $V \propto x$. If $V_0 \gg V$ the electrostatic force can be linearized: $F_{\mathrm{el}} = \alpha V_0^2 - 2\alpha V_0 V$. In the following we systematically ignore the first static term as we only pay attention to the potential stiffness. We therefore have a force proportional to the deflexion: $F_{\mathrm{el}}(x) = -k_{\mathrm{el}} x$, with k_{el} growing linearly with V_0. The system response to the feedback electrostatic force ruled by the SHO equation of motion (Eq. (1.44)) obeys:

$$m\ddot{x} = -kx - \gamma\dot{x} + F_{\mathrm{el}}(x) + F_\xi \tag{2.7}$$

$$= -(k + k_{\mathrm{el}})x - \gamma\dot{x} + F_\xi, \tag{2.8}$$

where the thermal force is defined in Eq. (1.4). As a consequence the system behaves as an underdamped oscillator in a virtual potential of effective stiffness $k_{\mathrm{eff}} = k + k_{\mathrm{el}}$, where $k_{\mathrm{el}} \propto V_0$ can be tuned at will.

2.4.3 Practical implementation and model of the feedback-loop

The block diagram in Fig. 2.4 summarizes the feedback-loop design that results in the desired virtual potential. First, the photodiodes signals are combined to obtain a voltage V_x proportional to the system position: the proportionality constant is called β so that $V_x = \beta x$. To remove the drifts and the static terms, the signal V_x then enters a high pass filter of cutoff frequency $f_{\mathrm{hp}} = \frac{1}{\tau_{\mathrm{hp}}} = 1\,\mathrm{Hz}$, whose transfer function is given by:

$$H_{\mathrm{hp}}(\omega) = \frac{V(\omega)}{V_x(\omega)} = \frac{i\omega\tau_{\mathrm{hp}}}{1 + i\omega\tau_{\mathrm{hp}}}. \tag{2.9}$$

[1] Doped Chromium and Platinium coated cantilever Budget Sensor All in One.

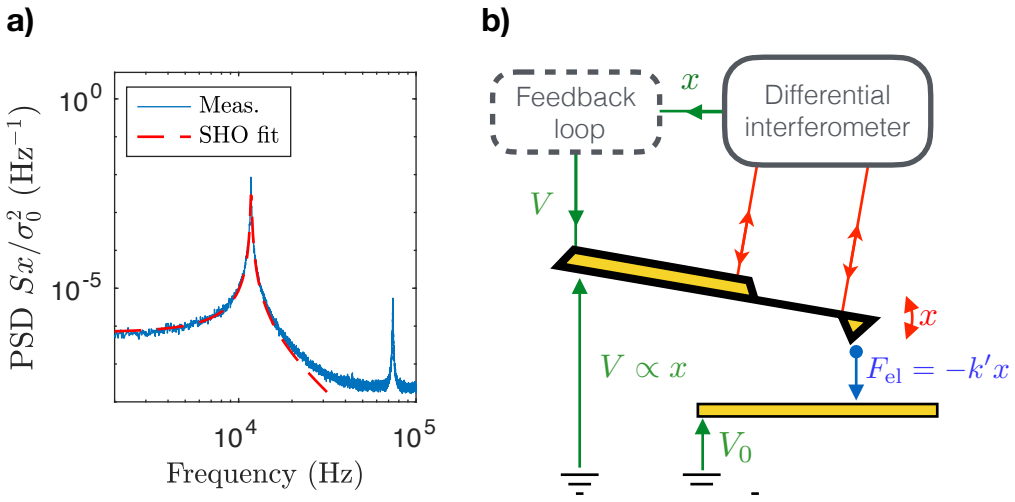

Figure 2.3 – a) **Measured Power Spectrum Density (PSD)** of the cantilever deflection thermal noise with no feedback ($V_0 = 0$, blue), and best fit by the theoretical thermal noise spectrum of a Simple Harmonic Oscillator (following Eq. (1.48), dashed red). Up to 50 kHz, the cantilever behaves like a resonator at $f_0 = 11.76$ kHz, with a quality factor $Q = 65$. We infer from this measurement the variance $\sigma_0^2 = \langle x^2 \rangle = k_B T_0/k$. **b) Schematic diagram of the experiment.** The conductive cantilever is sketched in yellow. Its deflection x is measured with a differential interferometer [9], through two laser beams focused respectively on the cantilever and on its base. The cantilever at voltage $V \propto x$ is facing an electrode at $V_0 \gg V$. The voltage difference $V_0 - V$ between them creates an attractive electrostatic force $F_{\rm el} = \alpha(V_0 - V)^2 \simeq -k_{\rm el} x$ (up to a static force). The dashed box encloses the feedback controller, consisting in the photodiode signals processing and filtering.

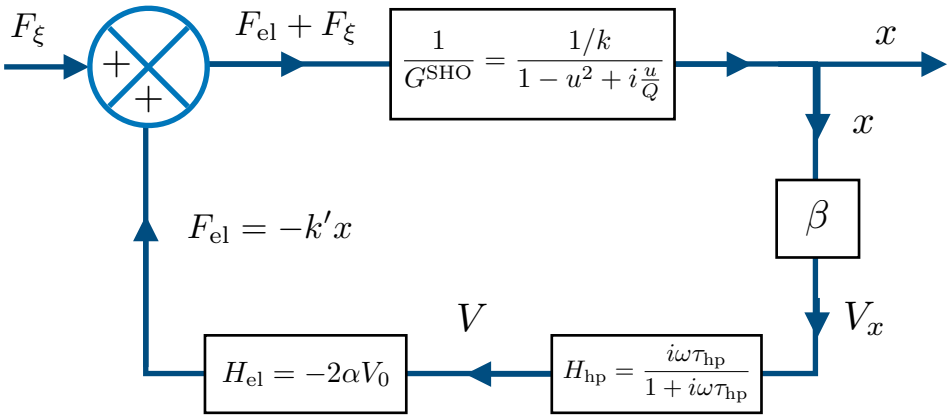

Figure 2.4 – **Feedback-loop block diagram**. The position x with feedback off only consists into the mechanical SHO response to the thermal force F_ξ. In contrast, with the feedback on, the response of the system is modified and is given by the feedback transfer function $H(\omega) = x(\omega)/F_\xi(\omega)$. H can be deduced from the diagram and the block expressions, with $u = \omega/\omega_0$. The feedback consists in converting the position x into a voltage V_x (block β), then filtering the static contribution to obtain the voltage V (block $H_{\rm hp}$), before polarizing the cantilever to create the electrostatic force $F_{\rm el}$ (block $H_{\rm el}$).

At high frequency (around the resonance), $H_{\rm hp} \sim 1$ so that this is transparent for the filtered voltage called V which is finally applied to the cantilever. As long as we impose $V_0 \gg \sqrt{\langle V^2 \rangle} \sim 10\,\text{mV}$, the resulting electrostatic force can be linearized and is worth $F_{\rm el} = -2\alpha\beta V_0 x$, up to a static term. In Fourier's space $F_{\rm el}(\omega) = H_{\rm el} \times \beta \times x(\omega)$ with $H_{\rm el} = -2\alpha V_0$. The stiffness $k_{\rm el}$ defined in the above section is therefore:

$$k_{\rm el} = 2\alpha\beta V_0. \tag{2.10}$$

Before computing the whole transfer function with the feedback on, it should be remembered that the mechanical response of the system to any external force is given by the mechanical response function defined in Eq. (1.46):

$$x(\omega) = \frac{1}{G^{\rm SHO}(\omega)} F(\omega) \tag{2.11}$$

All the feedback steps detailed above are expressed in Fourier's space in the diagram structure of Fig. 2.4. Using block diagram reduction rules we are able to model the system response to the thermal force with the feedback on. Indeed the feedback whole transfer function $H(\omega)$ can be simplified into:

$$H(\omega) = \frac{x(\omega)}{F_\xi(\omega)} \tag{2.12}$$

$$= \frac{1/G^{\rm SHO}}{1 - 1/G^{\rm SHO} \times \beta \times H_{\rm hp} \times H_{\rm el}} \tag{2.13}$$

$$= \frac{1}{G^{\rm SHO} + k_{\rm el}\left(\frac{i\omega\tau_{\rm hp}}{1+i\omega\tau_{\rm hp}}\right)} \tag{2.14}$$

As we are only interested in the system dynamic response, we will consider $\omega \gg 1/\tau_{\text{hp}} = 1$ in the following, so that Eq. (2.14) becomes:

$$H(\omega) = \frac{1}{G^{\text{SHO}} + k_{\text{el}}} \tag{2.15}$$

$$= \frac{1}{k(1 - u^2 + i\frac{u}{Q}) + k_{\text{el}}} \text{ with } u = \frac{\omega}{\omega_0} \tag{2.16}$$

$$= \frac{1}{k_{\text{eff}} - m\omega_{0,\text{eff}}^2 + i\omega_{0,\text{eff}}\gamma} = \frac{1}{G_{\text{eff}}^{\text{SHO}}}, \tag{2.17}$$

Hence, the feedback modeled in Fig. 2.4 corresponds to an effective SHO model of same mass m, same damping γ and effective stiffness: $k_{\text{eff}} = k + k_{\text{el}}$, so that $\omega_{0,\text{eff}} = \sqrt{k_{\text{eff}}/m} = \sqrt{k_{\text{eff}}/k} \times \omega_0$, and $Q_{\text{eff}} = \sqrt{k_{\text{eff}}/k} \times Q$

2.4.4 Calibration and Experimental results

To fully characterize the feedback operations, we need to calibrate the β and α parameters that govern the effective stiffness through Eq. (2.10). As α corresponds to the electrostatic force pre-factor (introduced in Eq. (1.40)), it can be deduced by measuring the mean position for growing polarisations V_0, with the feedback off ($V = 0\,\text{V}$). Indeed, the average position (set to the origin for $V_0 = 0\,\text{V}$) is $\langle x \rangle = \alpha V_0^2/k$. The calibration line in Fig. 2.5a) results in $\alpha = 9.7 \times 10^{-12}\,\text{N/V}^2$.

Furthermore, the parameter β defines the measurement sensitivity and depends on both the interferometer and the photodiodes signals conversion. We measure $\sqrt{\langle V_x^2 \rangle} = 13\,\text{mV}$, and knowing that $\sigma_0 = 0.14\,\text{nm}$, we directly deduce $\beta = 9 \times 10^7\,\text{V/m}$. We consider here that the detection system calibration doesn't depend on cantilever's position, that is to say that we assume β to remain constant.

We compare in Fig. 2.6 the experimental PSD of thermal fluctuation S_x, to the model (with no adjustable parameters) for a wide panel of V_0 values. The theoretical PSD, S^{th}, is computed using the feedback response function expressed in Eq. (2.14) and the thermal force PSD defined in Eq. (1.47):

$$S^{\text{th}}(\omega) = |H(\omega)|^2 \times S_\xi(\omega) \tag{2.18}$$

$$= \frac{2k_B T_0}{\pi}\gamma \times |H(\omega)|^2 \tag{2.19}$$

We have shown that for $\omega \gg 1$, $H(\omega)$ simplifies into Eq. (2.17) so that S^{th} corresponds the thermal noise spectrum of a Single Harmonic Oscillator of angular resonance frequency $\omega_{0,\text{eff}} = \sqrt{(k + k_{\text{el}})/m}$. Fig. 2.6 highlights that the model, using the calibration parameters, fits the experimental curves: the systems behaves as an effective oscillator whose stiffness can be tuned in a wide range with $-120\,\text{V} < V_0 < 120\,\text{V}$.

From the spectrums in Fig. 2.6, the model seems reliable to characterize the resulting effective frequency with the feedback on. To confirm this observation, we plot on Fig. 2.5c) the measured resonance frequencies and the corresponding stiffnesses. As predicted by the model, $k_{\text{eff}} = k + k_{\text{el}}$ increases linearly with V_0, and perfectly matches Eq. (2.10) with α and β from calibration. Besides for $V_0 = 0\,\text{V}$, there is no feedback anymore, so that we recover the natural stiffness of the cantilever $k = 0.22\,\text{N/m}$.

To put it in a nutshell, the implementation of the feedback loop successfully results in a harmonic oscillator behavior with an effective stiffness tuned within a wide range, as confirmed by the experimental potentials shapes plotted in Fig. 2.5. Indeed,

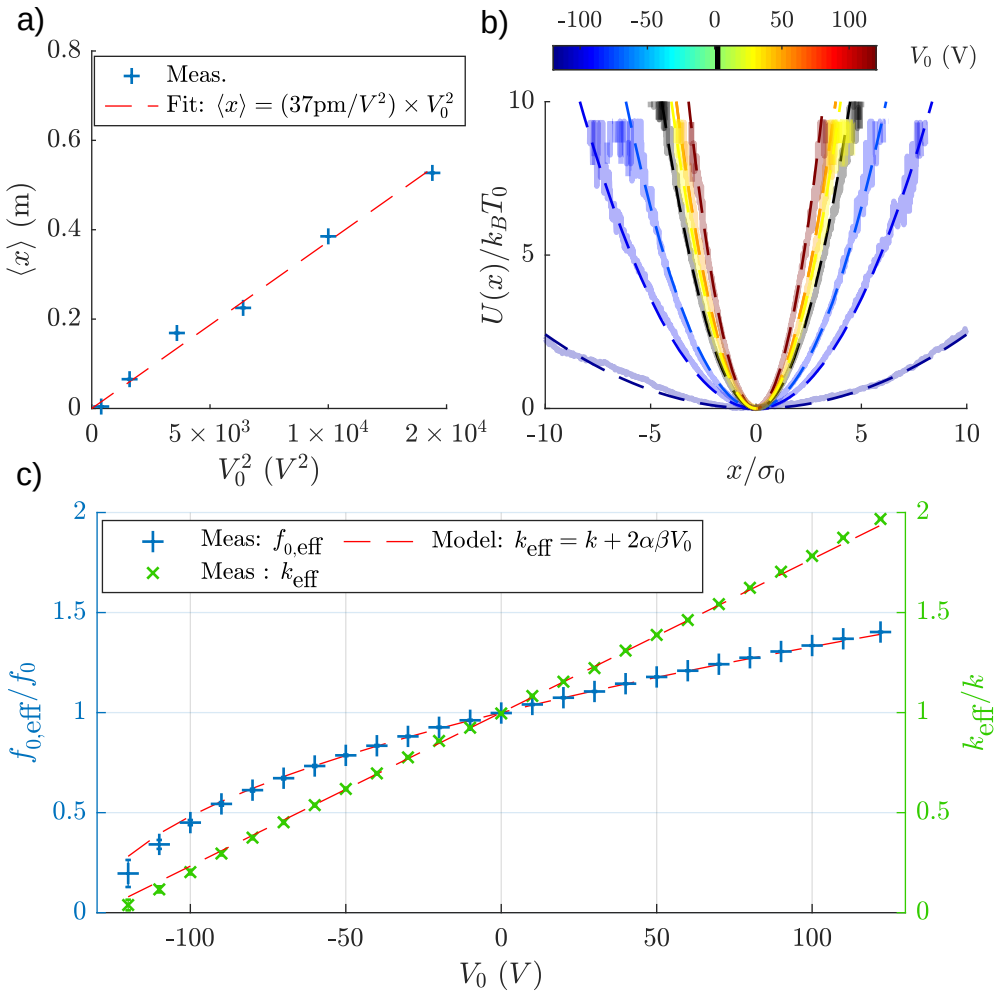

Figure 2.5 – **a) Calibration of the electrostatic force pre-factor** α. With the feedback off ($V = 0$), the electrostatic force is $F_{\text{el}} = \frac{1}{2}\partial_d C(d) V_0^2 = \alpha V_0^2$, so that $\langle x\rangle = \alpha V_0^2/k$. The linear fit (red) to the experimental calibration points (blue) confirms the expression of the force and results in $\alpha = 9.7 \times 10^{-12}\,\text{N/V}^2$. **b) Measured potential energy** (bold lines) obtained with the feedback on and V_0 from $-120\,\text{V}$ to $120\,\text{V}$. The potentials (centered on 0) are inferred from the measured Probability Density Function (PDF) of x during a 10 s acquisition and the Boltzmann distribution. The model $U(x) = \frac{1}{2}k_{\text{eff}}x^2$ with $k_{\text{eff}} = k + k_{\text{el}} = k + 2\alpha\beta V_0$ is superimposed in dashed line: using the α and β calibration values, the model is in perfect agreement with the experimental curves. The black lines corresponds to the physical potential with no feedback **c) Effective resonance frequency and effective stiffness tuned via** V_0. $f_{0,\text{eff}}$ (blue) and k_{eff} (green) are inferred from the experimental spectrums in Fig. 2.6: they cover respectively $3\% < k_{\text{eff}}/k < 200\%$ and $9\% < f_{0,\text{eff}}/f_0 < 142\%$ when $-120\,\text{V} < V_0 < 120\,\text{V}$, and are worth the natural system characteristics ($f_0 = 11.76\,\text{kHz}$ and $k = 0.22\,\text{N/m}$) when $V_0 = 0$. The model (dashed red), using calibration parameters, perfectly matches the experimental points.

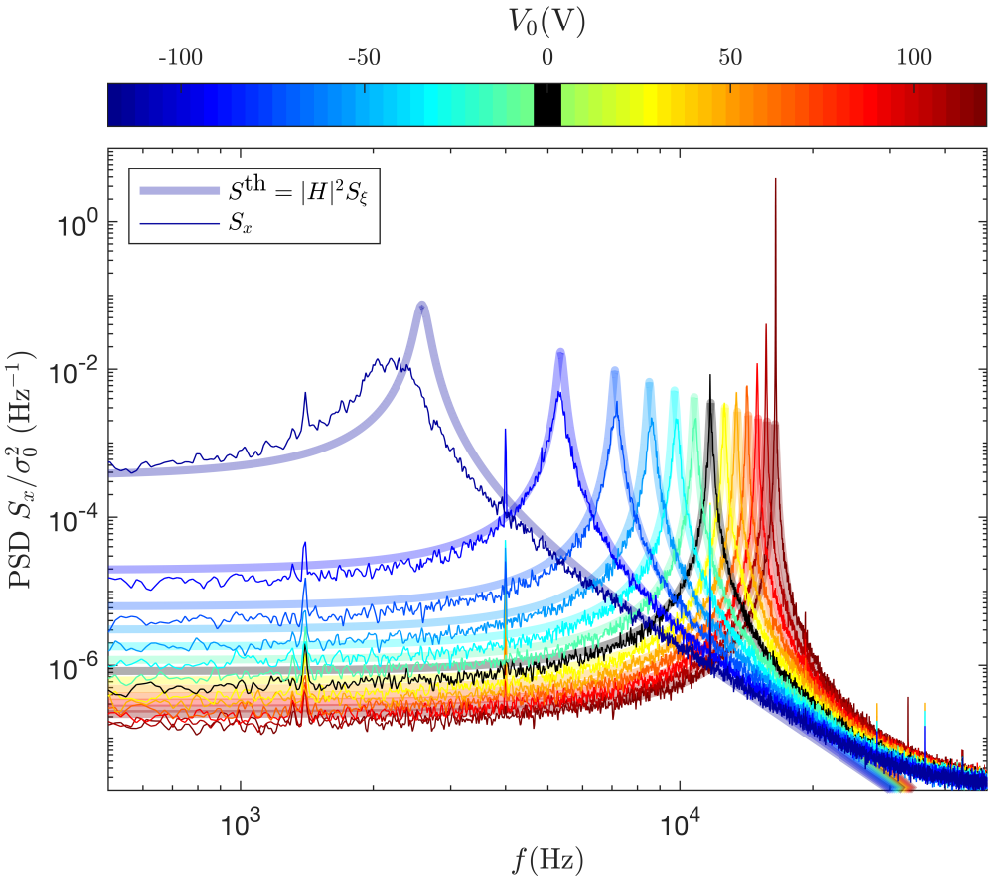

Figure 2.6 – **Thermal deflexion PSD with the feedback on**. The experimental PSD, S_x, demonstrate the success of the feedback loop: for negative V_0 (blue) the stiffness is virtually decreased and the resonance peak drift towards the low frequencies, and on the contrary for positive V_0 (red) the stiffness is virtually increased and the peaks drift toward the high frequencies. The black curve corresponds to the system natural PSD with the feedback off. The model S^{th} of Eq. (2.19) (with no adjustable parameters) is superimposed in bold transparent lines: it successfully predicts modification of the resonance. Nevertheless, the sharpness of the peaks is not perfectly modeled. Indeed the system response deviate from the model as it seems to diverge at the resonance for highly positive V_0, meanwhile it is smoothed for highly negative V_0.

for $-120\,\mathrm{V} < V_0 < 120\,\mathrm{V}$ the stiffness evolves between 3% and 200% of its natural value (see Fig. 2.5c)).The model of the system response with feedback detailed in section 2.4.3, is in perfect agreement with the experimental results (in Fig. 2.5b), c) and Fig. 2.6) as regards the effective stiffness, therefore allowing a reliable control.

Nevertheless, we see on Fig. 2.6 that even if the resonance frequency is successfully predicted, the model doesn't describe properly the sharpness of the resonance, mostly for the highest effective frequencies. Experimentally we indeed observe that for high V_0, the system response tends to diverge as the resonance becomes very peaked. We will show in the next section how to include this effect into the model, by studying the consequences of a feedback-delay.

2.4.5 Consequences of a feedback-delay

Refined model

The divergence of the resonance observed in the experimental spectrums of Fig. 2.6 corresponds to the rise of the quality factor $Q = \frac{\sqrt{km}}{\gamma}$ coming along with the stiffness increase. Actually, when the stiffness is modified by the feedback, the damping also is affected and the effective damping γ_{eff} evolves conversely. This unwanted damping contribution comes from the phase introduced during the feedback operations. Indeed the detection devices that converts the photodiode signals into the position voltage V_x has a finite pass band. It behaves as a low-pass filter of characteristic time τ:

$$F_{\mathrm{el}}(\omega) = -\frac{k_{\mathrm{el}}}{1+i\omega\tau}x(\omega) \tag{2.20}$$

$$= -\frac{k_{\mathrm{el}}}{1+(\omega\tau)^2}x - \frac{k_{\mathrm{el}}\tau}{1+(\omega\tau)^2}i\omega x \tag{2.21}$$

As a consequence, the resulting electrical force is no longer proportional to the position only, but also involves the position time derivative (in the Fourier's space $\dot{x} = i\omega x$). Since we considered a frequency range (near the resonance) much lower than the feedback band pass, $\omega\tau \ll 1$, Eq. (2.21) simplifies into:

$$F_{\mathrm{el}}(\omega) = -k_{\mathrm{el}}x - k_{\mathrm{el}}\tau i\omega x, \tag{2.22}$$

and the equation of motion (2.7) becomes:

$$m\ddot{x} = -(k+k_{\mathrm{el}})x - (\gamma - k_{\mathrm{el}}\tau)\dot{x} + F_\xi \tag{2.23}$$

$$= -k_{\mathrm{eff}}x - \gamma_{\mathrm{eff}}\dot{x} + F_\xi, \tag{2.24}$$

with $\gamma_{\mathrm{eff}} = \gamma - k_{\mathrm{el}}\tau$, and as previously $k_{\mathrm{eff}} = k + k_{\mathrm{el}}$.

All in all this model refinement explains why when the potential stiffness is virtually increased, the damping is on the contrary virtually decreased. When it vanishes, the resonance culminates and the system diverges, reaching a self oscillating state for negative damping.

Bias of the PSD in the virtual potential

When there is delay in the feedback, the position PSD in the virtual potential deviates from the SHO model. In other words, the virtual potential is not perfectly equivalent to a physical potential with tunable effective parameters.

Indeed, the system response model in Eq. (2.17), is modified to account for the feedback delay τ:

$$\tilde{H}(\omega) = \frac{1}{k - m\omega^2 + i\gamma\omega k_{\rm el} - ik_{\rm el}\tau\omega} \tag{2.25}$$

$$= \frac{1}{k_{\rm eff} - m\omega_{\rm eff}^2 + i\gamma_{\rm eff}\omega_{\rm eff}} \tag{2.26}$$

$$= \frac{1}{k_{\rm eff}(1 - u_{\rm eff}^2 + i\frac{u_{\rm eff}}{\tilde{Q}_{\rm eff}})} = \frac{1}{\tilde{G}^{\rm SHO}}, \tag{2.27}$$

introducing $\tilde{G}^{\rm SHO}$ the SHO mechanical response function of parameters $k_{\rm eff}$, $\omega_{0,\rm eff}$ (so that the reduced frequency is $u_{\rm eff} = \omega/\omega_{0,\rm eff}$) and $\tilde{Q}_{\rm eff} = m\omega_{0,\rm eff}/\gamma_{\rm eff}$. However, the thermal force PSD S_ξ remains the same (Eq. (1.47)), involving the bath damping γ rather than the virtual effective one $\gamma_{\rm eff}$. Hence, the system thermal fluctuations PSD in the virtual potential becomes in the presence of feedback delay:

$$\tilde{S}^{\rm th}(\omega) = |\tilde{H}(\omega)|^2 S_\xi(\omega) \tag{2.28}$$

$$= \frac{\gamma}{\gamma_{\rm eff}} \times \frac{2k_B T_0}{\pi\omega_{0,\rm eff}k_{\rm eff}} \frac{1/\tilde{Q}_{\rm eff}}{(1 - u_{\rm eff}^2)^2 + (\frac{u_{\rm eff}}{\tilde{Q}_{\rm eff}})^2} \tag{2.29}$$

$$= \frac{\gamma}{\gamma_{\rm eff}} \times S_x^{\rm SHO,eff}. \tag{2.30}$$

$\tilde{S}^{\rm th}(\omega)$ differs from the SHO model, of the form of Eq. (1.48) with effective parameters, by a factor $\frac{\gamma}{\gamma_{\rm eff}}$. The delay in the feedback loop virtually affects the effective temperature as well, with $T_{\rm eff} = \gamma/\gamma_{\rm eff}T_0 = 1/(1 - k_{\rm el}\tau\gamma)T_0$. To phrase it differently, the FDT doesn't apply in the virtual potential as it would do for a physical one with the same characteristics and temperature.

Comparison with experimental results

We fit the experimental PSD's (plotted again on Fig. 2.8) with the theoretical expression in Eq. (2.29) with $\tilde{Q}_{\rm eff}$ as only free parameter ($k_{\rm eff} = k + k_{\rm el}$ and consequently $u_{\rm eff}$ are fixed following Eq. (2.10)). We plot the corresponding damping, $\gamma_{\rm eff} = m\omega_{0,\rm eff}/\tilde{Q}_{\rm eff}$, as a function of $k_{\rm el}$ in Fig.2.7a): the linear behavior demonstrates the validity of the model $\gamma_{\rm eff} = \gamma - k_{\rm el}\tau$. Hence, the feedback delay τ is deduced from the best linear fit (dashed red): $\tau = 0.23\,\mu$s. This delay in the feedback is likely to come from the cut off frequency of the photodiodes' current to voltage amplifiers, $f_c \sim 4\,$MHz.

To complete the analysis, we highlight in Fig.2.7b) that $\tilde{Q}_{\rm eff}$ varies on a very wide range, between $\tilde{Q}_{\rm eff} = 6$ and $\tilde{Q}_{\rm eff} = 12400$ respectively reached for $V_0 = -120\,$V and $V_0 = 120\,$V, therefore explaining the depletion and the divergence of the resonance observed on the experimental PSD.

To conclude, we compare in Fig. 2.8 the refined model prediction of Eq. (2.29) (using calibration values for α, β and τ) to the experimental PSD. This time, the model perfectly accounts for both the resonance frequency modification and the associated evolution of the resonance sharpness.

2.4.6 Limitations and perspectives

The experiment conducted here is only preliminary, but turns out to be very encouraging. Indeed the feedback control of the potential allows to tune the stiffness within

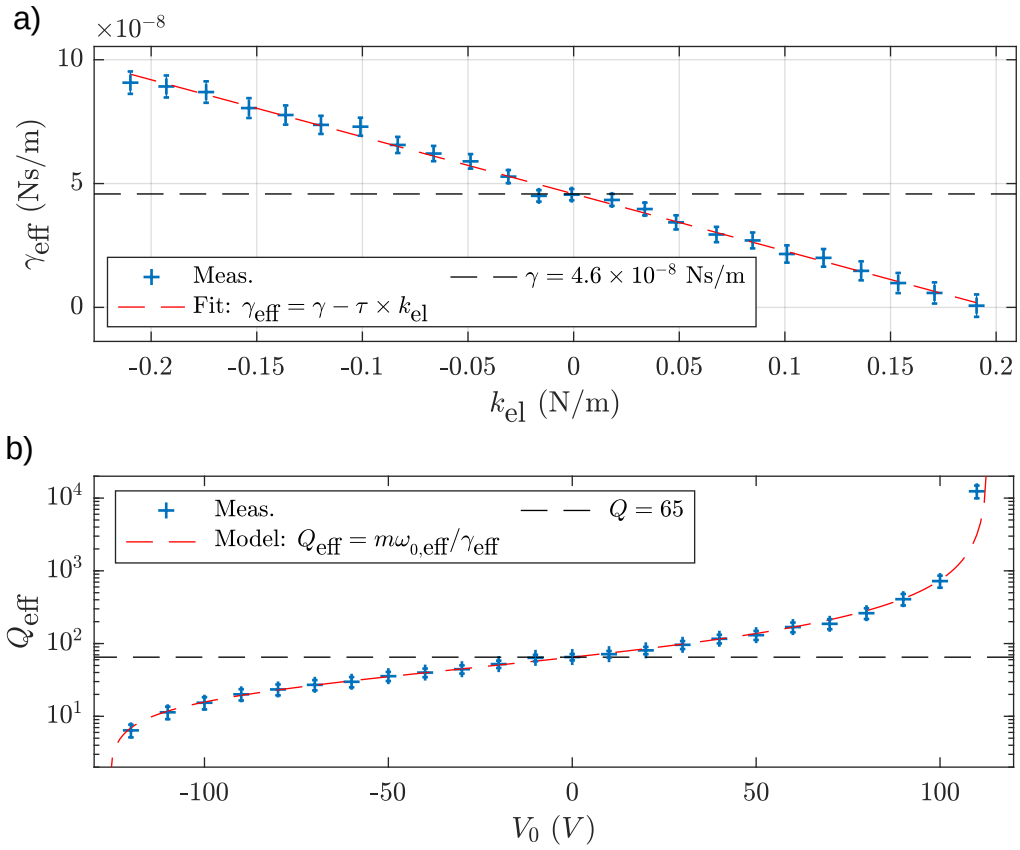

Figure 2.7 – **a) Effective damping evolution:** γ_{eff} (blue), inferred from the fit of the experimental PSDs following Eq. (2.29) (with k_{eff} fixed to its theoretical value), is plotted as a function of $k_{\text{el}} = 2\alpha\beta V_0$. The best linear fit (dashed red) validates the model prediction $\gamma_{\text{eff}} = \gamma - \tau k_{\text{el}}$ with $\gamma = m\omega_0/Q = 4.6 \times 10^{-8}$ Ns/m (dashed black), and allows to calibrate the time delay: $\tau = 0.23\,\mu$s. **b) Quality factor evolution with the feedback intensity**. $\tilde{Q}_{\text{eff}}$ (blue) is the only fitted parameter of the experimental PSD following Eq. (2.29). The feedback strongly modify its natural value $Q = 65$ (in dashed black): it goes from $\tilde{Q}_{\text{eff}} = 6$ for $V_0 = -120$ V, to $\tilde{Q}_{\text{eff}} = 12400$ when $V_0 = 120$ V (divergence for $\gamma_{\text{eff}} = 0$). The model using the calibrated parameters α, β and τ (dashed red) perfectly matches the experiment.

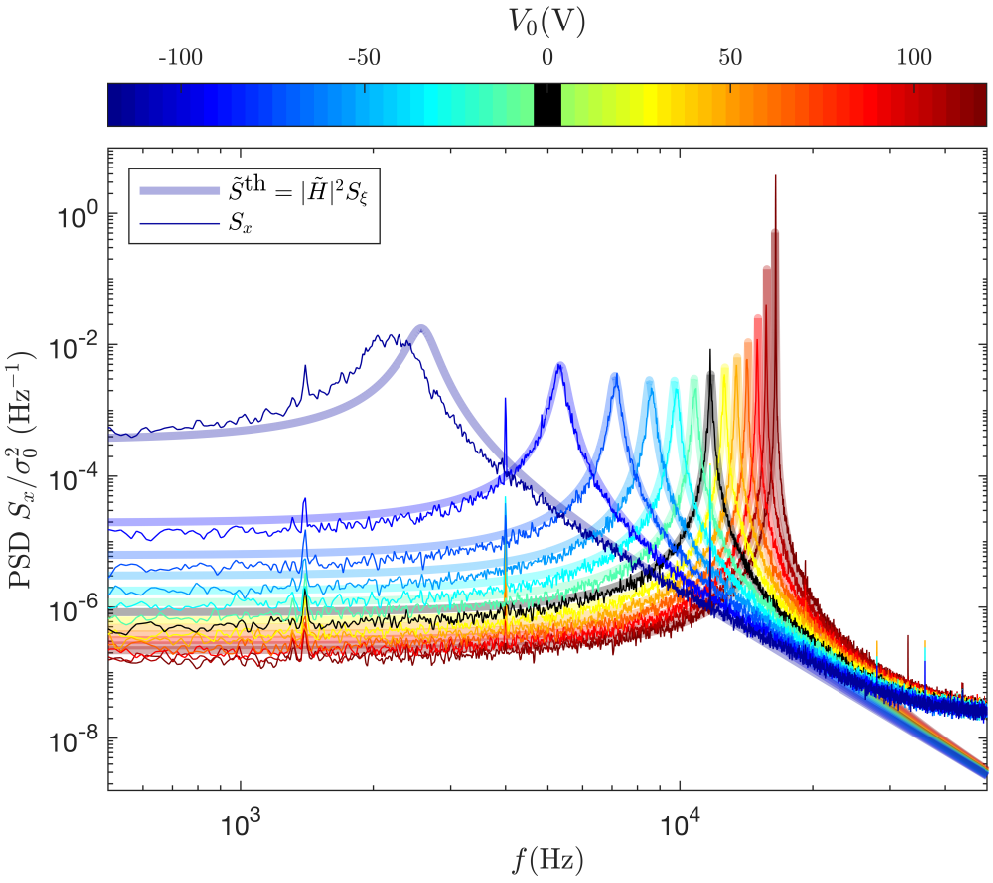

Figure 2.8 – **Refined model of the thermal deflexion PSD accounting for feedback delay**. The theoretical PSD, $\tilde{S}^{\rm th}$ expressed in Eq. (2.29) (transparent thick lines) is in very good agreement with the experimental PSD, S_x (plain lines). $\tilde{S}^{\rm th}$ is computed with no adjustable parameters, using only the calibrated parameters α, β and τ. Contrary to the first model displayed in Fig. 2.6, the refined model takes into account the delay τ in the feedback operations and therefore successfully predicts the resonance shape. For positive V_0 (red) both the resonance frequency and the resonance sharpness, ruled by the effective damping, increase, meanwhile the reverse occurs for negative V_0 (blue).

a wide range of value. Besides the model of the feedback, proven to be in very good agreement with experimental results, paves the way to a reliable and accurate control.

Nevertheless, the experimental implementation has two important limitations: on the one hand, the phase introduced in the feedback operation results in the modification of the effective damping. That is why the stiffness cannot be tuned to extremes values without degrading or enhancing the resonance amplitude, up to the divergence. Indeed even though the feedback delay remains small ($\omega_0\tau \sim 2 \times 10^{-2} \ll 1$) and has no noticeable effects on k_{eff}, it changes dramatically γ_{eff} and Q_{eff}. It stems from the fact that effective dissipation is ruled by $(k_{\text{eff}}/k)Q\omega_0\tau \sim 1$, so that the effect of the low pass filter is important on the effective temperature, thus on the velocity distribution. On the other hand, the static terms were left aside in the study, but the center of the potential actually drifts along with V_0 ($\langle x \rangle \propto V_0^2$). If one wants to tune the potential stiffness without moving the system, the relevant control parameter should be the amplification of the position signal (through β) rather that V_0. Indeed maintaining $V_0 = 100\,\text{V} \gg V_x$ while only tuning the $V_x = \beta x$ amplitude from negative to positive values would achieve exactly the same result as the above.

As a conclusion, this set-up cannot to be used yet for the underdamped ESE demonstration: such protocols are too sensitives to allow damping unwanted changes. However, those preliminary tests are very promising concerning the use of feedback control on underdamped systems. Indeed, with a better device (such as an FPGA target tackled in section 3.4) allowing to control both the amplification and the phase of the feedback output, respectively the stiffness and the damping could be tuned independently. This additional driving degree of freedom could lead to more regular protocols, with the stiffness ensuring the compression in the position space while the velocity degree of freedom would be taken care of through the damping. All in all, as suggested in Ref. 8, two control parameters would open interesting perspectives in terms of ESE protocols for compression, decompression or transport.

In the following, we will follow the lead of the feedback control of the potential but with a simpler purpose: creating a double-well potential.

2.5 References

[1] D. S. Lobser, A. E. S. Barentine, E. A. Cornell, and H. J. Lewandowski, Nature Physics **11**, 1009 (2015).

[2] D. Guéry-Odelin and E. Trizac, Nature Physics **11**, 988 (2015).

[3] D. Guéry-Odelin, J. G. Muga, M. J. Ruiz-Montero, and E. Trizac, Phys. Rev. Lett. **112**, 180602 (2014).

[4] D. Guéry-Odelin, A. Ruschhaupt, A. Kiely, E. Torrontegui, S. Martínez-Garaot, and J. G. Muga, Rev. Mod. Phys. **91**, 045001 (2019).

[5] I. A. Martínez, A. Petrosyan, D. Guéry-Odelin, E. Trizac, and S. Ciliberto, Nature Physics **12**, 843 (2016).

[6] S. Dago, B. Besga, R. Mothe, D. Guéry-Odelin, E. Trizac, A. Petrosyan, L. Bellon, and S. Ciliberto, SciPost Phys. **9**, 64 (2020).

[7] A. Le Cunuder, I. A. Martínez, A. Petrosyan, D. Guéry-Odelin, E. Trizac, and S. Ciliberto, Applied Physics Letters **109**, 113502 (2016).

[8] M. Chupeau, S. Ciliberto, D. Guéry-Odelin, and E. Trizac, New J. Phys. **20**, 075003 (2018).

[9] P. Paolino, F. Aguilar Sandoval, and L. Bellon, Rev. Sci. Instrum. **84**, 095001 (2013).

Chapter 3:

Virtual double-well potential for an underdamped oscillator created by a feedback loop

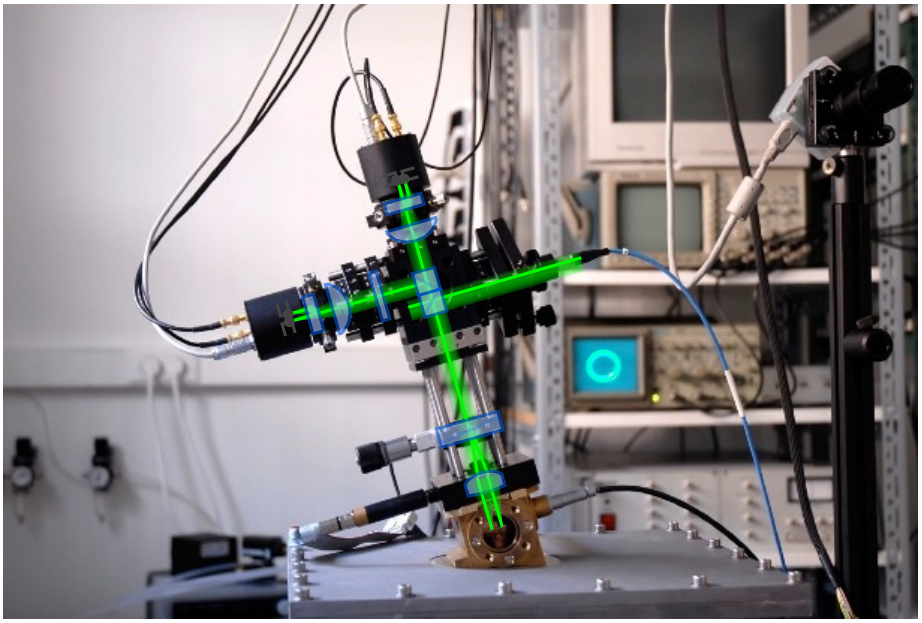

3.1 Context

Feedback loops on the system's position are used in the literature to study Landauer's principle by creating double-well potentials and using the trapped particle as a memory [1; 2]. To extend this study to the underdamped regime, we propose in this chapter an electrostatic feedback designed to create virtual double-well potentials acting on a micro-cantilever, which serves as an underdamped mechanical oscillator. The system offers a state-of-the-art flexibility and precision, with excellent quality in terms of position measurement and force tuning. Thanks to the thorough study of the feedback effects, we are able to create clean, reliable and tunable double-well potentials which outperform those produced by optical and magnetic tweezers (either physical or virtual), and have the added advantage of being analytically tractable.

The chapter is organised as follows: we first present in section 3.2 the experimental system and the principle of the feedback loop. We then refer to Ref. 3 that explores the non-idealities of a real-life analogical implementation for a quality factor $Q \sim 10$. In particular, it shows how an hysteresis in the switches between the wells, or, equivalently, a delay in the actuation, results in a bias of the energy exchanges with the thermal bath, effectively warming or cooling the oscillator Brownian noise (note that this subject will be raised again in chapter 5). The requirements that need to be met to mitigate imperfections in the analogical implementation are recalled in section 3.3. In order to conduct experiments at lower damping, $Q \sim 100$, we propose in section 3.4 to replace the analogical devices by a FPGA card which overcomes its predecessor limitations. Lastly we demonstrate the efficiency of the FPGA feedback at very low damping.

3.2 Virtual double well potential: principle

As sketched in Fig. 3.1, the underdamped oscillator is a conductive cantilever which is weakly damped by the surrounding air at room temperature T_0. Its deflection x is measured with very high accuracy and signal-to-noise ratio by a differential interferometer [4]. The Power Spectral Density (PSD) of the thermal fluctuations of x is plotted in Fig. 3.2: the fundamental mode dominates by 3 orders of magnitude the higher-order deflection modes of the cantilever. The second deflection mode at 8 kHz is conveniently removed from the measured signal by focusing the sensing laser beam on its node, at around 0.78% of the cantilever length. This adjustment helps in having a physical system very close to an ideal Simple Harmonic Oscillator (SHO). The fit of this PSD with the theoretical thermal noise spectrum of a SHO leads to its resonance frequency $f_0 = \omega_0/2\pi = 1270\,\mathrm{Hz}$ and quality factor $Q = 10$. The slight difference between the measurement and the model is due to frequency dependence of the viscous damping of the cantilever in air [5; 6]. From the PSD we compute the variance at equilibrium $\sigma_0^2 \sim 1\,\mathrm{nm}^2$, which is used as the length scale (see section 1.5).

In order to use the cantilever as a one-bit memory (see following chapters), we need to confine its motion in an energy potential consisting of two wells separated by a barrier, whose shape can be tuned at will. This potential U is created by a feedback loop, which compares the cantilever deflection x to an adjustable threshold x_0. After having multiplied the output of the comparator by an adjustable voltage V_1, the result is a feedback signal V which is $+V_1$ if $x > x_0$ and $-V_1$ if $x < x_0$. The voltage V is applied to the cantilever and the facing electrode is kept at $V_0 \sim 100\,\mathrm{V} \gg V_1$ so that, to a good approximation, $F_{\mathrm{el}} \propto \pm V_1$ up to a static term. All in all, this feedback

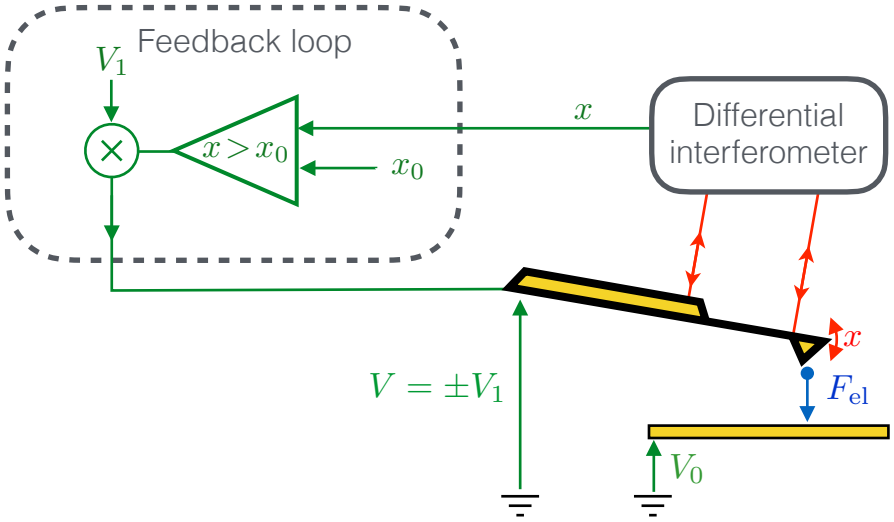

Figure 3.1 – **Experimental system.** The conductive cantilever is sketched in yellow. Its deflection x is measured with a differential interferometer [4], by two laser beams focused respectively on the cantilever and on its base. The cantilever at voltage $V = \pm V_1$ is facing an electrode at V_0. The voltage difference $V - V_0$ between them creates an attractive electrostatic force $F_{\text{el}} = \alpha(V - V_0)^2$. The dashed box encloses the feedback controller, consisting of a comparator and a multiplier, which create the double-well potential.

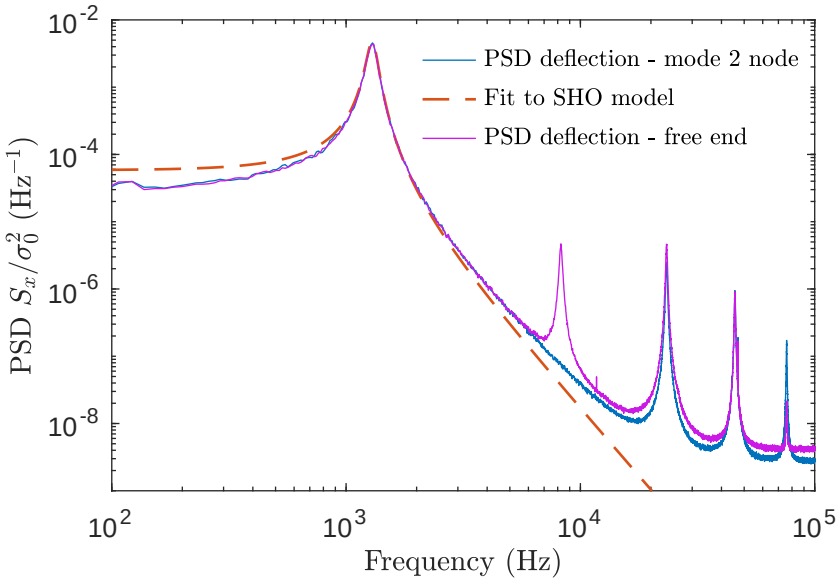

Figure 3.2 – **Power Spectral Density (PSD) of the cantilever deflection in a single well, in air.** Measured PSD of the thermal noise driven deflection with no feedback ($V_1 = 0$, solid lines), and best fit by the theoretical spectrum of a Simple Harmonic Oscillator (SHO, dashed line). The second deflection mode, visible at 8 kHz when the laser beam is focused at the free end of the cantilever (magenta), is successfully hidden by focusing the laser beam on the node of this mode (blue). At frequencies up to 10 kHz, the cantilever behaves like a SHO at $f_0 = 1270$ Hz, with a quality factor $Q = 10$. We infer from this measurement the variance $\sigma_0^2 \sim 1\,\text{nm}^2$

loop consists in the application of an external constant force whose sign depends on whether the cantilever is above or below the threshold x_0. As long as the reaction time of the feedback loop is very short (around $10^{-3} f_0^{-1}$), the switching transient is negligible thanks to the inertia of the cantilever. As a consequence, the oscillator evolves in a virtual static double-well potential, whose features are controlled by the two parameters x_0 and V_1. Specifically, the barrier position is set by x_0 and its height is controlled indirectly by V_1, which sets the wells centers $\pm x_1$ with:

$$x_1 = \frac{2\alpha V_0}{k} \times V_1, \tag{3.1}$$

where α is the proportionality constant introduced in Eq. (1.40). The potential energy constructed by this feedback is:

$$U(x, x_0, x_1) = \frac{1}{2} k \Big(x - S(x - x_0) x_1 \Big)^2, \tag{3.2}$$

where S is the sign function: $S(x) = -1$ if $x < 0$ and $S(x) = 1$ if $x > 0$. In the following, unless we specify otherwise, we will always consider the case of a symmetric potential, corresponding to $x_0 = 0$.

The potential energy in Eq. (3.2) can be experimentally measured from the Probability Distribution Function PDF(x) and the Boltzmann equilibrium distribution: PDF(x) $\propto e^{-U(x)/k_B T_0}$. Fig. 3.3 presents two examples of an experimental symmetric double-well potential generated by the feedback loop, tuned to have a barrier of $\frac{1}{2} k x_1^2 = 5 k_B T_0$ and $0.5 k_B T_0$ (respectively $x_1 = \sqrt{10}\sigma_0$ and $x_1 = \sigma_0$). The dashed red line is the best fit with Eq. (3.2), demonstrating that the feedback-generated potential behaves as a static one, in terms of the position PDF.

The second degree of freedom of the underdamped system is the velocity $v = \dot{x}$, and it is also expected to satisfy the Boltzmann equilibrium distribution. As the potential $U(x, x_0, x_1)$ does not depend on the speed, the equilibrium PDF of the velocity in the double-well is the same as the one in a single harmonic well and should be a Gaussian of variance $\sigma_{v,0}$ (defined in Eq. (1.30)): PDF(v) $\propto e^{-mv^2/(2k_B T_0)}$. The experimental challenge undertaken in Ref. 3 and in the following is to build a proper virtual potential identical to a physical one: the feedback loop should have no noticeable effect on the position and velocity equilibrium distributions.

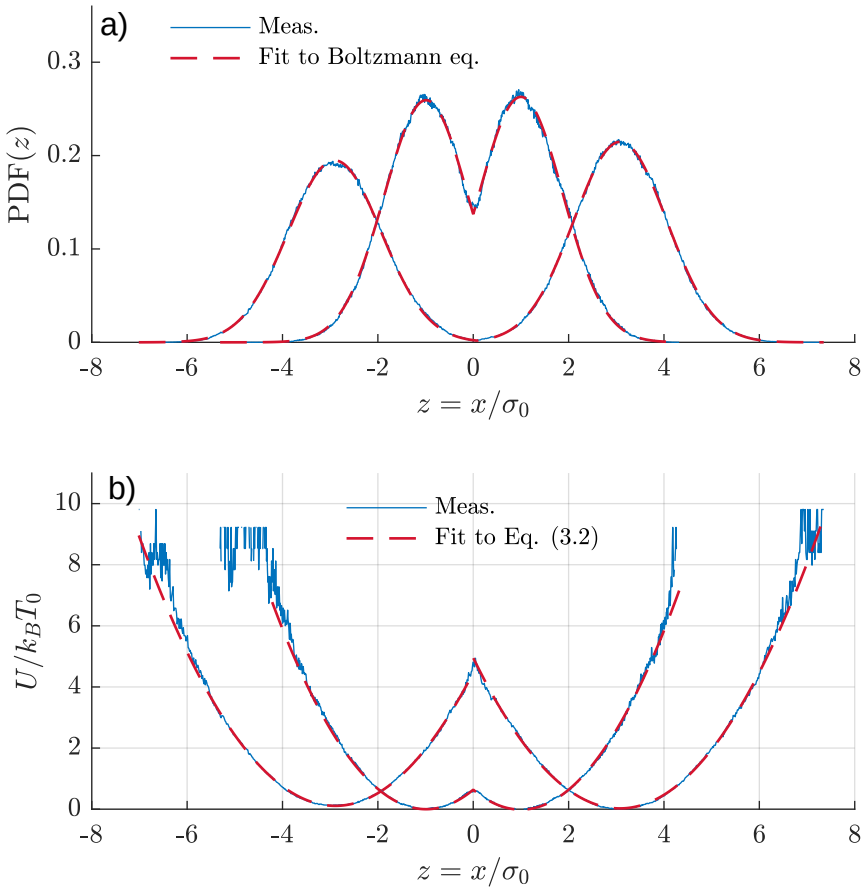

Figure 3.3 – **(a) Probability Density Function (PDF) of x.** The PDF of x (blue) measured during a 10 s acquisition with the feedback on, with $x_0 = 0$ and two values of V_1 adjusted to have respectively a $5\,k_BT_0$, and a $0.5\,k_BT_0$ energy barrier height. The fit using the Boltzmann equilibrium distribution with the potential shape in Eq. (3.2) (dashed red) is excellent. **(b) Double-well potential energy.** The measured potentials (blue) are inferred from the above measured PDF of x and the Boltzmann distribution: we obtain as expected the $5\,k_BT_0$ and $0.5\,k_BT_0$ barriers corresponding to the two values of V_1. The fits using Eq. (3.2) are again excellent (dashed red).

3.3 Analogical implementation

The analogical implementation is fully detailed in Ref. 3, reproduced in Appendix D. One of its main conclusion is that any switching delay or hysteresis in the feedback results in the cooling of the memory. Indeed the kinetic temperature T defined in Eq. (1.68), matching the bath T_0 at equilibrium in a physical bi-quadratic potential as prescribed by the Boltzmann distribution, decreases when the output voltage switch lags behind the barrier crossing. The consequence of an hysteresis on the system's temperature will be addressed in more details in chapter 5. For clarity purposes we only list the experimental constraints given in Ref. 3 to maintain $T = T_0$ within 5%, for a quality factor $Q = 10$:

- The hysteresis of the comparator has to be lower than 2% of σ_0.
- A temporal lock-up has to be implemented to remove parasitic switching, by freezing the comparator output after a switch during 1/4 of the oscillator's natural period.
- The position signal has to be filtered to remove high frequency noise and higher order deflexion modes' contributions.
- The phase introduced by the filter should correspond to a feedback delay much lower than $\tau_d = 1/(g^* Q\omega_0)$ with $g^* = 0.21$. It bounds the cut-off frequency of the low pass filter by $f_c \gg 5g^* Q f_0 = 13\,\text{kHz}$.

Nevertheless, the requirements listed above become more restrictive if the quality factor is increased. For example, if $Q \sim 100$, the response time of the feedback has to remain much lower than $\tau_d = 1/(g^* Q\omega_0) = 6\,\mu\text{s}$ ($f_c \gg 130\,\text{kHz}$), and the hysteresis lower than 0.1% of σ_0, to keep the velocity distribution in the virtual potential unbiased (less than 5% cooling): the analogical implementation of Ref. 3 doesn't meet the requirements anymore.

3.4 Digital implementation: FPGA card

To work at very low damping ($Q \sim 100$), we need the feedback operations to be performed without introducing any delay neither during the comparison nor the filtering step. That is why we turned to a digital implementation of the feedback, allowing to perform operations clocked up to 10 ns (100 MHz acquisition frequency, 200 MHz onboard clock) using a Fast Programming Gate Array (FPGA).

A Labview-based FPGA data acquisition system (FPGA 7975R + Adapter module Ni 5783) collects the voltage signals from the photodiodes and sends the feedback voltage to the cantilever. The FPGA card runs the control protocol (input, signal conversion using calibration, filtering, comparison and output) with a deterministic time step of 1.3 μs. Indeed, each basic operations takes a fixed tick number to be conducted and the overall feedback operations performed on the FPGA (including the analog to digital (ADC) and digital to analog (DAC) conversion steps accounting each for 25 ticks) lasts around 130 ticks. We detail in the following the digital feedback tasks illustrated in Fig. 3.4a).

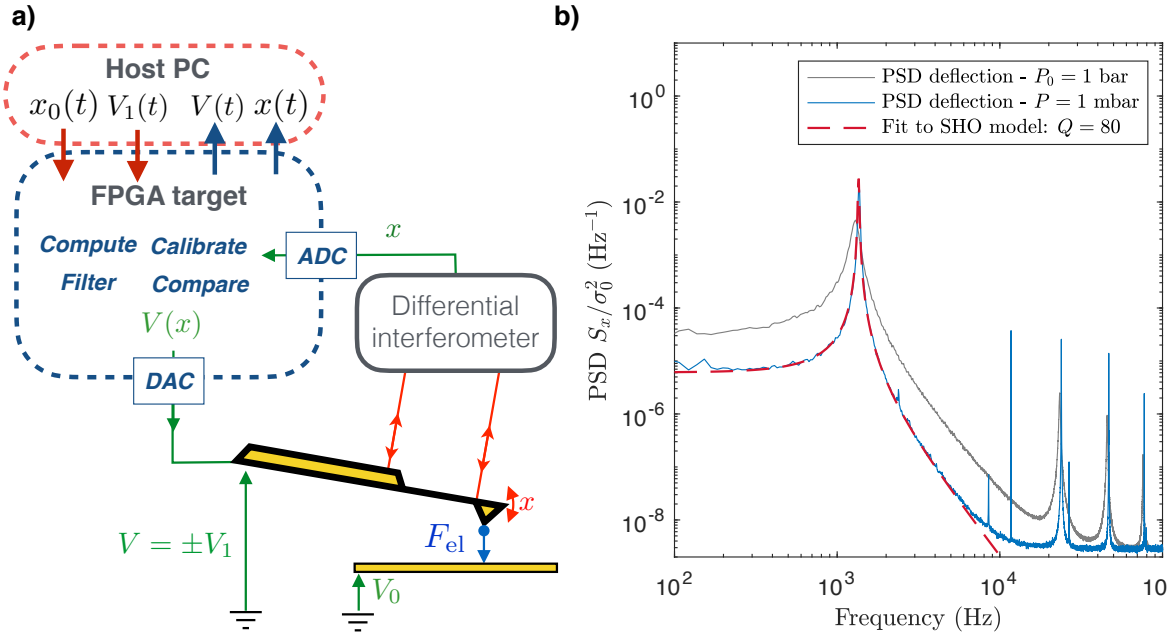

Figure 3.4 – **a) Schematic diagram of the experiment**: the conductive cantilever is sketched in yellow. The detection system is the same but the photodiodes signals are directly sent to the FPGA card that proceeds with the calibration, the filtering of x used for the comparison to $x_0(t)$, and the computation of the output voltage $V(x)$. All the signals are saved in the host PC. All in all, the FPGA operations result in an output voltage $\pm V_1$ depending on the protocol and the measured position. **b) Measured PSD at very low damping** of the cantilever thermal noise driven deflection with no feedback. The laser beam is focused on the node of the second deflexion mode to suppress its contribution. We compare the PSD in vacuum ($P = 1$ mbar, blue) with the one at ambiant pressure ($P_0 = 1$ bar, grey): removing the viscosity increases the amplitude and the sharpness of the resonances. The best fit by the theoretical spectrum of a Simple Harmonic Oscillator (SHO, dashed red line) confirms that up to 10 kHz the cantilever behaves in vacuum like a resonator at $f_0 = 1353$ Hz, with a quality factor $Q = 80$.

Before the experiment: calibration

We first perform a calibration step implementing in the FPGA the calibration coefficients to convert the interferometer four photodiodes voltage signals to an actual position x in nm [4]. We then apply a ramp in the voltage V applied to the tip and read the cantilever average position $\langle x \rangle$, to convert V_1 into x_1 and vice-versa (proportionality coefficient $2\alpha V_0/k$ in Eq. (3.1)). The origin of the x axis is periodically (every protocol) set to $(\langle x \rangle = 0, V = 0)$ in order to remove the drift in position during long experiments.

Position signal treatment: filtering

The photodiodes signals are acquired and converted into the deflexion signal x using the calibration parameters, but x remains to be filtered to remove higher order deflexion modes' contribution and the high frequency noise as specified in section 3.3. To do so, we design a low pass filter of cutoff frequency $f_c \sim 10\,\text{kHz}$. Such a drastic filtering couldn't be simply implemented analogically without a prohibitive feedback delay [3]. Nevertheless, it is possible to design a numerical filter removing the noise above f_c without impacting the phase at the cantilever natural resonance frequency f_0. Indeed IIR filters (Infinite Impulse Response filters working with the memory of previous outputs) can be tuned to have zero-phase at f_0. Moreover, such an IIR filter can be used to also compensate the delay of the other FPGA operations. In practice, the FPGA position signal filter is meant to correct the $1.3\,\mu$s feedback delay, so that the overall phase of FPGA feedback vanishes around the cantilever's resonance (see Fig. 3.5b)). Let us detail the key steps of the method followed to build the FPGA IIR filter:

- We compute the filtered position using a low pass Butterworth filter: $\tilde{x} = BW \otimes x$.
- We compute the speed $\tilde{v} = \dot{\tilde{x}}$ of the system, to anticipate the system's position after the overall $\tau_d \sim 1.3\,\mu$s feedback delay.
- We compensate the feedback delay in the final filtered position: $x_f = \tilde{x} + \tilde{v}\tau_d$. Hence in Fourier space: $x_f(\omega) = (1 + i\omega\tau_d)\, BW(\omega)\, x(\omega)$.
- The parameter τ_d is chosen to have zero phase at the cantilever's resonance frequency: τ_d is solution of $\text{Im}\{x_f(\omega_0)/x(\omega_0)\} = \text{Im}\{(1 + i\omega_0\tau_d)\, BW(\omega_0)\} = 0$.

All in all the filter transfer function is $\text{IIR}(\omega) = (1 + i\omega\tau_d)\, BW(\omega)$, whose anticipation coefficient τ_d is in practice fine tuned experimentally to enforce an unbiased velocity PDF in the resulting double-well potential. The Bode diagram of the overall FPGA operations on the position signal (ADC, conversion of the photodiode outputs into x signal, IIR filter and DAC) is displayed in Fig. 3.5a) and b). It consists in the gain and the phase of the transfer function between the real time position directly inferred from the photodiode outputs (no real time conversion, nor filtering, but only post treatment operations), and the position signal acquired, reconstructed, filtered and output by the FPGA card, x_f. We see in Fig. 3.5b) that the phase of the feedback is small enough at the resonance to limit the temperature cooling to the acceptance range of 5% required in section 3.3, even for $Q \sim 100$. It is worth noticing on Fig. 3.5a) that this real time zero-phase -at ω_0- filtering is performed at the expense of a very small resonance in the filter gain, which has negligible consequences on our experiments.

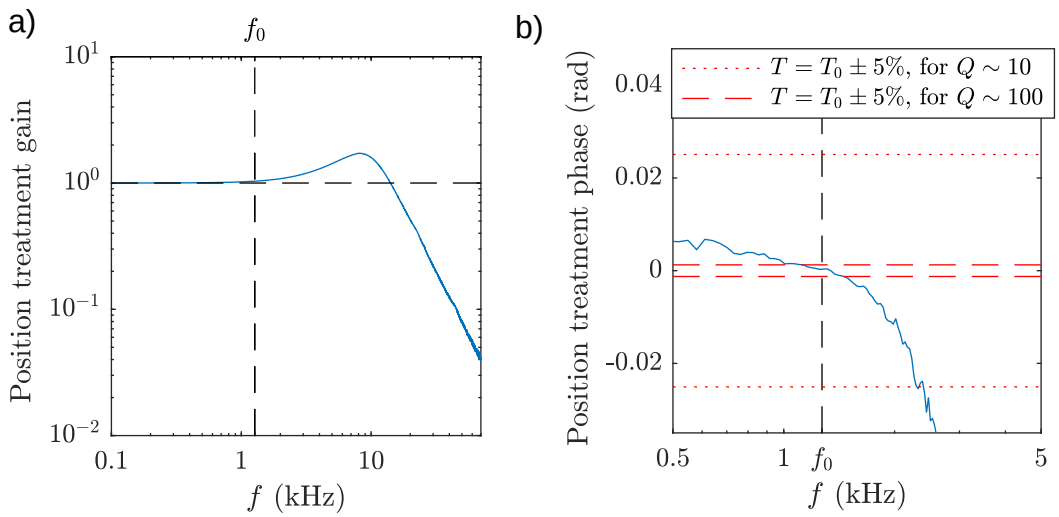

Figure 3.5 – **a) Gain of the FPGA position signal treatment**. As expected the gain of the feedback operations on the position signal (ADC, conversion of the photodiode outputs into x signal, IIR filter and DAC) is worth 1 (horizontal dashed black) within the frequency range of interest (f_0 in vertical dashed black), and is then filtered above $f_c = 10\,\text{kHz}$ to remove the 3rd deflexion mode contribution. We notice that there is a slight amplification above f_0 due to the resonance of the IIR filter. **b) Phase of the FPGA position signal treatment**: the IIR filter is designed to have a 0 phase for the overall processing of the position signal at f_0 (vertical dashed black), to avoid switching advance or delay, and hence meet the $T = T_0 \pm 5\%$ requirement on the kinetic temperature. The authorized range (computed following Ref. 3) corresponds to the interval between the red dashed lines for $Q \sim 100$, and between the dotted lines for $Q \sim 10$.

Let us also point out that the above IIR filter requires 9 FPGA clock ticks to operate, so that the input signal has to be first filtered against aliasing by a simple moving average FIR (Finite Impulse Filter) at 100 MHz/9.

Protocol computation

Once filtered, the position is compared the barrier position x_0, and the FPGA outputs the corresponding voltage V that tunes the well center position $\pm x_1$. The operator has full control on the x_0 and x_1 profiles from the host computer. Similarly to what is done in the analogical implementation [3], we add in the protocol a switching lock-up (mentioned in section 3.3) to remove parasitic switches. This time, it is all digital so that the operator can fine tune the lock-up time from the computer.

Recording and post-treatment analysis

To avoid saturating the FPGA card host computer bandwidth, we downsample the signals at $f_s = 2\,\text{MHz}$. Therefore, the signals sent from the FPGA to the host PC have to be filtered for antialiasing purposes. We program on the FPGA a distinct third order Butterworth filter of cutoff frequency $f_{c,\text{acq}} = f_s/3 = 667\,\text{kHz}$. All the signals, either the command ones x_0 and x_1, the measured position x_{acq} (only filtered for antialiasing purposes), the filtered position x_f (filtered by the real time FPGA filter and used to compute the feedback output voltage), the output volage V, and the calibration data are recorded by the host PC.

To compute the thermodynamics quantities we use the measured position x_{acq} properly filtered above 10 kHz in post-treatment analysis using a zero-phase filtering (processing the data in both the forward and reverse direction). This post-acquisition filter is better than the real time FPGA one (because it enforces 0 phase for all frequencies and not only f_0), that is why we do not use directly x_f for the analysis. Let us note that such zero phase filtering is not causal and thus cannot be implemented on the FPGA for real time operations. Thanks to the calibration of the data, no further post-treatment is required.

Results in the very low damping limit and perspectives

The FPGA reproduces with more flexibility, more control and more accuracy the results obtained using the analogical feedback loop. Thanks to the tunable IIR filter, no more caution is needed regarding the feedback delay, making it a very powerful tool to explore the very under-damped regime that was not accessible using the analogical counterpart.

Removing the air in the cantilever's chamber enhances the quality factor of the underdamped oscillator: as shown in Fig. 3.4b), at pressure $P = 1\,\text{mbar}$ the cantilever behaves like a SHO of quality factor $Q = 80$. We illustrate in Fig. 3.6a) and b) the very good results obtained using the digital feedback in these experimental conditions. Moreover, the velocity PDFs analysis in Fig. 3.6c) and d) confirms that the virtual potential behaves like a physical one without introducing any bias on the system temperature (within the 5% acceptance range).

Besides, as the operator can design the FPGA operations at will, it opens many possibilities regarding virtual potentials beyond the simple bi-quadratic shape. Indeed, if the center of the well is no more defined by only two x regions ($x_1(x > 0) = +X_1$, $x_1(x < 0) = -X_1$), but for every possible position ($x_1(x)$ function implemented as an array), the potential can be shaped at will. In particular $x_1(x) = k_{FB} \times x$ would result in a tunable virtual stiffness, and $x_1(x) = \gamma_{FB} \times \dot{x}$ in a tunable virtual damping, therefore paving the way to ESE protocols (see section 2.3).

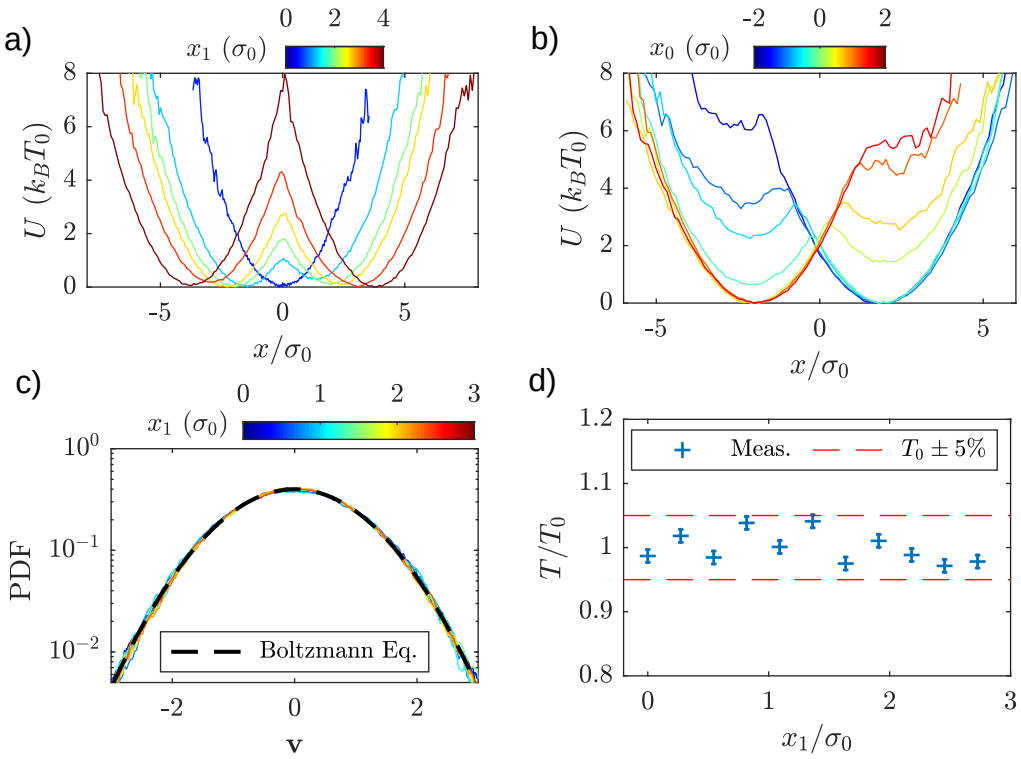

Figure 3.6 – **a)Virtual potential** inferred from the position PDF and the Boltzmann equilibrium distribution, for growing distances x_1 between the wells with $x_0 = 0$. The numerical feedback works perfectly for low damping, here $Q = 80$. **b) Same as a)** for growing position barrier x_0, with $x_1 = 2\sigma_0$. **c) Velocity PDF at** $Q = 80$ for growing half-distances x_1 between the wells. It confirms that the FPGA does not bias the equilibrium distribution emphasized in dashed black. **d) Kinetic equilibrium temperature** $T = \sigma_{\mathbf{v}}^2 \times T_0$ **for growing** x_1 inferred from the variances of the PDFs in e). The FPGA feedback successfully creates a virtual bistable potential at $Q = 80$ without more than 5% cooling, or warming (dashed red interval).

3.5 References

[1] Y. Jun, M. Gavrilov, and J. Bechhoefer, Phys. Rev. Lett. **113**, 190601 (2014).

[2] K. Proesmans, J. Ehrich, and J. Bechhoefer, Phys. Rev. Lett. **125**, 100602 (2020).

[3] S. Dago, J. Pereda, S. Ciliberto, and L. Bellon, Virtual double well potential for an underdamped oscillator created by a feedback loop (2022), under review JSTAT. arXiv: 2201.09870.

[4] P. Paolino, F. Aguilar Sandoval, and L. Bellon, Rev. Sci. Instrum. **84**, 095001 (2013).

[5] L. Bellon, Journal of Applied Physics **104**, 104906 (2008).

[6] J. E. Sader, Journal of Applied Physics **84**, 64 (1998).

Chapter 4:

Erasure cost of a 1-bit memory

4.1 Introduction

As introduced in section 1.4.4, erasing 1-bit of information costs at least the Landauer bound (LB): $k_B T_0 \ln 2$. This bound is reached asymptotically in the quasi-static regime, that is to say for slow erasures. In practice, finite time implementations require an overhead to Landauer's Bound (LB), observed to scale as $k_B T_0 \times B/\tau$, with τ the protocol duration and B close to the system relaxation time [1; 2]. Most experiments use overdamped systems, for which minimizing the overhead means minimizing the dissipation. Underdamped systems [3; 4] therefore seem natural to reduce this energetic cost: that is why we use as one-bit memory the underdamped micro-mechanical oscillator confined in a virtual double-well potential.

This chapter is organized as followed: in section 4.2 we demonstrate experimentally that the Landauer's bound is reached in our underdamped system with a 1 % uncertainty, with protocols as short as 100 ms (compared to the 30 s [5] previously needed). Besides we measure the divergence from LB for fast erasures, and estimate the parameter B ruling the overhead to LB in section 4.2.5. It remains to be seen what are the origins of this overhead: we therefore study the energy exchanges during erasure processes, and model quantitatively the cost of fast operation in section 4.3. The model, in very good agreement with experiments and numerical simulations paves the way to new optimisation strategies addressed in section 4.4, based on the thorough understanding of the energy exchanges. Ultimately, we study the robustness of the underdamped memory and the erasure cost evolution when it is used repeatedly in section 4.5.

4.2 Experimental demonstration of the Landauer's bound using an underdamped oscillator

4.2.1 Context and experimental set-up

Erasure procedures in underdamped systems have never been studied before, and it is interesting to verify the LB for a weak coupling to the thermostat. Both the relaxation time and the coupling to the bath of our system are orders of magnitude smaller than those of the overdamped systems of previous demonstrations, therefore allowing us to accumulate much more statistics. Furthermore, the virtual confining potential (see chapter 3) allows both a precise experimental control and an analytical computation of the work and heat on a trajectory.

The underdamped oscillator is the one introduced in section 1.2.2 and the experimental set-up corresponds to Fig. 2.4. We recall the system's characteristics at ambient pressure (from the spectrum in Fig. 3.2): $f_0 = 1270\,\mathrm{Hz}$, $Q = 10$ and $\sigma_0^2 \sim 1\,\mathrm{nm}^2$. The latter is used to normalize the deflexion, $z = x/\sigma_0$, and express energetic quantities in $k_B T_0$ units (using notations summarized in Tab. 1.1). In order to use the cantilever as a one-bit memory, we confine its motion in the virtual double-well energy potential displayed in Fig. 3.3. As we are for now working at $Q = 10$, the analogical implementation of the feedback is enough to provide an unbiased bi-stable potential whose equation is given by:

$$\mathbf{U}(z, z_0, z_1) = \frac{1}{2}\Big(z - S(z - z_0)z_1\Big)^2, \tag{4.1}$$

with z_0 the barrier position and $\pm z_1$ the center of the wells.

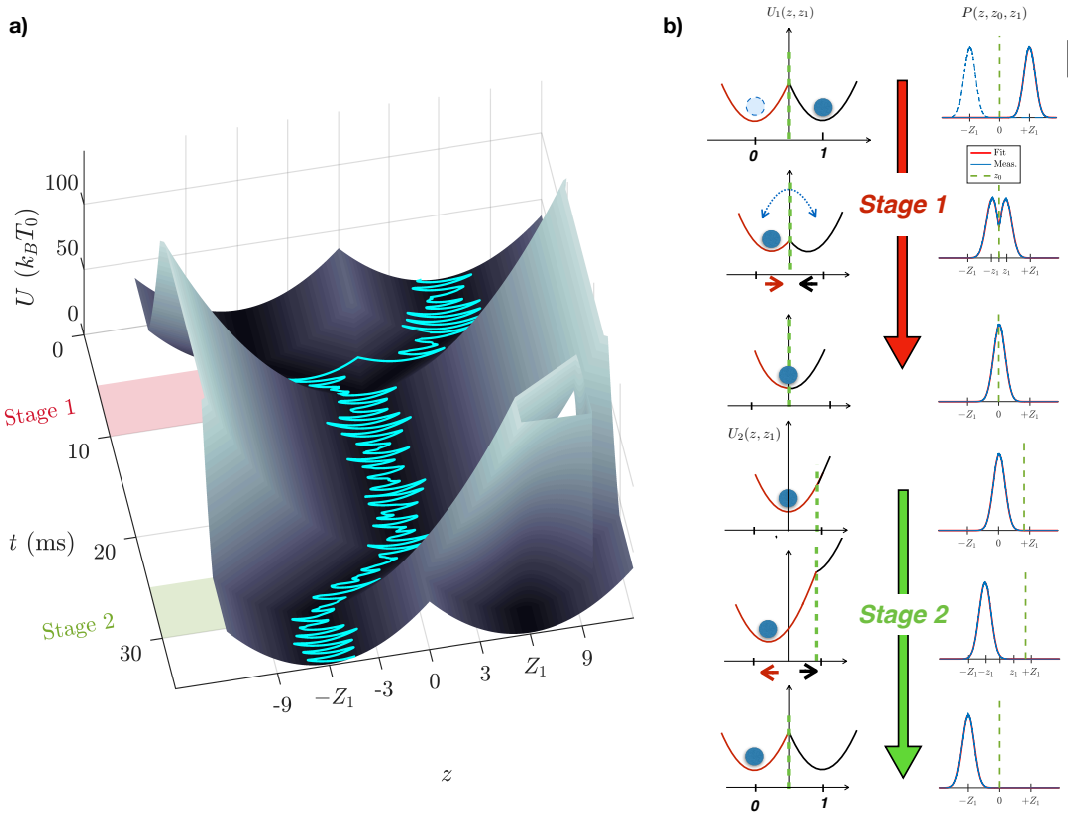

Figure 4.1 – **a) 3D spatio-temporal representation of the erasure protocol**. The two wells initially centered in $\pm Z_1$, far enough to secure the bit initial value (barrier height $\mathcal{B} = \frac{1}{2}Z_1^2$), are brought together during stage 1 until they merge into one single well in $z_1 = 0$. Then, during stage 2, the memory is reset by bringing back the well center to $-Z_1$, before rebuilding the bi-stable potential with the barrier at position $z_0 = 0$. A trajectory is superimposed on the energy surface in a 3D spatio-temporal plot. **b) Evolution of the potential U(z, z_0, z_1) and of the static PDF** $P(z, z_0, z_1)$. Experimental static PDF $P(z, z_0, z_1)$ (blue), best fit to the Boltzmann distribution (red), and position of the threshold z_0 (dashed green)

4.2.2 Protocol

The erasure protocol corresponds to the potential evolution described in Fig. 4.1, with the associated experimental static position distribution $P(z)$. Initially, the system is at equilibrium either in the state 0 (left-hand well centered in $-Z_1$) or in the state 1 (right-hand well centered in Z_1) with a probability $p_i = \frac{1}{2}$. Z_1 sets the height of the barrier in the initial state $\mathcal{B} = \frac{1}{2}Z_1^2$, chosen high enough to secure the initial and final states. The process must result in the final state 0 with probability $p_f = 1$, to perform a reliable erasure process. To do so, during the first stage we drive the wells closer until they merge into one single harmonic well centered in 0. After a short equilibration time, the barrier position (dashed green line) is pushed away to prevent the cantilever from visiting the right hand well (black parabola). It thus remains in the left hand well (red line), which is driven back to its initial position in $-Z_1$. The so-called stage 2 ends when the threshold is brought back in 0, to reach the final state 0 in the bi-stable potential, regardless of the initial state.

To implement the erasure procedure, the position of the center of the wells $\pm z_1$ (black and red parabolas), and the barrier position z_0 (green dashed line) are driven

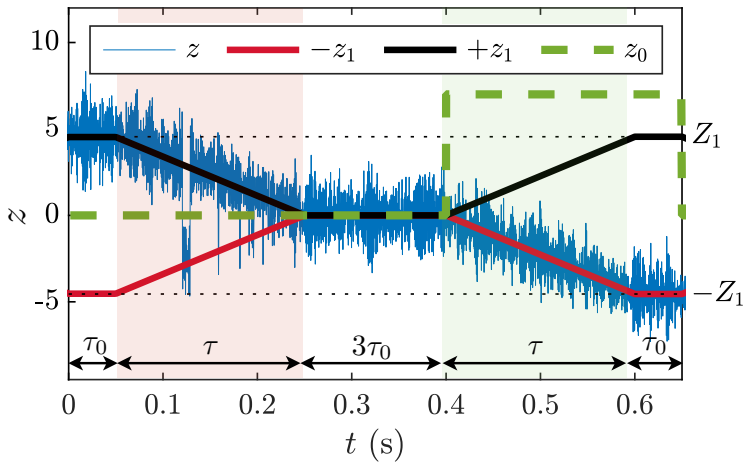

Figure 4.2 – **Slow erasure cycle**. Time recording of the cantilever deflection $z = x/\sigma_0$ on a single trajectory (blue, starting in state 1 in this example), superposed with the two wells' centers $+z_1$ (black) and $-z_1$ (red), and the threshold z_0 (dashed green). Stage 1 (red background) et 2 (green background) both last $\tau = 200\,\text{ms}$. τ is very long compared to the natural relaxation time $\tau_r = 2Q/\omega_0$ of the cantilever: $\tau\omega_0 \sim 1.5 \times 10^3 \gg \tau_r\omega_0 = 2Q \sim 20$. The equilibrium periods around stages 1 and 2 are chosen freely as long as they allow the cantilever to relax, in this example $\tau_0 = 50\,\text{ms} \gg \tau_r$.

accordingly to the profiles in Fig. 4.2. Initial equilibrium is ensured by a steady potential for a duration of τ_0, chosen longer than the natural relaxation time of the system $\tau_r = 2Q/\omega_0 = 2.5\,\text{ms}$. For clarity purposes, $\tau_0 = 50\,\text{ms}$ in Fig. 4.2. During stage 1 (red background), the system is confined in the symmetric double-well potential $\mathbf{U}_1(z, z_1) = \frac{1}{2}(|z| - z_1)^2$, whose center of the wells moves linearly from the initial state $z_1(0) = Z_1 \sim 5$ to $z_1(\tau) = 0$ in a time $\tau = 200\,\text{ms}$. When the two wells are close enough, the cantilever starts switching from one well to the other: the information is progressively lost. The cantilever is then allowed to relax at equilibrium in this single well for $3\tau_0$. During stage 2 (green background), the threshold z_0 is set at a large value (of order Z_1 or higher): the cantilever can no longer switch to the right hand side well. The cantilever is then brought back to the state 0 in the single well $\mathbf{U}_2(z, z_1) = \frac{1}{2}(z + z_1)^2$, as z_1 follows a linear ramp from 0 to Z_1, in the same time τ. The protocol ends at $\tau_f = 2\tau + 5\tau_0 \gtrsim 2\tau + 15\tau_r$ [1], after letting the system relax during τ_0 and bringing back z_0 to 0.

4.2.3 Work and Heat measurement

The data plotted in Fig. 4.2 contains all we need to compute the stochastic work and heat along a single trajectory (using Eq. (1.57) and Eq. (1.61) applied to the potential

[1] To set τ_0, we use the rule of thumb that a perturb system returns to equilibrium after $3\tau_r$, with τ_r the characteristic relaxation time in the exponential decay.

$\mathbf{U}(z, z_0, z_1)$ of Eq. (4.1)):

$$\boldsymbol{\mathcal{W}} = \int_0^{\tau_f} \sum_{i=0,1} \frac{\partial \mathbf{U}}{\partial z_i} \dot{z}_i dt = \int_0^{\tau_f} \Big(S(z-z_0)z - z_1 \Big) \dot{z}_1 dt \tag{4.2}$$

$$\begin{aligned} \boldsymbol{\mathcal{Q}} &= -\int_0^{\tau_f} \frac{\partial \mathbf{U}}{\partial z} \dot{z} dt - \Big[\mathbf{K} \Big]_0^{\tau_f} \\ &= \int_0^{\tau_f} \Big(S(z-z_0)z_1 - z \Big) \dot{z} dt - \frac{1}{2\omega_0^2} \Big[\dot{z}^2 \Big]_0^{\tau_f}. \end{aligned} \tag{4.3}$$

Indeed, the term $(\partial \mathbf{U}/\partial z_0)\dot{z}_0 \propto \delta(z-z_0)z_1\dot{z}_0$ disappears in the work expression: in our protocol $\dot{z}_0 = 0$, except at two particular times corresponding to the beginning and end of stage 2. The former corresponds to $z_1 = 0$, and the latter corresponds to the situation where z and z_0 cannot cross, which constrains this term to 0. Similarly, in the heat expression, the contribution of the $\partial S/\partial z$ term in $(\partial \mathbf{U}/\partial z)\dot{z}$ is proportional to $\delta(z-z_0)z_1 z\dot{z}$ and vanishing as well: assuming that $z(t)$ and $z_0(t)$ intersect at $t = t_0$, this contribution is

$$\int_{\sim t_0} \delta(z-z_0)z_1 z\dot{z} dt = \frac{z_1(t_0)z(t_0)\dot{z}(t_0)}{\dot{z}(t_0) - \dot{z}_0(t_0)} = 0, \tag{4.4}$$

since during our protocol z and z_0 only intersect during stage 1 where $\dot{z}_0 = 0$ at all times. The above simplifies in the case of a symmetric double well potential ($z_0 = 0$):

$$\boldsymbol{\mathcal{W}} = \int_0^{\tau_f} \Big(|z| - z_1 \Big) \dot{z}_1 dt \tag{4.5}$$

$$\boldsymbol{\mathcal{Q}} = \int_0^{\tau_f} \Big(S(z)z_1 - z \Big) \dot{z} dt - \frac{1}{2\omega_0^2} \Big[\dot{z}^2 \Big]_0^{\tau_f}. \tag{4.6}$$

Since at τ_f the system has relaxed to equilibrium, and the initial and the final states of the protocol are the same, $\langle \Delta \mathbf{U} \rangle = \langle \Delta \mathbf{K} \rangle = 0$, thus the energy balance equation Eq. (1.60) states that on average $\langle \boldsymbol{\mathcal{W}} \rangle = \langle \boldsymbol{\mathcal{Q}} \rangle$.

It should be noted that in the computation of the mean dissipated heat, we did not include the kinetic term which vanishes on average. These general expressions can be used to deduce work and heat during stage 1 or during stage 2, by adapting the integration bounds. It is straightforward to compute $\boldsymbol{\mathcal{W}}$, since $\dot{z}_1 = 0$ outside the ramps. For $\boldsymbol{\mathcal{Q}}$, we add at least 5 ms after reaching the final state, i.e. at least 2 relaxation times, so that the system is very close to equilibrium.

4.2.4 Experimental demonstration of the Landauer's bound

Long protocols satisfying $\tau \gg \tau_r$ can be considered as quasi-static erasures, hence we present in Fig. 4.3 the results obtained from 2000 trajectories, equivalent to the one of Fig. 4.2. It should be emphasized that the protocol is perfectly reliable from an information processing point of view: all 2000 trajectories ended in the prescribed well, regardless of the initial condition. As expected for a slow translation of a single well, stage 2 requires nearly no power: $\langle \boldsymbol{\mathcal{W}}_2 \rangle = 0 \pm 0.008$. During stage 1 however, the power increases when the cantilever starts switching between the wells. Of course, the equilibrium stage never contributes to the erasure work. Summing the dissipated power along the process gives: $\langle \boldsymbol{\mathcal{W}}_1 \rangle = 0.702 \pm 0.006$ as shown in Fig. 4.3b).

Furthermore, we superimpose on Fig. 4.3c) the work and the heat distributions. The work distribution is gaussian. Meanwhile, the heat distribution presents exponential

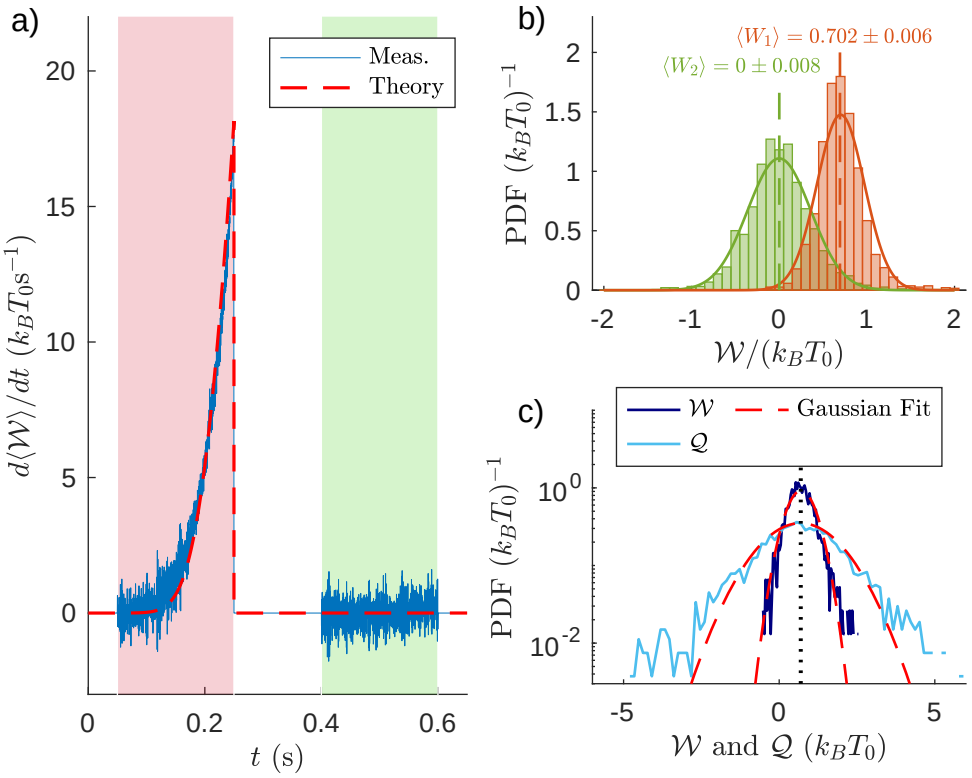

Figure 4.3 – **a) Time evolution of the mean power** over 2000 trajectories following the slow protocol of Fig. 4.2. The work takes off when the cantilever starts switching between the wells, during stage 1 (red background). Since the process is quasi-static, stage 2 (green background) doesn't contribute on average. The red dashed line is the analytical prediction in the quasi-static regime (see section 4.3). **b) Work distributions for step 1 and step 2**. The distributions are inferred from the 2000 trajectories during stage 1 ($\boldsymbol{\mathcal{W}}_1$, red) and 2 ($\boldsymbol{\mathcal{W}}_2$, green) fitted by gaussians (plain lines). As theoretically predicted for a slow erasure, stage 1 reaches LB of 0.693 (dashed red) while stage 2 requires negligible work (dashed green). **c) Work and Heat distribution**. The total work (dark blue) and heat (light blue) distributions are respectively centered on $\langle\boldsymbol{\mathcal{W}}\rangle = 0.702 \pm 0.006$ and $\langle\boldsymbol{\mathcal{Q}}\rangle = 0.68 \pm 0.03$, in very good agreement with LB (dotted black vertical line). The gaussian shape of the work PDF is highlighted by the best fit to a gaussian distribution (dashed red line). The heat is far more dispersed than the work and presents exponential tails.

tails. This observation is in agreement with the study of Ref. 6: $\mathcal{Q}$ is the convolution product of a gaussian and an exponential distribution. Besides, both distributions are centered on LB as the mean dissipated heat during the whole procedure is worth $\langle\boldsymbol{\mathcal{Q}}\rangle = 0.68 \pm 0.03$. These results are in perfect agreement with the Landauer principle: in a quasi-static process, the mean work or heat required to erase 1 bit of information is $\ln 2 = 0.693$.

4.2.5 Fast erasures and divergence from LB

After providing experimental evidence that our system matches LB in the quasi-static limit, we study how fast the procedure can be performed before paying an extra energetic cost for the erasure. We therefore repeat the experiment for increasing speeds, and report the results in Figs. 4.4 and 4.5. The initial distance between the wells

may vary slightly from one set of experiments to the other ($Z_1 = 5$ to 6, but Z_1 is constant for the 2000 experiments of any given τ), so we use the driving speed $\mathbf{v}_1 = Z_1/(\tau\omega_0)$ (dimensionless quantity defined in Tab. 1.1) to represent how far from a quasi-static protocol we stand. For example the quasi-static erasure in Fig. 4.2 corresponds to $\mathbf{v}_1 = 3.8 \times 10^{-3}$, three order of magnitudes lower than the rms thermal velocity at rest ($\sigma_\mathbf{v} = 1$). The fastest erasure expressed in Fig. 4.4 corresponds to $\mathbf{v}_1 = 0.12$. As expected, the slow procedures meet the LB and quick ones require an extra cost. For finite τ, it has been reported in earlier demonstrations of the LB [7; 8] that $\langle \boldsymbol{\mathcal{W}} \rangle \sim (\ln 2 + B/\tau)$, with B a constant depending on the system and applied protocol. More generally, this $1/\tau$ asymptotical behavior is expected for the mean stochastic work or heat for finite time transformations both in overdamped [1; 9; 10] and underdamped [11] systems. This suggests a fit of our results with $\mathbf{L}_\infty + \mathbf{B}'Z_1/\tau$. It leads to $\mathbf{B}' = (3.43 \pm 0.21)\,\omega_0^{-1} = (437 \pm 27)\,\mu\text{s}$ and $\mathbf{L}_\infty = 0.695 \pm 0.012$, which validates, again with great accuracy, the Landauer principle. It is noteworthy that using protocols of only $\tau_f \sim 100\,\text{ms}$ (with $\tau = 30\,\text{ms}$, that is to say speed $\mathbf{v}_1 = 0.02$, and $\tau_0 = 3\tau_r = 7.5\,\text{ms}$), the energy cost of erasure is only 10% larger than the LB. We didn't explore here cycles faster than $\mathbf{v}_1 = 0.12$ per ramp, which already corresponds to $\tau \sim 40\omega_0^{-1}$, only twice the relaxation time $\tau_r = 2Q\omega_0^{-1}$.

One may wonder if the extra cost at high speed is due either to the erasure protocol itself, or to the damping losses during the ramps. In the inset of Fig. 4.5, we plot the contribution $\boldsymbol{\mathcal{W}}_2$ or $\boldsymbol{\mathcal{Q}}_2$ of the ramp of stage 2. In a first approximation (neglecting transients), the cantilever follows the well center z_1 at the driving speed $\mathbf{v}_1$, while experiencing a viscous drag force $\gamma\mathbf{v}_1\sigma_0\omega_0 = k\sigma_0\mathbf{v}_1/Q$. We thus expect the ramp cost to be $\langle \boldsymbol{\mathcal{W}}_2 \rangle = \langle \boldsymbol{\mathcal{Q}}_2 \rangle \sim B_2' Z_1/\tau$, with $\mathbf{B}_2' = Z_1/(Q\omega_0)$. This approximation with no adjustable parameters is reported in the inset of Fig. 4.5 (dotted red), and matches perfectly the experimental data within the erasure speed under study here ($\mathbf{v}_1 < 0.1$). We compute $\mathbf{B}_2' \sim 0.6\,\omega_0^{-1} = 75\,\mu\text{s}$ for $Z_1 \sim 6$: the ramp contribution is not enough to explain the extra cost of fast erasures, since $2\mathbf{B}_2'$ (one contribution for each stage) would explain only 30 % of the overhead to $\ln 2$. Indeed, contrary to the over-damped regime in which the overhead to LB mainly comes from the dissipation, in the underdamped regime it stems from the heating of the memory we will explain in the next section.

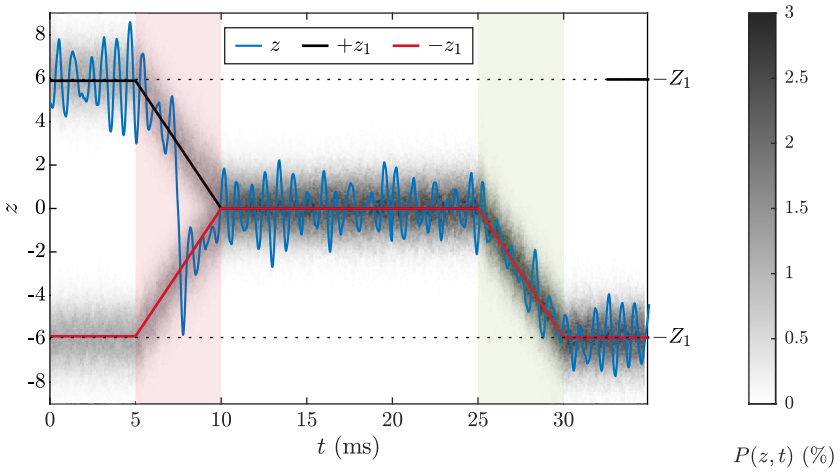

Figure 4.4 – **Fast erasure cycle**. Time recording of the cantilever deflection z on a single trajectory (blue, starting in state 1 in this example), superposed with the centers of two wells: $+z_1$ (black) and $-z_1$ (red) initially being worth $\pm Z_1 = \pm 6$. Stage 1 (red background) et 2 (green background) both last $\tau = 5\,\text{ms}$, so that the driving speed is worth $\mathbf{v}_1 = 0.12$. The grey map corresponds to the position PDF, computed from $N = 2000$ experimental trajectories of the erasure process.

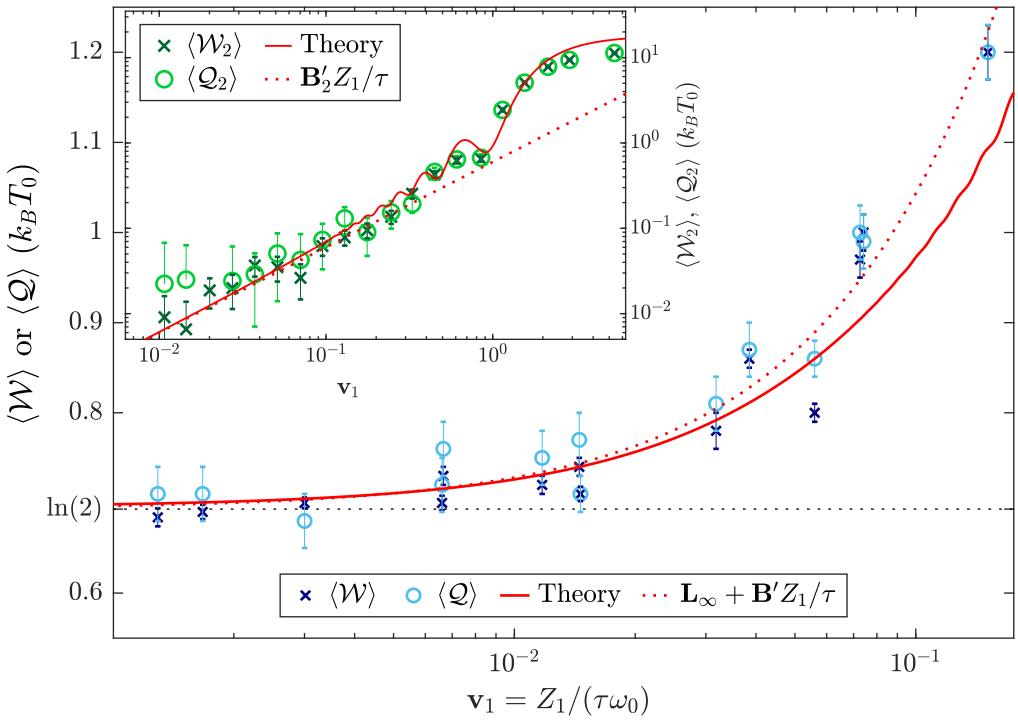

Figure 4.5 – **Divergence from Landauer's limit for fast erasures.** Energy cost ($\langle \boldsymbol{\mathcal{W}} \rangle$ and $\langle \boldsymbol{\mathcal{Q}} \rangle$) for erasure protocols at different driving speeds $\mathbf{v}_1$, with $Z_1 \sim 6$. Experimental data (blue) are fitted by $\mathbf{L}_\infty + \mathbf{B}' Z_1/\tau$ (dotted red), with $\mathbf{B}' = (3.43 \pm 0.21)\,\omega_0^{-1} = (437 \pm 27)$ µs and $\mathbf{L}_\infty = 0.695 \pm 0.012$. It is in good agreement with the model of section 4.3(red line). Inset: same considering only the translational motion in step 2 at different speeds. The theoretical prediction $\mathbf{B}'_2 Z_1/\tau$ (dashed red) with $\mathbf{B}'_2 = Z_1/Q\omega_0$ works perfectly (no adjustable parameters) within the erasure speed range under study in this section. For very fast motion $\mathbf{v}_1 > 0.1$, the transient must be accounted for with the theoretical model detailed in section 4.3 (red line).

4.3 Energetic study

4.3.1 Fast Erasures model (FE Model)

In the following, we explain the origin of the overhead to LB increasing with the speed: it comes in underdamped memories from the transient rise of the effective temperature T_{eff}, a source of energy loss that fundamentally differs from the viscous dissipation contribution of overdamped systems.

For this purpose, we measure the mean kinetic and potential energy during either a quasi-static erasure (Fig. 4.6a-b) and a fast one (Fig. 4.6c-d). When we proceed in a quasi-static fashion, the mean kinetic energy stays as expected at its equilibrium value $\frac{1}{2}k_BT_0$, while the odd evolution of the mean potential energy complies with equipartition for the bi-quadratic shape of U_1 as detailed in section 1.1.4 and in Eq. (1.34). For fast operations, the energy profiles are completely different: in particular they strongly increase during stage 1, before relaxing during the equilibration step. K can be decomposed into $\langle K\rangle = \frac{1}{2}m(\langle v\rangle^2 + \sigma_v^2)$, summing the contribution of the velocity mean value $\langle v\rangle$ that reflects the response to the well motion, and the velocity variance σ_v^2 which defines the kinetic temperature (following Eq. (1.68)). The first term is responsible for the transient oscillations at the beginning of step 1 and during step 2, but the energy rise during step 1 mainly comes from the thermal term: $\frac{1}{2}m\langle v\rangle^2 \sim \frac{1}{2}k_BT_0\mathbf{v}_1^2 \ll \frac{1}{2}k_BT_0$. It therefore demonstrates a transient temperature rise.

This warming and its consequences on the operation cost can be interpreted using a simple analogy: during step 1, the system behaves as a single-particle gas [12] at pressure p, compressed so that the available volume $\mathcal{V}$ is divided by 2 as illustrated on Fig. 4.7. The infinitesimal work required for the compression is $d\mathcal{W}^c = -pd\mathcal{V} = -k_BTd\ln\mathcal{V}$. If the transformation is quasi-static, $T = T_0$ and the work simplifies into $\mathcal{W}^c = k_BT_0\ln 2$. On the contrary, if the process is too fast to allow heat exchanges with the surrounding thermostat, the transformation is adiabatic, and the temperature T of the gas increases during the compression. Hence, the compression work for fast operations writes:

$$\mathcal{W}^c = k_B\int_0^\tau Td\ln\mathcal{V} = k_BT_{\text{eff}}\ln 2, \tag{4.7}$$

with $T_{\text{eff}} \geq T_0$. The heat exchanges after the adiabatic compression will then allow the system to thermalize at T_0.

Following the analogy sketched in Fig. 4.7, we will also call "compression" the reduction of the phase space volume explored when the bi-stable potential progressively shrinks until reaching a single well during step 1. This analogy highlights the fact that the warming during the compression is specific to the underdamped system, and would not exist if a strong coupling to the bath allowed efficient heat exchanges. The objective of the following sections is to build a model which describes both the compression and translational motion as observed in experiment. The heat $\langle\mathcal{Q}\rangle$ is given by Eq. (1.69). To compute the other energetic terms ($\langle\mathcal{W}\rangle$, $\langle K\rangle$ and $\langle U\rangle$), we rely on the PDF of position x and speed v. Let us introduce this PDF during the compression stage, supposing that the system is at equilibrium: it is governed by the Boltzmann

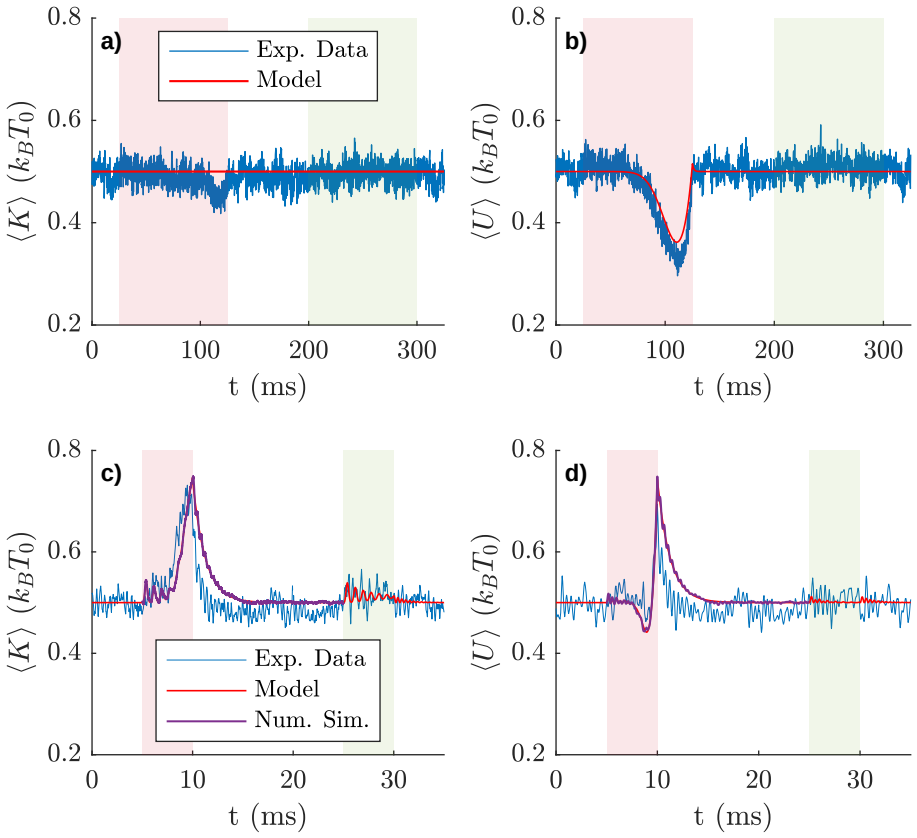

Figure 4.6 – **Energy evolution during an erasure procedure**. (a) In blue, the time evolution of the mean kinetic energy $\langle K \rangle$ over $N = 2000$ iterations of a quasi-static erasure ($\mathbf{v}_1 \ll 1$): stage 1 and stage 2 (red and green backgrounds) both last $\tau = 100\,\mathrm{ms}$. The red line corresponds to the equipartition detailed in section 1.1.4. (b) Same, with the mean potential energy $\langle U \rangle$. The dip in the potential matches the equipartition in a double well (rather than in a single quadratic one) as highlighted by the red line corresponding to Eq. (1.34) (c) and (d) Same for a fast erasure: $\tau = 5\,\mathrm{ms}$ ($\mathbf{v}_1 = 0.12$). The red line corresponds to the theoretical prediction detailed in the section 4.3. We add in purple line the results of a numerical simulation for step 1 that provides more samples than the experiment, $N_{\mathrm{sim}} = 5 \times 10^6$, and is thus free of statistical uncertainty.

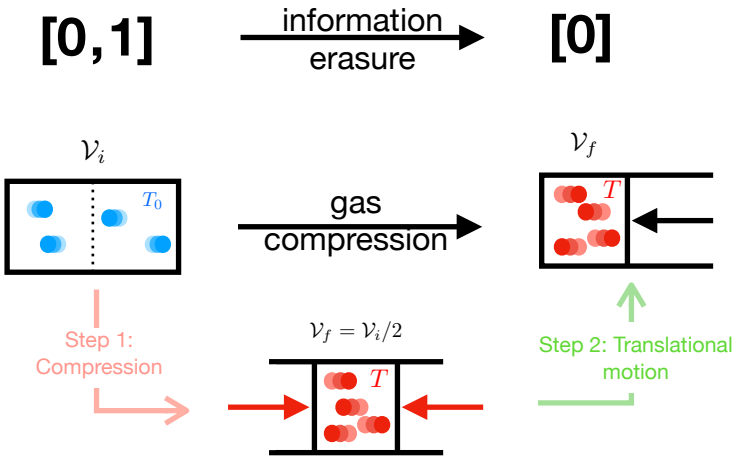

Figure 4.7 – **Simple analogy between information erasure and gas compression**

distribution

$$P^c(x,v) = \frac{1}{Z^c} e^{-\frac{1}{2}\beta m v^2} e^{-\frac{1}{2}\beta k(|x|-x_1)^2} \tag{4.8a}$$

$$Z^c(\beta, x_1) = \frac{2\pi}{\sqrt{km\beta}}\mathcal{V}, \quad \mathcal{V} = 1 + \mathrm{erf}\left(\sqrt{\frac{k\beta}{2}}x_1\right), \tag{4.8b}$$

with $\beta = 1/(k_B T)$, Z^c the partition function, and $\mathcal{V}$ a volume-like function that shrinks by a factor 2 when x_1 decreases from X_1 to 0. We can directly apply this PDF to the slow erasures, in equilibrium at temperature T_0 at all time. We extend the use of this PDF to the case of fast erasures as well, under the hypotheses that (i) the cantilever oscillates several times in the double-well before its shape changes significantly ($|\mathbf{v}_1| \ll 1$), so that the phase space is adequately sampled and (ii) a Boltzmann-like distribution still holds. In this case, however, we let the temperature T as a parameter free to evolve due to a possible heating. Note that the PDF $P^c(x,v)$ only describes the volume compression and does not include any transients, leaving aside any coupling between x and v. The main transient, due to the translational motion of the wells, is addressed in the next paragraph. In Appendix F, we compare the PDF of our ansatz with one sampled on a large numerical simulation, demonstrating its relevancy.

During stage 2, or at the beginning of stage 1 before the oscillator crosses the barrier, the dynamics is ruled by a linear Langevin equation: the potential energy is quadratic (no switching). $x(t)$ is therefore the sum of the stochastic response to the thermal fluctuations, and of the deterministic response $\pm x_D(t)$ to the driving force $F_D(t) = \pm k x_1(t)$ (the sign depending of which well is considered). $x_D(t)$ can be easily computed for our simple $x_1(t)$ ramps, and the PDF $P^t(x,v)$ which determines the translational motion is then described by [13; 14]:

$$P^t(x,v) = \frac{1}{Z^t} e^{-\frac{1}{2}\beta m(v-\dot{x}_D)^2} e^{-\frac{1}{2}\beta k(x-x_D)^2} \tag{4.9a}$$

$$Z^t = \frac{2\pi}{\sqrt{km\beta}}\mathcal{V}, \quad \mathcal{V} = 1. \tag{4.9b}$$

We easily retrieve $\langle x \rangle = x_D$ and $\langle v \rangle = \dot{x}_D$. In complement to Eq. (1.69) for the mean heat, the knowledge of the PDF allows the computation of all mean energetic quantities.

During compression for example, the mean energy is $\langle E^c \rangle = -\partial \ln Z^c / \partial \beta$, while the mean work derivative is $\langle \dot{\mathcal{W}}^c \rangle = \langle \partial U / \partial x_1 \rangle \dot{x}_1 = -\dot{x}_1 / \beta \, \partial \ln Z^c / \partial x_1$. In Appendix F, we derive the following expressions, valid for all stages:

$$\frac{d\langle \mathcal{Q} \rangle}{dt} = \frac{\omega_0}{Q}\Big(2K_D + k_B T - k_B T_0\Big) \tag{4.10a}$$

$$\frac{d\langle \mathcal{W} \rangle}{dt} = \frac{d\mathcal{W}_D}{dt} - k_B T \frac{\partial \ln \mathcal{V}}{\partial x_1}\dot{x}_1 \tag{4.10b}$$

$$\langle K \rangle = K_D + \frac{1}{2}k_B T \tag{4.10c}$$

$$\langle U \rangle = U_D + \frac{1}{2}k_B T + k_B T^2 \frac{\partial \ln \mathcal{V}}{\partial T} \tag{4.10d}$$

where $\mathcal{W}_D$, K_D and U_D are respectively the deterministic work, kinetic and potential energy which vanish in the quasi-static regime. With Eq. (4.10b) for a quasi-static compression in equilibrium at T_0, we recover the gas analogy $d\mathcal{W}^c = -k_B T_0 d \ln \mathcal{V}$, hence LB: $\langle \mathcal{W}^c \rangle = k_B T_0 \ln 2$. Fig. 4.3 highlights the very good agreement between the model and the experimental results.

Using the energy balance, Eq.(1.60), and Eqs.(4.10), we derive a differential equation governing the time evolution of the temperature: the deterministic terms cancels out, since they comply to the energy balance as well, and we're left with

$$\frac{d\langle E \rangle}{dt} = \frac{\partial \langle E \rangle}{\partial T}\dot{T} + \frac{\partial \langle E \rangle}{\partial x_1}\dot{x}_1 = -k_B T \frac{\partial \ln \mathcal{V}}{\partial x_1}\dot{x}_1 + \frac{k_B \omega_0}{Q}(T - T_0). \tag{4.11}$$

Explicit formulas for $\partial \langle E \rangle / \partial T$ and $\partial \langle E \rangle / \partial x_1$ are readily computed from Eqs. (4.10c-4.10d). When we proceed in a quasistatic fashion ($\dot{x}_1 \sim 0$), or when the volume is constant ($\partial / \partial x_1 = 0$) , we observe no heating: $T = T_0$. For fast compressions, this equation can be solved numerically and leads to the evolution of the kinetic temperature $T(t)$.

Thanks to the knowledge of $T(t)$, our model describes the evolution of all energetic quantities in Eqs. (4.10) during the erasure process. For slow erasures, kinetic (Fig. 4.8a) and potential (Fig. 4.8b) energies comply as expected with equipartition. For fast erasures, we obtain a strong temperature increase[2] during step 1, visible on both energy profiles. The system then thermalizes, before responding to the translational motion of step 2 with transient oscillations. Those theoretical results superimposed on Fig. 4.6 in red lines are in very good agreement with the experimental observations for both slow and fast erasures, with no adjustable parameters. We supplemented the model validation by numerical simulation data (see Appendix E): the black curve on Fig. 4.6c-d closely matches the model, except for tiny ripples during the thermalization that correspond to transients unaccounted for. Additionally, the model predicts that a fast erasure cycle will cause a mean power evolution that displays transient oscillations and a rise during compression, both of which are consistent with the experimental data of Fig. 4.8c, and perfectly matches the simulation results.

All in all, we propose an efficient theoretical framework to predict the energy exchanges and explore the fast information erasure cost. The model called the FE model only requires the system parameters (ω_0 and Q) and the protocol ones (X_1 and τ) to estimate the erasure cost. As a further illustration of the model reliability, in Fig. 4.5

[2] Since $\langle v \rangle^2 \ll \sigma_v$, $< K > \sim \frac{1}{2}k_B T$ and the temperature profile can be read directly on the kinetic energy curve.

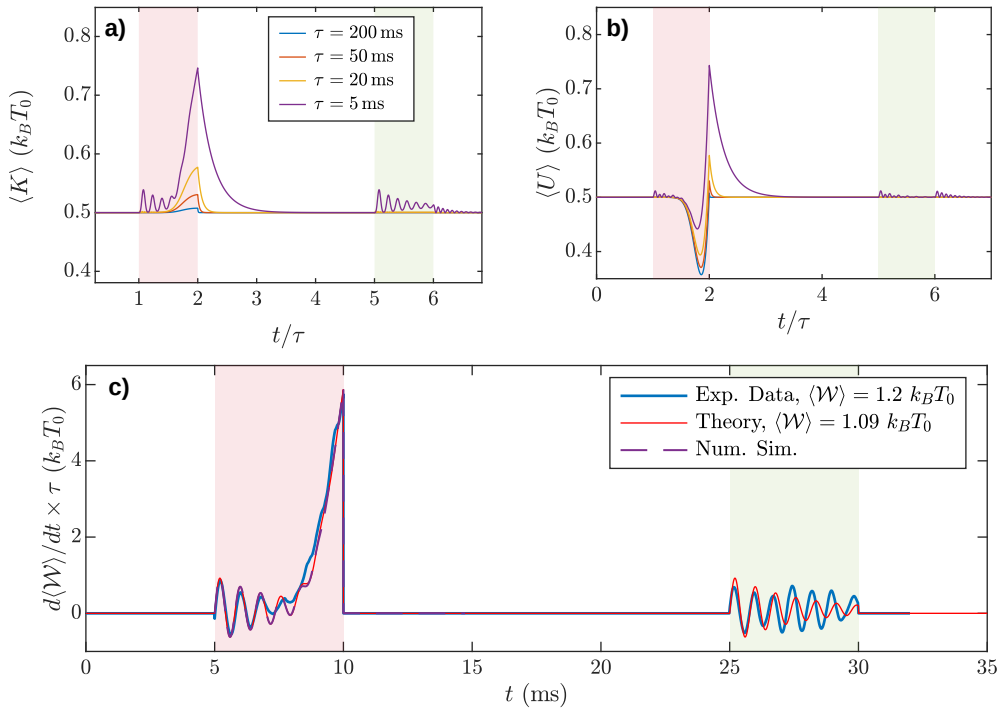

Figure 4.8 – **a) Model prediction: Time evolution of the mean kinetic energy** $\langle K \rangle$ for different duration τ of the erasure steps computed from Eq. (4.10c). For small τ, $\langle K \rangle$ is affected during step 1 (red background) by a transient oscillation due to the dragging, followed by a strong rise in temperature. Only the dragging transient appears during step 2 (green background). **b) Same plot for the potential energy** $\langle U \rangle$ from Eq. (4.10d). **c) Stochastic work profile.** Time evolution of the mean power over 2000 trajectories, following the fast protocol ($\tau = 5$ ms) corresponding to Fig. 4.4 (blue). The red line is computed using Eq. (4.10b) and closely matches the experimental results. Results of a numerical simulation (purple), corresponding to 5×10^6 trajectories, match the model so well that we cannot distinguish the curves.

we compute the erasure cost for growing driving speeds and compare this prediction with the experimental points. The obtained theoretical curve is also compared with the empirical description of the overhead scaling as $\langle \boldsymbol{\mathcal{W}} \rangle = \ln 2 + \mathbf{B}/\tau$: it successfully quantifies the divergence from LB as the speed is increased. The remaining difference may result from calibration drifts or experimental imperfections (see Ref. 15 reproduced in Appendix D), or from the shortcomings of the model with respect to transients.

Furthermore, the model distinguishes the part of the overhead due to the compression to the one due to the translational motion. The latter expressed in Eq. (F.9) and plotted in the inset of Fig. 4.5, behaves at first order as $(Z_1/Q \times \mathbf{v}_1)k_B T_0$. On the contrary, the former increases with the quality factor Q: it behaves as $k_B T_{\text{eff}} \ln 2$, with $T_{\text{eff}} > T_0$ the effective temperature during the process (details in Appendix F), rising when the heat exchanges with the bath are reduced (at high speeds or high Q).

4.3.2 Adiabatic limit

For large quality factors, heat exchanges with the bath are negligible: $d\langle \mathcal{Q} \rangle = 0$. Such compressions, called adiabatic compressions (or mean adiabatic [16]), correspond to the highest temperature rise because the kinetic temperature of the system cannot dissipate in the bath. Let us remind that the entropy variation during an adiabatic compression (assumed reversible) vanishes: $dS = d\langle \mathcal{Q} \rangle / T = 0$. Consequently, we have by definition of the entropy (using the partition function in Eq. (4.8b)):

$$\Delta S = \Delta(k_B \ln Z^c + \frac{\langle E^c \rangle}{T}) = 0 \tag{4.12}$$

As for $X_1 \gg \sigma_0$ the system starts and ends in the same quadratic potential, the energy in the initial and final states satisfies $\langle E_i^c \rangle / T_0 = \langle E_f^c \rangle / T_f = k_B$ (derived from equipartition, or equivalently from $\langle E^c \rangle = \partial \ln Z^c / \partial \beta$).

Therefore, only remains in Eq. (4.12) the variation of the compression partition function written in Eq. (4.8b):

$$\Delta(k_B \ln Z^c) = 0 \;\rightarrow\; \Delta(T\mathcal{V}) = 0 \tag{4.13}$$

As the volume is divided by two, the temperatures doubles during the adiabatic compression: $T_f = 2T_0 = T_a$. The corresponding work is given by the first law of thermodynamics (with $\langle Q \rangle = 0$):

$$\begin{aligned} \langle \mathcal{W}^c \rangle &= \Delta \langle E^c \rangle && (4.14)\\ &= k_B T_f - k_B T_0 && (4.15)\\ &= k_B T_0 = \mathcal{W}_a && (4.16) \end{aligned}$$

Hence, an adiabatic compression results in doubling the system temperature (and therefore the kinetic energy, $K_a = k_B T_0$) and requires on average $\mathcal{W}_a = k_B T_0$ of work, as the conservation of the phase space volume enslave the variations of the temperature to those of the volume. Let us point out that the adiabatic limit can be reached even for moderate quality factor $Q \sim 10$ if the erasure speed is high enough: in such case the heat exchanges are negligible during the compression step, and delayed to the relaxation period after step 1.

These considerations and the model built to predict the overhead to the LB for fast erasures open several possibilities to optimise the information processing.

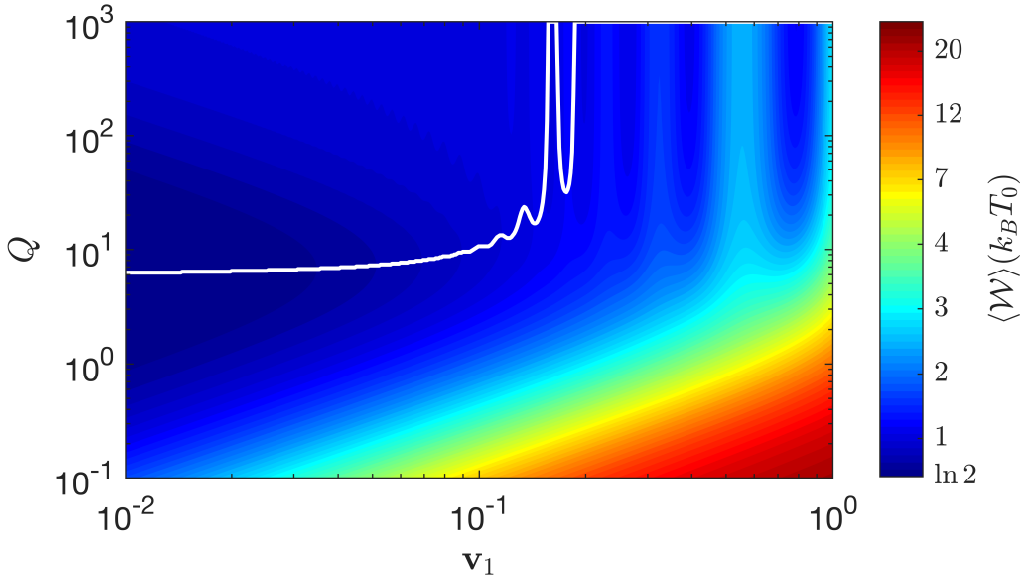

Figure 4.9 – **Erasure cost table from the FE Model**. Average work required for an erasure as a function of the protocol driving speed $\mathbf{v}_1 = Z_1/(\tau\omega_0)$ and the memory quality factor Q, using the FE model detailed in section 4.3. The white curve corresponds to the quality factor minimizing the erasure cost. On the first hand, optimizing very fast erasures ($\mathbf{v}_1 > 0.1$) means enhancing the quality factor. On the other hand, for moderate speeds ($\mathbf{v}_1 < 0.1$) the optimal damping is around $Q = 10$.

4.4 Optimisation

4.4.1 Strategy 1: Quality factor optimisation

Principle

There are three sources of energetic losses during an erasure: first, the very well known entropic part that accounts for $k_B T_0 \ln 2$; second, the dissipative cost coming from the translational motion of the system in the bath (mentioned in the literature for over-damped dynamics); and third the cost from the heating of the memory. As the first contribution cannot be avoided, we want to minimize the contribution of the dissipative and the warming terms. On the first hand the work required to compensate the viscosity analytically expressed in Appendix F.2 behaves as $1/Q$, and is therefore minimized at low damping. On the other hand we demonstrated in section 4.3.2 that the thermal contribution is bounded by the adiabatic limit (when there are no heat exchanges during the procedure), so that at very high quality factor the work from the compression cannot overreach $k_B T_0$. These considerations are summarized by the erasure cost table built using the FE model plotted in Fig. 4.9. It shows that working at very low damping should optimize very fast erasures for which the adiabatic limit is always reached ($\mathbf{v}_1 > 0.1$). On the contrary, for moderate speeds ($\mathbf{v}_1 < 0.1$), the optimal damping is around $Q = 10$, corresponding to the best balance between the warming and the damping contribution.

Experimental results at very low damping

We experimentally implement the erasure protocol at higher quality factor to confirm the above conclusions. To do so, we turn to the experimental set-up of Fig. 3.4 ($f_0 = 1.3\,\mathrm{kHz}$, $Q = 80$) using the FPGA feedback better suited for high quality factors. Let us point out that this second set-up allows us to explore a wider panel of erasure speeds, up to $\tau \sim 1\,\mathrm{ms}$. The experimental results perfectly match the FE model predictions for both the temperature and work evolutions as illustrated respectively in Fig. 4.10 and Fig. 4.11.

On the first hand, we see in Fig. 4.10a) that the kinetic energy nearly reaches the adiabatic limit $K_a = k_B T_0$ for $\tau = 5\,\mathrm{ms}$ ($\mathbf{v}_1 = 0.12$), hence greatly exceeding the results obtained at lower quality factor. It confirms that increasing Q enhances the compression warming, up to the adiabatic limit reached for $\tau = 2\,\mathrm{ms}$ ($\mathbf{v}_1 = 0.3$) in Fig. 4.10b). All in all the results from experiments and from simulations validate the FE model at higher quality factor, and illustrate the adiabatic limit.

On the other hand, the experimental results in Fig. 4.11 validate the erasure cost table stemmed from the model (Fig. 4.9) and the conclusion drawn in terms of quality factor optimisation.

4.4.2 Strategy 2: optimal protocol for the translational motion

The oscillations in the work visible in both Fig. 4.9 and Fig. 4.11 come from the dissipative cost that oscillates with the translational motion speed (see Eq. (F.9)). Another optimisation strategy (that can be combined with the first one) therefore consists in adapting the translational driving to always minimize the viscous work. In Ref. 2 one can find an optimal erasure designed for over-damped systems that cuts the dissipative cost by reducing the translational driving amplitude at the expense of an out-of-equilibrium final state.

Using a different approach we aim here to replace all the linear translational drivings by optimal protocols explicitly computed in Ref. 11 (and also tackled in Ref. 17). Basically, the deterministic translational motion is now done at an optimal constant speed, getting rid of the transient oscillations, by applying force peaks at the initial and final instant of the ramp as displayed on Fig. 4.12a). As demonstrated in Fig. 4.12b) the optimal protocol successfully forces the cantilever to move at constant (mean) speed and suppresses the dragging oscillations visible in response to the linear driving. The lowest possible work required to move the underdamped system of a distance Z_1 in a time τ is therefore obtained using this optimal protocol, and is worth:

$$\mathcal{W}_{D,\mathrm{opt}} = \frac{Z_1^2}{2 + Q\tau\omega_0}, \tag{4.17}$$

We numerically simulate (following the method in Appendix. E) our erasure protocol after replacing all the linear translational drivings by optimal ones expressed in Refs. 11. Let us point out that the final force peak designed to brake the system after the translational motion is not adapted to step 1, at the end of which the system can switch between the two moving wells. Nevertheless, we see in Fig. 4.13a) that the resulting optimal erasure protocol still significantly reduces the work required for very fast erasures.

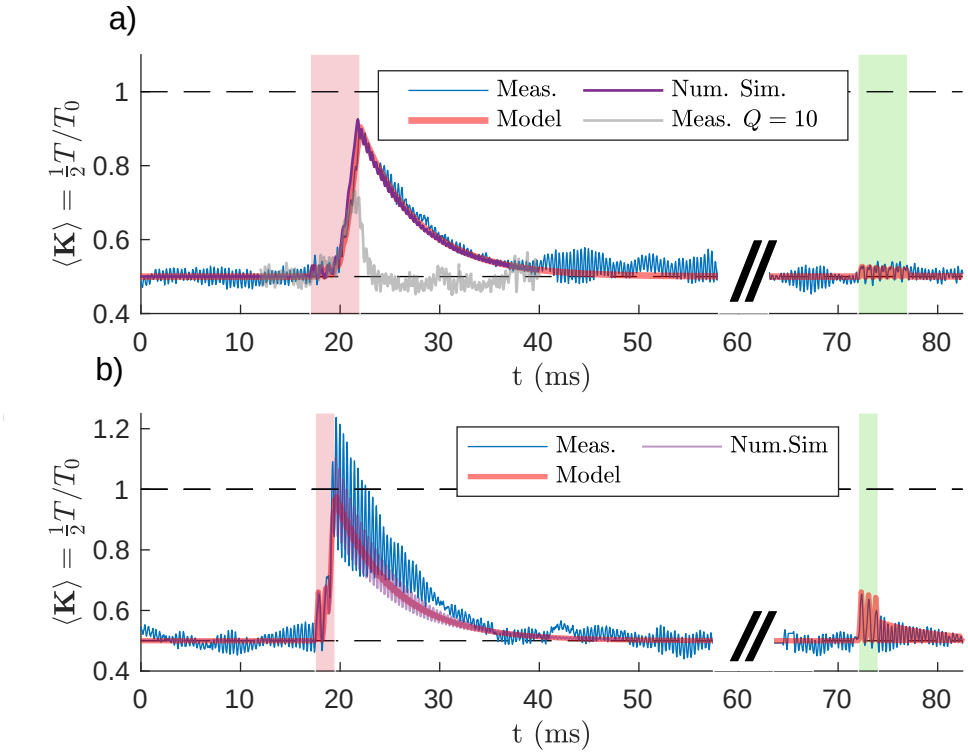

Figure 4.10 – **a) Kinetic energy during a fast erasure process ($\mathbf{v}_1 = 0.12$) at high quality factor ($Q = 80$).** Step 1 in red background lasts $\tau = 5\,\mathrm{ms}$ (with $Z_1 = 5$) and results in a strong temperature rise visible on the kinetic energy profile: $\langle K \rangle$ culminates at $0.92\,\mathrm{k_B T_0}$, ie at 92% of the adiabatic limit $K_a = k_B T_0$. At the end of the compression step, the system thermalizes with the surrounding bath in $\tau_{relax} \sim 20\,\mathrm{ms}$ so that the kinetic energy relaxes to its equilibrium value $K_{\mathrm{eq}} = \frac{1}{2} k_B T_0$. Then, the translational motion of duration τ (step 2 in green background) only produces tiny oscillations. The experimental curve averaged from $N = 1000$ trajectories (blue), nicely matches the model detailed in previous chapters (red) and the simulation result for step 1 (purple) obtained from $N_{\mathrm{simu}} = 10^5$ simulated trajectories. The measurement at the same speed but for $Q = 10$ is reported from Fig. 4.6c) for comparison. **b) Kinetic energy in the adiabatic limit: $\mathbf{v}_1 = 0.3$ and $Q = 80$.** This time the adiabatic limit is reached during the compression of duration $\tau = 2\,\mathrm{ms}$ as predicted by the model and confirmed by the numerical simulation. The average kinetic energy even exceeds $K_a = k_B T_0$ because of the transient oscillations from deterministic contribution K_D. Step 2 translational motion also triggers larger oscillations that the one observed in a).

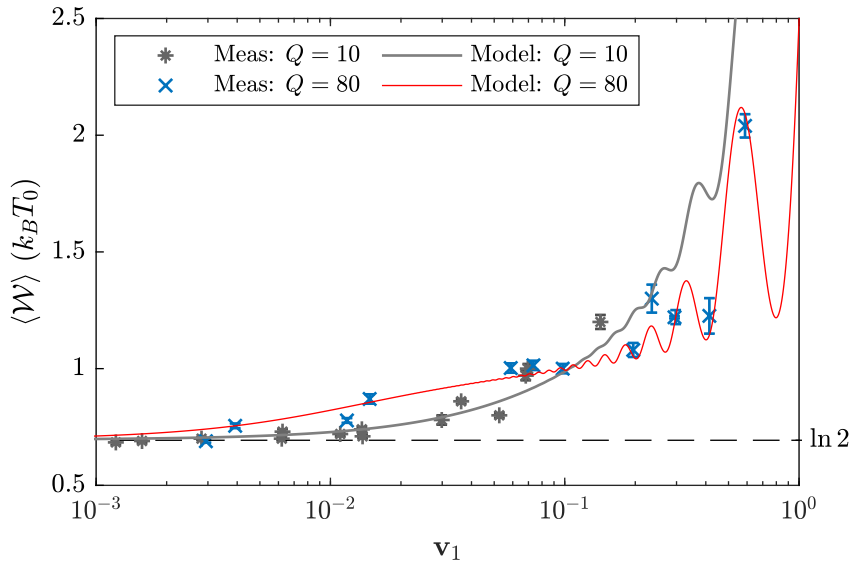

Figure 4.11 – **Influence of the damping on the divergence from Landauer's limit for fast erasures**. As for the results at $Q = 10$ (results from Fig. 4.5 reproduced in grey), the experimental points (blue crosses) obtained at lower damping $Q = 80$ (and $Z_1 \sim 5$) again validate FE Model (red). We identify two speed regions in which the optimisation strategy in terms of quality factor differs. In the moderate speeds region $\mathbf{v}_1 < 0.1$ (here $Z_1 \sim 5$ so that it corresponds to $\tau < 6\,\mathrm{ms}$), the optimal damping corresponds to $Q = 10$, since at higher quality factor $Q = 80$ what is won on the viscous work is lost by the more substantial warming cost. On the contrary, for very fast erasures ($\mathbf{v}_1 > 0.1$), the overall cost is lower at $Q = 80$, as it is ruled by the dissipative term only, the compression contribution being bounded by $\mathcal{W}_a = k_B T_0$.

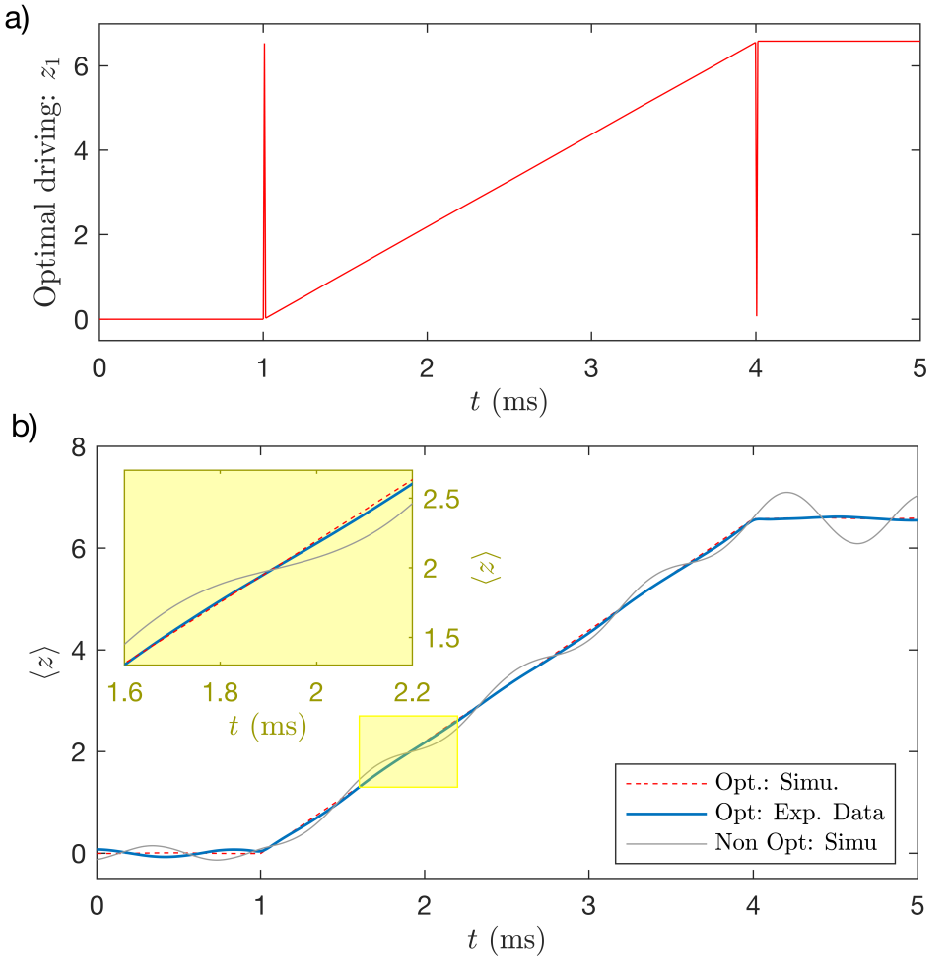

Figure 4.12 – **a) Optimal translational driving** of the center of the well, z_1, computed from Ref. 11 to move a underdamped system of quality factor $Q = 80$ from 0 to $Z_1 = 6.5$ in a time 3 ms at a minimal cost given in Eq. (4.17). This optimal protocol forces the mean velocity to instantly jump at the beginning of the process from its initial equilibrium value ($\langle v \rangle = 0$) to the optimal constant speed. The final peak corresponds to setting the final velocity back to zero. The amplitude of the delta peaks depends on the quality factor, the amplitude and the duration of the translational driving. **b) Response to the optimal translational driving.** Both for the experimental results (blue) and the simulation ones (dotted red), the optimal protocol drives the system at the optimal constant mean velocity which minimises the dissipation. Indeed the optimal protocol in a) suppresses the transient oscillations in the mean position $\langle z \rangle$ of the system visible in the response to the basic linear driving computed from $N_{\text{simu}} = 10^4$ trajectories and plotted in grey. The zoom window in yellow background emphasizes the difference between the linear and optimal driving responses.

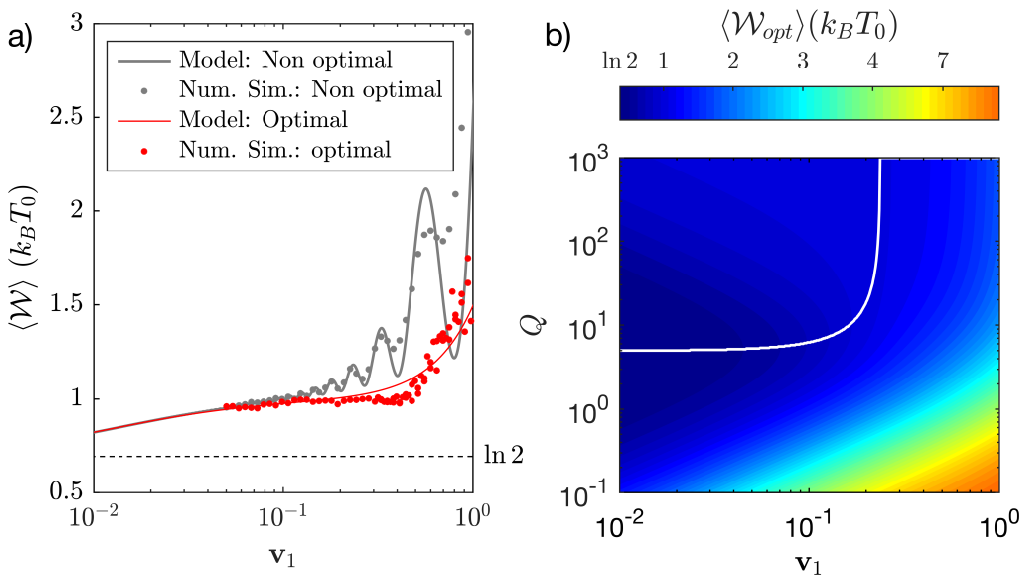

Figure 4.13 – **a) Numerical Simulation of the optimal protocol for** $Q = 80$. Simulation results (red circles) of the optimal protocol in which all the translational drivings are replaced by optimal drivings designed to minimize the dissipative cost such as the one displayed on Fig. 4.12a). The optimal erasure is more efficient than the previous non optimal protocol (grey), in particular at very high speeds ($\mathbf{v}_1 > 0.1$) when the viscous work prevails. For both the non optimal and the optimal protocol, the simulation results (circles) and the model (line) are in good agreement. In the very high speeds region, when the assumption $\mathbf{v}_1 \ll 1$ is no longer valid, the model starts deviating from the simulation. **b) Optimal erasure cost table** obtained using the FE model adapted to the optimal protocol, with the quality factor minimizing the erasure cost highlighted in white. The optimal protocol gives better results than the classic one whose cost table is in Fig. 4.9. The same color scale is used for easier comparison.

We extend the FE model to the optimal erasure protocol by 1) replacing the deterministic contribution $\mathcal{W}_D$ by the optimal translational cost $\mathcal{W}_{D,\text{opt}}$ expressed in Eq. (4.17); and 2) adding the kinetic energy given to the system through the initial force peak at the beginning of step 1, and assumed to not be recovered through the final force peak at the final instant. These modifications of the FE Model perfectly describe step 2, and approximate well the system's response during step 1: we illustrate in Fig. 4.13a) its good agreement with the simulation results. The slight overestimation of the optimal erasure cost observed on Fig. 4.13a) is likely to come from the fact that the final force peak is not totally inefficient to bring back the average velocity to 0 after step 1 as assumed in the model. Furthermore, at high speeds the model assumption $\mathbf{v}_1 \ll 1$ stops being true, causing the deviation from the simulation results. Despite these small approximations, the model is reliable enough to draw the optimal erasure cost table in Fig. 4.13b): we see that in the high speed region $\mathbf{v}_1 > 0.1$, the optimal protocol strongly minimizes the erasure cost compared to the classic protocol in Fig. 4.9.

As a conclusion, implementing optimal driving for translational motions in the erasure protocol (strategy 2), and working in the underdamped regime $Q > 1$ is the most efficient way to erase a bit. Depending on the erasure speed, the quality factor can be tuned to minimize the erasure cost (strategy 1): at moderate speeds $Q \sim 10$

seems a good compromise while at very high speeds Q should be increased as much as possible.

4.5 Repeated use of the memory

4.5.1 Context

The erasure of 1-bit of information in the underdamped regime has been thoroughly studied, and a wide panel of erasure speed is covered in previous sections. It was demonstrated that for fast operations the kinetic energy rises as a consequence of the memory heating. This phenomenon is amplified when the damping decreases so that at very high quality factor ($Q \sim 90$), we show in section 4.3.2 that the memory's temperature rise saturates at the adiabatic limit $T_a = 2T_0$ for high erasure speeds. As illustrated on Fig. 4.10a) for $\mathbf{v}_1 = 0.12$, the kinetic energy $K = \frac{1}{2}k_BT$ grows during step 1 and approaches the adiabatic limit $K_a = \frac{1}{2}k_BT_a = k_BT_0$, then it relaxes to the equilibrium value $K_{\text{eq}} = \frac{1}{2}k_BT_0$ during the thermalization. During step 2, we observe only transient oscillations due to the deterministic contribution of the translational motion.

Even though the underdamped regime reduces the cost of fast erasures, the low heat exchanges with the bath slow down the thermalization (scaling as Q/ω_0), therefore imposing a long relaxation stage to reach the equilibrium before each step. Only then, the memory can perform successive and equivalent erasures, maintaining a constant operation cost. Nevertheless, one may wonder on a practical point of view, what happens if the erasures are repeated without waiting for equilibrium before each steps. Such a procedure would get rid of the long relaxation times (for example 20 ms in Fig. 4.10) and significantly shorten the process.

At high damping, the instant thermalization allows us to sequence erasures without consequences on the thermodynamics, but faster erasure requires a huge energetic cost (to compensate the viscosity). That is why, to optimize the information processing speed and cost it is worth considering the very low damping regime. In this context, we will detail in the following how the erasure cost is impacted by the removal of equilibration steps and by the repetition. In the light of previous findings, for fast erasures we expect the temperature to increase continuously in average: rising during the compression without enough time to relax to T_0 before a new compression. The temperature increments could nevertheless saturate at one point, if the energy surplus stored at each compression is compensated by the heat exchanges with the bath.

4.5.2 Protocol and analysis criteria

The experimental set-up is the one illustrated Fig. 3.4: the cantilever evolves in vacuum ($P \sim 1$ mbar) corresponding to a quality factor $Q \sim 90$ deduced from the best fit of PSD. The tunable virtual potential is created using the FPGA card that processes the feedback operations fast enough to work at very low damping. Similarly to the previous chapter, we call $\pm X_1 = \pm 5\sigma_0$ the initial position of the wells' centers providing a barrier $\mathcal{B} = \frac{1}{2}kX_1^2 = 12.5k_BT_0$ high enough to safely encode the information in the memory; x_0 the barrier position; and $\pm x_1$ the wells position. The cantilever evolves in the potential $U(x, x_1, x_0) = \frac{1}{2}k(x - S(x - x_0)x_1)^2$, which simplifies into the double well potential $U_1(x) = \frac{1}{2}k(|x| - x_1)^2$ during step 1 ($x_0 = 0$), and into a single well

$U_2(x) = \frac{1}{2}k(x \pm x_1)^2$ during step 2 when the barrier is driven out of range ($x_0 = \pm 6\sigma_0$ depending desired final state).

To explore the sustainability of repeated operations in a small amount of time, we implement in the FPGA a protocol of 45 successive erasures as the one sketched in Fig. 4.14a). One erasure consists in 1) starting in the double well potential $U_1^0(x) = \frac{1}{2}k(|x| - X_1)^2$ before merging the wells together during stage 1 (duration τ); 2) immediately starting stage 2 and bringing back the system in a single well to the reset state (duration τ); 3) recreating, after 0.5 ms in the single well, the initial double well potential and impose 1.5 ms free evolution into U_1^0 to evaluate the success of the erasure. We introduce $\tau_r = 2$ ms the duration of the third stage.

Contrary to the previous protocol for one erasure, there is no equilibration step between stage 1 and 2, and the final state is not systematically the state 0. Indeed we tackle the 2 erasures procedures $(0,1) \to 0$ and $(0,1) \to 1$, that reset the memory to respectively state 0 or state 1. As we sequence the operations, the initial state of one erasure corresponds to the final state of the previous one: to cover equivalently the whole $(0,1)$ initial state space (and provide for each reset state $p_i = 0.5 \to p_f = 1$) we choose to cycle on 4 erasures $\overline{\hookrightarrow 1 \to 0 \to 0 \to 1\hookrightarrow}$. The choice of the final state does't make any differences in the thermodynamics because our erasing procedure is symmetric: any configuration therefore contributes evenly to the statistics.

Fig. 4.14b) shows a cycle of four successful operations, the first two erasing to state 0 and the last two to state 1. In contrast, we plot on Fig. 4.14c) an erasure failing: the system ends up with more energy than the barrier $\mathcal{B}$ so that the final state (state 0 here) is not secure. As a consequence, during the 1.5 ms free evolution in U_1^0 before the next repetition starts, the systems switches between state 0 and state 1. This erasure is classified as a failure. When the procedure fails once, we consider all the subsequent erasures as failures as well.

Fig. 4.14c) is a zoom on the first failure of the protocol plotted in Fig. 4.14a). We see indeed the deflection excursion growing progressively, until the systems no longer ends in a secured final state after $i = 22$ erasures. We note N_i the number of trajectories ensuring a successful outcome of the erasure i. We deduce from the $N_{\text{tot}} = 2000$ protocols the average success rate at each repetition: $R_i^{\text{s}} = N_i/N_{\text{tot}}$. When an erasure is a success we compute the stochastic work and heat, and deduce the average values from the N_i trajectories.

4.5.3 Experimental results

The goal of the experiment is to explore the robustness of the memory to repeated erasures depending on the speed imposed to perform one operation. That is why we compare the response for $\tau = 6$ ms, $\tau = 4$ ms, $\tau = 3$ ms and $\tau = 1$ ms, tackling the speed high limit of our set-up. It correspond to $\mathbf{v}_1 = 0.1$, $\mathbf{v}_1 = 0.15$, $\mathbf{v}_1 = 0.2$ and $\mathbf{v}_1 = 0.58$, so that the last dataset allows only one oscillation for each step. Let us point out that the total erasure duration is worth $2\tau + \tau_r$ with τ_r fixed to 2 ms.

For different speeds we compute the success rate R_i^{s} of the erasure i, the probability density in position $P(x,t)$, the average kinetic energy evolution $\langle K \rangle$, and the average work $\langle \mathcal{W} \rangle$ required for each successful erasure.

Let us first tackle the success rate and the probability density plotted respectively on Fig. 4.15a) and b). Without surprise, the faster the information is processed, the less reliable the operation becomes. Indeed for $\tau = 6$ ms and $\tau = 4$ ms the success rate after 45 repeated erasures stays above 70%; meanwhile for $\tau = 3$ ms and $\tau =$

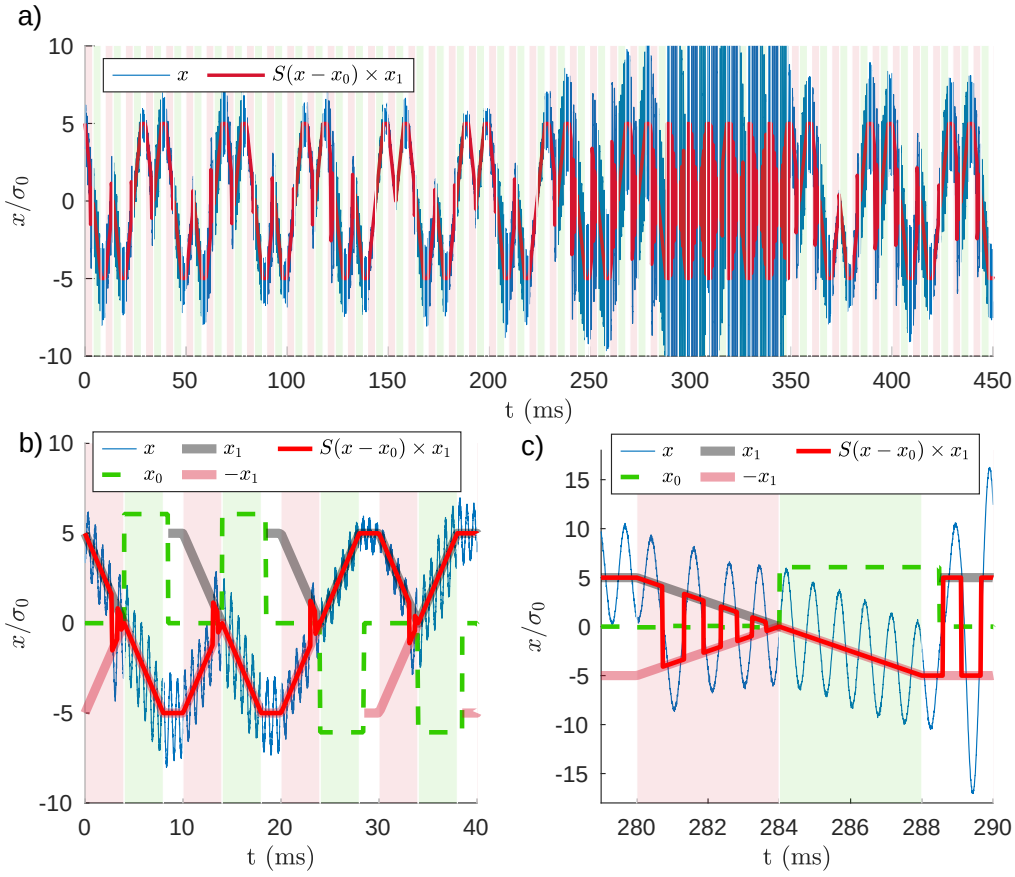

Figure 4.14 – **a) Protocol of 45 repeated erasures with $\tau = 4\,\mathrm{ms}$.** The compression and translational stage of each erasures (duration τ) are respectively highlighted in red background for step 1 and green one for step 2. During step 1 switches between the wells are allowed in the double well potential, whereas during step 2 the cantilever is supposed to be brought back to the desired final state without switching. At all time, the trajectory of the cantilever (blue) evolves into the well centered in $S(x-x_0)\times x_1$ (red). During the first 280 s, 22 erasures are performed successfully. Afterwards, the operation fails several times because the system energy has become too high. **b) Zoom on the 4 first successful erasures.** The cycle covers all combinations $(0,1) \to 0$ and $(0,1) \to 1$. Each erasure starts with a double well potential U_1^0 ($x_0 = 0$, $X_1 = 5\sigma_0$), then merged into one single well during step 1 ($x_0 = 0$, $x_1 \to 0$), driven back to the final state (state 0 for the first two and state 1 for the last two) during step 2 ($x_0 = \pm 6\sigma_0$ depending on the final state, $x_1 \to X_1$), and finally recreated. After step 2, we wait 0.5 ms before recreating U_1^0 ($x_0 \to 0$), and then we let the system freely evolve into U_1^0 during 1.5 ms to evaluate the success of the erasure. At all time the actual center of the potential seen by the cantilever writes $S(x-x_0)\times x_1$ (red) and depends on the barrier position x_0 (dashed green), the wells half distance x_1 (light red and black) and the cantilever position x (blue). **c) Zoom on the first failure at** 280 s. During the free evolution in the final double well (white area) the cantilever escapes the final state (here state 0): the erasure fails.

1 ms it immediately collapses after a few erasures and the probability to complete the whole protocol is null. These two driving speed regimes ($\mathbf{v}_1 < 0.2$ called region C for Converging and $\mathbf{v}_1 \geq 0.2$ called region D for Diverging) are also visible on the probability density in Fig. 4.15b). Within the speed region C ($\tau = 6\,\text{ms}$ and $4\,\text{ms}$) the cantilever trajectories remains contained by the double well barrier height and the information isn't lost ($R_{45}^{\text{s}} > 70\%$). On the contrary, very fast procedures (speed region D, $\tau = 3\,\text{ms}$ and $1\,\text{ms}$) result in the blurring of $P(x,t)$, because the cantilever escapes more and more often the double well potential: the reset systematically fails at the end of the protocol ($R_{45}^{\text{s}} < 2\%$).

The success rate can be explained by the temperature profile of the memory visible through the average kinetic energy plotted in Fig. 4.17. During the first repetitions, the temperature nearly doubles at each compression, and decreases afterward without fully thermalizing. For $\tau = 6\,\text{ms}$ and $\tau = 4\,\text{ms}$ it finally stops increasing by step and reaches a permanent regime below the barrier allowing a secure encoding of the information. On the other hand, for $\tau = 3\,\text{ms}$ and $\tau = 1\,\text{ms}$ the kinetic energy skyrockets and exceeds the energy barrier. We recover through the temperature behavior the two speed regions identified when analyzing the success rate.

When the erasure succeeds, it is also interesting to quantify the work required on average. Indeed at the same speed, we expect the work after a repeated use of the memory to be higher than the one required for a single erasure studied in section 4.3.2. As we tackle the erasure work, we restrict the study to region C where there are enough successful operations to compute properly the erasure cost for the 45 iterations: the operation cost for speeds $\tau = 6\,\text{ms}$ and $\tau = 4\,\text{ms}$ is displayed in Fig. 4.16. It highlights that not only the failure rate increases with the speed, but also the work required to process the information. Indeed after a quick transient, the work reaches a plateau whose value grows with the speed of the process. We detail in the next sections first a simple model that helps understanding and predicting the energy behavior, and second a more complete description to provide quantitative results.

Before that, let us make a parenthetical remark: for cycle processes starting and ending in a similar equilibrium state, the heat equals the work on average. Indeed as the energy balance of the system imposes $\Delta U + \Delta K = \mathcal{W} - \mathcal{Q}$, when the energy equipartition imposes the same initial and final values of $\langle U \rangle$ and $\langle K \rangle$, we have straightforwardly $\langle \mathcal{W} \rangle = \langle \mathcal{Q} \rangle$. Nevertheless, for the processes under scrutiny starting and ending out of equilibrium there are substantial and varying $\Delta\langle K \rangle$ and $\Delta\langle U \rangle$, even in the permanent regime because of the different deterministic contributions during the 4 erasures cycle. This is why the heat is not anymore equal to the work on average on a single cycle, and comparing the measure of the heat with the work as it was done in previous sections is not relevant anymore.

4.5.4 Simple Model

The goal of this section is to propose a very simple model to grasp the behavior of the memory in response to successive use, and in particular to understand the two speed regimes observed experimentally. Indeed within region D the kinetic energy widely exceeds the barrier, leading to the systematic failure of the protocol after several repetitions. On the other hand erasures in region C has a kinetic energy converging below the barrier and a good success rate. This behavior can be explained by the balance between the warming during the compression and the heat released into the bath afterwards. Depending on the relative importance of this two opposite phenomenon appears

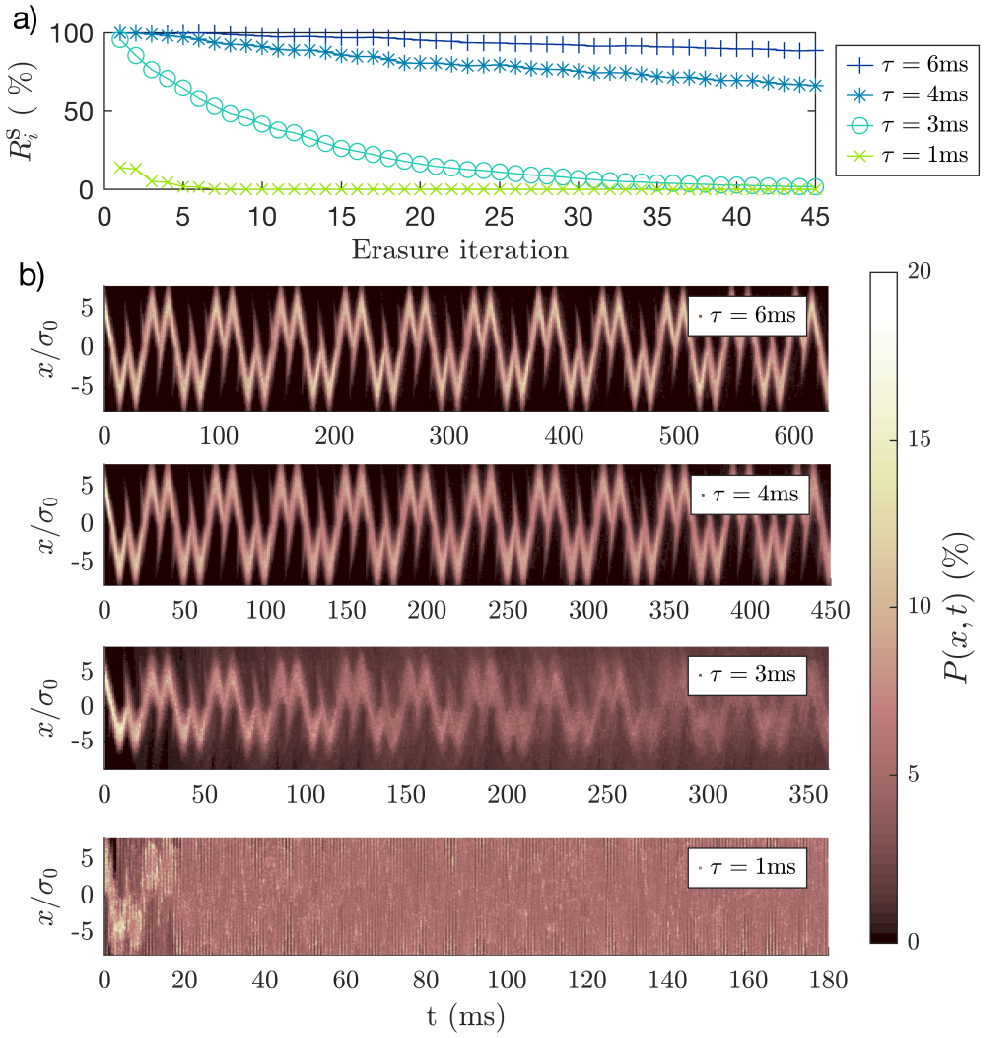

Figure 4.15 – **a) Success of repeated erasures for different operation speeds.** Success rate of the iteration i of the 45 repeated erasures: $R_i^s = N_i/N_{\text{tot}}$, computed from $N_{\text{tot}} = 2000$ procedures at $\tau = 6\,\text{ms}$, $\tau = 4\,\text{ms}$, $\tau = 3\,\text{ms}$ and $\tau = 1\,\text{ms}$. An erasure is classified as a success as long as the cantilever stays in the desired final state during the 1.5 ms free evolution in U_1^0 at the end. We distinguish the speed region C ($\mathbf{v}_1 < 0.2$, corresponding here to $\tau = 4\,\text{ms}$ and 6 ms) resulting for the major part in a protocol success ($R_{45}^s > 70\%$), from the region D ($\mathbf{v}_1 \geq 0.2$, corresponding to $\tau = 1\,\text{ms}$ and 3 ms) in which the memory fails to repeat successfully the operation ($R_{45}^s < 2\%$). **b) Measured probability density** $P(x,t)$ inferred from $N_{\text{tot}} = 2000$ trajectories for different speeds. $P(x,t)$ is normalized at each time step. The blurring of the probability density is consistent with the success rate: when the excursion goes huge, the trajectories escape the driving and the information is lost.

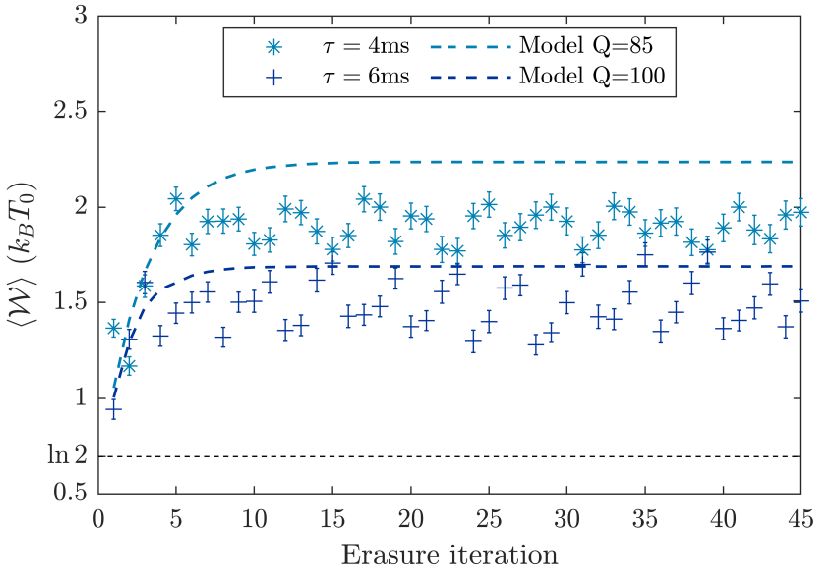

Figure 4.16 – **Average work required for the 45 repeated erasures for** $\tau = 4\,\mathrm{ms}$ **and** $\tau = 6\,\mathrm{ms}$**.** $\langle \mathcal{W} \rangle$ of the erasures i is inferred from the N_i successful trajectories, for the 2 erasure speeds in region C allowing enough successful erasures. After a couple of repetition the average work reaches a plateau depending on τ : $\mathcal{W}_{\mathrm{sat}}(\tau = 6\,\mathrm{ms}) = 1.5\,\mathrm{k_B T_0}$, and $\mathcal{W}_{\mathrm{sat}}(\tau = 4\,\mathrm{ms}) = 1.9\,\mathrm{k_B T_0}$. The model (dashed line) successfully predicts the converging behavior and is in reasonable agreement with the experimental result considering the approximations made and the fact that near the region boundary it is very sensitive to the calibration parameters. The quality factor Q used for the model is the same as the one tuned to match the kinetic energy profile in Fig. 4.20 and Fig. 4.19.

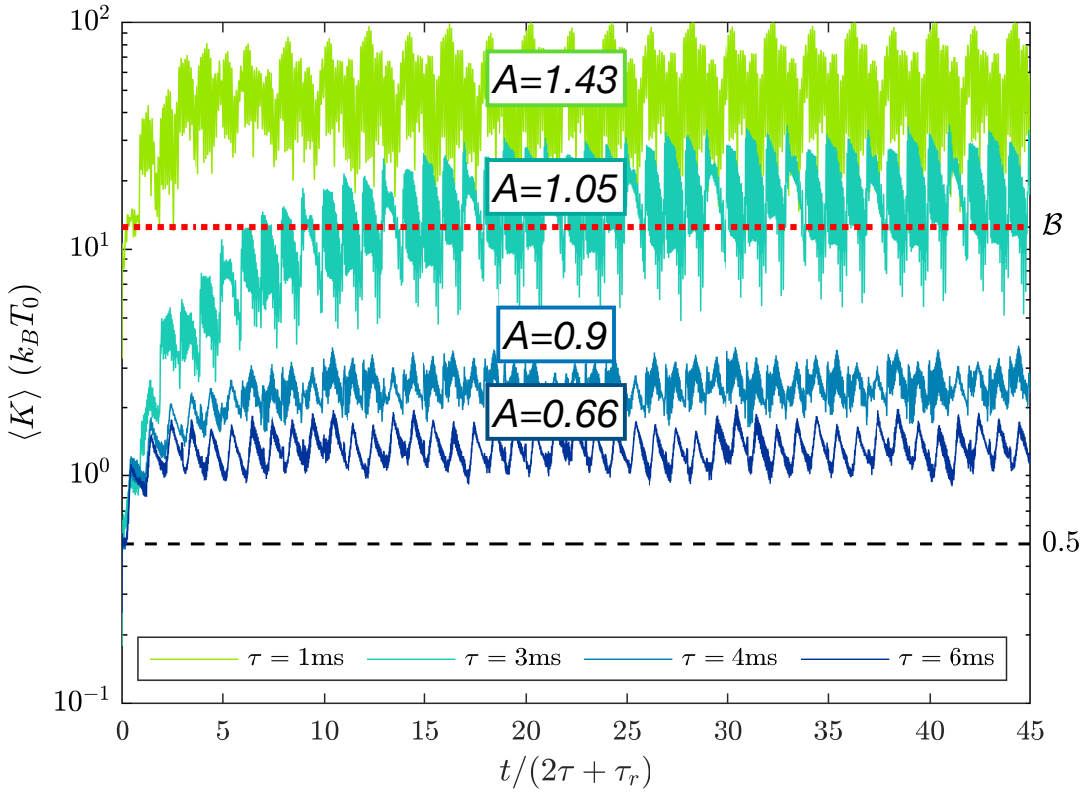

Figure 4.17 – **Average kinetic energy evolution during 45 successive erasures for different duration.** For speed region C ($\mathbf{v}_1 \leq 0.2$), $\langle K \rangle$ starts from its equilibrium value ($\frac{1}{2}k_B T_0$ in dashed line) and nearly doubles during the first successive adiabatic compressions. The thermalization afterward is very partial and is not enough to stabilize the temperature for the first iterations. Eventually the kinetic energy converges to a plateau after a couple of erasures; the higher the speed the higher the saturation value. On the other hand, for speed region D ($\mathbf{v}_1 > 0.2$) the kinetic energy strongly increases and overreaches the barrier height (dotted blue): the thermalization doesn't balance the compression warming anymore. Moreover, if the operation fails the systems in the wrong well takes an energy kick when the potential U_1^0 is rebuilt. As a consequence, a runaway occurs because more failures result in energy peaks and energy rise leads to more failures. The simple model successfully predicts these two regimes with the indicator A (computed with Eq. (4.27) assuming $Q = 90$): $A < 1$ in speed region C (Convergence to a plateau below $\mathcal{B}$) and $A > 1$ in speed region D (Divergence beyond $\mathcal{B}$).

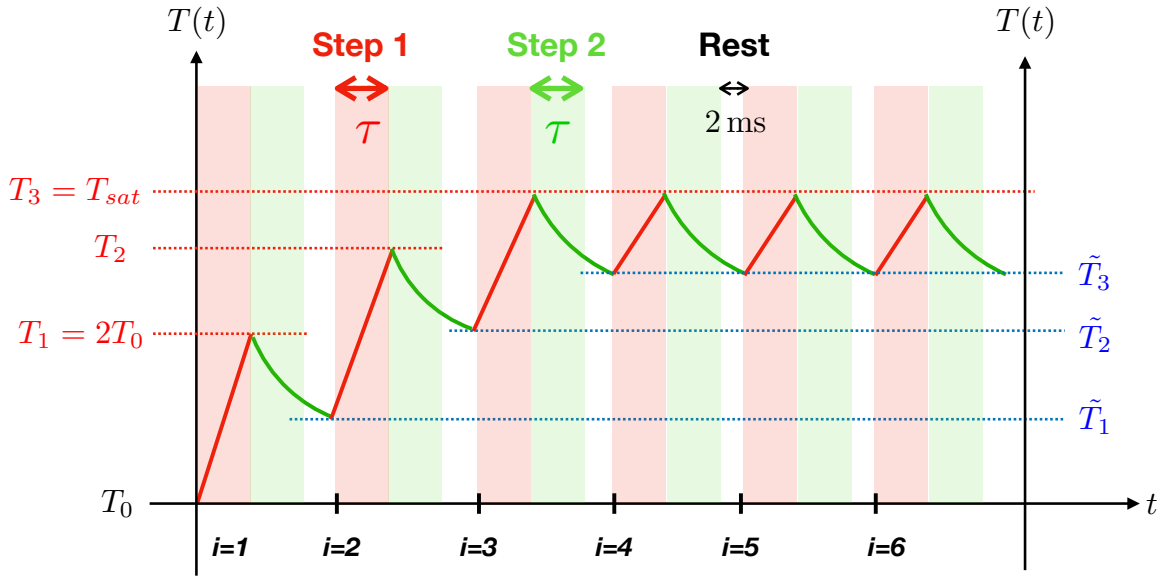

Figure 4.18 – **Schematic description of the simple model**. We decompose the protocol in successive step 1 (red segments, duration τ), followed by step 2 and resting step (green segments, duration $\tau_r = 2\,\text{ms} + \tau$). For each erasure i we call T_i the temperature after step 1 and $\tilde{T}_i$ the temperature after the relaxation. After some repetitions the temperature can either converge and saturate to a permanent regime, or diverge and exceed the barrier.

or not a saturation temperature allowing the two to compensate each-other.

To build the simple model we start with the energetic balance of the system:

$$\frac{d\langle E\rangle}{dt} = \frac{d\langle \mathcal{W}\rangle}{dt} - \frac{d\langle \mathcal{Q}\rangle}{dt} \tag{4.18}$$

Several assumptions justified by the high speed and quality factor are made to simplify the description:

(i) The work expression in the adiabatic limit holds

(ii) Deterministic contributions (K_D and U_D) are neglected

(iii) The time derivatives in Eq. (4.18) are approximated at first order

(iv) The first erasure is adiabatic

(v) Step 2 does not require work.

The erasures are decomposed into the compression, step 1 lasting τ; and the thermalization, consisting in the translational motion in step 2 followed by the resting step, therefore of overall duration $\tau + \tau_r$. We introduce the following notations (illustrated on Fig. 4.18): the maximum temperature of erasure i reached at the end of the step 1 is written $T_i = \alpha_i T_0$, and the temperature at the end of the thermalization is written $\tilde{T}_i$.

Hypothesis (ii) and (v) allow to simplify Eq. (4.18) during the thermalization into (using again the general expression of the heat derivative of Eq. (1.70)):

$$\frac{d\langle E\rangle}{dt} = -\frac{d\langle \mathcal{Q}\rangle}{dt} \tag{4.19}$$

$$\frac{dT}{dt} = -\frac{\omega_0}{Q}(T(t) - T_0). \tag{4.20}$$

Therefore the temperature initially at T_i relaxes during $\tau + \tau_r$ to $\tilde{T}_i$ (green segments in Fig. 4.18), and $\tilde{T}_i$ is deduced from Eq. (4.20):

$$\tilde{T}_i = (T_i - T_0) \times e^{-\frac{(\tau_r+\tau)\omega_0}{Q}} + T_0 \tag{4.21}$$

$$= (1-r)T_0 + rT_i \ \text{, with } r = e^{-\frac{(\tau_r+\tau)\omega_0}{Q}} \tag{4.22}$$

$$= T_0 \times [1 + r(\alpha_i - 1)]. \tag{4.23}$$

Furthermore, we address the erasures step 1 (red segments in Fig. 4.18). On the basis of hypothesis (i) we can express the work required for the fast compression $i+1$ assumed adiabatic and starting at temperature $\tilde{T}_i$: $\langle \mathcal{W}_{i+1} \rangle = k_B \tilde{T}_i$. Finally assuming (iii) in Eq. (4.18), and taking as relevant heat derivative its initial point ($\frac{d\langle \mathcal{Q} \rangle}{dt}(t) \simeq k_B \frac{\omega_0}{Q}(\tilde{T}_i - T_0)$), we obtain:

$$k_B \frac{T_{i+1} - \tilde{T}_i}{\tau} = -\frac{\omega_0}{Q} k_B (\tilde{T}_i - T_0) + \frac{\langle \mathcal{W}_{i+1} \rangle}{\tau} \tag{4.24}$$

$$\frac{\alpha_{i+1} - 1 - r(\alpha_i - 1)}{\tau} = -\frac{\omega_0}{Q} r(\alpha_i - 1) + \frac{1 + r(\alpha_i - 1)}{\tau} \tag{4.25}$$

$$\alpha_{i+1} = r(2 - \frac{\omega_0 \tau}{Q})(\alpha_i - 1) + 2 \tag{4.26}$$

We recognize geometric a serie: $\alpha_{i+1} = A \times \alpha_i + B$, with $\alpha_0 = 1$, $B = 2 - A$ and:

$$A = e^{-\frac{(\tau_r+\tau)\omega_0}{Q}} (2 - \frac{\omega_0 \tau}{Q}). \tag{4.27}$$

Let us point out that $\alpha_1 = 2$ is consistent with assumption (iv). All in all the model, exhibits two regimes: if $A < 1$ the warming and thermalization compensates after some iteration, so that the temperature converges to $T_{sat} = (1 + \frac{1}{1-A}) \times T_0$; and if $A > 1$, the heat exchange is inefficient to compensate the energetic influx from the successive compressions and the temperature diverges. The parameter A controlling the convergence, decreases with τ and increases with Q: these dependences fit with the experimental observations. We apply the simple model (assuming $Q = 90$) and compute A with Eq. (4.27) for the different experimental durations in Fig. 4.17: the model successfully predicts the booming of the energy in region D.

As a conclusion, the simple model proposed in this section includes a lot of approximation but turns out to be enough to recover the speed region C and D corresponding to a converging or diverging evolution of the energy (respectively $A < 1$ and $A > 1$). The frontier $A = 1$ corresponds to $\tau = 3.34\,\text{ms}$ which is again in very good agreement with the experimental results. Nevertheless in the very fast and very slow limits, most of the assumptions made stop being relevant. In particular, the systems doesn't actually diverges when $A > 1$ as predicted by the model but reaches a very high plateau. Indeed, if the system's energy broadly exceeds the barrier height, the potential driving protocol impact on the system's behavior becomes negligible, therefore making the above model meaningless. In particular the peaks observed in the permanent kinetic energy profile for region D in Fig. 4.17 no longer comes from the compression, but from the energy kicks given to the system when the barrier is restored to $x_0 = 0$ if the cantilever ended up in the wrong well.

4.5.5 Quantitative Model

In this section we propose a more detailed and complete model designed to quantitatively predict the system behavior in the converging region C. Indeed now we have

identified the speed interval allowed to successfully process repeated erasures, the point is to quantitively estimate the corresponding energetic cost and temperature evolution. In all the following we restrict the study to speed region C, and consider only successful erasures: in particular the average experimental kinetic energy $\langle K \rangle$ is now inferred from the successful operations only.

At the basis of the quantitative description is the model developed in previous sections to describe Landauer's fast erasures (FE model built in section 4.3). It has proven reliable to describe a single erasure starting at equilibrium and including an equilibration step between stage 1 and 2. We modify the FE model to remove the equilibration step: while the thermal contribution relaxes from step 1, there are transient oscillations due to the translational motion deterministic contribution. Doing so we successfully describe the first erasure and obtain the final temperature $\tilde{T}_1$. The strategy is then to use the FE model with a different initial condition: the initial temperature is no more set to T_0 but to $\tilde{T}_1$. All in all, the quantitative model of Repeated Erasure called RE model consists in applying the FE model successively starting each time with the final temperature $\tilde{T}_i$ as initial temperature for the next iteration. Fig. 4.19 and Fig. 4.20 compare the RE model (red curve) to the experimental data (blue curve) for $\tau = 6\,\text{ms}$ and $\tau = 4\,\text{ms}$. All the parameters are taken from the experimental data (ω_0, τ, τ_r and X_1) except from the quality factor that is being tuned within the interval $80 < Q < 100$ to provide the best fit to the experimental curves. Indeed the experimental PSD of position doesn't allow a high accuracy on the quality factor estimation, and the RE model becomes quite sensitive to the Q value near the divergence.

The RE model also computes the average work required for the repeated use of the memory: the prediction plotted in dashed lines on Fig. 4.16 is reasonable (taking the same parameters as the one for the kinetic energy profile). Hence, the operator can theoretically estimate the excess of work required to perform successive erasure compared to a single one, and the number of repetition before reaching a permanent regime. However, even though the RE model has proven effective, it has some limitations. The deterministic part of the kinetic energy and of the work is inferred from translational motions starting from equilibrium, whereas in reality whether it is during step 1 or step 2 the systems is always out of equilibrium. For example, this approximation hides the 4-repetition cycling pattern. Besides, the model is inefficient to predict the consequences of an operation failure on the energy divergence: it only describes successful erasures.

Strong of the theoretical knowledge of the temperature profile we are also able to approximate the success rate R_i^s of i successful repetitions of the operation. Indeed, the ratio $k_B T/\mathcal{B}$ is all we need to compute the escape rate in the final double well potential, using the expression of $\Gamma(\mathcal{B}, T)$ derived in Eq. (1.39). If we assume that the temperature during the 1.5 ms final free evolution in U_i^0 is being worth $\tilde{T}_i$ (computed with the RE Model) we obtain the following success rate:

$$R_i^s = \prod_{k=0}^{i-1} (1 - \Gamma(\mathcal{B}, \tilde{T}_k)). \tag{4.28}$$

The result plotted on Fig. 4.21 is consistent with the experimental observations and quantify the consequence of the temperature rise on the success of the operation. Nevertheless, the Eq. (1.39) accounts for the average escape time of a system at equilibrium in the initial well (at effective temperature T), while in reality there is a strong deterministic contribution just after step 2 that tends to push the system far from the barrier.

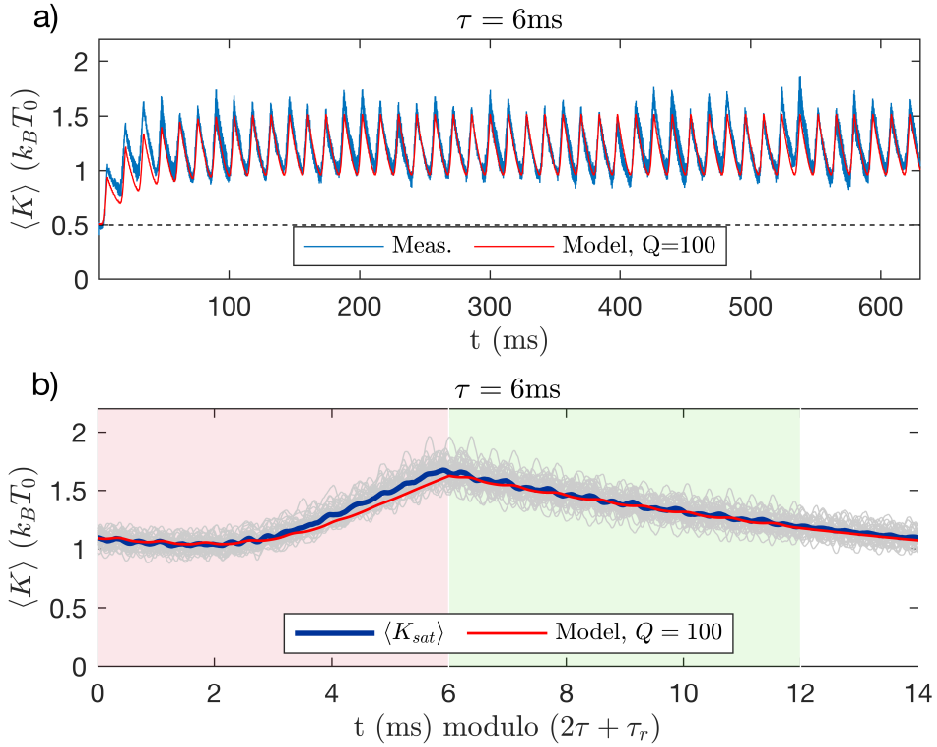

Figure 4.19 – **a) Kinetic energy evolution for 45 repeated erasures of duration** $\tau = 6\,\text{ms}$. The average kinetic energy $\langle K \rangle$ during the whole protocol (blue) is inferred from the N_i successful trajectories of the erasure i (as we are in speed region C, $N_i \sim N_{tot}$). Initially at the equilibrium value ($\frac{1}{2}k_B T_0$ in dashed line), $\langle K \rangle$ nearly doubles during the 3 first compressions without fully thermalizing in-between, and eventually reaches a plateau around $K_{sat} = 1.3 k_B T_0$. The quantitative model (red) is in very good agreement with the experimental result with no adjustable parameters except from the tiny adjustment of the quality factor: $Q = 100$. **b) Saturation profile of the kinetic energy.** When the permanent regime is established, $\langle K \rangle$ follows a repeated pattern every $2\tau + \tau_r$: these similar profiles are superimposed in grey lines. The saturation curve (blue) is the average of the permanent regime profiles of the 40 last operations. The systems first continues to relax from $1.1 k_B T_0$ at the beginning of step 1 (transient oscillations appear due to the translational motion), until the compression actually starts (when the two wells get close enough) and provokes the temperature rise. During step 2 (green background) the system thermalizes with again transient oscillations, and keep on relaxing during the final $\tau_r = 2\,\text{ms}$ rest. The quantitive model (red) nicely matches the experimental curve: it consists in the theoretical model of Landauer's erasure (FE Model) using as initial kinetic temperature the experimental value $T_{sat} = 2.2 T_0$ measured on the permanent regime profile.

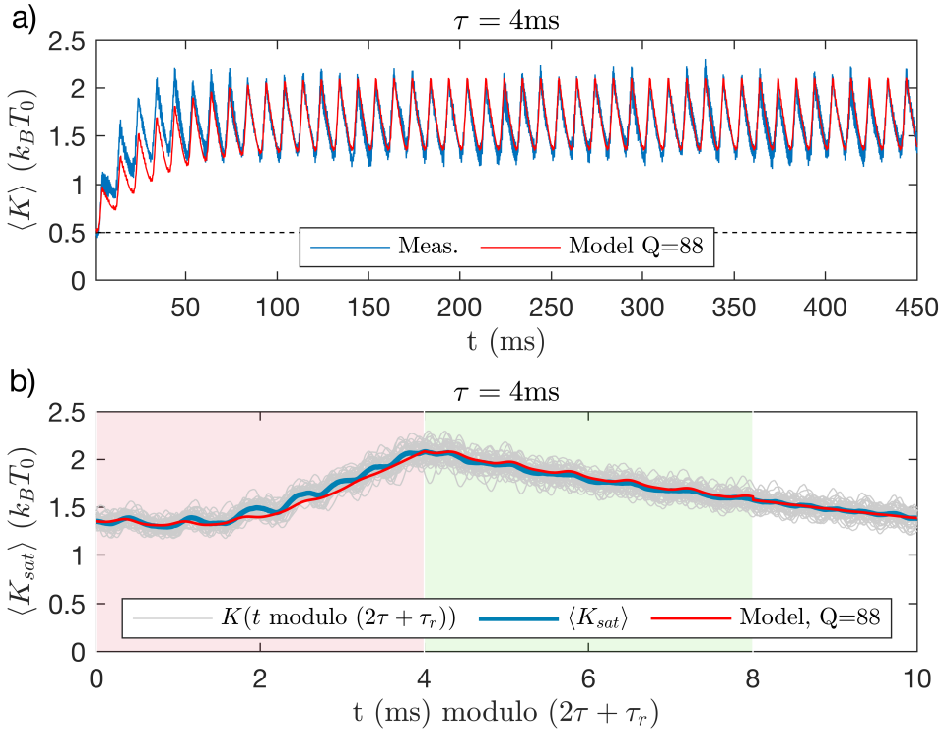

Figure 4.20 – **a) Kinetic energy evolution for 45 repeated erasures of duration** $\tau = 4\,\text{ms}$. Same as Fig. 4.19a): the kinetic energy saturates around $K_{sat} = 1.8 k_B T_0$ after 5 iterations. The quantitative model again matches the experiment assuming $Q = 88$. **b) Saturation profile of the kinetic energy.** Same as Fig. 4.19b) but for $\tau = 4\,\text{ms}$.

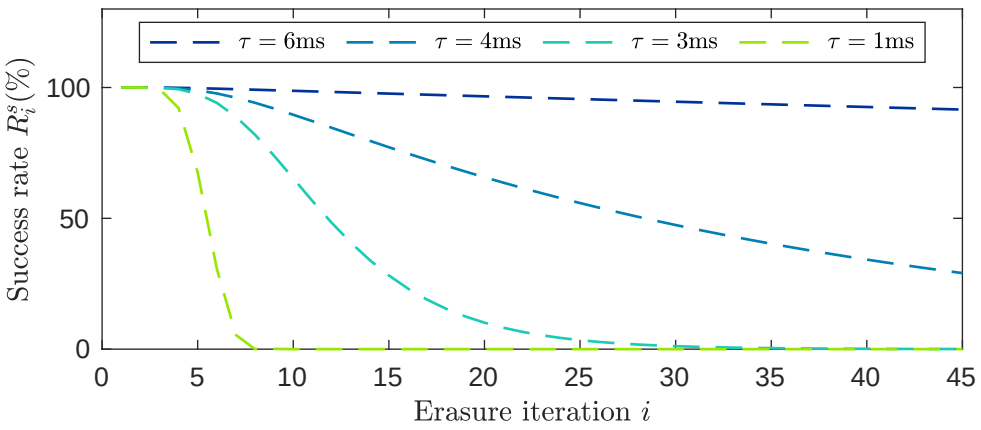

Figure 4.21 – **Theoretical prediction of the erasure success rate for different speeds.** Assuming $Q = 90$, we compute the escape rates $\Gamma(\mathcal{B}, \tilde{T}_k)$ using for $\tilde{T}_k$ the temperature theoretical profile (red in Fig. 4.20 and Fig. 4.19), and deduce from Eq. (4.28) the success rate R_i^s after i erasures for the different τ. Hence the model results in the probability of loosing the final information during the 1.5 ms free evolution in the final potential. As expected R_i^s is lower for higher speeds, and we identify region D in which the probability to successfully finish the whole protocol is null.

4.5.6 Discussion

Based on the previous study of the energetic exchanges in an underdamped memory, we are able to grasp the consequences of its repeated use. Even though the low damping allows fast erasing at low energetic cost, the price to pay lies in the warming of the memory. As a consequence, if the memory is used straight after a previous operation without letting the system thermalizing with its environnement, the temperature will rise by step so that the thermal energy can exceed the memory encoding barrier. The success of repeated operations therefore depends on the damping and the speed. On the first hand, the lower the damping the longer the thermalization and the higher the compression warming: for a fixed speed, reducing the damping enhances the temperature diverging behavior. On the other hand, the higher the speed, the higher the compression warming and the shorter the time allowed to thermalize: high speeds also favor the divergence.

As a conclusion, on a practical point of view, the underdamped regime is the best choice to perform fast and repeated use of the memory at low cost. Indeed, the underdamped systems turns out to be very robust to continuous information processing at high speed (up to 10 ms operations) at a stable and rather moderate cost (below $2k_BT_0$). But depending on the number of successive erasures one wants to perform and on the success rate required, the quality factor or the speed of the erasure have to be tuned to avoid divergences. We developed an efficient tool (the simple model) to predict the divergence of the energy, and therefore deduce the speed region allowed to ensure a good success rate. Moreover, a more complete model can be used (the RE model) to quantitively estimate the energy and work evolution profile in response to repeated uses, and in particular the permanent regime reached after a couple of iterations.

4.6 References

[1] K. Sekimoto and S. Sasa, Journal of the Physical Society of Japan **66**, 3326 (1997).

[2] K. Proesmans, J. Ehrich, and J. Bechhoefer, Phys. Rev. Lett. **125**, 100602 (2020).

[3] J. Gieseler and J. Millen, Entropy **20**, 326 (2018).

[4] J. Gieseler, L. Novotny, C. Moritz, and C. Dellago, New J. Phys. **17**, 045011 (2015).

[5] A. Bérut, A. Petrosyan, and S. Ciliberto, Journal of Statistical Mechanics: Theory and Experiment **2015**, P06015 (2015).

[6] S. Ciliberto, Phys. Rev. X **7**, 021051 (2017).

[7] A. Bérut, A. Arakelyan, A. Petrosyan, S. Ciliberto, R. Dillenschneider, and E. Lutz, Nature **483**, 187 (2012).

[8] Y. Jun, M. Gavrilov, and J. Bechhoefer, Phys. Rev. Lett. **113**, 190601 (2014).

[9] E. Aurell, K. Gawędzki, C. Mejía-Monasterio, R. Mohayaee, and P. Muratore-Ginanneschi, Journal of Statistical Physics **147**, 487 (2012).

[10] P. Muratore-Ginanneschi and K. Schwieger, Entropy **19**, 379 (2017).

[11] A. Gomez-Marin, T. Schmiedl, and U. Seifert, The Journal of Chemical Physics **129**, 024114 (2008).

[12] C. H. Bennett, Scientific American **257**, 108 (1987).

[13] A. Le Cunuder, I. A. Martínez, A. Petrosyan, D. Guéry-Odelin, E. Trizac, and S. Ciliberto, Applied Physics Letters **109**, 113502 (2016).

[14] I. A. Martinez, E. Roldan, L. Dinis, D. Petrov, and R. A. Rica, Supplemental Material for Ref. [16] (2015).

[15] S. Dago, J. Pereda, S. Ciliberto, and L. Bellon, Virtual double well potential for an underdamped oscillator created by a feedback loop (2022), under review JSTAT. arXiv: 2201.09870.

[16] I. A. Martinez, E. Roldan, L. Dinis, D. Petrov, and R. A. Rica, Phys. Rev. Lett. **114**, 120601 (2015).

[17] P. Geiger and C. Dellago, Phys. Rev. E **81**, 021127 (2010).

Chapter 5:

Consequences of a feedback bias on thermodynamics

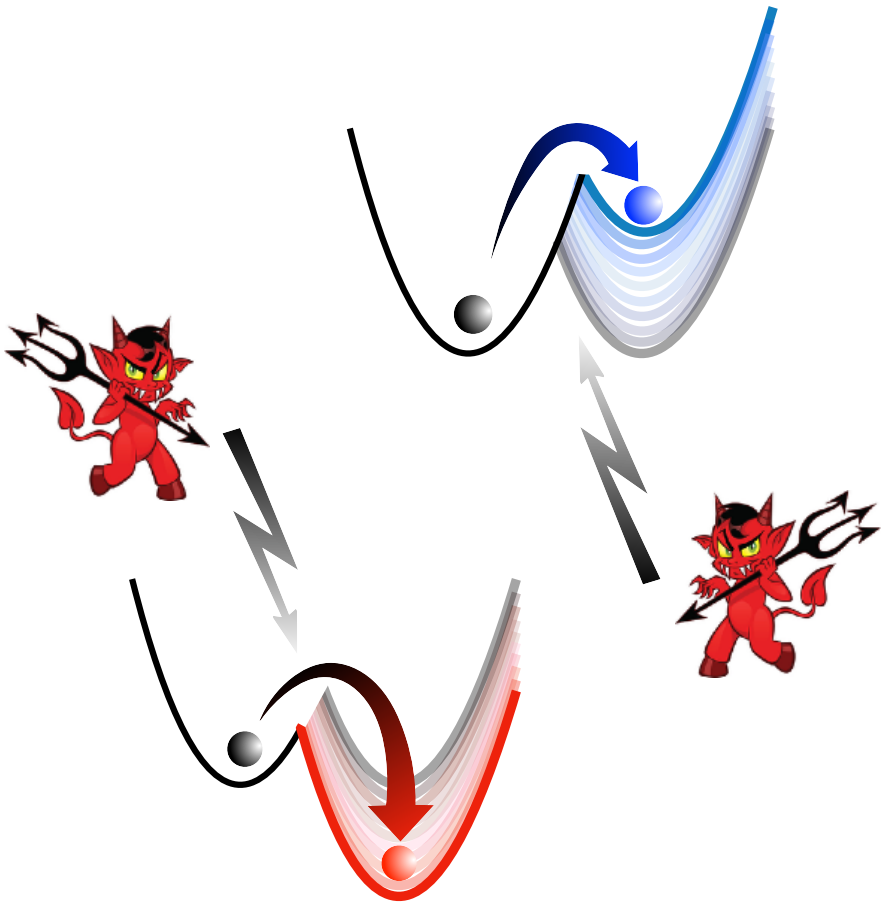

5.1 Context

In Ref. 1 we study how experimental biases can impact the equilibrium velocity distribution. We conclude that the feedback devices have to meet strict requirements in terms of switching delay when the cantilever switches from one well to the other, in order to create a proper virtual potential perfectly equivalent to a physical one. In particular, the comparator hysteresis is one source of switching delay, and is carefully addressed in the feedback implementations proposed in chapter 3. Hence, in the LB study of chapter 4, the feedback is completely transparent and has no consequences on the thermodynamics.

In a totally different perspective, we now aim to further explore the consequences of a feedback hysteresis on the system's behavior. We demonstrate in Ref. 1 that the kinetic temperature varies in the presence of hysteresis. In other words, if the feedback potential depends on the memory of the system's position, the overall thermodynamic is impacted by an higher or lower temperature. This chapter's goal is to explore in greater details the link between the amount of hysteresis (memory information used by the feedback), and the thermodynamic of the system evolving in the resulting virtual potential.

To do so, we first study experimentally the consequences of the hysteresis (positive and negative) on the system's kinetic temperature in a static double well potential in section 5.2.1, and propose in section 5.2.2 a complete theoretical model that supports the experimental results. Then we investigate in section 5.3 how the energy exchanges during a Landauer erasure, and therefore the erasure cost, are affected by an hysteresis. We will ultimately initiate a discussion on a possible interpretation considering the feedback as a Maxwell demon [2; 3].

5.2 Consequence of a feedback hysteresis on the temperature

5.2.1 Experimental observations

In all the following the experimental system is a cantilever of resonance frequency $f_0 = 1270\,\text{Hz}$, and position variance at rest $\sigma_0^2 \sim 1\,\text{nm}^2$. The quality factor is $Q = 10$ at atmospheric pressure, and can be increased to $Q = 70$ by removing the air in the cantilever's chamber. The trapping double well potential is created by feedback: the cantilever evolves in a physical harmonic potential centered in $\pm x_1$ and whenever it crosses the barrier position $x_0 = 0$ the potential switches to an harmonic potential centered in the opposite position $\mp x_1$ (see chapter 3).

The FPGA feedback addressed in section 3.4 allows a full control on the feedback parameters. In particular, contrary to the analogical implementation, we are able to fine tune the comparator hysteresis (parameter h). Instead of triggering the potential change exactly when the cantilever crosses the 0, the switching position is modified into $\pm h$ depending on whether the system comes from the left or the right hand well. As sketched on Fig. 5.1, when h is positive, it means that the system overreaches the barrier at each crossing, and on the contrary when h is negative the system anticipates the switch. The latter case is only possible because we forbid successive switches too close in time (temporal lock up for a quarter of period, see section 3.3).

To evaluate the impact of the hysteresis h, we measure the velocity PDFs in the

double well for hysteresis varying between $h = -22\%\,\sigma_0$ and $h = 32\%\,\sigma_0$, and plot it on Fig. 5.2a). The half distance between the wells is chosen to be $x_1 = \sigma_0$ to maximize the temperature variations (the dependency on x_1 is addressed in the following). While the speed distributions keep a satisfactory Gaussian shape with hysteresis, its variances are altered compared to the Boltzmann equilibrium distribution perfectly matched for $h = 0$: the velocity PDF for $h < 0$ and $h > 0$ is respectively wider (higher variance) and sharper (lower variance).

Therefore the kinetic temperature (T defined in Eq. (1.68)) turns out to be an adequate observable to summarize the effect of the hysteresis on the thermodynamic: $h > 0$ cools down the system whereas $h < 0$ warms it up. We use the dimensionless temperature $\theta = T/T_0 = \sigma_{\mathbf{v}}^2$ defined in Tab. 1.1 to quantify the warming or cooling effect as a function of the hysteresis in Fig. 5.2b). The system's temperature can be tuned between $70\%\,T_0$ and $155\%\,T_0$ by imposing $\mathbf{h} = h/\sigma_0$ between respectively $\mathbf{h} = 0.32$ and $\mathbf{h} = -0.22$. Besides we see on Fig. 5.2c) that the consequences of the hysteresis on the temperature are much more important at high quality factor ($Q = 70$ here): the temperatures is divided by two for $\mathbf{h} = 0.16$ and multiplied by 6 for $\mathbf{h} = -0.16$. Let us point out that when the kinetic temperature exceeds $3T_0$ the PDF is not a proper gaussian anymore, so that $T = \sigma_{\mathbf{v}}^2 \times T_0$ can no longer be simply interpreted as a temperature.

Furthermore, we study in Fig. 5.3 the intensity of the cooling/warming effect depending on the half-distances between the wells, x_1. In the following we stay at air pressure ($Q = 10$) to limit the temperature variations in a reasonable range, and avoid deviating from the gaussian shape of the velocity PDF. For all distances between the wells, the temperature evolution with the hysteresis has a profile similar to the one in Fig. 5.2b), but the intensity of the warming or cooling varies with x_1. We observe Fig. 5.3 that the effect is the greatest when $x_1 \sim \sigma_0$, and vanishes at both very small and high distances.

To put it in a nutshell, depending on x_1 and h appears a non-equilibrium steady state of modified temperature T, similarly to what can be obtained by feedback cooling [4; 5]. In the next section we develop a model that supports all these experimental observations.

5.2.2 Theoretical model

The energy balance of Eq. (1.60) is again the starting point of the model developed in the following to link the feedback hysteresis to the system temperature. In a stationary state when no external work is performed, there is no average kinetic energy changes nor deterministic terms. Nevertheless we have to consider potential energy variations (because of the hysteresis), that are related only to the heat expressed in Eq. (1.70), hence Eq. (1.60) reduces to:

$$\langle \frac{dU}{dt} \rangle = \frac{\omega_0}{Q} k_B T_0 (1 - \theta) \tag{5.1}$$

If there is a switching hysteresis, the comparator triggers only when $x = \pm h$ (sign depending on the previous position) instead of $x = 0$: the cantilever overreaches (or anticipates if $h < 0$) the barrier at each crossing. As sketched in Fig. 5.1 this extra-distance traveled by the system (positive or negative) corresponds to a potential energy

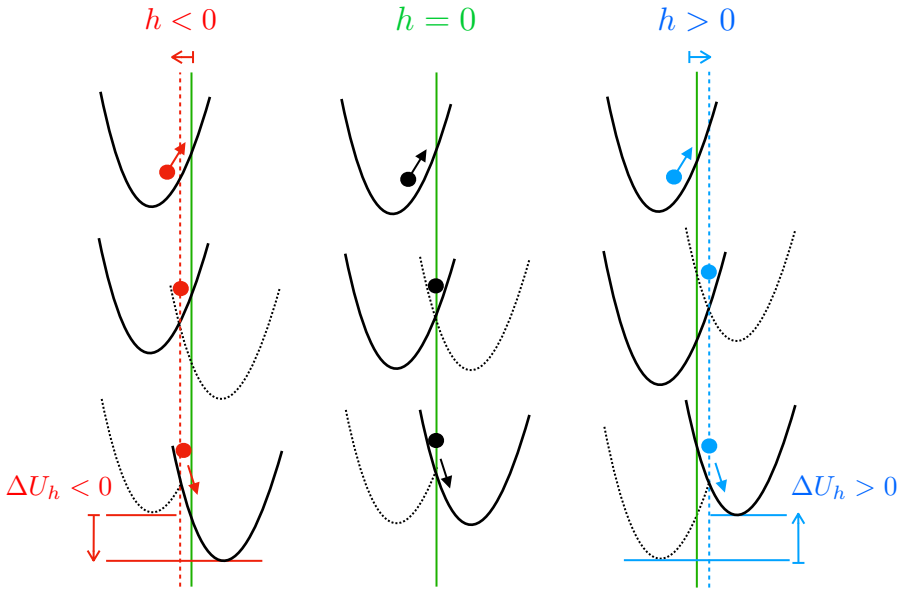

Figure 5.1 – **Schematic overview of a potential switch with hysteresis**. When $h < 0$ (red, left) the systems triggers the switch before the barrier position (green line), and ends up in a lower potential energy: $\Delta U_h < 0$. At each switch the corresponding energy is gained by the system: it is a warming process. Without hysteresis $h = 0$ (black, middle), the double well potential is symmetric and unbiased. Finally, when $h > 0$ (blue, right) the systems overreaches the barrier position and finishes in the second well at a higher potential energy: $\Delta U_h > 0$. Therefore at each crossing the system looses energy to "climb up" the potential ladder: it is a cooling process.

step:

$$\begin{aligned} \Delta U_h &= \frac{1}{2}k\left[(x_1 + h)^2 - (x_1 - h)^2\right] \\ &= 2kx_1h \end{aligned} \tag{5.2}$$

This amount of potential energy is exchanged each time the cantilever crosses the barrier: if $\Delta U_h > 0$ the corresponding energy is lost by the system; if $\Delta U_h \leq 0$ it is gained by the system. To express the energy balance of the system, we need to quantify how often on average the cantilever crosses the threshold. In Eq. (1.38), we derive the crossing rate $\Gamma(\mathcal{B}, T)$ of the potential barrier $\mathcal{B}$ for a system at temperature T. Using Eq. (1.38) applied to the actual barrier energy $\mathcal{B} = \frac{1}{2}k(x_1 + h)^2$, we can express the potential contribution in Eq. (5.1) and derive:

$$\begin{aligned} \Gamma(\frac{1}{2}k(x_1 + h)^2, \theta T_0) \times \Delta U_h &= \frac{\omega_0}{Q}k_B T_0(1 - \theta) \\ \Gamma(\frac{1}{2}k(x_1 + h)^2, \theta T_0) \times 2kx_1h &= \frac{\omega_0}{Q}k_B T_0(1 - \theta) \end{aligned} \tag{5.3}$$

Eq. (5.3) corresponds to the balance between the energy taken from the system to climb up the potential steps at each switch (respectively gained by the system if it goes down the potential ladder), and the energy refill from the bath through the heat transfer (respectively the energy leak into the bath). The system temperature is the

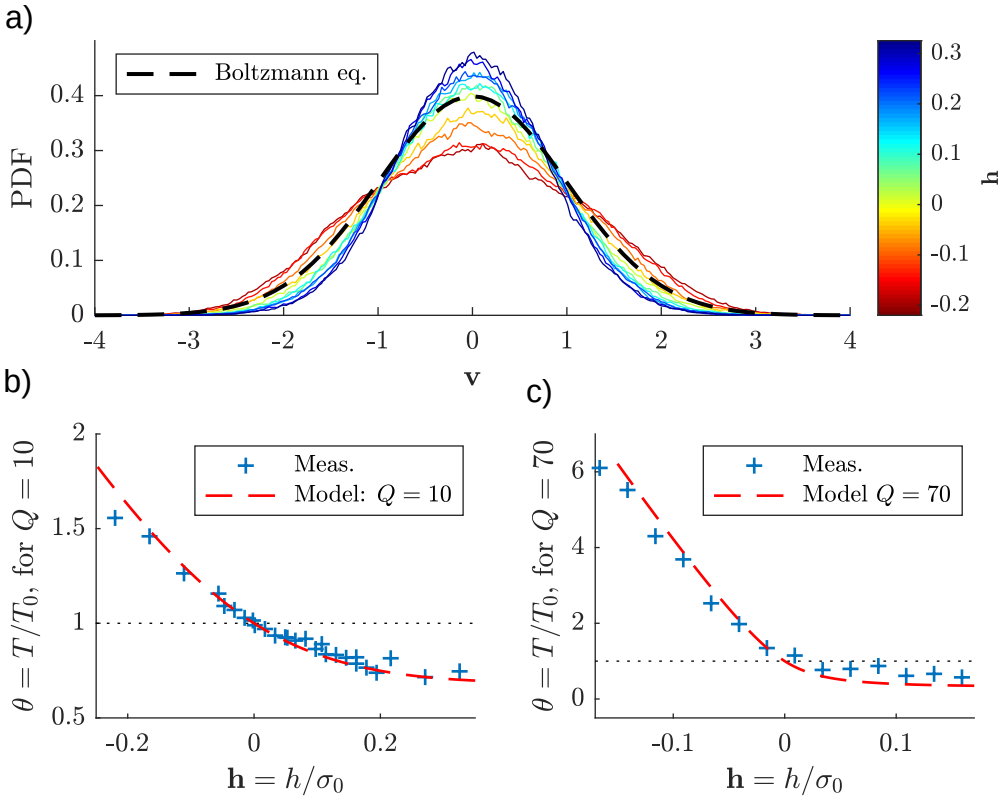

Figure 5.2 – **a) Experimental velocity PDF with feedback hysteresis, for** $Q = 10$. The distribution of $\mathbf{v}$ (dimensionless quantity defined in Tab. 1.1) is inferred from a 10 s free evolution in the static double-well potential of centers $\pm x_1 = \pm\sigma_0$ with a feedback hysteresis h. The speed PDFs keep satisfactorily Gaussian shapes: for negative hysteresis the velocity variance is increased, and on the contrary for positive hysteresis it is reduced, as highlighted by the corresponding points in b)(blue crosses). It is worth noticing that for $h = 0$ we recover the Boltzmann equilibrium distribution of variance $\sigma^2_{\mathbf{v}} = 1$ (dashed black). **b) Consequence of the feedback hysteresis on the kinetic temperature for** $Q = 10$ **and** $x_1 = \sigma_0$. $\theta = T/T_0$ is obtained from the velocity PDF ($\theta = \sigma^2_{\mathbf{v}}$) as the ones displayed a). Negative hysteresis warms up the system while positive one cools it down. The chosen half distance between the wells, $x_1 = \sigma_0$, maximizes the hysteresis impact, as demonstrated in Fig. 5.3. The theoretical model (dashed red) provided by Eq. (5.3) is in very good agreement with the experimental data. **c) Same as b) for** $Q = 70$. The temperature bias is increased compared to $Q = 10$, all the more for negative hysteresis (note that the scale of both axes is different from panel b)). The theoretical model (dashed red) is again in very good agreement with the experimental data.

implicit solution of Eq. (5.3) and allows the two fluxes to compensate:

$$\theta = \frac{T}{T_0} = f(x_1, h) \tag{5.4}$$

Eq. (5.3) is numerically solved and $T(x_1, h) = f(x_1, h) \times T_0$ is plotted on Fig. 5.3 as a function of x_1: the kinetic temperature variation culminates around $x_1 \lesssim \sigma_0$, all the more when $|h|$ is high. These trend can be easily understood (taking $h > 0$ for example): firstly, the larger the hysteresis, the greater the energy loss at each switch, and, therefore, the lower the system temperature. Secondly, the energy loss per switch is proportional to x_1, but the barrier crossing rate decreases with x_1: in the high barrier

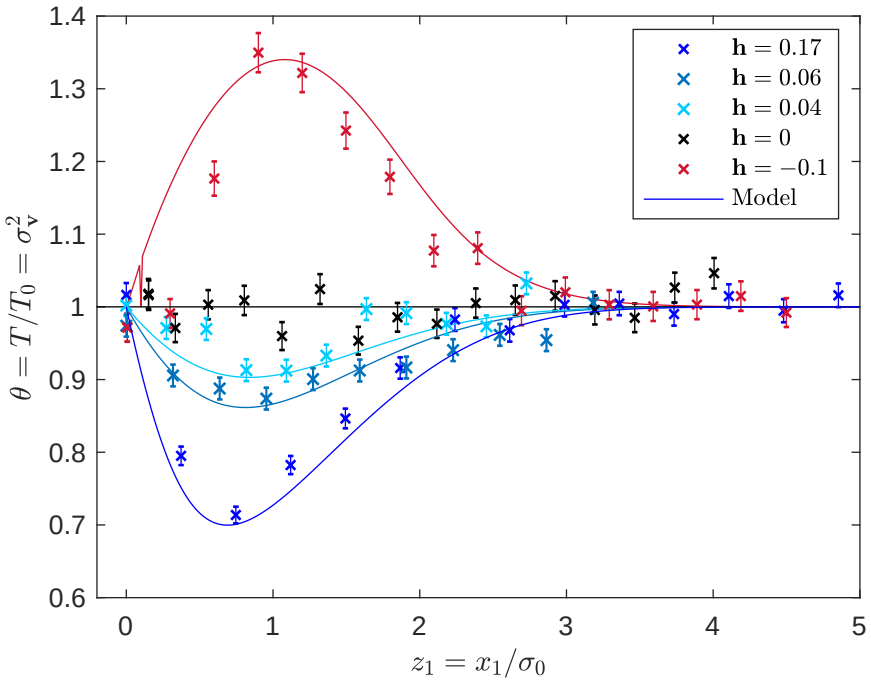

Figure 5.3 – **Kinetic temperature with feedback hysteresis as a function of z_1.** θ is plotted as a function of the half-distance between the wells z_1. For positive hysteresis (blue markers), $\mathbf{h} = 0.17$, $\mathbf{h} = 0.06$ and $\mathbf{h} = 0.04$, the system's temperature is decreased below the bath temperature T_0. On the contrary for negative hysteresis (red markers) $\mathbf{h} = -0.10$, the system is warmed up, and as expected for $\mathbf{h} = 0$ (black markers) we recover $\theta = 1$. The dependance on x_1 comes from the balance between the barrier crossing rate (decreasing with x_1) and the energy step due to the hysteresis at each switch (increasing with x_1). The theoretical model in plain lines provided by Eq. (5.3) matches the experimental results for all hysteresis values.

limit there are no more switches and $T = T_0$, and in the low barrier limit there is no more energy step at the switch, so that $T = T_0$ as well. The effect on the temperature is maximized for $x_1 \sim \sigma_0$ when the two opposing effects counteract each other the most. The same reasoning holds for negative hysteresis to explain the warming effect dependency on x_1 and h.

To conclude, let us emphasize that the model (Eq. (5.4)), matches the experimental data in Fig. 5.3 and in Fig. 5.2b) and c), for both moderate and low damping ($Q = 10$ and $Q = 70$). On the latter, we see that the temperature bias is all the more important that the exchanges with the bath are reduced. Indeed, at larger quality factor the heat exchanges with the bath are less efficient to compensate the energy ΔU_h lost or gained at each switch, so that a higher temperature difference is required to reach the balance between the two energetic fluxes.

5.2.3 Conclusion

We have demonstrated adding small hysteresis into a feedback virtual double-well potential results in a steady state at temperature $T \neq T_0$, cooling down or warming up the system depending on its sign. The system's equilibrium kinetic temperature is set

by the hysteresis and the distance between the well: $T(x_1, h)$ as modeled by Eq. (5.4). Of course it also depends on the system parameters, ω_0 and Q, and in particular the temperature variation is enhanced when Q is high.

Let us conclude this section with two remarks. On the one hand, the position PDF is similarly impacted by the hysteresis and consists in the Boltzmann distribution at temperature T rather than T_0. Nevertheless, as the PDF in the double well potential is complex, it is more immediate to look at the gaussian velocity PDF to study the consequences of the hysteresis. And on the other hand, for the system to behave as it would in equilibrium with a thermostat at T, the temperature difference with the actual bath, $T - T_0$ shouldn't be too high. Indeed, if $T > 3T_0$, the system velocity and position distributions no longer keep their equilibrium shapes.

5.3 Landauer's erasure

It remains to see whether the impact on the thermodynamic observed in the static case is still visible during information processing. Indeed if the system's temperature is tuned by the hysteresis, will the Landauer limit varies accordingly? In particular, is it possible to artificially beat the LB by cooling down a memory using feedback hysteresis? To answer these questions, we implement Landauer's erasures of Fig. 4.1 using a virtual double well potential biased with an hysteresis h for step 1. We start by studying the temperature profile during a quasi-static erasure, through the kinetic energy measurement.

5.3.1 Kinetic energy profile

Theoretical description

For quasi-static erasures we expect the average kinetic energy to be worth its equilibrium value $K_{eq} = \frac{1}{2}k_B T_0$ during the whole procedure. Nevertheless, in the presence of hysteresis, the kinetic temperature T varies during step 1 with the half-distance between the wells: $x_1(t) = X_1(1 - t/\tau)$. In the quasi-static regime, the static model in Eq. (5.3) holds for step 1, as the system is assumed to be in equilibrium at all time in $U_1(x, x_1(t))$: the temperature profile is given by $T(x_1(t), h)$. Let us note that the temperature profile is expected to peak around time $t^* = (1 - \sigma_0/X_1) \times \tau$ as the hysteresis cooling/warming effect culminates when $x_1 \sim \sigma_0$. During step 2, the potential simplifies into a single well potential and the system thermalizes: $T = T_0$.

Experimental results

We apply the erasure protocol of Fig. 4.1 with $X_1 = 5\sigma_0$ and $\tau = 1\,\mathrm{s}$ (quasi-static erasure) to the cantilever of parameters $f_0 = 1270\,\mathrm{Hz}$ and $Q = 10$. The average kinetic energy profiles for hysteresis $\mathbf{h} = 0.17$ and $\mathbf{h} = -0.1$ are plotted in Fig. 5.4. Let us note that these hysteresis values are studied in Fig 5.3 within the static framework.

As $\langle \mathbf{K} \rangle = \frac{1}{2}\theta$, we can follow in Fig. 5.4 the temperature evolution during a quasi-static erasure: for $\mathbf{h} = -0.1$ the warming reaches 125% of the bath temperature, while for $\mathbf{h} = 0.17$ the cooling gets down to 65%. Both extrema are observed around $t^* = 0.8\,\mathrm{s}$ as predicted by the theoretical analysis above. The static model $T(x_1(t), h)$ from Eq. (5.3) matches the experimental data. The small difference between the two

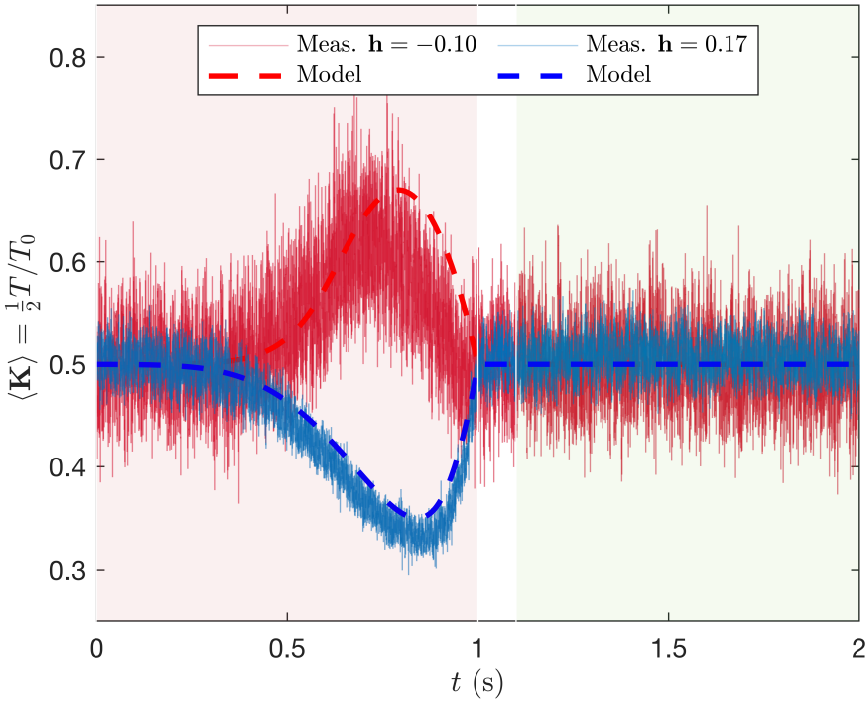

Figure 5.4 – **Kinetic energy profile for quasi-static erasures with feedback hysteresis**. During stage 1 lasting $\tau = 1\,\mathrm{s}$ and starting from $X_1 = 5\sigma_0$ (red background), the hysteresis $\mathbf{h}$ impacts the system temperature and consequently the average kinetic energy $\langle \mathbf{K} \rangle = \frac{1}{2}\theta$. Both the warming for $\mathbf{h} = -10\%$ (red) and the cooling for $\mathbf{h} = 17\%$ (blue) observed experimentally are supported by the static model (dashed), as expected in the quasi-static regime ($\tau\omega_0 \gg 1$). The small amount of experimental trajectories used to compute the average for $\mathbf{h} = -0.10$ ($N = 500$) is much smaller than for $\mathbf{h} = 0.17$ ($N = 2000$), what explains the higher fluctuations visible on the red experimental curve.

may come from the fact that even though $\tau\omega_0 \gg 1$ the system behavior deviates from the static description.

5.3.2 Effective Landauer Bound

Theoretical description

Following our reasoning in chapter 4 for fast erasures, if the system temperature varies, the erasure cost should be impacted accordingly and be worth $k_B T_{\text{eff}} \ln 2$, where T_{eff} is a weighted average of the actual temperature of the memory during the process. In the fast erasures context addressed in section 4.3, the T_{eff} originates into the fast compression warming, so that for slow erasures the LB remains unchanged: $T_{\text{eff}} = T_0$.

On the contrary, in the presence of hysteresis the temperature is modified for quasi-static erasures, being worth $T(x_1(t), h)$ during step 1. The origin of the temperature variation is different, but the formalism developed in section 4.3 to quantify its consequences on the erasure cost remains the same. In particular, as only step 1 contributes for slow erasures, the overall erasure work is given by Eq. (F.16):

$$\langle \mathcal{W} \rangle = -k_B \int T \frac{d \ln \mathcal{V}}{dt} \left(1 + \frac{d \ln T}{d \ln (x_1^2 / T)} \right), \tag{5.5}$$

with $x_1 = X_1(1 - t/\tau)$ during step 1, $\mathcal{V} = 1 + \mathrm{erf}\left(\sqrt{\frac{k}{2k_BT}}x_1\right)$ defined in Eq. (4.8b), and $T = T(x_1, h)$ modeled using Eq. (5.3) in very good agreement with experimental results as shown in Fig. 5.4. The above amount of work is required in the quasi-static regime and therefore corresponds to a lower bound. That is why we define the effective LB in the presence of hysteresis as:

$$L_h = k_B T_h \ln 2 = -k_B \int T \frac{d \ln \mathcal{V}}{dt} \left(1 + \frac{d \ln T}{d \ln(x_1^2/T)}\right) \tag{5.6}$$

In a nutshell, in the presence of hysteresis the LB, $L_0 = k_B T_0 \ln 2$, becomes an effective LB, $L_h = k_B T_h \ln 2$, introducing T_h the effective temperature with hysteresis with Eq. (5.6). T_h is a weighted average on the $T(x_1, h)$ profile, so that $T_h > T_0$ for negative hysteresis and $T_h < T_0$ for positive ones. This prediction is validated experimentally in the next section.

Experimental results

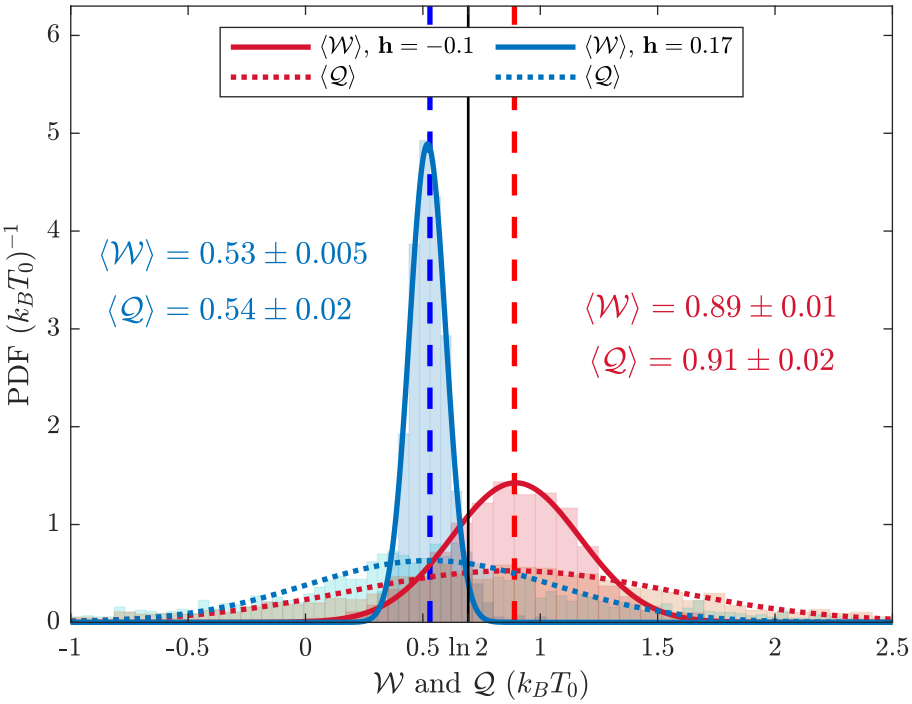

Figure 5.5 – **Work and heat distribution for quasi-static erasures with hysteresis $\mathbf{h} = 0.17$ and $\mathbf{h} = -0.10$.** The average heat (PDF in dotted lines) perfectly matches the average work (PDF in plain lines) in both cases. For $\mathbf{h} = 0.17$ (blue), the system is cooled down and the quasi-static erasure (duration $\tau = 1\,\mathrm{s}$, same as Fig. 5.4) requires on average (dashed blue vertical line): $\langle \boldsymbol{\mathcal{W}} \rangle = 0.53 \pm 0.005$ and $\langle \boldsymbol{\mathcal{Q}} \rangle = 0.54 \pm 0.02$, in perfect agreement with the effective LB predicted by the model in Eq. (5.7). For $\mathbf{h} = -0.10$ (red), the system is warmed up and we measure the average energy cost (dashed red vertical line), again in reasonable agreement with the model in Eq. (5.8): $\langle \boldsymbol{\mathcal{W}} \rangle = 0.89 \pm 0.015$ and $\langle \boldsymbol{\mathcal{Q}} \rangle = 0.91 \pm 0.02$. Similarly to the what we observed in Fig. 4.3c) without hysteresis, the heat distribution is wider than the work PDF and has exponential tails.

We plot in Fig. 5.5 the work and heat distributions inferred from quasi-static erasures with hysteresis $\mathbf{h} = 0.17$ and $\mathbf{h} = -0.10$. The LB is beaten by 22% when the

system is cooled down by $\mathbf{h} = 0.17$: $\langle \mathcal{W} \rangle \approx \langle \mathcal{Q} \rangle \approx 0.54\,\mathrm{k_B T_0}$. On the contrary when the system is warmed up by the negative hysteresis $\mathbf{h} = 0.10$, the LB is exceeded of 30%: $\langle \mathcal{W} \rangle \approx \langle \mathcal{Q} \rangle \approx 0.9\,\mathrm{k_B T_0}$. Besides, the distributions shapes seem also affected by the temperature changes: the cold system provides sharper distributions than the hot one. Nevertheless more statistics are required to address this aspect (the $\mathbf{h} = -0.1$ distributions are drawn from $N = 500$ trajectories only) and we for now restrict the study to the average values.

Let us compare the experimental erasure costs with the model prediction of the effective LB in Eq. (5.6):

$$L_h = 0.54\, k_B T_0 = 78\%\, L_0 \quad \text{for } \mathbf{h} = 0.17 \tag{5.7}$$

$$L_h = 0.84\, k_B T_0 = 120\%\, L_0 \quad \text{for } \mathbf{h} = -0.10 \tag{5.8}$$

Hence, the experimental results displayed in Fig. 5.5 validates the effective LB model as the average match respectively Eq (5.7) and Eq. (5.8). The tiny error made for $\mathbf{h} = -0.10$ ($\langle \boldsymbol{\mathcal{W}} \rangle = 0.89 \gtrsim \mathbf{L}_h = 0.84$) can be a repercussion of the difference between the measured temperature profile and the theoretical expression used in the model already visible in Fig. 5.4.

All in all, the above confirms that the fundamental limit of Landauer can be tuned by cheating on the system temperature using feedback hysteresis.

5.3.3 Approach to the effective LB

A last question arises: does the erasure with hysteresis perfectly mimics an erasure at temperature T_h ? In particular, is the divergence from the effective LB similar when the speed increases?

In section 4.2.5 we fit the divergence from the LB plotted in Fig. 4.5 by:

$$\langle \mathcal{W} \rangle = k_B T_0 \times (\mathbf{L}_\infty + \mathbf{B}' \frac{Z_1}{\tau}) \tag{5.9}$$

with $\mathbf{B}' = (437 \pm 27)\,\mu\mathrm{s}$ and $\mathbf{L}_\infty = 0.695 \pm 0.012$, which is consistent with the LB $L_0 = k_B T_0 \ln 2$ when $\tau \to \infty$. We compare these previous results to results obtained with an hysteresis $\mathbf{h} = 0.17$ in Fig. 5.6. The effective temperature T_h is deduced for $\mathbf{h} = 0.17$ from the model in Eq. (5.6),

$$L_h = k_B T_h \ln 2 \quad \text{with } T_h = 0.78\, T_0. \tag{5.10}$$

Hence we fit the divergence from the effective LB with the same scaling as Eq. (5.9):

$$\langle \mathcal{W} \rangle = k_B T_h \times (\mathbf{L}_{h,\infty} + \mathbf{B}'_h \frac{Z_1}{\tau}). \tag{5.11}$$

We obtain $\mathbf{B}'_h = (320 \pm 40)\mu\mathrm{s}$ and $\mathbf{L}_{h,\infty} = 0.68 \pm 0.01$. The asymptotic limit of the fit set by $L_{h,\infty} = 0.68$ is consistent with the effective LB $L_h = k_B T_h \ln 2$ predicted by the model, and measured in Fig. 5.5. Furthermore, the scaling parameters $\mathbf{B}'_h$ and $\mathbf{B}'$ are of the same order of magnitude: the divergence from the effective LB in the presence of hysteresis is similar to the divergence from the natural LB. The small discrepancy between the two values may have physical origin, or may just come from a small deviation in the experimental conditions between the two series of measurements (different cantilever, hence slightly different resonance frequencies f_0 and quality factors Q, and small changes in the initial distance $Z_1 \sim 5$).

To conclude, in first approximation, erasing 1-bit of information with positive hysteresis in the feedback is equivalent to cooling down the bath from T_0 to T_h defined in Eq. (5.6). Indeed the erasure cost lower bound reached for slow erasures in decreased accordingly, the effective LB being worth $L_h = k_B T_h \ln 2$, and the extra-cost required to increase the driving speed follows the same scaling in B/τ. However, there is some limitation to this equivalence: the hysteresis effect on the temperature is derived in the static case and may not be perfectly accurate when the erasure speed increases.

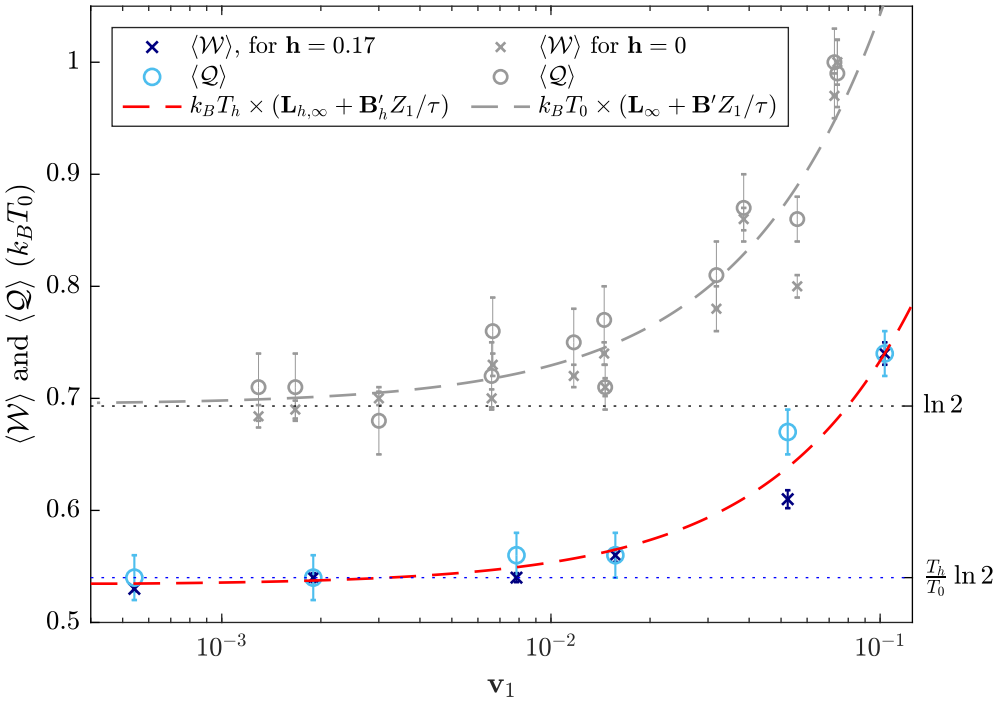

Figure 5.6 – **Divergence from the effective LB for fast erasures.** Energy cost $\langle \boldsymbol{\mathcal{W}} \rangle$ and $\langle \boldsymbol{\mathcal{Q}} \rangle$ for erasure protocols at different driving speeds $\mathbf{v}_1$ with feedback hysteresis $\mathbf{h} = 0.17$. Experimental data (blue) are fitted by $k_B T_h \times (\mathbf{L}_{h,\infty} + \mathbf{B}' Z_1/\tau)$ (red), with $T_h = 0.78\, T_0$ deduced from the model in Eq. (5.6). We obtain $\mathbf{B}'_h = (320 \pm 40)\mu$s and $\mathbf{L}_{h,\infty} = 0.68 \pm 0.01$. The asymptotic limit $\mathbf{L}_{h,\infty}$ when $\mathbf{v}_1 \to 0$ is consistent with the effective LB, $L_h = k_B T_h \ln 2$, predicted by the model (dotted blue line). The scaling when the speed increases is similar to the one observed in the case without hysteresis reproduced in grey from Fig. 4.5.

5.4 Perspectives

The underdamped regime offers new insights on a wide variety of fundamental questions on the connections between feedback and thermodynamics [6–9]. For example, articles by Rosinberg and coworkers study the effect on entropy and information in the presence of a continuous feedback [10–13] introducing the concept of mutual information.

We demonstrate in this chapter that the fundamental lower limit to information processing, directly related to the free energy variation, can be tuned by the hysteresis of the potential in which evolves the memory. As the hysteresis doesn't not require work (using the Sekimoto's definition of work), the gain in the erasure cost can be considered as the work of a demon (an intelligent creature able to monitor the system). In other

word, the feedback would be acting as a demon through the knowledge of the position memory before the barrier crossing (hysteresis), hence reducing the work the operator has to pay to perform the Landauer erasure. From that point of view, the information used by the feedback remains to be linked to the hysteresis in the double-well potential. The concept of mutual information seems to be a promising tool to build a formalism around these observations, following the theory around the Sagawa's demon [14]. Once properly understood, the hysteresis in the virtual double-well potential could also be used to enhance stochastic engines efficiency [15].

5.5 References

[1] S. Dago, J. Pereda, S. Ciliberto, and L. Bellon, Virtual double well potential for an underdamped oscillator created by a feedback loop (2022), under review JSTAT. arXiv: 2201.09870.

[2] H. Leff and A. Rex, *Maxwell's Demon: Entropy, Classical and Quantum Information, Computing* (Institute of Physics, Philadelphia, 2003).

[3] E. Lutz and S. Ciliberto, Physics Today **68**, 30 (2015).

[4] J. Gieseler and J. Millen, Entropy **20**, 326 (2018).

[5] J. Gieseler, L. Novotny, C. Moritz, and C. Dellago, New J. Phys. **17**, 045011 (2015).

[6] U. Seifert, Reports on Progress in Physics **75**, 126001 (2012).

[7] K. H. Kim and H. Qian, Phys. Rev. Lett. **93**, 120602 (2004).

[8] L. Granger and H. Kantz, Phys. Rev. E **84**, 061110 (2011).

[9] M. L. Rosinberg, T. Munakata, and G. Tarjus, Phys. Rev. E **91**, 042114 (2015).

[10] M. L. Rosinberg and J. M. Horowitz, EPL (Europhysics Letters) **116**, 10007 (2016).

[11] T. Munakata and M. L. Rosinberg, Journal of Statistical Mechanics: Theory and Experiment **2012**, P05010 (2012).

[12] T. Munakata and M. L. Rosinberg, Journal of Statistical Mechanics: Theory and Experiment **2013**, P06014 (2013).

[13] R. Chétrite, M. L. Rosinberg, T. Sagawa, and G. Tarjus, Journal of Statistical Mechanics: Theory and Experiment **2019**, 114002 (2019).

[14] T. Sagawa and M. Ueda, Phys. Rev. Lett. **104**, 090602 (2010).

[15] J.-M. Park, J. S. Lee, and J. D. Noh, Phys. Rev. E **93**, 032146 (2016).

Chapter 6:

Logical and physical reversibility

IN	OUT
0	1
1	0

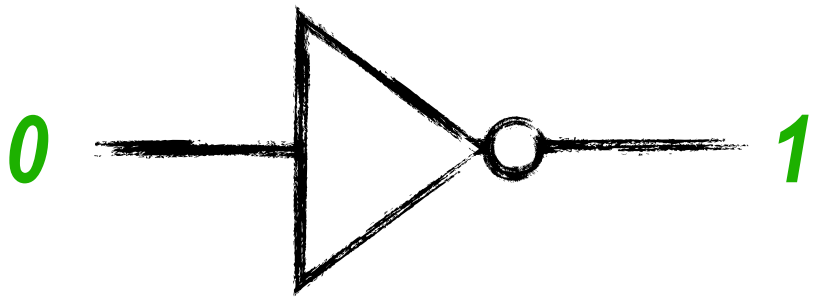

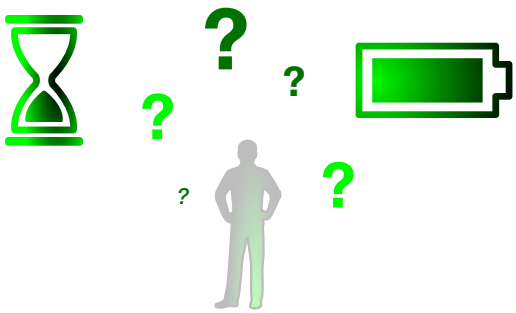

6.1 Context and experimental framework

In this section we complete the study of all 1-bit operations with the implementation of operation NOT. Indeed, starting from $(0,1)$, only four outcomes are possible: $(0,1) \rightarrow (0,1)$ [HOLD], $(0,1) \rightarrow (0,0)$ [RESET to 0], $(0,1) \rightarrow (1,1)$ [RESET to 1] and $(0,1) \rightarrow (1,0)$ [NOT]. The first one is trivial (do nothing), the second and the third are erasures studied in previous chapters, and the last is a bit-flip. Contrary to the erasure of 1-bit of information which is logically irreversible, the bit-flip is fully reversible as it does not comes with any information loss. We will explore in the following the physical reversibility of the bit-flip. Indeed as there is no entropic loss, there should be a way to operate in a physically reversible fashion: that is to say without any energetic loss nor work required to proceed.

Following the reasoning of Ref. [1], the bit-flip operation in stochastic but Markovian 1D memories (highly damped memories, $Q \ll 1$), whose dynamics only depends on the current state, is impossible. Indeed, as sketched in Fig. 6.1, the bit-flip protocol using only one degree of freedom (DOF) has to pass through the same state in the phase space, weither the system is initially in state 0 or state 1: the information is lost. That is why, a second degree of freedom is required to proceed: it can be a second spatial dimension y, but if we stick to a 1-dimensional memory it has to be the speed $v = \dot{x}$. Therefore being in the underdamped regime (Non-Markovian dynamics), where the inertia allows the control of the speed, is a mandatory requirement. That is why we work with an underdamped system ensuring a quality factor $Q = 100$. The experimental set-up is the same as the one used in section 3.4 with a slightly stronger vacuum, and with a cantilever of resonance frequency $f_0 = 1.39\,\text{kHz}$ (ie a period $\mathcal{T}_0 = 0.68\,\text{ms}$).

In that context, to meet success rate requirements, the bit-flip protocol has to be designed to avoid the overlap of the two possible informations in the phase space. Indeed a full overlap would result in the impossibility mentioned for the single degree of freedom case, while a partial overlap (when the speed is bounded by a moderate damping, $Q \sim 1$) would damage the success rate, because the information is likely to 'slip' to the wrong state. In the following, we impose as safety criterion that the two states' PDF must be separated at all time by 10 times their characteristic spreading in the phase space (2D gaussian in Fig. 6.1), that is to say the position and speed standard deviation along the two axis (respectively σ_0 and $\omega_0\sigma_0$). From that perspective, in the experimental set-up, the initial information is encoded in a double well potential $U_i = 1/2k(|x| - X_1)^2$, with the center of the wells $\pm X_1 \sim 5\sigma_0$ meeting the above criterion and maintaining an energy barrier $\mathcal{B} = \frac{1}{2}kX_1^2 \sim 12.5k_BT_0$.

Let us point out that there are usually two strategies to reduce the energetic cost: proceeding at low speed in a quasi-static fashion, or work at very low damping. Here, we have to eliminate the first one because a reasonable speed is imposed to safely convey the information: when $\langle x \rangle = 0$, the safety criterion translates into $\langle |\mathbf{v}| \rangle > 5\sigma_0\omega_0$. Therefore, to maintain physical reversibility without damaging the success rate, the viscous damping of the environment must be removed ($Q \gg 1$).

We propose in the next section a protocol meeting the bit safety criterion, and designed to be physically reversible.

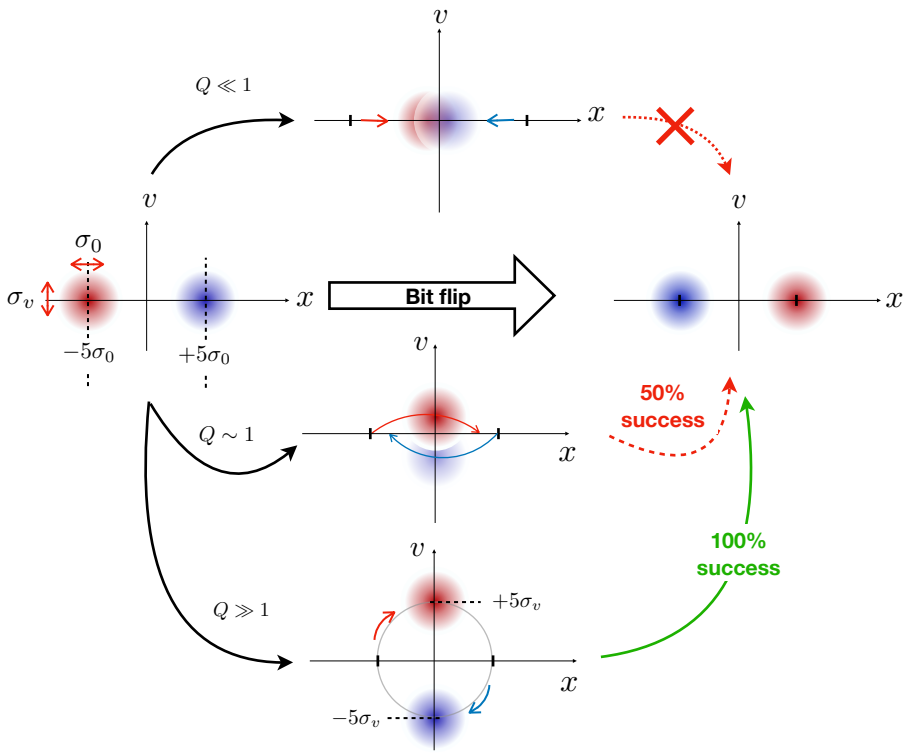

Figure 6.1 – **Schematic overview of the bit-flip success requirements**. The system two-dimensional PDF are sketched by red (state 0 initial information) and blue 2D gaussians (state 1 initial information) in the phase space (x,v). On the first hand, using only one DOF (if $Q \ll 1$, only the position can be driven) makes the bit-flip operation impossible: when the system passes through the phase space central point, the Markovian dynamic makes the information indistinguishable. On the other hand, the underdamped regime opens a second DOF to process the information: the speed $v = \dot{x}$. Moderate damping ($Q \sim 1$) limits the velocity range accessible and results in a partial overlap of the memory PDF in the two different states: the operation can fail. To prevent the overlap and ensure a 100% success rate, we impose the two states to be separated by a minimal distance, hence we fix: $(\frac{x_D}{\sigma_0})^2 + (\frac{v_D}{\sigma_{v,0}})^2 > 5$ as safety criterion, σ_0^2 and $\sigma_{v,0}^2 = (\sigma_0\omega_0)^2$ being the position et velocity variance. Bit-flips protocol allowing such velocities requires the memory quality factor to be high enough ($Q \gg 1$).

6.2 Reversible bit-flip protocol

Following Ref. 1, the operation consists in suddenly moving both the wells' center to $\pm x_1(t_i^+) = 0$: the potential becomes a single harmonic well $U(t_i^+) = \frac{1}{2}kx^2$. The starting time of each bit-flip operation is called t_i and is aligned to $t_i = 0\,\text{ms}$ in all the experimental data. After half a cantilever period $\mathcal{T}_0/2$, the wells' center are brought back to $\pm x_1(t_i + \mathcal{T}_0/2^+) = \pm X_1$ to rebuild U_i. In the following we introduce $t_f = \mathcal{T}_0/2$. The $x_1(t)$ monitoring is displayed in grey line on Fig. 6.2. An example of a single system trajectory in blue, and the corresponding trapping well center ($S(x) \times x_1$ in red) demonstrate the success of the bit-flip operation (here a $0 \to 1$ bit-flip).

The above bit-flip protocol sketched in Fig. 6.3a) has been design to be physically reversible when the dissipation can be neglected ($Q \to \infty$). For clarity purposes, let us consider that the system is initially in state 0: $\langle x \rangle_i = -X_1$ and $\langle v \rangle = 0$. After the first potential change, the cantilever starts an oscillation into the single well potential, and after half a period it reaches without speed the opposite maximal position: $\langle x \rangle_f = +X_1$. Therefore, the second change in potential at this exact moment doesn't affect the average position of the system, nor its velocity. Let us point out that between the two changes, the velocity reaches $\langle |v| \rangle = 5\sigma_{v,0}$ when $\langle x \rangle = 0$ as required by the safety criterion recalled in Fig. 6.1. The operation results in changing the position of the cantilever from $\langle x \rangle_i = -X_1$ to $\langle x \rangle_f = +X_1$ using only the free evolution of the system inside the potential: it is a reversible bitflip.

Regarding the theoretical formalism, as the cantilever initial and final state is at equilibrium in U_i, the average heat dissipated during the procedure is equal to the average work required : $\langle \mathcal{Q} \rangle = \langle \mathcal{W} \rangle$. Besides, as the potential remains quadratic during the operation, the Fokker-Planck equation ruling the stochastic dynamic is linear: the system response is at all time the sum of the deterministic contribution and the thermal stochastic one: $x = x_{\text{th}} + x_D$, with $x_D = \langle x \rangle$. As the system always evolves in an harmonic potential of constant stiffness (indeed, in U_i the second well is inaccessible), the thermal contribution is not impacted by the bit-flip operation and remains at equilibrium: $\langle x_{\text{th}}^2 \rangle = k_B T_0/k$. Therefore the bit-flip response is ruled by the deterministic trajectory of the cantilever.

In the ideal case without any dissipation, the energy given to the system at the first potential change is fully recovered when U_i is restored: the operation is reversible and no work is required for the process. Formally if the changes are instantaneous the work corresponds to the potential loss during the flip called $\langle \Delta U^{\text{flip}} \rangle$. Indeed the work can be expressed using from the work definition in Eq. (4.2) and the control parameter derivative, $\dot{x}_1 = -\delta(t - t_i)X_1 + \delta(t - t_i - t_f)X_1$:

$$\langle \mathcal{W} \rangle = -\langle U \rangle(t_i^+) + \langle U \rangle(t_f^-) \tag{6.1}$$

$$= -\langle \Delta U^{\text{flip}} \rangle \tag{6.2}$$

Hence without dissipation we have:

$$\langle U \rangle(t_i^+) = \frac{1}{2}kx_D(t_i^+)^2 + \frac{1}{2}k_B T_0 = \frac{1}{2}(kX_1^2 + k_B T_0) \tag{6.3}$$

$$\text{and } \langle U \rangle(t_f^-) = \frac{1}{2}k(|x_D(t_f^-)| - X_1)^2 + \frac{1}{2}k_B T_0 = \frac{1}{2}(kX_1^2 + k_B T_0) \tag{6.4}$$

so that the average work vanishes.

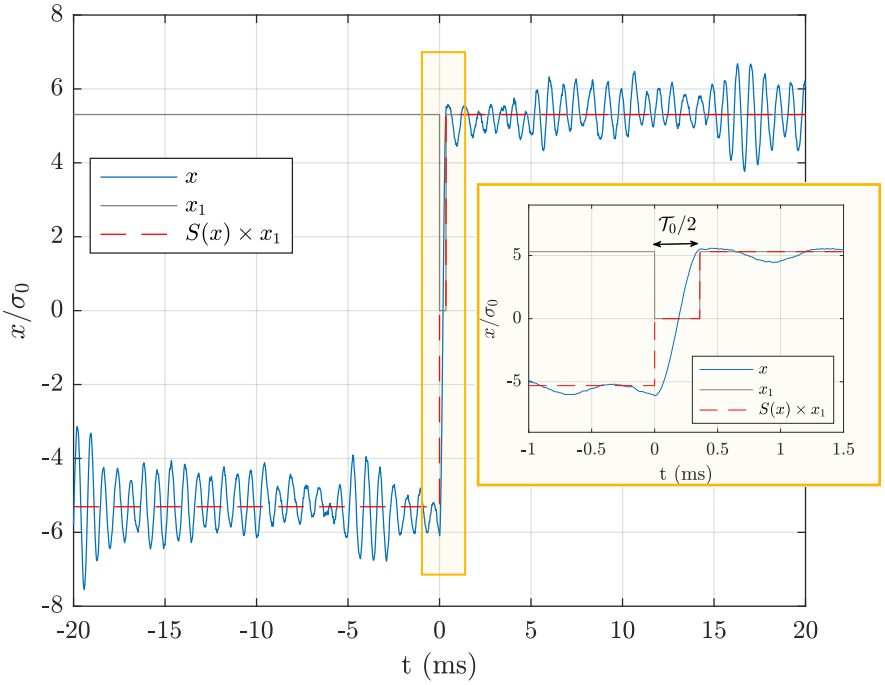

Figure 6.2 – **Experimental response to the bit-flip protocol**. The bit-flip started at $t_i = 0\,\text{ms}$ successfully drives the system from its initial state 0 to state 1 in half a period, $\mathcal{T}_0/2 = 0.34\,\text{ms}$. The bit-flip protocol consists in suddenly changing the well center position x_1 from $x_1(t_i^-) = X_1$ to $x_1(t_i^+) = 0$, and changing it back to X_1 after half a period. Doing so, the cantilever trajectory (blue) starts in equilibrium at $\langle x \rangle_i = -X_1$, naturally evolves in the transient single well and ends up at $\langle x \rangle_f = +X_1$. The center of the well in which the cantilever is trapped is plotted in dashed red.

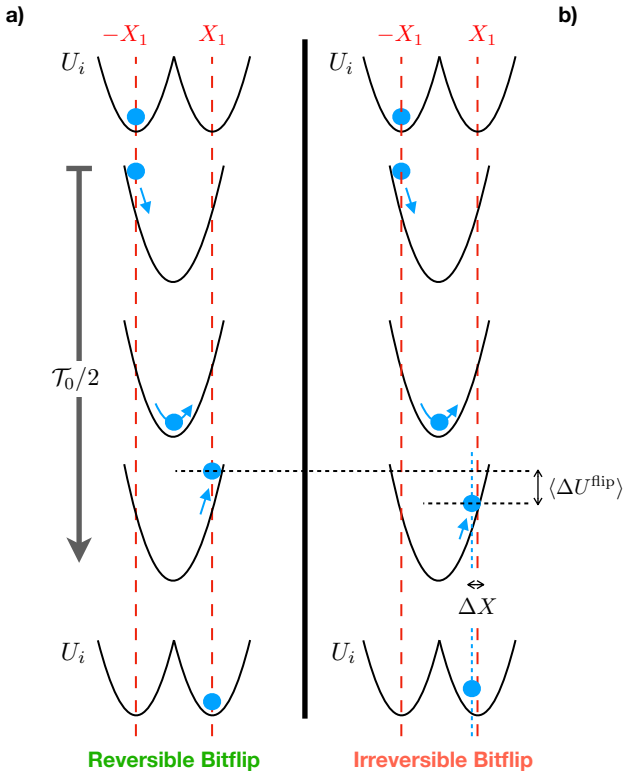

Figure 6.3 – **Schematic overview of the bit-flip protocol. a) Reversible operation in the ideal case without damping**. The systems starts in state 0 in the encoding potential U_i. The operation starts with a sudden change of the potential into a single well centered in 0. The system without velocity on average therefore initiates an oscillation at the resonance frequency f_0 from the average position $-X_1$. After half a period $\mathcal{T}_0/2$, the trajectory reaches on average the opposite position $+X_1$ without velocity. At this exact moment, the potential U_i is restored, so that the system ends up at equilibrium in state 1. **b) Origin of the irreversibility**. When the system oscillation is damped by the viscous force, the system cannot reach $+X_1$ and culminates at $X_1 - \Delta X$. Therefore the operator has to pay for the potential energy difference $\langle \Delta U^{\text{flip}} \rangle$. Besides, the system doesn't not finish in perfect equilibrium in state 1 and has to relax to the well center.

6.3 Experimental result

The initial distance is calibrated using the position signal during the equilibrium steps: $X_1 = 5.3\,\sigma_0$, so that $\mathcal{B} = 14\,\mathrm{k_B T_0}$. We record $N_{tot} = 2000$ trajectories, alternating between $0 \to 1$ and $1 \to 0$ operations, with 100% of success, to compute the average potential and kinetic energy displayed on Fig. 6.4. Both energetic quantities rises when the bit-flip begins (at $t_i = 0\,\mathrm{ms}$), and immediately go back to their equilibrium value prescribed by the equipartition ($K_{eq} = U_{eq} = \frac{1}{2}k_B T_0$) at the end of the protocol (at $t_f = \mathcal{T}_0/2$). We distinguish the two peaks in the potential profile corresponding to the two extreme positions of the system in the single well potential.

Furthermore, we compute the stochastic work and heat using the expression in Eq. (4.5) and Eq. (4.6) and compute the mean values from the N_{tot} trajectories. In the data analysis, the $\dot{x_1}$ term involved in the work expression is not composed of real Dirac's functions, because the steps in x_1 are actually steep slopes from which a non infinite derivative can be deduced. Let us point out that the work could be inferred from the potential energy measure using Eq. (6.2), but we prefer to provide two independent values for the potential energy and the work computations.

The work and heat distributions are displayed on Fig. 6.5: we deduce $\langle \mathcal{W} \rangle = 0.46 \pm 0.02 k_B T_0$ and $\langle \mathcal{Q} \rangle = 0.43 \pm 0.03 k_B T_0$. These non null values can be explained by the small damping at the origin of the irreversibility, as detailed in section 6.4. Nevertheless the experimental bit-flip still requires less than the lowest possible cost for irreversible operation on a 1-bit memory, the Landauer's bound $k_B T_0 \ln 2 \sim 0.69 k_B T_0$. Furthermore, this logically reversible operation can be conducted in a very small time (0.34 ms here), contrary to irreversible operations such as erasures for which operating fast requires to exceed the LB by several $k_B T_0$. Finally, the equilibrium is restored just after the procedure, so that bit-flips can be repeated successively without worsening the memory response.

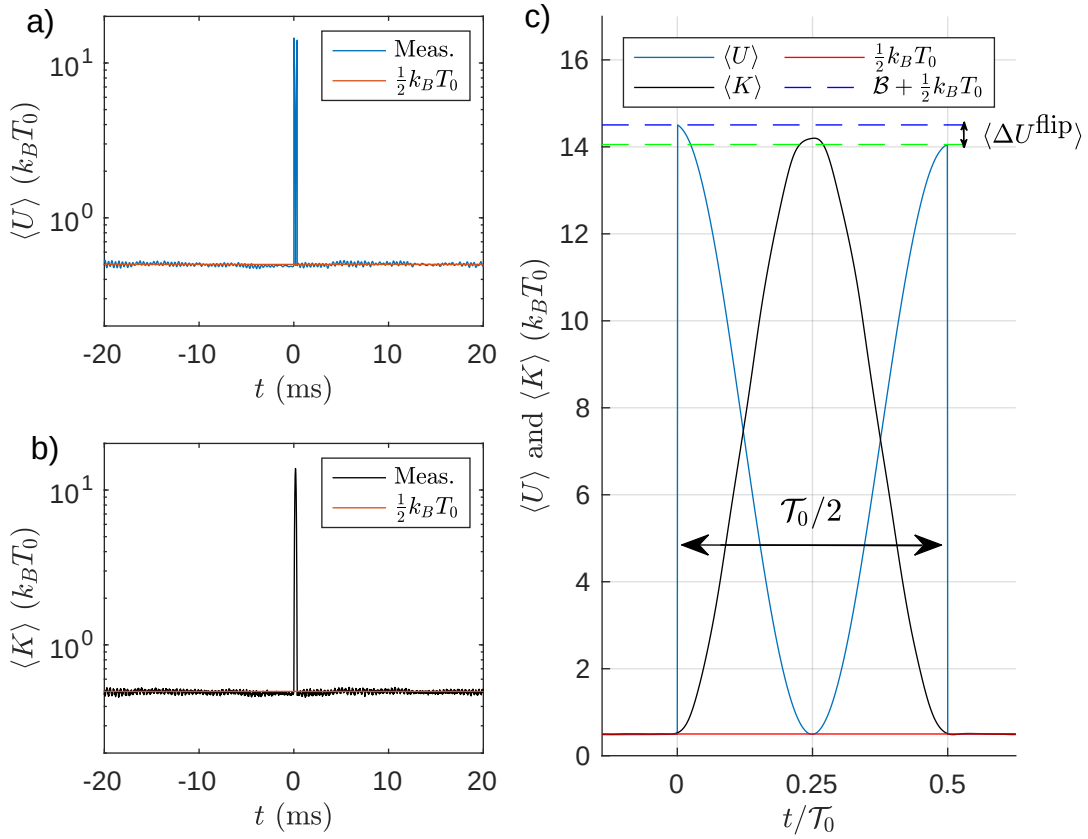

Figure 6.4 – **a) Average potential energy**. $\langle U\rangle$ (blue), inferred from $N_{tot} = 2000$ trajectories, starts at thermal equilibrium and jumps at $t_i = 0\,\text{ms}$ when the bit-flip begins. At $t_f = \mathcal{T}_0/2 = 0.34\,\text{ms}$, the potential energy recovers its equilibrium value. The peaked evolution in between is detailed in c). The very good accuracy of the calibration and the measurements, results in the perfect agreement between the experimental curves during the equilibration steps and the equipartition prescription $U_{eq} = \frac{1}{2}k_BT_0$ in red line. **b) Average kinetic energy**. $\langle K\rangle$ matches also perfectly the thermal equilibrium value ($K_{eq} = \frac{1}{2}k_BT_0$ in red line), except during the bit-flip operation where the deterministic speed contribution prevails. **c) Irreversibility in the average potential energy during the damped bit-flip.** We zoom on the experimental potential (blue) and kinetic (black) evolution during the $\mathcal{T}_0/2 = 0.34\,\text{ms}$ bit-flip step: as expected for a free oscillator the kinetic and the potential energy has opposite profiles. Both consist in the sum of the thermal contribution being worth $\frac{1}{2}k_BT_0$ (red line) and the deterministic one during the transient evolution in the single well, $U_D = \frac{1}{2}kx_D^2$ and $K_D = \frac{1}{2}mv_D^2$. Regarding the kinetic energy, the system starts with no velocity on average at the edge of the single well potential, so that during the half oscillation the speed increases and culminates in the center of the well at $t = \mathcal{T}_0/4$, before decreasing again and vanishing at the opposite edge. On the contrary, regarding the potential energy, the systems gains the barrier energy (dashed blue line) when the double well potential is suddenly changed into a single well centered on 0 at $t_i = 0\,\text{ms}$: $U_D(t_i) = \mathcal{B}$. The experimental value of the first peak measured at $14.5k_BT_0$ therefore perfectly matches the barrier calibration $\mathcal{B} = 14k_BT_0$. Then, the systems half oscillation reaches a potential minimum ($U_D(\mathcal{T}_0/4) = 0$), before stopping with no speed at the second potential peak (green dashed line). Because of the damping we measure a potential energy difference $\langle \Delta U^{\text{flip}}_{\text{meas}}\rangle = -0.450 \pm 0.002$ between the two extreme potential values.

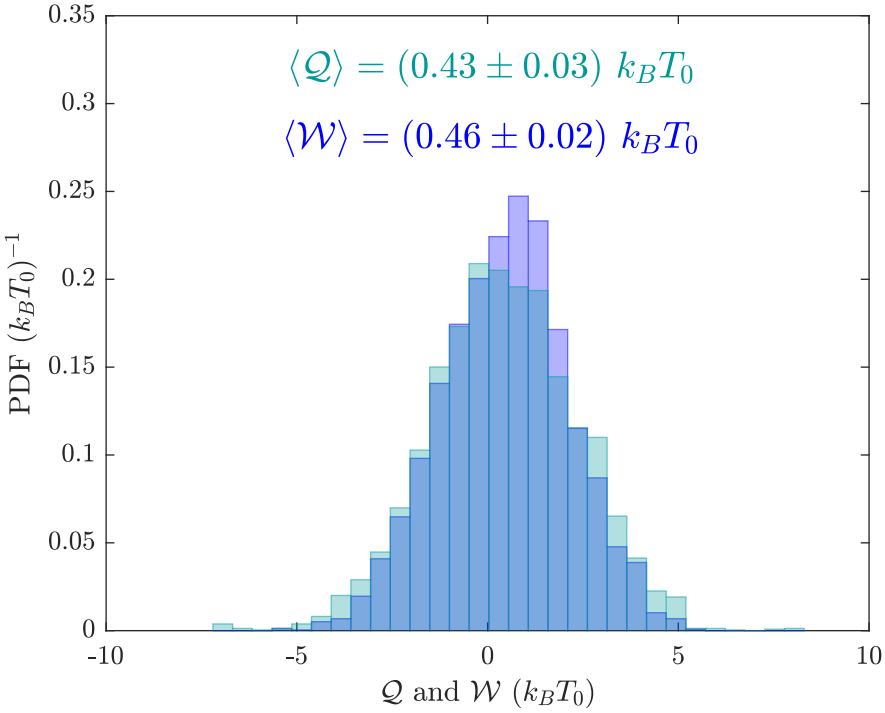

Figure 6.5 – **Work and Heat distribution**. The work (blue) and heat (green) mean values and their confidence interval are computed from the $N_{tot} = 2000$ bit-flip trajectories.

6.4 Origin of the irreversibility

We tackle in this section the origin of the irreversibility detected through the work and heat mean values: it is the residual damping in the vacuum in which evolves the cantilever. Indeed because of the dissipation during the half oscillation, the potential energy given back by the system is lower than the one initially given by the operator, so that in total, work is required to proceed. To phrase it differently: the damped oscillator launched in $-X_1$ stops at zero speed after half a period a little bit before the exact opposite position as sketched on Fig. 6.3b). To provide a quantitive description, let us express the deterministic term of trajectory x_D during a $0 \to 1$ operation. The oscillation initiated in $x_D(0) = -X_1$ and $v_D(0) = 0$ obeys :

$$x_D(t) = X_1 e^{\frac{-t\omega_0}{2Q}} \left(\frac{\omega_0}{2Q\Omega} \sin \Omega t - \cos \Omega t\right) \tag{6.5}$$

where $\Omega = \omega_0 \sqrt{1 - 1/(4Q)^2}$ can be assimilated to ω_0 at high quality factor. Hence, after half a period the cantilever reaches on average the extreme position:

$$\langle x \rangle_f = x_D\left(\frac{\mathcal{T}_0}{2}\right) = X_1 e^{-\frac{\pi}{2Q}} \tag{6.6}$$

Without damping, $Q \to \infty$ so that we recover $\langle x \rangle_f = X_1$ and consequently a reversible behavior. Meanwhile in a viscous environment, the cantilever undershoots the targeted position by $\Delta X = X_1(1 - e^{-\frac{\pi}{2Q}}) \simeq \frac{\pi}{2Q} X_1$. For $Q = 100$, we have $\Delta X / X_1 = 1.56\%$. As a consequence, there is a potential energy loss $\langle \Delta U^{\text{flip}} \rangle$ (illustrated on Fig. 6.3b))

being worth:

$$\langle \Delta U^{\text{flip}} \rangle = \frac{1}{2}k(X_1 - \Delta X)^2 - \frac{1}{2}kX_1^2 \tag{6.7}$$

$$= -\mathcal{B}(1 - e^{-\frac{\pi}{Q}}) \simeq -\frac{\pi}{Q}\mathcal{B} \tag{6.8}$$

$$= -0.44 k_B T_0 \tag{6.9}$$

The value in Eq. (6.9) corresponds to the theoretical prediction knowing the parameters $Q = 100$ and $\mathcal{B} = (14 \pm 0.05) k_B T_0$ from calibration. We compare it with the experimental value measured on the zoom picture of the experimental potential energy evolution displayed on Fig. 6.4c): $\langle \Delta U^{\text{flip}}_{\text{meas}} \rangle = (-0.450 \pm 0.002) k_B T_0$. The errors are inferred from the error on σ_0 calibrated before each of the N_{tot} operations. The theory and the experiment are in very good agreement. Besides, the first peak value in Fig. 6.4c) is also consistent with the model, being worth the thermal energy plus the barrier energy (deterministic contribution): $\mathcal{B} + \frac{1}{2}k_B T_0 = 14.5\,\mathrm{k_B T_0}$. All in all, taking into account the damping in the theoretical analysis perfectly explains the experimental observations.

6.5 Conclusion and optimisation perspectives

We have experimentally illustrated the connection between physically reversibility and logically reversibility in information processing. The bit-flip protocol designed to be secure and cost-free [1] has been tested experimentally: it successfully performs the NOT operation in $\mathcal{T}_0/2 = 0.34\,\mathrm{ms}$ for a very small amount of work. Indeed contrary to irreversible operations requiring at least the LB, the cost here doesn't exceeds 66% of the LB. The deviation from the desired zero-work operation is fully explained by the coupling of the memory to the surrounding bath: even very low damping introduces irreversibility. The theoretical description has proven reliable to quantify the irreversibility, measured with high accuracy in our experimental set up through the energetic quantities. We summarize in the list below the agreement between the experimental results obtained from independent data analysis, and the model results (in $k_B T_0$ units):

- $\langle \boldsymbol{\mathcal{W}} \rangle = 0.46 \pm 0.02 \simeq -\langle \Delta \mathbf{U}^{\text{flip}}_{\text{meas}} \rangle = 0.450 \pm 0.002$
- $\langle \boldsymbol{\mathcal{W}} \rangle = 0.46 \pm 0.02 \simeq \langle \boldsymbol{\mathcal{Q}} \rangle = 0.43 \pm 0.03$
- $\langle \mathbf{U} \rangle (t_i^+) = 14.5 \pm 0.002 \simeq \boldsymbol{\mathcal{B}} + \frac{1}{2} = 14.55$
- $\langle \Delta \mathbf{U}^{\text{flip}}_{\text{meas}} \rangle = -0.450 \pm 0.002 \simeq \frac{\pi}{Q}\boldsymbol{\mathcal{B}} = -0.44$

To conclude, let us emphasize the parameters to be tuned in order to approach the reversibility while maintaining a good success rate. We recall the average work in the presence of damping (from Eq. (6.2) and Eq. (6.8)): $\langle \mathcal{W} \rangle = \frac{\pi}{Q}\mathcal{B}$. But if we want to comply with the safety criterion, that is to say maintaining at least $\langle x \rangle (t_f) = \pm 5\sigma_0$, the distance between the wells in U_i has to be higher than $Z_1 = 5$ and be worth $\tilde{Z}_1 = 5 \times e^{\frac{\pi}{2Q}}$ (increasing with the damping). The cost required to proceed with the bit-flip while meeting the safety requirement is therefore:

$$\langle \boldsymbol{\mathcal{W}} \rangle = \frac{\pi}{Q}\tilde{\boldsymbol{\mathcal{B}}} \text{ , with } \tilde{\boldsymbol{\mathcal{B}}} = \frac{1}{2}\tilde{Z}_1^2 = \boldsymbol{\mathcal{B}} e^{\frac{\pi}{Q}} \tag{6.10}$$

Hence, the best way to cut the bit-flip cost is to enhance the quality factor as displayed in Fig. 6.6. In particular, to ensure less than 5% of the LB, the quality factor has to exceed $Q = 1000$.

On the opposite trend for dissipation, our protocol flipping the states in the (x, v) plane cannot work for $Q < 0.5$, because it needs the system to oscillate. That is why, as mentioned in the introduction, using a second spatial DOF[1] instead of the speed DOF would be an alternative. Maintaining the bit-flip success rate ensured by the safety criterion ($10\sigma_0$ between the two states at all time) would in this case cost at least the work required to proceed a circle in the (x, y) 2D plane (from Eq. (F.9)):

$$\langle \mathcal{W} \rangle = k\left(\frac{10\pi\sigma_0}{\tau} \times \frac{10\pi\sigma_0}{Q\omega_0}\right) \tag{6.11}$$

$$= \left(\frac{50\pi}{Q} \times \frac{\mathcal{T}_0}{\tau}\right) k_B T_0 \tag{6.12}$$

For operations as fast as $\tau = \mathcal{T}_0/2$, our protocol in the (x, v) plane (only possible for $Q > 0.5$) is always better than its spatial (x, y) counterpart, as illustrated on Fig. 6.6. However, the bit-flip in the (x, y) plane allows to reduce the operation speed and get close to a quasi-static motion of the system in the viscous bath. As shown in Fig. 6.6, if one accepts to extend the duration to $\tau = 50\mathcal{T}_0$, then the (x, y) bit-flip protocol becomes the optimal process. In particular, contrary to our protocol, the (x, y) bit-flip would reached the quasi-reversibility ($\langle \mathcal{W} \rangle < 5\%$LB) at $Q = 100$ used in the experimental study.

[1] For a colloidal particle optically trapped, the y coordinate is a natural second DOF. For a micro-beam oscillator, this could also be the case for a rod (instead of a cantilever), with equivalent stiffness in the 2 directions perpendicular to its length.

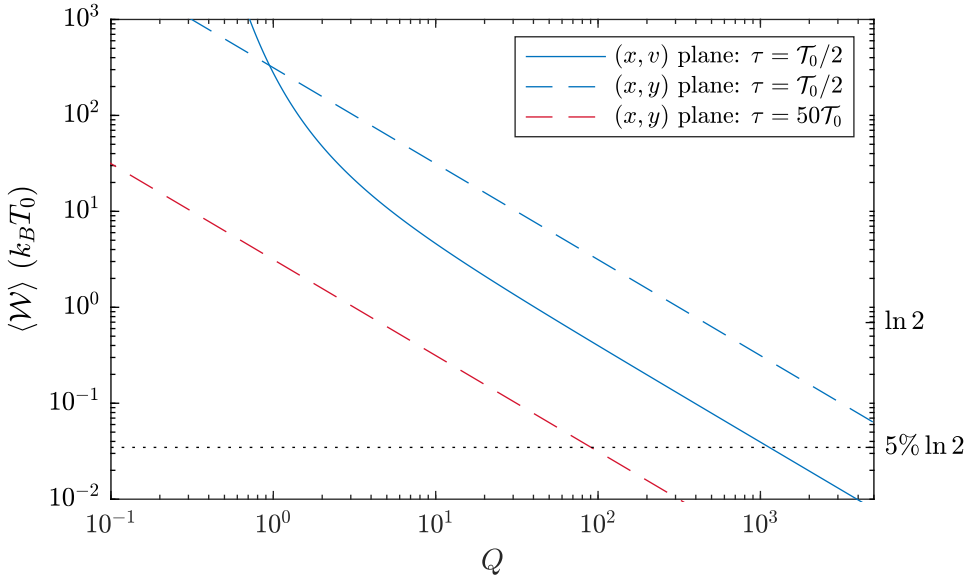

Figure 6.6 – **Work of a Bit-flip protocol depending on the quality factor Q and the operation duration τ.** Our protocol (plain blue), corresponding to a bit-flip in the (x, v) plane whose cost to ensure the safety criterion is given by Eq. (6.10), allows very fast erasures: $\tau = \mathcal{T}_0/2$. Increasing the quality factor reduces the bit-flip cost: the quasi-reversibility ($\langle \mathcal{W} \rangle < 5\%$LB in dotted black) is reached for $Q > 1000$. Proceeding at the same speed using the 2D spatial alternative (bit-flip in the (x, y) plane, dashed blue) requires much more energy, as expressed in Eq. (6.12). However, the (x, y) bit-flip allows to reduce the operation speed and therefore significantly cut the bit-flip cost. For a slower operation, $\tau = 50\mathcal{T}_0$, the (x, y) bit-flip becomes optimal, reaching the quasi-reversibility for $Q = 90$.

6.6 References

[1] K. J. Ray, G. W. Wimsatt, A. B. Boyd, and J. P. Crutchfield, Phys. Rev. Research **3**, 023164 (2021).

Conclusion

In conclusion, we have met the experimental challenge of driving brownian systems affected by thermal fluctuations, which allows us to explore fundamental principles in statistical physics. All our findings pave the way to fast and optimal control of micro-objects, with great applications in information processing. In the following, we put into perspective the main results of the thesis and suggest some ways forward by outlining avenues for further research.

Driving micro-systems

In my thesis, I propose different experimental set-ups designed to drive brownian systems with great accuracy. On the first hand, I use in chapter 2 tunable optical tweezers to trap coupled over-damped colloidal particles and drive them independently. On the other hand, I build a tunable virtual potential to control an underdamped micro-resonator in chapter 2 (stiffness driving) and chapter 3 (double-well potential driving). These two complementary experiments allow us to examine in depth fundamental statistical physics principles ruling the behavior of over-damped and underdamped brownian objects. In particular, we show in chapter 2 that specific protocols (ESE protocols) designed to shortcut the system relaxation after a change in a control parameter can be deduced from the system evolution equations and experimentally applied on hydrodynamically coupled particules. ESE processes designed for the underdamped regime are harder to implement experimentally, but we propose in chapter 2 all the building blocks to achieve it in the future.

Cost of information processing

The precise control of the underdamped micro-resonator detailed in chapter 3 opens new possibilities in terms of information processing, using the latter as 1-bit memory. Indeed, we conduct with our experimental set-up all possible logical operations: $(0,1) \to (0,1)$ [HOLD] (obvious implementation), $(0,1) \to (0,0)$ [RESET to 0], $(0,1) \to (1,1)$ [RESET to 1] and $(0,1) \to (1,0)$ [NOT].

In chapter 4 we tackle [RESET] operations: the underdamped cantilever turns out to be the fastest and the most efficient classical 1-bit logic gate, reaching LB 300 times faster than the state-of-the-art based on over-damped memories. The precision of the measurements allows us to model the energy exchanges during the [RESET] and deduce the cost of fast operations, displayed in Fig. Cl.1a as a function of the damping and erasure speed. In particular we show that weakly damped memories tend to warm up when irreversible logical operations are performed at high speeds. This thorough understanding of the source of energy loss opens up exciting new optimisation approaches: choosing the optimal damping (accordingly to the white line in Fig. Cl.1a), implementing optimal translational driving protocols (Fig. Cl.1b), or doing both (white line on Fig. Cl.1b). Besides, let us also mention that adjusting the relative duration of step 1 and step 2 (while keeping the overall erasure duration constant) on the basis of the model prediction of the compression and translational motion respective costs is another optimisation strategy very simple to implement.

Finally we explore in chapter 6 the [NOT] operation and propose an efficient bit-flip protocol that takes advantage on the velocity degree of freedom of the underdamped system to process the operation very fast, in only $\mathcal{T}_0/2 = 0.4\,\mathrm{ms}$. Even if the operation is logically reversible, physical sources of irreversibility result in a small energetic cost, successfully modeled in chapter 6. Fig. Cl.2a) gives the optimal bit-flip cost increasing with the damping and the operation speed. We also point out that at high speeds the

bit-flip using the velocity degree of freedom is optimal, meanwhile for slow operations an alternative protocol using two spatial degrees of freedom would be more efficient.

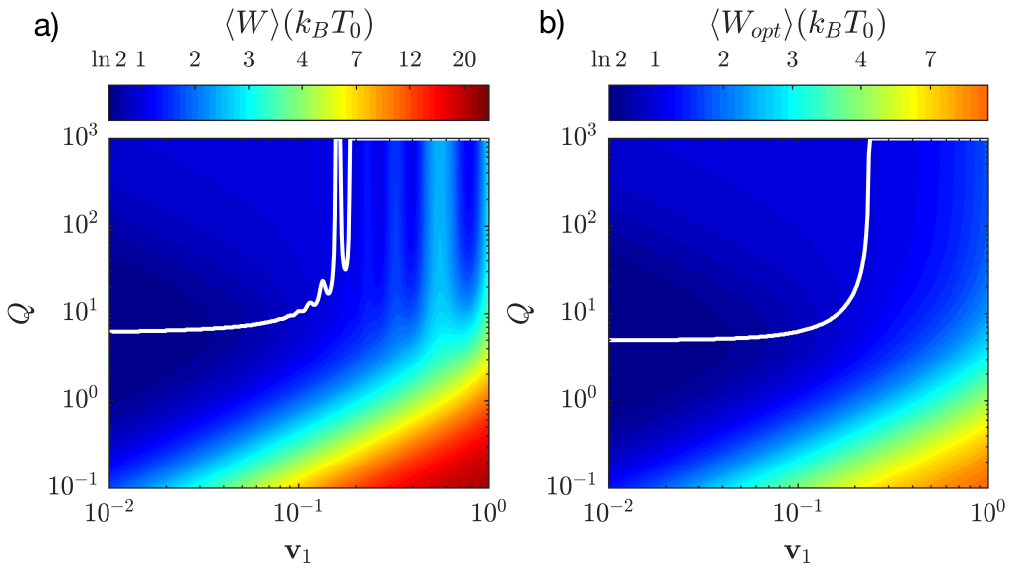

Figure Cl.1 – **a) Energetic consumption of a [RESET] operation**, computed from the model detailed and experimentally validated in chapter 4 (same as Fig. 4.9). The average work required to erase 1-bit of information is displayed as a function of the driving speed $\mathbf{v}_1 = Z_1/(\tau\omega_0)$ and the memory quality factor Q. The optimal damping is emphasized in white: it results from a balance between the price of the compression warming prevailing when Q is high (but bounded by the adiabatic limit), and the dissipation cost prevailing when Q is low. Let us point out that as the operation is logically irreversible the energetic consumption is bounded by the Landauer's fundamental lower limit. **b) Energetic consumption of an optimal [RESET] operation** computed from the model adapted to the optimal protocol, and validated by simulation results (same as Fig. 4.13b)). Applying optimal translational drivings substantially reduces the erasure cost for all damping regimes and driving speeds as highlighted by the common color scale used for a) and b). Similarly to the observations in a), the optimal quality factor (white line) is around $Q = 8$ at low speed, and increases strongly for fast operations.

Towards faster and more energy efficient logic-gates

In a very practical perspective, we have to wonder about the stability of the underdamped memory in response to frequent and repeated uses. We show in section 4.5 that working at high quality factor tends to minimize the erasure cost of a single erasure but may provoke a huge failure rate if the device repeats the operation several times. Again, we are able to model the response of the underdamped memory to successive erasures: its energy consumption (per operation) and its reliability are illustrated in Fig. Cl.2b.

All in all, if one wants to use the micro-resonator as a 1-bit logic gate, the performance of the device will be quantified through its energy consumption and its margin of error. As the [HOLD] operation is free, the power consumption of the logic gate can be given by the average between the energetic cost of successive [RESET] and [NOT] operations (assuming equivalent usage of both operations). We are therefore

able to draw in Fig. Cl.3 the energy consumption table of our logic-gate, weighted by the robustness of the information processing. We can conclude that, to our knowledge, a micro-system of quality factor $Q \sim 40$ (white line on Fig. Cl.3) happens to be the most energy efficient 1-bit memory. A compromise should be made at high speed by lowering the quality factor to keep the information processing safe.

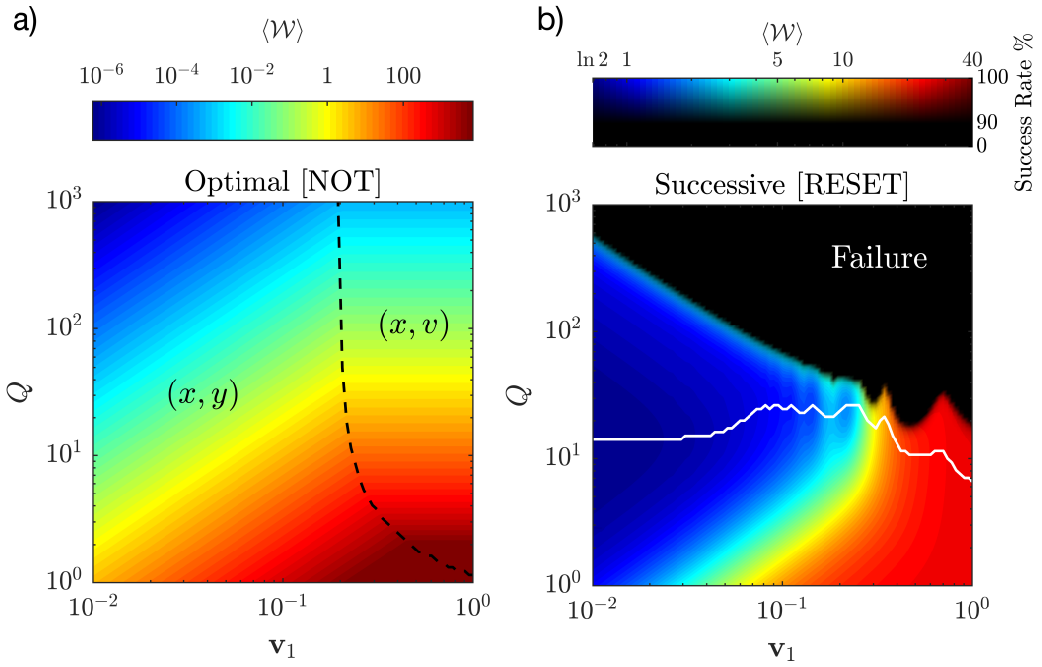

Figure Cl.2 – **a) Energetic consumption of an optimal [NOT] operation** meeting strong reliability requirement, computed with the model built in chapter 6 in agreement with experimental observations. The operation being logically reversible, there is no fundamental lower bound and we can reach the physical reversibility (almost no work required in the blue area) at high quality factor. Depending on the desired operation speed, the protocol resulting in the most energy efficient bit-flip differs. That is why for every parameters choice (Q and $\mathbf{v}_1$) we use the optimal protocol to compute the energetic cost, and the dashed line separates the regions where each one of the two possible protocols is the best. Indeed, for very fast operation (right hand side of the dashed line) the optimal protocol is the one using the speed degree of freedom (that is to say in the (x, v) plan) studied in chapter 6, meanwhile for slower operations (left hand side) it is the alternative protocol using 2 spatial degrees of freedom (that is to say in the (x, y) plan) mentioned in the end of the chapter. **b) Energetic consumption of repeated [RESET] operations** (in the permanent regime) computed with the model in chapter 4 proven to be in very good agreement with experimental results. The energetic cost is again encoded by the colormap (red area corresponding to very consuming procedures and blue ones corresponding to frugal ones), and the shading gives the success rate of the operation (black area corresponding to a success rate below 90%). Indeed we demonstrate that a repeated use of the memory without relaxation steps, differs from single [RESET] operations, and may lower the success rate of the information processing. In particular, we observe that successive operations fail at very high quality factor, contrary to single erasures where enhancing the quality factor reduces the energetic cost. Therefore the optimal damping for sustainable and continuous 1-bit erasures is around $Q = 10$ (white line).

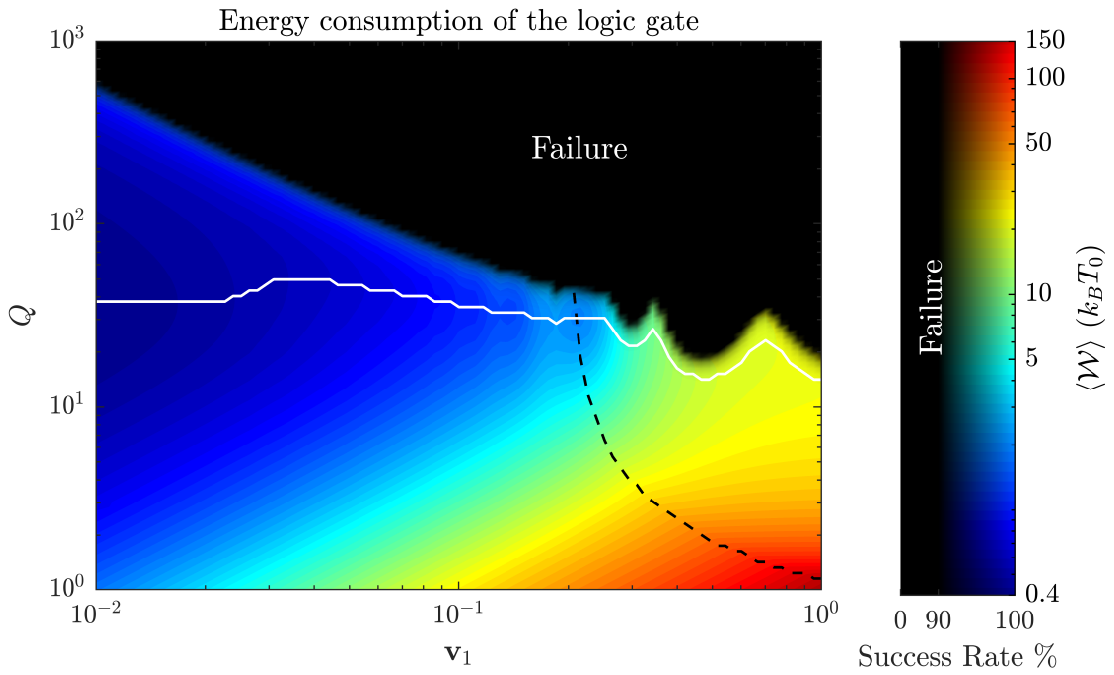

Figure Cl.3 – **Overall performance of the logic gate**. The [HOLD] operations being free, the average energetic consumption of the 1-bit memory for continuous information processing is deduced from the mean energetic cost of [RESET] operations (within the repeated use framework) and [NOT] operations (the dashed line separating the two optimal protocols). The sustainability of the logic gate is given by the operation success rate encoded by the map shading: the opaque black area corresponds to a success rate lower than 90% after several uses. The most energy efficient memory (white line) has a quality factor of $Q \sim 40$, which may be chosen smaller at very high speeds to maintain a reasonable margin of error in the information processing.

Other optimisation perspectives

We demonstrate in chapter 4 that the erasure price of fast operations saturates at high quality factors: it is the adiabatic limit corresponding to $\mathcal{W}_a = \frac{1}{2} k_B T_a = k_B T_0$. This is fundamentally linked to the relation between the temperature and the phase space volume evolution during the irreversible operation. In quadratic potentials, adiabatic transformations maintain the product $T\mathcal{V}$ constant, so that dividing the volume by two during the erasure makes the temperature double: $T_a = 2T_0$. However, a non-quadratic potential shape would lead to a different relation between temperature and volume in the adiabatic limit. In other words, the thermal capacity of the memory can be tuned by shaping the bi-stable potential. In particular, triangle double-wells would result in the conservation of the product $T\mathcal{V}^{\frac{2}{3}}$ so that the warming effect, bounded by the adiabatic case, would be diminished compared to the bi-quadratic shape. Indeed the adiabatic temperature becomes $T_a = 2^{\frac{2}{3}} T_0$, and the adiabatic energy cost is $\mathcal{W}_a = 0.79 k_B T_0$. Testing this optimisation experimentally is perfectly achievable using the FPGA (Fast Programming Gate Array) feedback loop: a triangular potential of the form $U(x, x_1) = F_0 ||x| - x_1|$ can be easily implemented with a comparator switching between constant forces $\pm F_0$.

Besides, once the compression cost (bounded by the adiabatic limit) carefully minimized by shaping the bi-stable potential, it remains to address the relaxation time after the operation to envision fast successive operations without damaging the suc-

cess rate. Indeed fast erasures end up out of equilibrium at temperature T_a, and the subsequent thermalization is all the more slow since heat exchanges with the bath are reduced at high quality factors. That is why it would be a huge advance to shortcut the relaxation of the system and prepare the memory for another operation in a very small amount of time. For this end, ESE protocols are a very promising path towards faster and more reliable information processing. The stiffness of the bi-stable potential could for example be tuned following an ESE procedure, in addition to conducting the erasure compression by bringing the two wells together. The FPGA feedback introduced in chapter 3 is a tool powerful enough to implement ESE protocols in the information manipulation, in keeping with the work done in chapter 2. Of course, such ESE procedures require energy (increasing with the desired equilibration speed), and a compromise should be found between accelerating successive use of the logic gate, and maintaining a low energy consumption.

The above discussion on fast erasures optimisation perspectives is summarized in Fig. Cl.4.

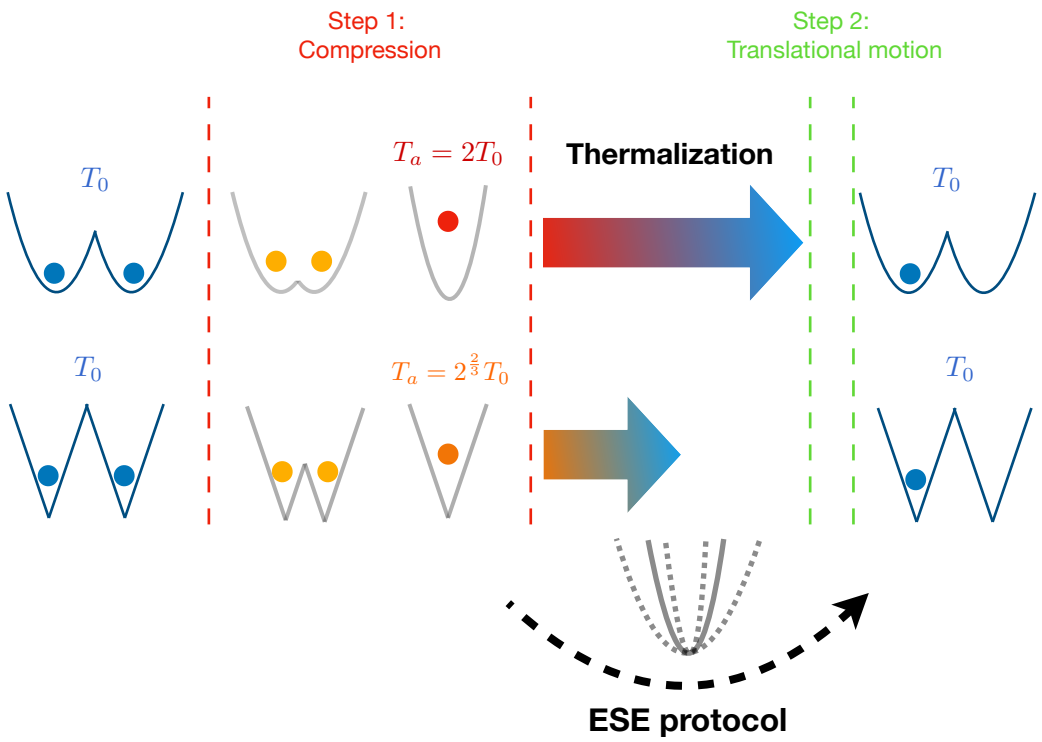

Figure Cl.4 – **Schematic overview of fast erasures optimisation perspectives**. On the first hand, changing the shape of the bi-stable potential, for example from quadratic to triangular wells, modifies the adiabatic limit of the compression warming: $T_a = 2^{\frac{2}{3}}T_0$ for triangular wells is lower than $T_a = 2T_0$ observed using quadratic ones. Other shapes may also be investigated. On the other hand, implementing ESE protocols to restore quickly the equilibrium of the memory after the compression warming is a promising strategy to optimize its repeated use. Those protocols could be implemented by imposing specific profiles on the potential shape either in addition to compression process during step 1, or in addition to the translational driving during step 2, or in between the two steps.

Harvesting energy from information

Finally, studying the link between information and thermodynamics has raised some interesting possibilities to convert information into energy. This kind of approach corresponds to the Maxwell demon paradox: if the thermal energy is by essence impossible to convert into work because of its random nature, removing the uncertainty using information on the system allows the harvesting of the work from the thermal noise. In other words, it is possible to extract useful mechanical work from a system just by observing its state. The knowledge of the system position comes from the demon and appears to be free. But in reality, the demon work can be quantified through the concept of mutual information and be explicitly incorporated into the second law. That is why information, entropy and energy should be treated on equal footings [1]. Within this framework, the efficiency of a Carnot engine could be beaten and work could even be extracted from a single reservoir using feedback (source of mutual information) [2], which would be impossible in standard thermodynamics.

These considerations opens a lot of promising perspectives in terms of generic information engines based on feedback processes. Besides, this trade off between feedback information and energy may also be used to build more energy efficient logic gates as it is suggested in chapter 5. Indeed we already demonstrate that the fundamental limit for the energetic cost of information processing is beaten in the presence of hysteresis in the feedback: in a way, the information contained in the hysteresis partially replaces the operator work.

References

[1] E. Lutz and S. Ciliberto, Physics Today **68**, 30 (2015).

[2] T. Sagawa and M. Ueda, Phys. Rev. Lett. **104**, 090602 (2010).

Bibliography

- Albay, J.A.C., Lai, P.Y., Jun, Y.: Realization of finite-rate isothermal compression and expansion using optical feedback trap. Applied Physics Letters 116(10), 103706 (2020), https://doi.org/10.1063/1.5143602

- Ashkin, A.: Acceleration and trapping of particles by radiation pressure. Phys. Rev. Lett. 24, 156–159 (Jan 1970), https://doi.org/10.1103/PhysRevLett.24.156

- Ashkin, A., Dziedzic, J.M., Bjorkholm, J.E., Chu, S.: Observation of a single-beam gradient force optical trap for dielectric particles. Opt. Lett. 11(5), 288–290 (May 1986), https://doi.org/10.1364/OL.11.000288

- Aurell, E., Gawędzki, K., Mejía-Monasterio, C., Mohayaee, R., Muratore-Ginanneschi, P.: Refined second law of thermodynamics for fast random processes. Journal of Statistical Physics 147(3), 487–505 (2012), https://doi.org/10.1007/s10955-012-0478-x

- Bellon, L.: Thermal noise of micro cantilevers in viscous fluids. Journal of Applied Physics 104(10), 104906 (2008), https://doi.org/10.1063/1.3021102

- Bellon, L.: Exploring nano-mechanics through thermal fluctuations. Habilitation à diriger des recherches, Ecole normale supérieure de lyon - ENS LYON (Nov 2010), https://tel.archives-ouvertes.fr/tel-00541336

- Bennett, C.H.: Demons, engines and the second law. Scientific American 257(5), 108–117 (1987), https://doi.org/10.1038/scientificamerican1187-108

- Bérut, A., Arakelyan, A., Petrosyan, A., Ciliberto, S., Dillenschneider, R., Lutz, E.: Experimental verification of landauer's principle linking information and thermodynamics. Nature 483(7388), 187–189 (2012), https://doi.org/10.1038/nature10872

- Bérut, A., Petrosyan, A., Ciliberto, S.: Information and thermodynamics: experimental verification of landauer's erasure principle. Journal of Statistical Mechanics: Theory and Experiment 2015(6), P06015 (2015), https://doi.org/10.1088/1742-5468/2015/06/p06015

- Binnig, G., Quate, C.F., Gerber, C.: Atomic force microscope. Phys. Rev. Lett. 56, 930–933 (Mar 1986), https://doi.org/10.1103/PhysRevLett.56.930

- Brown, R.: "A brief account of microscopical observations made in the months of june, july, and august, 1827 on the particles contained in the pollen of plants, and on the general existence of active molecules in organic and inorganic bodies", The miscellaneous botanical works of Robert Brown, vol. 1 (1828)

- Burrage, K., Burrage, P., Higham, D.J., Kloeden, P.E., Platen, E.: Comment on "numerical methods for stochastic differential equations". Phys. Rev. E 74, 068701 (Dec 2006), https://doi.org/10.1103/PhysRevE.74.068701
- Butt, H.J., Jaschke, M.: Calculation of thermal noise in atomic force microscopy. Nanotechnology 6(1), 1–7 (Jan 1995), https://doi.org/10.1088/0957-4484/6/1/001
- Butt, H.J., Cappella, B., Kappl, M.: Force measurements with the atomic force microscope: Technique, interpretation and applications. Surface Science Reports 59(1-6), 1–152 (2005), https://doi.org/10.1016/j.surfrep.2005.08.003
- Callen, H.B., Greene, R.F.: On a theorem of irreversible thermodynamics. Phys. Rev. 86, 702–710 (Jun 1952), https://doi.org/10.1103/PhysRev.86.702
- Chétrite, R., Rosinberg, M.L., Sagawa, T., Tarjus, G.: Information thermodynamics for interacting stochastic systems without bipartite structure. Journal of Statistical Mechanics: Theory and Experiment 2019(11), 114002 (Nov 2019), https://doi.org/10.1088/1742-5468/ab47fe
- Chupeau, M., Ciliberto, S., Guéry-Odelin, D., Trizac, E.: Engineered swift equilibration for Brownian objects: from underdamped to overdamped dynamics. New J. Phys. 20(7), 075003 (Jul 2018), https://doi.org/10.1088/1367-2630/aac875
- Ciliberto, S.: Experiments in stochastic thermodynamics: Short history and perspectives. Phys. Rev. X 7, 021051 (2017), https://doi.org/10.1103/PhysRevX.7.021051
- Cohen, A.E.: Control of nanoparticles with arbitrary two-dimensional force fields. Phys. Rev. Lett. 94, 118102 (Mar 2005), https://doi.org/10.1103/PhysRevLett.94.118102
- Dago, S., Bellon, L.: Dynamics of information erasure and extension of landauer's bound to fast processes. Phys. Rev. Lett. 128, 070604 (Feb 2022), https://doi.org/10.1103/PhysRevLett.128.070604
- Dago, S., Pereda, J., Barros, N., Ciliberto, S., Bellon, L.: Information and thermodynamics: Fast and precise approach to landauer's bound in an underdamped micromechanical oscillator. Phys. Rev. Lett. 126, 170601 (2021), https://doi.org/10.1103/PhysRevLett.126.170601
- Dago, S., Pereda, J., Ciliberto, S., Bellon, L.: Virtual double well potential for an underdamped oscillator created by a feedback loop (2022), https://doi.org/10.48550/arXiv.2201.09870, under review JSTAT. arXiv: 2201.09870
- Dago, S., Besga, B., Mothe, R., Guéry-Odelin, D., Trizac, E., Petrosyan, A., Bellon, L., Ciliberto, S.: Engineered Swift Equilibration of brownian particles: consequences of hydrodynamic coupling. SciPost Phys. 9, 64 (2020), https://doi.org/10.21468/SciPostPhys.9.5.064
- Einstein, A.: Uber die von der molekularkinetischen theorie der warme geforderte bewegung von in ruhenden flussigkeiten suspendierten teilchen. Annalen der Physik 322(8), 549–560 (1905), https://doi.org/10.1002/andp.19053220806

- Fokker, A.: The median energy of rotating electrical dipoles in radiation fields. Annalen Der Physik 43, 810–820 (1914)
- Gardiner, C.: Stochastic Methods: A Handbook for the Natural and Social Sciences. Springer Series in Synergetics, Springer Berlin Heidelberg (2010), https://books.google.tn/books?id=321EuQAACAAJ
- Gaudenzi, R., Burzuri, E., Maegawa, S., van der Zant, H.S.J., Luis, F.: Quantum landauer erasure with a molecular nanomagnet. Nature Physics 14(6), 565–568 (2018), https://doi.org/10.1038/s41567-018-0070-7
- Gavrilov, M., Bechhoefer, J.: Arbitrarily slow, non-quasistatic, isothermal transformations. EPL (Europhysics Letters) 114(5), 50002 (2016), https://doi.org/10.1209/0295-5075/114/50002
- Gavrilov, M., Jun, Y., Bechhoefer, J.: Real-time calibration of a feedback trap. Review of Scientific Instruments 85(9), 095102 (Sep 2014), https://doi.org/10.1063/1.4894383
- Geiger, P., Dellago, C.: Optimum protocol for fast-switching free-energy calculations. Phys. Rev. E 81, 021127 (Feb 2010), https://doi.org/10.1103/PhysRevE.81.021127
- Gieseler, J., Millen, J.: Levitated Nanoparticles for Microscopic Thermodynamics—A Review. Entropy 20(5), 326 (Apr 2018), https://doi.org/10.3390/e20050326
- Gieseler, J., Novotny, L., Moritz, C., Dellago, C.: Non-equilibrium steady state of a driven levitated particle with feedback cooling. New J. Phys. 17(4), 045011 (Apr 2015), https://doi.org/10.1088/1367-2630/17/4/045011
- Gomez-Marin, A., Schmiedl, T., Seifert, U.: Optimal protocols for minimal work processes in underdamped stochastic thermodynamics. The Journal of Chemical Physics 129(2), 024114 (2008), https://doi.org/10.1063/1.2948948
- Granger, L., Kantz, H.: Thermodynamic cost of measurements. Phys. Rev. E 84, 061110 (Dec 2011), https://doi.org/10.1103/PhysRevE.84.061110
- Green, C.P., Sader, J.E.: Frequency response of cantilever beams immersed in viscous fluids near a solid surface with applications to the atomic force microscope. Journal of Applied Physics 98(11), 114913 (2005), https://doi.org/10.1063/1.2136418
- Grier, D.G.: A revolution in optical manipulation. Nature 424(6950), 810–816 (Aug 2003), https://doi.org/10.1038/nature01935
- Guéry-Odelin, D., Muga, J.G., Ruiz-Montero, M.J., Trizac, E.: Nonequilibrium solutions of the boltzmann equation under the action of an external force. Phys. Rev. Lett. 112, 180602 (2014), https://doi.org/10.1103/PhysRevLett.112.180602
- Guéry-Odelin, D., Ruschhaupt, A., Kiely, A., Torrontegui, E., Martínez-Garaot, S., Muga, J.G.: Shortcuts to adiabaticity: Concepts, methods, and applications. Rev. Mod. Phys. 91, 045001 (Oct 2019), https://doi.org/10.1103/RevModPhys.91.045001

- Guéry-Odelin, D., Trizac, E.: Boltzmann avenged. Nature Physics 11(12), 988–988 (2015), https://doi.org/10.1038/nphys3522
- Hebestreit, E.: Thermal Properties of Levitated Nanoparticles. Ph.D. thesis, ETH Zurich (2017), https://doi.org/10.3929/ethz-b-000250832, appendix A
- Hong, J., Lambson, B., Dhuey, S., Bokor, J.: Experimental test of landauer's principle in single-bit operations on nanomagnetic memory bits. Sci. Adv. 2, e1501492 (2016), https://doi.org/10.1126/sciadv.1501492
- Itô, K.: Stochastic integral. Proceedings of the Imperial Academy 20(8), 519 – 524 (1944), https://doi.org/10.3792/pia/1195572786
- Jarzynski, C.: Equalities and inequalities: Irreversibility and the second law of thermodynamics at the nanoscale. Annual Review of Condensed Matter Physics 2(1), 329–351 (2011), https://doi.org/10.1146/annurev-conmatphys-062910-140506
- Jun, Y., Gavrilov, M., Bechhoefer, J.: High-precision test of landauer's principle in a feedback trap. Phys. Rev. Lett. 113, 190601 (2014), https://doi.org/10.1103/PhysRevLett.113.190601
- Jun, Y., Bechhoefer, J.: Virtual potentials for feedback traps. Phys. Rev. E 86, 061106 (Dec 2012), https://doi.org/10.1103/PhysRevE.86.061106
- Kim, K.H., Qian, H.: Entropy production of brownian macromolecules with inertia. Phys. Rev. Lett. 93, 120602 (Sep 2004), https://doi.org/10.1103/PhysRevLett.93.120602
- Konopik, M., Korten, T., Lutz, E., Linke, H.: Fundamental energy cost of finite-time computing (2021), https://doi.org/10.48550/arXiv.2101.07075
- Koski, J.V., Maisi, V.F., Pekola, J.P., Averin, D.V.: Experimental realization of a szilard engine with a single electron. Proceedings of the National Academy of Sciences 111(38), 13786 (2014), https://doi.org/10.1073/pnas.1406966111
- Kramers, H.: Brownian motion in a field of force and the diffusion model of chemical reactions. Physica 7(4), 284–304 (1940), https://doi.org/10.1016/S0031-8914(40)90098-2
- Landauer, R.: Irreversibility and heat generation in the computing process. IBM Journal of Research and Development 5(3), 183–191 (1961), https://doi.org/10.1147/rd.53.0183
- Le Cunuder, A., Martínez, I.A., Petrosyan, A., Guéry-Odelin, D., Trizac, E., Ciliberto, S.: Fast equilibrium switch of a micro mechanical oscillator. Applied Physics Letters 109(11), 113502 (2016), https://doi.org/10.1063/1.4962825
- Leff, H., Rex, A.: Maxwell's Demon: Entropy, Classical and Quantum Information, Computing. Institute of Physics, Philadelphia (2003)
- Lemons, D.S., Gythiel, A.: Paul langevin's 1908 paper "on the theory of brownian motion" ["sur la théorie du mouvement brownien," c. r. acad. sci. (paris) 146, 530–533 (1908)]. American Journal of Physics 65(11), 1079–1081 (1997), https://doi.org/10.1119/1.18725

- Lent, C., Orlov, A., Porod, W., Snider, G.: Energy Limits in Computation. Springer (2018)
- Lobser, D.S., Barentine, A.E.S., Cornell, E.A., Lewandowski, H.J.: Observation of a persistent non-equilibrium state in cold atoms. Nature Physics 11(12), 1009–1012 (2015), https://doi.org/10.1038/nphys3491
- López-Suárez, M., Neri, I., Gammaitoni, L.: Sub-kbt micro-electromechanical irreversible logic gate. Nat Commun. 7, 12068 (2016), https://doi.org/10.1038/ncomms12068
- Lutz, E., Ciliberto, S.: Information: From maxwell's demon to landauer's eraser. Physics Today 68(9), 30 (2015), https://doi.org/10.1063/PT.3.2912
- Martínez, I.A., Petrosyan, A., Guéry-Odelin, D., Trizac, E., Ciliberto, S.: Engineered swift equilibration of a Brownian particle. Nature Physics 12(9), 843–846 (2016), https://doi.org/10.1038/nphys3758
- Martinez, I.A., Roldan, E., Dinis, L., Petrov, D., Rica, R.A.: Adiabatic Processes Realized with a Trapped Brownian Particle. Phys. Rev. Lett. 114, 120601 (2015), https://doi.org/10.1103/PhysRevLett.114.120601
- Martinez, I.A., Roldan, E., Dinis, L., Petrov, D., Rica, R.A.: Supplemental Material for Ref. [59] (2015), https://doi.org/10.1103/PhysRevLett.114.120601
- Martini, L., Pancaldi, M., Madami, M., Vavassori, P., Gubbiotti, G., Tacchi, S., Hartmann, F., Emmerling, M., Höfling, S., Worschech, L., Carlotti, G.: Experimental and theoretical analysis of landauer erasure in nano-magnetic switches of different sizes. Nano Energy 19, 108 – 116 (2016), https://doi.org/10.1016/j.nanoen.2015.10.028
- Mel'nikov, V.: The Kramers problem: Fifty years of development. Physics Reports 209(1-2), 1–71 (Dec 1991), https://doi.org/10.1016/0370-1573(91)90108-X
- Munakata, T., Rosinberg, M.L.: Entropy production and fluctuation theorems under feedback control: the molecular refrigerator model revisited. Journal of Statistical Mechanics: Theory and Experiment 2012(05), P05010 (May 2012), https://doi.org/10.1088/1742-5468/2012/05/p05010
- Munakata, T., Rosinberg, M.L.: Feedback cooling, measurement errors, and entropy production. Journal of Statistical Mechanics: Theory and Experiment 2013(06), P06014 (Jun 2013), https://doi.org/10.1088/1742-5468/2013/06/p06014
- Muratore-Ginanneschi, P., Schwieger, K.: An application of pontryagin's principle to brownian particle engineered equilibration. Entropy 19(7), 379 (2017), https://doi.org/10.3390/e19070379
- Orlov, A.O., Lent, C.S., Thorpe, C.C., Boechler, G.P., Snider, G.L.: Experimental test of landauer's principle at the sub-k_bt level. Japanese Journal of Applied Physics 51(6S), 06FE10 (2012), https://doi.org/10.1143/jjap.51.06fe10
- Padgett, M., Molloy, J., McGloin, D.: Optical Tweezers: Methods and Applications. Chapman and Hall/CRC (2010), https://doi.org/10.1201/EBK1420074123

- Paolino, P., Aguilar Sandoval, F., Bellon, L.: Quadrature phase interferometer for high resolution force spectroscopy. Rev. Sci. Instrum. 84, 095001 (2013), https://doi.org/10.1063/1.4819743
- Park, J.M., Lee, J.S., Noh, J.D.: Optimal tuning of a confined brownian information engine. Phys. Rev. E 93, 032146 (Mar 2016), https://doi.org/10.1103/PhysRevE.93.032146
- Parrondo, J.M.R., Horowitz, J.M., Sagawa, T.: Thermodynamics of information. Nature Physics 11(2), 131–139 (2015), https://doi.org/10.1038/nphys3230
- Planck, M.: Über einen datz der statistischen dynamik und seine erweiterung in der quantentheorie. Sitzungsberichte der Königlich Preussischen Akademie der Wissenschaften zu Berlin. 24, 324–341 (1917)
- Proesmans, K., Ehrich, J., Bechhoefer, J.: Finite-time landauer principle. Phys. Rev. Lett. 125, 100602 (2020), https://doi.org/10.1103/PhysRevLett.125.100602
- Ray, K.J., Wimsatt, G.W., Boyd, A.B., Crutchfield, J.P.: Non-Markovian Momentum Computing: Universal and Efficient. Phys. Rev. Research 3(2), 023164 (Jun 2021), https://doi.org/10.1103/PhysRevResearch.3.023164
- Roldán, É., Martínez, I.A., Parrondo, J.M.R., Petrov, D.: Universal features in the energetics of symmetry breaking. Nature Physics 10(6), 457–461 (2014), https://doi.org/10.1038/nphys2940
- Rosinberg, M.L., Munakata, T., Tarjus, G.: Stochastic thermodynamics of Langevin systems under time-delayed feedback control: Second-law-like inequalities. Phys. Rev. E 91(4), 042114 (Apr 2015), https://doi.org/10.1103/PhysRevE.91.042114
- Rosinberg, M.L., Horowitz, J.M.: Continuous information flow fluctuations. EPL (Europhysics Letters) 116(1), 10007 (Oct 2016), https://doi.org/10.1209/0295-5075/116/10007
- Sader, J.E.: Frequency response of cantilever beams immersed in viscous fluids with applications to the atomic force microscope. Journal of Applied Physics 84(1), 64–76 (1998), https://doi.org/10.1063/1.368002
- Sader, J.E.: Frequency response of cantilever beams immersed in viscous fluids with applications to the atomic force microscope. Journal of Applied Physics 84(1), 64–76 (1998), https://doi.org/10.1063/1.368002
- Sagawa, T., Ueda, M.: Generalized jarzynski equality under nonequilibrium feedback control. Phys. Rev. Lett. 104, 090602 (Mar 2010), https://doi.org/10.1103/PhysRevLett.104.090602
- Seifert, U.: Stochastic thermodynamics: principles and perspectives. The European Physical Journal B 64(3), 423–431 (Aug 2008), https://doi.org/10.1140/epjb/e2008-00001-9
- Seifert, U.: Entropy production along a stochastic trajectory and an integral fluctuation theorem. Phys. Rev. Lett. 95, 040602 (Jul 2005), https://doi.org/10.1103/PhysRevLett.95.040602

- Seifert, U.: Stochastic thermodynamics, fluctuation theorems and molecular machines. Reports on Progress in Physics 75(12), 126001 (Nov 2012), https://doi.org/10.1088/0034-4885/75/12/126001
- Sekimoto, K.: Stochastic Energetics, Lecture Notes in Physics, vol. 799. Springer (2010), https://doi.org/10.1007/978-3-642-05411-2
- Sekimoto, K.: Langevin Equation and Thermodynamics. Progress of Theoretical Physics Supplement 130, 17–27 (1998), https://doi.org/10.1143/PTPS.130.17
- Sekimoto, K., Sasa, S.: Complementarity relation for irreversible process derived from stochastic energetics. Journal of the Physical Society of Japan 66(11), 3326–3328 (1997), https://doi.org/10.1143/JPSJ.66.3326
- Toyabe, S., Sagawa, T., Ueda, M., Muneyuki, M., Sano, M.: Experimental demonstration of information-to-energy conversion and validation of the generalized Jarzynski equality. Nature Phys. 6, 988–992 (2010), https://doi.org/10.1038/nphys1821
- Van Eysden, C.A., Sader, J.E.: Frequency response of cantilever beams immersed in viscous fluids with applications to the atomic force microscope: Arbitrary mode order. Journal of Applied Physics 101(4), 044908 (2007), https://doi.org/10.1063/1.2654274
- Yan, L.L., Xiong, T.P., Rehan, K., Zhou, F., Liang, D.F., Chen, L., Zhang, J.Q., Yang, W.L., Ma, Z.H., Feng, M.: Single-atom demonstration of the quantum landauer principle. Phys. Rev. Lett. 120, 210601 (2018), https://doi.org/10.1103/PhysRevLett.120.210601

Appendix A:

Engineered swift equilibration of brownian particles: consequences of hydrodynamic coupling

We attach in this section our article in Ref. 1.

SciPost Phys. 9, 064 (2020)

Engineered swift equilibration of brownian particles: consequences of hydrodynamic coupling

Salambô Dago[1], Benjamin Besga[1], Raphaël Mothe[1], David Guéry-Odelin[2], Emmanuel Trizac[3], Artyom Petrosyan[1], Ludovic Bellon[1⋆] and Sergio Ciliberto[1]

1 Univ Lyon, Ens de Lyon, Univ Claude Bernard Lyon 1, CNRS, Laboratoire de Physique, F-69342 Lyon, France
2 Laboratoire de Collisions Agrégats Réactivité, CNRS, UMR 5589, IRSAMC, France
3 Université Paris-Saclay, CNRS, LPTMS, 91405, Orsay, France.

⋆ ludovic.bellon@ens-lyon.fr

Abstract

We present a detailed theoretical and experimental analysis of Engineered Swift Equilibration (ESE) protocols applied to two hydrodynamically coupled colloids in optical traps. The second particle disturbs slightly (10% at most) the response to an ESE compression applied to a single particle. This effect is quantitatively explained by a model of hydrodynamic coupling. Then we design a coupled ESE protocol for the two particles, allowing the perfect control of one target particle while the second is enslaved to the first. The calibration errors and the limitations of the model are finally discussed in detail.

Received 12-05-2020
Accepted 06-10-2020
Published 05-11-2020
doi:10.21468/SciPostPhys.9.5.064

Check for updates

Contents

SciPost SciPost Phys. 9, 064 (2020)

1 Introduction

Speeding-up an equilibration process is a delicate task, because the relaxation time is an intrinsic property of a system which depends on parameters such as the dissipation, the potential strength, the inertia, or the number of degrees of freedom. Furthermore, when a control parameter is suddenly changed, the system may pass through states that differ widely from the target one. One way of speeding up a specific transformation between well defined equilibrium states is to apply complex protocols in which the time dependence of one or several control parameters is tuned in a highly specific fashion, to reach the final target in a selected short amount of time. This problem, related to optimal control theory, can be traced back to Boltzmann [1–3]. It has recently received sustained attention within the framework of the so-called "Shortcut To Adiabaticity" protocols, which study such complex procedures for specific transformations [4, 5].

We are interested here in overdamped systems in contact with a thermostat, for which we have defined protocols of Engineered Swift Equilibration (ESE) that have been applied to the control of Brownian particles trapped by optical tweezers [6]. For example, one can achieve the compression of a single particle trapped in an harmonic well by increasing the potential stiffness K between an initial state in equilibrium at K_i and a final state in equilibrium at K_f. After a sudden change in K (STEP protocol) the bead will equilibrate in its natural relaxation time. Using an ESE protocol for the time evolution of $K(t)$, the same final state can be reached several orders of magnitude faster than STEP [6]. We will refer to this fast compression protocol as the **basic ESE**. When designing these protocols, one of the key questions lies in the stability against external perturbations. In this context, we tackle in this article the case of two hydro-dynamically coupled particles trapped in different potentials, to understand to what extent the equilibration dynamics imposed by the *basic ESE* is modified by the hydrodynamic interactions with another bead. A deep understanding of the physical consequences of the coupling on the particles behaviour (correlation) is necessary to work out the consequences of this perturbation. The goal here is twofold: on the one hand, it is a simple test bench to probe the robustness of the *basic ESE*. Indeed, we can see the second particle as a perturbation to the first, and monitor how far the protocol misses its target if we neglect this perturbation. And on the other hand, it is a first step towards the control of more complex systems with several degrees of freedom.

The article is organised as follows: in a first part, we investigate robustness of the *basic ESE* to the coupling interaction. To do so, we conduct experiments using the experimental set up described in section 2, and present the results in section 3. To support our experimental results, we then use in section 4 a simple model from refs. [7–10] to describe the coupled system, and predict the dynamics of the correlations at equilibrium and the general dynamics of the moments. We subsequently turn to the second goal of the paper: extending the scope of ESE protocols to more complex systems. The model used is precise enough to provide a basis for the construction of new ESE protocols adapted to the coupled system. In particular we explore in section 5 the construction of ESE protocols that do not depend on the coupling intensity, and are thus very robust. Then we demonstrate experimentally the validity of this extension. Finally we draw the experimental limits of this new strategy in section 6.

2 Experimental set up and method

To test the robustness of the *basic ESE* to the coupling interaction, we conduct experiments on two silica beads of radius $r = 1\,\mu$m immersed in miliQ water (to avoid trapping impurities) at a temperature T and trapped by two optical tweezers separated by the distance d (see Fig. 1).

SciPost SciPost Phys. 9, 064 (2020)

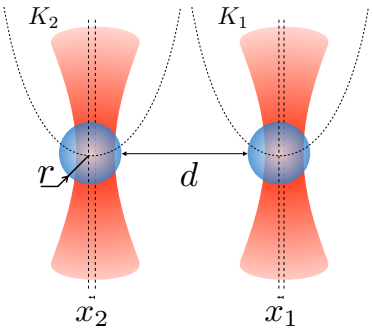

Figure 1: Two Brownian particles trapped by optical tweezers into two harmonic potentials of stiffness K_1 and K_2. x_j represents the position of the particle $j = 1, 2$ relative to the trap center x_j^0, and in the following, $\widetilde{x_j} = x_j + x_j^0$ represents the absolute position. d is the mean distance to contact between the two particles of radius $r = 1\,\mu$m: $d = |x_2^0 - x_1^0| - 2r$.

We use a very small concentration of silica micro-spheres in water and a specific design of the cell containing the particles, in order to have very few beads in the measuring volume. This enables us to take long measurements without any spurious perturbation. The two beads are trapped at 20 μm from the bottom plate of the cell. The traps are realized using a near-infrared single mode DPSS laser (Laser Quantum, $\lambda = 1064\,$nm used at a power of 1 W) expanded and injected through an oil-immersed objective (Leica, 63 × NA 1.40) into the fluid chamber. An Acousto-Optic Deflector (AOD) controls the intensity and the position of the trapping beams with the amplitude and frequency of the control signal, respectively. We thus create two harmonic potentials at a distance d along the x direction $U_j(\widetilde{x_j}, t) = -K_j(t)(\widetilde{x_j} - x_j^0)^2/2$, with $j = 1, 2$, where $\widetilde{x_j}$ are the absolute particle positions. The potential minimum x_j^0 and stiffness K_j are controlled respectively by the frequency and amplitude of the AOD input signal. As the AOD responds linearly, a sum of sine waveforms of different frequencies results in two potentials $U_{j=1,2}$ separated by a distance proportional to the difference between the sine frequencies. We can also use a second version of the setup with two AODs (one for each trap) to have two perfectly uncoupled static traps with orthogonally polarized beam (which is needed in particular when $K_1(t) \neq K_2(t)$). The detection of the particle position is performed using a fiber coupled single mode laser diode (Thorlabs, $\lambda = 635\,$nm, power 1 mW lowered to 100 μW with a neutral density filter) which is collimated after the fiber and sent through the trapping objective. The forward-scattered detection beam is collected by a condenser (Leica, NA 0.53), and its back focal-plane field distribution projected onto a four quadrant detector (QPD from First Sensor with a bandpass of 1 MHz with custom made electronic) which gives a signal proportional to the particle position. Before every acquisition, a calibration procedure described in Appendix A.1 is conducted.

As regards the acquisition process, the approach consists in comparing the situation when the particles are strongly coupled ($d \lesssim r$), with the situation when the coupling is negligible ($d \gg r$), in order to conclude on the perturbation induced by the coupling. Because the procedure is very sensitive to the instrument calibration and to the external parameters, to compare properly the 2 cases described above, we apply the following protocol: we start at small distance and record the particle position during a dozen of ESE protocols, then we smoothly separate the 2 particles and record again a dozen protocols, before bringing again the 2 particles closer and restart the cycle. Doing so enables us to compare the response to the

SciPost SciPost Phys. 9, 064 (2020)

ESE protocol in the coupled and uncoupled cases in the same experimental conditions. The recording lasts 10000 protocols to reduce statistical uncertainty. The same approach can be adjusted for other comparisons, the point being always to maintain the same working conditions between the two acquisitions.

3 Consequences of coupling perturbation on the *basic ESE protocol*

This section aims to see to what extent the response of the particle to the *basic ESE* deviates from the 0-coupling case successfully tested in ref. [6], when it is affected by the coupling perturbation created by another particle at distance d.

Indeed, the *basic ESE* defined in ref. [6] is designed for a single particle trapped in the potential $U(t) = \frac{1}{2}K(t)x^2$, and whose over-damped dynamics is described by a Langevin equation that introduces the friction coefficient $\gamma = 6\pi\eta r$, η being the kinetic viscosity and $r = 1\,\mu$m the radius of the particle. The *basic ESE* consists in changing the stiffness over a period of time t_f to reach a new equilibrium at K_f. The corresponding stiffness profile is the following, using the dimensionless quantities $k(t) = K(t)/K_i$ (in particular $k_f = K_f/K_i$), $s = t/t_f$ and $\Gamma = \gamma/(K_i t_f)$ (ratio of relevant timescales):

$$k(s) = 1 + (k_f - 1)(3 - 2s)s^2 - \frac{3\Gamma(k_f - 1)(s - 1)s}{1 + (k_f - 1)(3 - 2s)s^2}\,. \tag{1}$$

One may expect that if the ESE final time t_f is small enough compared to the characteristic correlation time τ_{corr}, the particles will behave as in the free case. To test this hypothesis we study the evolution of the variance of the first particle during what we call the **symmetric protocol**: the stiffness of both wells is simultaneously driven ($K_1(s) = K_2(s) = K(s)$) according to the *basic ESE* of eq. (1). In what follows we associate with the first particle variance $\langle x_1^2 \rangle$ the dimensionless quantity $\sigma_{11} = K_i\langle x_1^2\rangle/(2k_BT)$. In the *symmetric protocol* context $\sigma_{11} = \sigma_{22} = \sigma$. We carry out this procedure for an ESE time t_f one order of magnitude smaller than the typical characteristic times $\tau_{\text{corr}} \sim \tau_{\text{relax}} \sim 15\,$ms. To cycle the procedure we use the stiffness profile of Fig. 2 (left) for both traps: a simple step decompression followed by the *basic ESE* compression. The experimental results are plotted in plain lines on Fig. 2 (right), in purple for a small distance and in black for a large distance. Since we look for tiny effects, all results in the article are plotted using the normalised variance $\sigma_n = (\sigma(t) - \sigma_f)/(\sigma_i - \sigma_f)$. In response to the step decompression, the particle reaches equilibrium in its natural relaxation time τ_{relax}. We notice that the coupling also affects this natural relaxation (by slightly slowing it down). Then we apply the *basic ESE protocol* to both wells, and we observe that at small d the coupling induces a rebound in the variance evolution (indicated by the red arrow on the figure) and prevents the particle to reach equilibrium in the expected time. The ESE is also very sensitive to other external perturbations, indeed a small drift in calibration may be responsible for the very small slip of the black curve under its final value at t_f. These observations are very reproducible and one may see in Appendix A.2 complementary results highlighting the increase of the rebound height with the intensity of the coupling.

To put it in a nutshell, Fig. 2 highlights that even though the protocol is designed to be much faster than the coupling characteristic time, the coupling perturbation impacts the response to the *basic ESE*. Our sensitive experimental setup enables us to observe experimentally the tiny effect of hydrodynamic coupling: the particle variance features a rebound at t_f and will not reach equilibrium before its natural relaxation time. Nevertheless the *basic ESE* is rather robust, as for moderate coupling, this bounce is modest compared to the natural relaxation amplitude evolution. Indeed *basic ESE* still provides correct results, with a 10% deviation to

SciPost SciPost Phys. 9, 064 (2020)

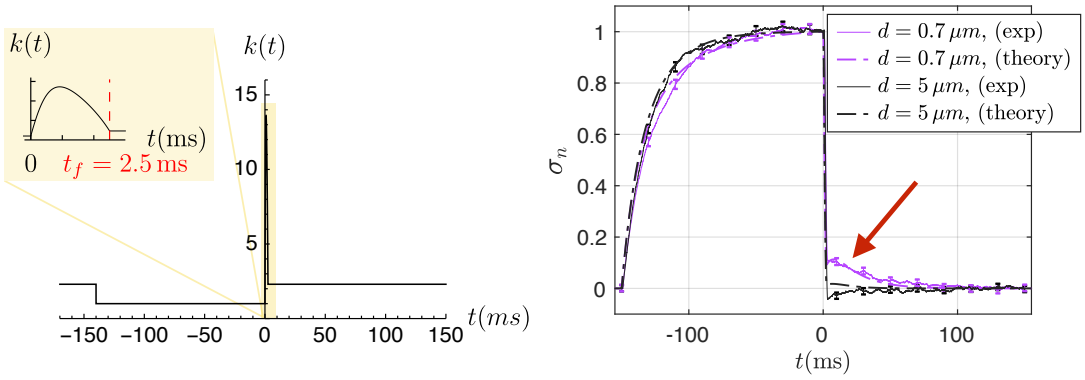

Figure 2: On the left, the stiffness profile applied to both wells: a STEP decompression at $t = -140\,\text{ms}$ followed by a *basic ESE* protocol for compression for $0 < t < t_f$. This procedure is called the *symmetric protocol*. At $t = -140\,\text{ms}$, the stiffness jumps from $k_f = 2.3$ to $k_i = 1$. At $t = 0$ the particle is thus in its initial equilibrium when we apply an ESE protocol finishing at t_f to bring back the particle to its final state at k_f. The ESE parameters are: $t_f = 2.5\,\text{ms}$, $K_i = 4 \times 10^{-7}\,\text{N/m}$, $k_f = 2.3$, and $\Gamma = 18.9$. This stiffness profile emphasizes the difference between the relaxation after a step function, and the response to the ESE protocol. On the right, normalized variance of the first particle $\sigma_n = (\sigma(t) - \sigma_f)/(\sigma_i - \sigma_f)$, corresponding to the *symmetric protocol* on the left. The plain lines are the experimental results with their error bars. The dashed curves are numerically computed from the theoretical analysis of section 4, plugging the experimental parameters from the calibration. The same process is applied for particles separated by $d = 5\,\mu\text{m}$ (black) and $d = 0.7\,\mu\text{m}$ (purple) corresponding respectively to a coupling constant (introduced in section 4) $\epsilon = 0.21$ and $\epsilon = 0.5$. A small rebound (around 10% of the step) pointed by the red arrow and long relaxation time are visible for close particles.

the 0-coupling case. Within this framework a measure with a poor statistics will hide the effect inside the statistical error.

It remains to be seen whether this experimental results can be supported by a theoretical analysis. To this end we devote the next section to study the coupled system's dynamics, first in equilibrium and then when driven by the *symmetric protocol*.

4 Theoretical analysis

To describe the evolution of two trapped brownian particles which are hydrodynamically coupled, we write the coupled Langevin equations,

$$\begin{pmatrix} \dot{x_1} \\ \dot{x_2} \end{pmatrix} = \mathcal{H} \begin{pmatrix} F_1 \\ F_2 \end{pmatrix}, \tag{2}$$

where x_j is the position of the particle $j = 1, 2$ relative to its trapping position (see Fig. 1), $\dot{x_j}$ is the time derivative of x_j, and $\mathcal{H}$ is the hydrodynamic coupling tensor. The Langevin equations govern the system evolution in general whether or not it is at equilibrium. Besides, the Langevin equations (2) do not include any acceleration term: we assume the over-damped regime which is fully justified for colloidal objects (see Appendix A.3). At equilibrium the forces

SciPost SciPost Phys. 9, 064 (2020)

acting on the particles are:

$$F_j = -K_j x_j + f_j\,, \tag{3}$$

where K_j is the stiffness of the trap j and f_j is the Brownian random noise. For two identical particles of radius r separated by a distance d (see Fig. 1), assuming that their displacements are small compared to the mean distance between them, the hydrodynamic coupling tensor reads [7–10]:

$$\mathcal{H} = \frac{1}{\gamma}\begin{pmatrix} 1 & \epsilon \\ \epsilon & 1 \end{pmatrix}. \tag{4}$$

In some approximations described in Appendix A.4 we can write $\epsilon = \frac{3}{2}\nu - \nu^3$, where $\nu = r/(2r+d)$.

Let us first study how the particles behave at equilibrium (K_j constant in time), and in particular how they influence their neighbour. At equilibrium the two particles are statistically independent: $\langle x_1 x_2\rangle_{eq} = 0$, $\langle x_1^2\rangle_{eq} = k_B T/K_1$, and $\langle x_2^2\rangle_{eq} = k_B T/K_2$ (with k_B the Boltzmann's constant and T the bath temperature). However, the 2 particles are coupled by eq. (2). Extending the computation of refs. [9, 11] to the more general case of two potentials with different stiffnesses, we show in Appendix A.5 that, at equilibrium, auto-correlations $\langle x_j(0)x_j(t)\rangle$ and cross-correlations $\langle x_j(0)x_k(t)\rangle$ (with $j \neq k$) of positions read as:

$$\langle x_1(t)x_1(0)\rangle = \frac{k_B T}{2K_1\kappa}\Big[e^{-\frac{t}{\tau_+}}(K_1 - K_2 + \kappa) + e^{-\frac{t}{\tau_-}}(K_2 - K_1 + \kappa)\Big], \tag{5}$$

$$\langle x_2(t)x_2(0)\rangle = \frac{k_B T}{2K_2\kappa}\Big[e^{-\frac{t}{\tau_+}}(K_2 - K_1 + \kappa) + e^{-\frac{t}{\tau_-}}(K_1 - K_2 + \kappa)\Big], \tag{6}$$

$$\langle x_1(t)x_2(0)\rangle = \frac{\epsilon k_B T}{\kappa}\Big[e^{-\frac{t}{\tau_+}} - e^{-\frac{t}{\tau_-}}\Big], \tag{7}$$

with

$$\kappa = \sqrt{(K_1 - K_2)^2 + 4\epsilon^2 K_1 K_2}\,, \tag{8}$$

$$\tau_- = \frac{2\gamma}{K_1 + K_2 - \kappa}\,, \tag{9}$$

$$\tau_+ = \frac{2\gamma}{K_1 + K_2 + \kappa}\,. \tag{10}$$

We report the computed behaviour in Fig. 3. Those correlation functions involve two characteristic times τ_+ and τ_- that are very close to the natural relaxation time of the harmonic well $\tau_{\text{relax}} = \gamma/K_1 \sim 15\,\text{ms}$. We consequently introduce a slow mode and a fast mode associated respectively with τ_- and τ_+. The slow mode vanishes when $x_1 \propto x_2$, and the fast mode when $x_1 \propto -x_2$: ie correlation enhances the fast mode (correlated mode) and anti-correlation the slow mode (anti-correlated mode). In the symmetric case, the two modes may be interpreted as the barycentre of the system $x_M = (x_1 + x_2)/2$, and the particles separation $x_\mu = (x_2 - x_1)/2$. Naturally, x_μ embodies the slow mode and x_M the fast one, as the evolution of x_μ requires a fluid displacement between the particles, while the barycentre evolution relies on the fact that one sphere tends to drag the other in its wake (details in [9]). As far as auto-correlation functions are concerned, the shape of decaying exponential in Fig. 3 is rather common. The negative cross-correlation might however be surprising. This feature stems first from the fact that the cross-correlation has to vanish at $t = 0$ (a consequence of independence at equilibrium), and second from the fact that the anti-correlated mode (associated with x_μ) lives longer than the correlated mode (associated with x_M).

We now focus on the dynamics of the particles when the potentials change with time. It proves convenient to convert the coupled Langevin equations into equations describing the

SciPost SciPost Phys. 9, 064 (2020)

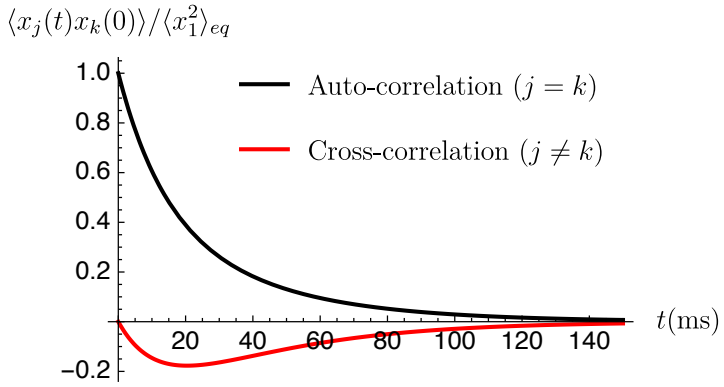

Figure 3: Auto- and cross-correlation functions normalized by $\langle x_1^2\rangle_{eq}$ as a function of time, when $\gamma = 1.88 \times 10^{-8}$ sN/m, $K_1 = K_2 = 10^{-6}$ N/m and $d = 1\,\mu$m, so that $\sigma_{11,eq} = k_B T/K_1 = 4 \times 10^3$ nm^2 and $\epsilon = 0.46$. We recover at $t = 0$ the values of the moments at equilibrium, in particular $\sigma_{12,eq} = 0$.

dynamics of the moments $\langle x_1^2\rangle(t)$, $\langle x_2^2\rangle(t)$ and $\langle x_1 x_2\rangle(t)$. Using the dimensionless quantities $\sigma_{jk} = K_{1,i}\langle x_j x_k\rangle/(2k_B T)$, we obtain the following system to describe the evolution of the moments (see Appendix A.6):

$$\Gamma\frac{d\sigma_{11}}{ds} = -2k_1\sigma_{11} - 2\epsilon k_2\sigma_{12} + 1\,, \tag{11}$$

$$\Gamma\frac{d\sigma_{22}}{ds} = -2k_2\sigma_{22} - 2\epsilon k_1\sigma_{12} + 1\,, \tag{12}$$

$$\Gamma\frac{d\sigma_{12}}{ds} = -(k_1 + k_2)\sigma_{12} - \epsilon(k_2\sigma_{22} + k_1\sigma_{11} - 1)\,, \tag{13}$$

where $s = t/t_f$ as before, $k_j(s) = K_j(s)/K_{1,i}$ ($K_{1,i}$ being the initial stiffness of the first well), and $\Gamma = \gamma/(K_{1,i}t_f)$. The above equations contain all the information about the dynamics of the system, as the joint probability distribution remains Gaussian out of equilibrium (see Appendix A.7) and is thus fully described by σ_{11}, σ_{22} and σ_{12}. The *basic ESE* in eq. (1) is defined in ref. [6] using eq. (11) without the cross term $\epsilon\sigma_{12}$ term. Therefore it cannot be operational for the coupled system.

We compute numerically the evolution of the first particle variance corresponding to the *symmetric protocol* where the stiffness of both wells is simultaneously driven according to the *basic ESE*. The results of these computations are summarized in Fig. 4: it should be recalled that in the *symmetric protocol* context ($K_1 = K_2 = K$), the above equations simplify and $\sigma_{11} = \sigma_{22}$ can be written σ.

The theoretical predictions of Fig. 4 seem to be consistent with the experimental conclusions drawn in section 3. To confirm that the model prediction and the experimental curves match, we superimpose in dashed lines on Fig. 2 the theoretical curves obtained using the same ESE parameters and the external parameters from calibration. We see that the results are in very good accordance. Besides, the validity of the theory during the STEP to prepare the system at K_i confirms that the calibration is relevant to estimate the external parameters during the experiment.

The model of the hydrodynamic coupling proves to be precise enough to be used for ESE computations. We are thus equipped to propose a new strategy to drive a coupled system without any compromise on the shortcut efficiency. Indeed we can take into account the hydrodynamic coupling in the construction of a new ESE protocol thereby eliminating the small although spurious bounce identified above.

SciPost SciPost Phys. 9, 064 (2020)

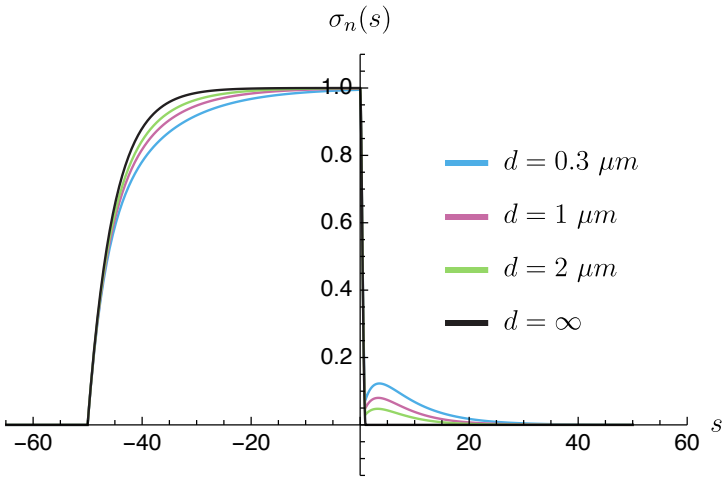

Figure 4: Evolution of the normalized variance $\sigma_n = (\sigma(t) - \sigma_f)/(\sigma_i - \sigma_f)$ of one particle in response to the *symmetric protocol* for different values of the distance d between the particles. The parameters of the ESE protocol (shaped as in Fig. 2) are the following: $t_f = 2\,\text{ms}$, $k_f = K_f/K_i = 1.5$, $K_i = 10^{-6}\,\text{N/m}$, and $\Gamma = 9.42$. Without coupling (when $d = \infty$) the response to the ESE is shortcut to t_f. The hydrodynamic coupling results in a rebound on the variance curve, which no longer reaches its equilibrium value at t_f, but after a few natural relaxation times $\tau_{\text{relax}} \approx 15\,\text{ms}$. As expected from experimental results, the smaller the distance d, the higher the rebound and so the deviation from the 0-coupling case.

5 Coupled ESE protocol

Our strategy to design a *coupled protocol* is now to look for an ESE scheme that would drive the first particle from $(t_i = 0, K_i)$ to (t_f, K_f) while being robust to coupling interaction. A solution to achieve this requirement is to design a protocol that does not depend on the coupling intensity (ie independent of the ϵ parameter). This strong constraint can be met if we require particle independence at all time, that is to say $\langle x_1 x_2 \rangle(t) = 0$ during all the process and not only at equilibrium states. Indeed insofar as we require independence, the results no longer depend on the strength of the coupling.

As detailed in Appendix A.8, the independence requirement ($\sigma_{12} = 0$ during the process) enables us to simplify the evolution equations eq. (11)-(13) and to find an ESE protocol that meets the requirements detailed above: we find a shape for $k_1(s)$ and $k_2(s)$ independent of ϵ that satisfies the equilibrium at t_f of both particles (see Fig. 5). The expression of $k_1(s)$ is therefore the same as in the single particle case, but the second potential has to be driven appropriately with a different stiffness profile $k_2(s)$.

The price to pay to drive the particle 1 from $K_{1,i}$ to $K_{1,f}$ is to enforce a nearly opposite profile on the second potential. In particular the final value of the second well stiffness $K_{2,f}$ is imposed by the parameters chosen for the first particle and is therefore not chosen a priori. Besides, a sum rule ensues, such that $k_1\sigma_{11} + k_2\sigma_{22}$ is conserved. To maintain independence, the two wells tend to evolve in opposition because of the correlation due to the coupling. Indeed the coupling term ϵF_1 in eq. (2) can be interpreted as an extra random noise:

$$\gamma \dot{x_2} = -K_2 x_2 + f_2 + \epsilon F_1\,. \tag{14}$$

This coupling term behaves as the random noises with the following characteristics (at equi-

SciPost SciPost Phys. 9, 064 (2020)

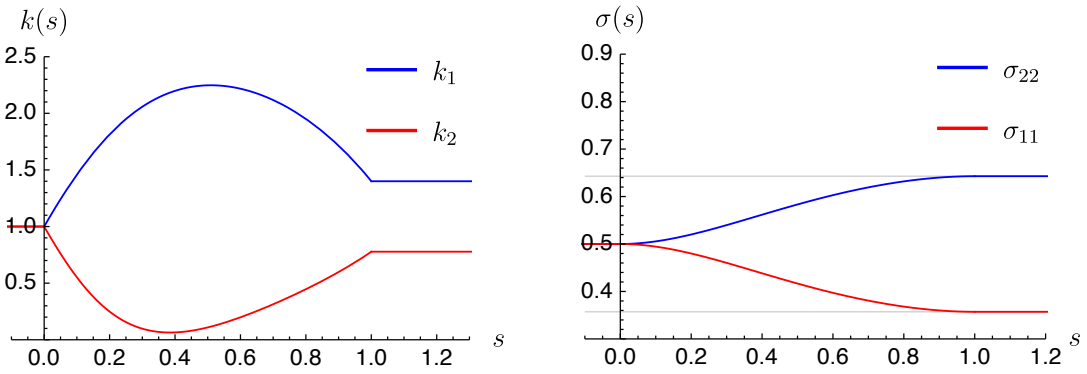

Figure 5: (Left) Profiles $k_1(s)$ and $k_2(s)$ computed for the *coupled ESE protocol* that maintains independence between the particles for parameters: $k_f = 1.4$, $K_i = K_{2,i} = 1.8 \times 10^{-6}\,\mathrm{N/m}$, $t_f = 2.5\,\mathrm{ms}$, and $\Gamma = 4.19$. While k_1 (red) reaches the target value at $s = 1$, the second well stiffness k_2 (blue) has to adapt itself. In particular its final stiffness value is determined by the other parameters of the ESE: $k_{2f} = k_{2i}k_f/(k_{2i}k_f + k_f - k_{2i})$. This protocol does not depend on the coupling constant ϵ and so works for any distance d between the particles. (Right) Result of the computation for the dimensionless variances of the two particles using the ESE protocol on top: σ_{11} in red, and σ_{22} in blue. The plot confirms that Boltzmann equilibrium (horizontal grey lines) is reached for both particles at initial and final times. Let us remind that $\sigma_{12} = 0$ all along.

librium),

$$\langle \epsilon F_1 \rangle = -\epsilon K_1 \langle x_1 \rangle + \epsilon \langle f_1 \rangle = 0\,, \tag{15}$$

$$\langle \epsilon^2 F_1^2 \rangle = \epsilon^2 k_1^2 \langle x_1^2 \rangle + \epsilon^2 \langle f_1^2 \rangle = \epsilon^2 k_B T k_1 + \epsilon^2 \langle f_1^2 \rangle\,. \tag{16}$$

Thus if k_1 increases, the noise imposed to particle 2 by the coupling increases as well, and consequently so does the variance of particle 2. To pretend that the two particles are independent and that this increase in the particle 2 variance is not due to the behaviour of the particle 1, the second well should open up. That is why to maintain a vanishing cross term $\sigma_{12} = 0$ the second well should behave in opposition to the first one (see Fig. 5).

The experimental implementation of the *coupled protocol* is illustrated in Fig. 6. The distance between the particles is set to $d = 0.8\,\mu\mathrm{m}$ to ensure strong coupling. We compare the response of the system to the *symmetric protocol* in which the two potentials are driven similarly, with the response to the *coupled ESE*.

In this new set of experiments, the rebound in response to the *symmetric protocol* is naturally still present, but disappears when applying the *coupled ESE protocol*. This result validates the efficiency of enforcing independence for coupled particles. Indeed this protocol is very stable against the coupling interaction because it does not depend on the strength of the coupling (ϵ in our model). Thanks to this process we achieve the same efficiency of shortcut to equilibrium we had for a single particle, but now for coupled ones. This extension of the validity of ESE protocol has nevertheless a cost: the second particle, coupled to the particle of interest, has to be driven to a final equilibrium state defined by the other parameters of the protocol (K_{2i} and k_f).

SciPost SciPost Phys. 9, 064 (2020)

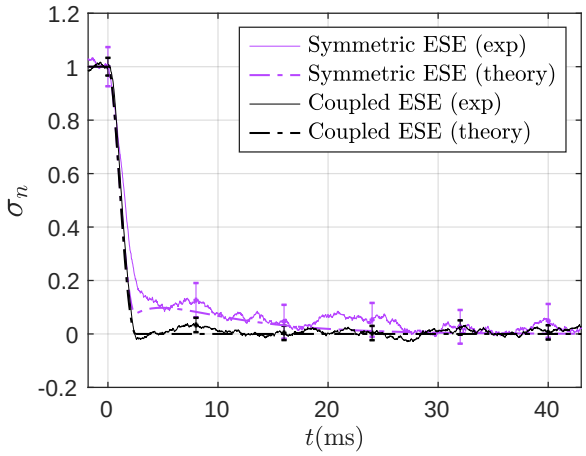

Figure 6: Normalized variance $\sigma_n = (\sigma(t) - \sigma_f)/(\sigma_i - \sigma_f)$ of the first particle when the potentials are driven by the *symmetric protocol* (purple) or by the *coupled ESE protocol* (black). The parameters of the experiment are: $k_f = 1.4$, $K_{1,i} = K_{2,i} = 1.8 \times 10^{-6}$ N/m, $t_f = 2.5$ ms, $d = 0.8\,\mu$m, and thus $\epsilon = 0.49$ and $\Gamma = 4.19$. The *symmetric protocol* leads to the rebound predicted in section 4. On the contrary the *coupled protocol* designed to cancel the correlations between the particles works as expected: the rebound is essentially suppressed and the particle reaches equilibrium at t_f. Furthermore, the experimental results (plain lines) are again consistent with the theoretical predictions (dashed lines) based on measured parameters only and not on adjustable ones.

6 Limits and other approaches

We are experimentally facing two limitations in the implementation of the *Coupled ESE*. First, stiffnesses have to remain positive (ie attractive potentials), and second they cannot exceed maximum values above which the particles can be damaged. Actually it is possible to mimic repulsive potentials and go beyond the first constraint [12], but considering our basic optical tweezers set up, it is far more convenient to stick to positive stiffness. In the case of the *Coupled ESE*, assuming that $k_{2,i} = 1$ and $k_f > 1$, these limitations translate into $k_2 > 0$ and $k_1 < k_{\max}$. Using the expression of $k_2(s)$ and $k_1(s)$ the first limit can be expressed as a constraint on the acceleration factor Γ, or equivalently on t_f and K_i as $\Gamma = \gamma/(K_i t_f)$. Indeed maintaining $k_2 > 0$ requires

$$\Gamma < \Gamma_{\text{lim},1} = \min[-\frac{1}{\dot{\sigma}_{11}(s)}, 0 < s < 1]. \tag{17}$$

$\Gamma_{\text{lim},1}$ depends on k_f (yellow curve in Fig. 7): the more one wants to compress the well, the smaller Γ should be, and so the higher t_f will be.
Concerning the second limit $k_1 < k_{\max}$ a similar computation gives us the corresponding constraint on Γ. We introduce:

$$\Gamma_{\text{lim}}(s) = \frac{((k_f-1)s^2(2s-3)-1)(k_{max}-1+(k_f-1)s^2(2s-3))}{3(k_f-1)s(s-1)}, \tag{18}$$

Then,

$$\Gamma_{\text{lim},2} = \min[\Gamma_{\text{lim}}(s), 0 < s < 1]. \tag{19}$$

SciPost SciPost Phys. 9, 064 (2020)

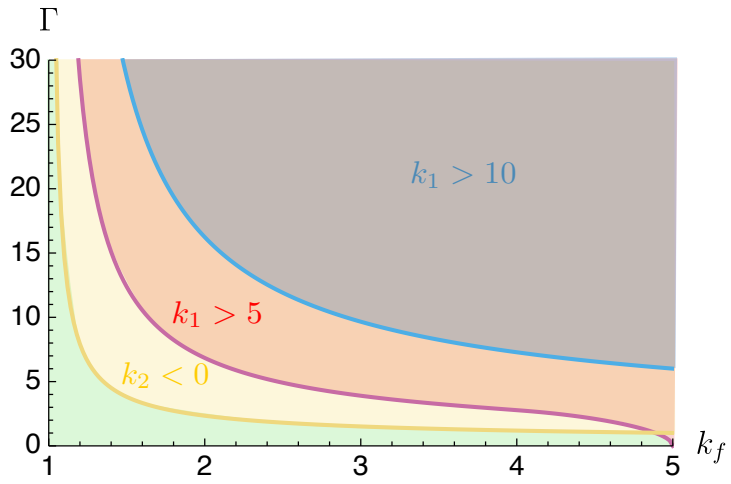

Figure 7: Experimental limits of the *coupled ESE protocol* in terms of the speed-up parameter Γ for a compression of the first particle ($k_f > 1$). The yellow line represents the higher limit Γ should not exceed to maintain $k_2 > 0$, the red one to maintain $k_1 < 5$ and the blue one to maintain $k_1 < 10$. The requirement $k_2 > 0$ being the most restrictive, the limit to respect during experiments is the yellow line that corresponds to $\Gamma_{lim,1}$. In other words, the working region where all the constraints are met is the green region. The yellow, red and blue regions delineate the domains where the respective requirements are not met anymore.

To summarize, we plot in the Fig. 7 the maximum boundary Γ_{lim} to comply with the constraints $k_2 > 0$ (yellow curve) and $k_1 < k_{\text{max}}$ for $k_{\text{max}} = 5$ (red curve) and $k_{\text{max}} = 10$ (blue curve). As expected, the stronger is the compression, the smaller is the region accessible for Γ, because it has to remain under Γ_{lim}. The limit $k_2 > 0$ is the most restrictive, and that is why $\Gamma_{\text{lim},1}$ in yellow delimits the working region. To provide shortcuts outside the accessible region, some new strategies should be developed such as what has been done in ref. [13] for the *basic ESE*.

Enforcing independence through the *coupled ESE protocol* is a successful strategy to extend the family of ESE protocols to more complex systems which cannot be managed with full efficiency by the *basic ESE*. Within the limits we highlighted above, this particular solution independent of ϵ turns out to be very powerful. Yet, the solution panel to the coupled case problem is wide, and there is more to find in this direction. In particular, it is possible to guide the two particles with the same stiffness profile to a chosen target state. This *symmetric coupled ESE protocol* detailed in Appendix A.9 has nevertheless a cost: cross-correlations appear during the process and vanish only at equilibrium. Therefore, the independency is no longer required in this protocol, which makes it depend on the coupling intensity. That is why this ϵ dependent protocol is harder to implement experimentally. Further work is required to extend ESE protocols to more complex systems, and every solution will have specific advantages and limits.

7 Conclusion

In conclusion, we explored shortcut to adiabadicity schemes for coupled systems: in particular two hydro-dynamically coupled particles. The first objective of this paper was to test the

SciPost SciPost Phys. 9, 064 (2020)

stability of the *basic ESE protocol* designed for single systems against the coupling interaction. Our experiments, in very good accordance with the model, proved its relative robustness: the coupling perturbation deviates the response of a dozen of percents compared to the 0-coupling case. It is nevertheless possible to work out explicitly ESE solutions that take due account of the coupling, and are therefore immune to it: this is the second message of this article. The model used to describe the coupling proved reliable enough to build a new family of ESE solutions with the same method of retro-computing used to find the single particle ESE protocol. We thus propose a very robust protocol, because ϵ independent, that enforces independence between the particles. Experimental tests confirm the efficiency of this shortcut strategy within the experimental limits described in the last part of the paper. Other solutions can be investigated such as a symmetric protocol designed for coupled particles (more difficult to implement because ϵ dependent).

Acknowledgements

We thank Loïc Rondin for interesting discussions.

Funding information This work has been financially supported by the Agence Nationale de la Recherche through grant ANR-18-CE30-0013.

Supporting material Experimental datasets and codes are publicly available on doi:10.5281/zenodo.4242922.

A Appendix

A.1 Calibration procedure

As the effect under scrutiny is tiny, a very accurate calibration is necessary to observe it. Thus we detail in this section the calibration procedure conducted before the experimental tests of ESE protocols. It is performed as follows: first we have to find the connection between the amplitude A of the sine wave driving the AOD and the stiffness K applied by the optical trap to the particle. To do so, we acquire the position variance ($\sigma^2 = k_B T/K$) for different amplitudes A. This calibration curve enables us to convert the ESE protocol in driving amplitude for the AOD. Then, the only dependence on external parameters of the ESE protocol lies in the parameter $\Gamma = \gamma/(K_i t_f)$. To estimate Γ we conduct the acquisition of the cut off frequency [14] ($f_0 = K/(2\pi\gamma)$) when the particle is in the initial state of the ESE, $f_{0,i}$, through the particle's Brownian noise spectrum in position corresponding to the initial value of amplitude A_i. Then we deduce $\Gamma = 1/(2\pi f_{0,i} t_f)$.

One may now wonder to what extent small drifts in calibration may impact the experimental results. Indeed during the typical time of our experiments (up to a few hours), we observe that the stiffness K and the parameter Γ decrease by a small amount: 4% at most. The stiffness variation can be a consequence of the variation of the AOD efficiency because the AOD warms up with time. On the other side, Γ is modified because of the following phenomena: the stiffness variation, the water viscosity dependency on the temperature, and the damping coefficient correction due to the distance h to the cell walls. Indeed at first order in r/h we can expand [15] $\gamma(T,h) = 6\pi r \eta_0(T) \times (1 + 9/16 \times r/h)$, with $\eta_0(T)$ decreasing of 2% per Kelvin, and the term in r/h leading to an additional 1% per 5 μm in h.

SciPost SciPost Phys. 9, 064 (2020)

Those variation in K and Γ are small, leading to a small error on the ESE protocols themselves. Moreover, our cycle procedure of acquisition makes the comparison of protocols in equivalent experimental conditions. Drifts in Γ have the same consequences on the different responses we compare: the relative differences between the curves are only weakly sensitive to variations in Γ. Finally, drifts in K_i, K_f (thus σ_i, σ_f) are wiped out by plotting the normalised variance.

Furthermore, the local drift of the bath temperature due to the power of the lasers (measuring laser and trapping laser), amplifies the deviation of the particle variance also affected by the stiffness drift. Indeed the standard deviation σ can increase up to 2% during an acquisition. As we are studying σ jumps of 20% with ESE, it is better to get rid of the 2% error due to external parameters small deviations. To do so, we normalize the results at regular time intervals to minimize the drift effect in the results.

A.2 Complementary experimental results

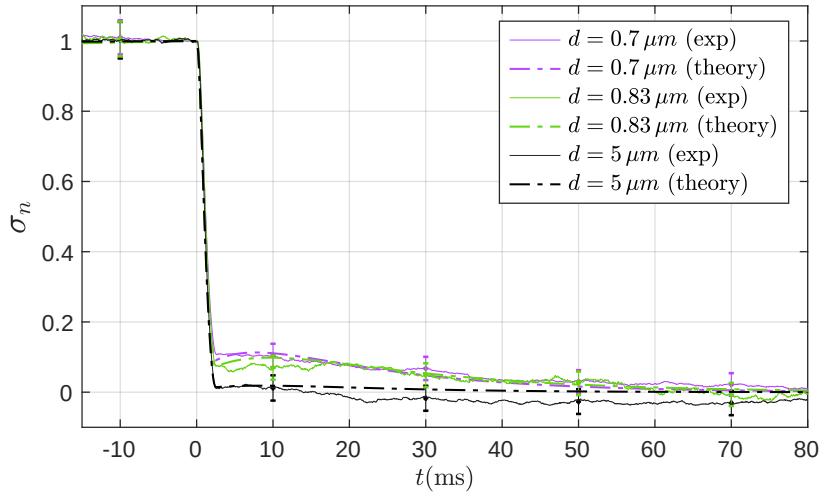

Figure 8: Same as Fig. 2 but with three distances: $d = 5\,\mu$m in black, $d = 0.83\,\mu$m in green and $d = 0.7\,\mu$m in purple.

As a complement to the results presented in Fig. 2, we propose another experimental result in Fig. 8. All the parameters are the same as in Fig. 2 but the experiment is performed with 3 different distances between the particles. From it, we can affirm first that the results are very reproducible and always consistent with the theory, and second that the rebound decreases with the coupling as pointed out in Fig. 4.

A.3 Over-damped regime

The influence of the inertia lasts on a characteristic time $\tau_{\text{inertia}} = m/\gamma = 2\mu r^2/(9\eta)$, with μ being the volumic mass of the particles. As we consider usual fluids such as water, $\eta = 10^{-3}$ Pa s, and $\mu = 10^3\,\text{kg}\,\text{m}^{-3}$. The point is then to compare τ_{inertia} with the time needed for the particle to diffuse over a distance equivalent to its diameter, τ_{diff}. In a usual diffusion process we have, $\tau_{\text{diff}} = (2r)^2/D$, using the diffusion coefficient $D = k_B T/(6\pi\eta r)$. Therefore, on the one hand, the r region where $\tau_{\text{inertia}} \ll \tau_{\text{diff}}$ corresponds to $r \gg 0.01$ pm.

On the other hand, to get an upper limit, we compare τ_{inertia} to the characteristic time of the experiment $\tau_{ESE} = 1$ ms. Indeed in the context of shortcuts, the time of the ESE is more restric-

SciPost SciPost Phys. 9, 064 (2020)

tive than the natural relaxation time $\tau_{\text{relax}} = \gamma/K \sim 15\,\text{ms}$. The assumption $\tau_{\text{inertia}} \ll \tau_{ESE}$ remains valid while $r \ll 70\,\mu\text{m}$. To conclude, the r region of the over-damped regime is $0.01\,\text{pm} \ll r \ll 70\,\mu\text{m}$.

We are thus working in the r region where the inertia faded too fast as compared to the other phenomena to be noticed (indeed for $r = 1\,\mu\text{m}$, $\tau_{\text{inertia}} \sim 0.2\,\mu\text{s}$ and $\tau_{\text{diff}} \sim 20\,\text{s}$): the regime is over-damped.

A.4 Model for Hydrodynamic coupling

The hydrodynamic interactions of the particles with the surrounding fluid are described by their mobility matrix $\mathcal{H}$ (eq. (4)), which is also known as the Rotne-Prager diffusion tensor [7–9]. The Rotne-Prager diffusion tensor consists in adding third order correction in $(r/d)^3$ to the off-diagonal elements of the Oseen tensor. Under our experimental conditions, this corrections is always smaller than 3.5%. The form of the coupling parameter ϵ depends on different approximations. Here we assume ϵ to be constant: it involves only the distance between the wells d and not the distance between the particles $(x_1 - x_2)(t)$. This assumption is supported by the following order of magnitudes: one particle can diffuse up to its rms displacement $\delta x_{\text{rms}} = \sqrt{k_B T/k} \sim 60\,\text{nm} \ll d$, so that in first approximation $|x_1 - x_2| = d$ and $\epsilon = f(d)$. The expression of $\epsilon = f(d)$ is given by the Rotne-Prager approximation: for particle distances larger than $d = r$, we can write $\epsilon = \frac{3}{2}\nu - \nu^3$, where $\nu = \frac{r}{d}$. The term ν becomes more important when particles are close to each other. At very short distances, when $d \lesssim r/10$, lubrication forces would have to be taken into account explicitly. On the contrary, in the small ν limit, we reach the Oseen approximation where $\epsilon = \frac{3}{2}\nu$.

A.5 Auto and Cross-Correlation

We start from the coupled Langevin equations (2):

$$\gamma \dot{x_1} = -K_1 x_1 - \epsilon K_2 x_2 + f_1 + \epsilon f_2\,, \tag{20}$$
$$\gamma \dot{x_2} = -K_2 x_2 - \epsilon K_1 x_1 + f_2 + \epsilon f_1\,, \tag{21}$$

and we use the Laplace Transform:

$$\widehat{x}(s) = \int_0^{+\infty} x(t) e^{-st} dt\,. \tag{22}$$

After having Laplace transformed the system (20), (21) we obtain (to simplify we stop indicating variables s and t, $\widehat{x}$ transformed functions implies s variable, and x functions t):

$$\gamma(s\widehat{x_1} - x_1(0)) = -k_1\widehat{x_1} - \epsilon k_2\widehat{x_2} + \widehat{f_1} + \epsilon\widehat{f_2}\,, \tag{23}$$
$$\gamma(s\widehat{x_2} - x_2(0)) = -k_2\widehat{x_2} - \epsilon k_1\widehat{x_1} + \widehat{f_2} + \epsilon\widehat{f_1}\,. \tag{24}$$

We then multiply the two above equations by $x_2(0)$ and take the mean value:

$$\gamma(s\langle\widehat{x_1}x_2(0)\rangle - \sigma_{12}^2) = -k_1\langle\widehat{x_1}x_2(0)\rangle - \epsilon k_2\langle\widehat{x_2}x_2(0)\rangle\,,$$
$$\gamma(s\langle\widehat{x_2}x_2(0)\rangle - \sigma_{22}^2) = -k_2\langle\widehat{x_2}x_2(0)\rangle - \epsilon k_1\langle\widehat{x_1}x_2(0)\rangle\,.$$

This system is now easy to solve (knowing the values of σ_{22} and σ_{12} at equilibrium at $t = 0$). The last step only consists in taking the Inverse Laplace Transform of the expressions obtained, that leads to the expression of $\langle x_1(t)x_2(0)\rangle$ and $\langle x_2(t)x_2(0)\rangle$ of eqs. (7) and (6). We can reproduce the procedure by multiplying this time by $x_1(0)$ to obtain the expression of $\langle x_1(t)x_1(0)\rangle$ of eq. (5).

SciPost SciPost Phys. 9, 064 (2020)

A.6 Evolution of the moments

To meet the Boltzmann equilibrium prediction the random noises f_j in eq. (2) and in eqs. (20)-(21) should verify:

$$\langle f_1(0)f_1(t)\rangle = 2k_BT\gamma\frac{1}{1-\epsilon^2}\delta(t) = \langle f_2(0)f_2(t)\rangle\,, \tag{25}$$

$$\langle f_1(0)f_2(t)\rangle = -2k_BT\gamma\frac{\epsilon}{1-\epsilon^2}\delta(t)\,. \tag{26}$$

Then, starting with the coupled Langevin equation (2), we want to deduce the evolution of the moments of the joint probability in position. To do so we follow the Ito prescription ($\langle f_1(t)x_1(t)\rangle = 0$) and apply the Ito chain rule on $x_1^2(t)$. Combined with equation (2), and after taking the mean value, we obtain:

$$\gamma\langle x_1\frac{dx_1}{dt}\rangle = -K_1\langle x_1^2\rangle - \epsilon K_2\langle x_1x_2\rangle + \epsilon^2\langle f_2^2\rangle + \langle f_1^2\rangle + 2\epsilon\langle f_1f_2\rangle\,. \tag{27}$$

Using the auto-correlation values of the f_j's in (25) and (26), we readily obtain:

$$\frac{\gamma}{2}\frac{d\langle x_1^2\rangle}{dt} = -K_1\langle x_1^2\rangle - \epsilon K_2\langle x_1x_2\rangle + kT\,. \tag{28}$$

Finally we reproduce the procedure for the other moments and using again dimensionless quantities ($\sigma_{jk} = \langle x_jx_k\rangle\frac{K_{1,i}}{2k_BT}$) we obtain the system to describe the dynamics of the moments given above in eqs. (11), (12) and (13).

A.7 Gaussian behaviour of the coupled particles joint probability distribution

Similarly to the single particle case, we can describe the system through the evolution of its probability density to find the first particle in x_1 and the second in x_2 at time t, $P(x_1,x_2,t)$. The time evolution of the joint Probability $P(x_1,x_2,t)$ is governed by the Fokker-Planck equation:

$$\frac{\partial P}{\partial t} = -\sum_{j=1}^{j=2}\frac{\partial g_jP}{\partial x_j} - \sum_{j,k=1}^{j,k=2}\theta_{jk}\frac{\partial^2 P}{\partial x_j\partial x_k}\,, \tag{29}$$

where,

$$g_1 = -\frac{1}{\gamma}K_1x_1 - \frac{\epsilon}{\gamma}K_2x_2\,, \tag{30}$$

$$g_2 = -\frac{1}{\gamma}K_2x_2 - \frac{\epsilon}{\gamma}K_1x_1\,, \tag{31}$$

$$\theta_{jj} = \frac{k_BT}{\gamma}\,, \tag{32}$$

$$\theta_{jk} = \frac{k_BT\epsilon}{\gamma}\text{ for } j\neq k\,. \tag{33}$$

In order to prove the Gaussian behaviour of the joint Probability, we propose a 2D generalisation of the computation made in ref. [16]. We introduce the 2D Fourier Transform:

$$G(p_1,p_2,t) = \int\!\!\int_{-\infty}^{+\infty} e^{ip_1x_1}e^{ip_2x_2}P(x_1,x_2,t)dx_1dx_2\,. \tag{34}$$

SciPost SciPost Phys. 9, 064 (2020)

We apply this Fourier Transform to Fokker-Plank eq. (29)

$$\frac{\partial G}{\partial t} = -\frac{K_1(p_1+\epsilon p_2)}{\gamma}\frac{\partial G}{\partial p_1} - \frac{K_2(p_2+\epsilon p_1)}{\gamma}\frac{\partial G}{\partial p_2} - \frac{k_B T}{\gamma} G[(p_1^2+p_2^2)+\epsilon p_1 p_2], \tag{35}$$

$$\frac{\partial \ln G}{\partial t} = -\frac{K_1(p_1+\epsilon p_2)}{\gamma}\frac{\partial \ln G}{\partial p_1} - \frac{K_2(p_2+\epsilon p_1)}{\gamma}\frac{\partial \ln G}{\partial p_2} - \frac{k_B T}{\gamma}[(p_1^2+p_2^2)-2\epsilon p_1 p_2]. \tag{36}$$

On the one hand, the expansion of G generates the moments $\mu_{n,m} = \langle x_1^n x_2^m \rangle$, since $G(p_1,p_2,t) = \sum_{n,m=0}^{+\infty} (ip_1)^n (ip_2)^m \mu_{n,m}(t)/n!m!$. On the other hand the expansion of $\ln(G)$ generates the cumulants $\chi_{n,m}(t)$:

$$\ln G(p_1,p_2,t) = \sum_{n,m=1}^{+\infty} \frac{(ip_1)^n (ip_2)^m}{n!m!} \chi_{n,m}(t). \tag{37}$$

In particular, the two first cumulants in n are the mean and the variance of the first particle position: $\chi_{1,0} = \mu_{1,0} = \langle x_1 \rangle = 0$ and $\chi_{2,0} = \mu_{2,0} - \mu_{1,0}^2 = \langle x_1^2 \rangle - \langle x_1 \rangle^2 = \langle x_1^2 \rangle$. Thus we identify the power of p_1 and p_2 in eq. (36) and we deduce:

$$\begin{aligned}\gamma \dot{\chi}_{nm} = &-(nK_1 + mK_2)\chi_{nm} - \epsilon(mK_1\chi_{n+1,m-1} + nK_2\chi_{n-1,m+1}) \\ &+ 2k_B T(\delta_{n,2}\delta_{m,0} + \delta_{m,2}\delta_{n,0} + \epsilon\delta_{m,1}\delta_{n,1}).\end{aligned} \tag{38}$$

For $(n,m) = (2,0)$ (that corresponds to σ_{11}), $(n,m) = (0,2)$ (σ_{22}), and $(n,m) = (1,1)$ (σ_{12}), we recover the evolution equations eq. (11)-(13). But in addition, eq. (38) for $(n+m) > 2$ entails that an initially Gaussian distribution remains Gaussian at all times. Indeed it can be easily deduced that if $\chi_{n,m}(0) = 0$ for all $(n+m) > 2$ in the equilibrium state, we have $\chi_{n,m}(t) = 0$ for all time for all $(n+m) > 2$.

A.8 Coupled ESE enforcing independence

Requiring particle independence at all times consists in demanding $\sigma_{12} = 0$. The evolution eqs. (11)-(13) can then be simplified into:

$$\Gamma \frac{d\sigma_{11}}{ds} = -2k_1\sigma_{11} + 1, \tag{39}$$

$$\Gamma \frac{d\sigma_{22}}{ds} = -2k_2\sigma_{22} + 1, \tag{40}$$

$$1 = k_2\sigma_{22} + k_1\sigma_{11}. \tag{41}$$

We straightforwardly deduce how the second particle variance is linked to the first and how the two stiffness profiles are related,

$$\sigma_{22}(s) = -\sigma_{11}(s) + \frac{1}{2} + \frac{1}{k_{2i}}, \tag{42}$$

$$k_2(s) = \frac{2k_{2i}(1-k_1(s)\sigma_{11}(s))}{k_{2i} - 2k_{2i}\sigma_{11}(s) + 2}. \tag{43}$$

Moreover, we observe that eq. (39) that describes the σ_{11} evolution is the same as in the single particle case. Thus if the same ESE profile is imposed on $k_1(s)$, the equilibrium requirements on the 1st particle will be met. The corresponding $k_2(s)$ can be deduced from eq. (43). We finally obtain for the coupled particles ESE protocol:

$$k_1(s) = 1 + (k_{1f}-1)(3-2s)s^2 - \frac{3\Gamma(k_{1f}-1)(s-1)s}{1+(k_{1f}-1)(3-2s)s^2}, \tag{44}$$

$$\begin{aligned}k_2(s) = &\, 1 + (k_{1f}-1)(3-2s)s^2 \\ &+ \frac{3\Gamma(k_{1f}-1)(s-1)s}{1+(k_{1f}-1)(3-2s)s^2}\,\frac{k_{2i}}{1+(1+k_{2i})(k_{1f}-1)(3-2s)s^2}.\end{aligned} \tag{45}$$

SciPost SciPost Phys. 9, 064 (2020)

A.9 Symmetric coupled ESE solution

We explored a new family of ESE solutions adapted to the coupled system by proposing the *coupled ESE* that enforces independence between the particles. But it was at the expense of having the evolution of particle 2 enslaved to that of particle 1, and thereby not a priori controlled. This results in the fact that the two particles cannot be treated symmetrically. It is thus interesting to look for another solution to the coupled problem: an ESE protocol that jointly drives the two potentials and treats the two particles in a symmetric fashion. Contrary to the *coupled ESE*, such a protocol will introduce cross-correlations between particles.
Now that we require for all time $K_1(t) = K_2(t) = K(t)$ (and so $\sigma_{11}(t) = \sigma_{22}(t)$), two modes arise from evolution equations, $u = \sigma_{11} + \sigma_{12}$ and $v = \sigma_{11} - \sigma_{12}$ that satisfy the following decoupled system:

$$\Gamma \frac{du}{ds} = -2k(s)(1+\epsilon)u(s) + (1+\epsilon), \tag{46}$$

$$\Gamma \frac{dv}{ds} = -2k(s)(1-\epsilon)v(s) + (1-\epsilon). \tag{47}$$

The modes evolve following the same form of equation with 2 different time scales $\tau_u < \tau_v$ that correspond to the τ_- and τ_+ appearing into the correlation functions for the symmetric case. Indeed one may notice that $u = \sigma_{11} + \sigma_{12} = 2\langle x_M^2 \rangle$ and $v = \sigma_{11} - \sigma_{12} = 2\langle x_\mu^2 \rangle$. We naturally recover the modes corresponding to the barycentre and the particles separation evolution, with the barycentre moving faster because it does not require displacement of the fluid between the particles to do so.
The strategy to outline an ESE protocol from eqs. (46)-(47) is the following: first we propose a fifth order polynomial form of $v(s)$ with one degree of freedom (called parameter p) satisfying initial and final conditions of equilibrium. Secondly, we find the expression of $u(s)$ as a function of $v(s,p)$:

$$u(s) = \frac{1}{I(s)} \left(1 + \frac{2(1+\epsilon)}{\Gamma}\right) \int_0^s I(y)dy, \tag{48}$$

with

$$I(y) = \exp\left\{\frac{2(1+\epsilon)}{\Gamma} \int_0^y k(x)dx\right\} = \exp\left\{\frac{1+\epsilon}{1-\epsilon} \int_0^y \frac{(1-\dot{v}(x))}{v(x)}dx\right\}. \tag{49}$$

Finally, we tune the parameter p of the ansatz of $v(s)$ to satisfy boundary conditions for $u(s)$ from eq. (48). A simple procedure of dichotomy that iterates on the value of the p parameter does the job. Knowing the expression of $u(s)$ and $v(s)$, the stiffness profile can be easily deduced from eq. (46).
Fig. 9 plots an example of *symmetric coupled ESE protocol* obtained with this procedure. It is important to point out that this protocol which guides jointly the two particles of a coupled system depends on the coupling intensity (ϵ). This property makes it hard to implement experimentally.

SciPost SciPost Phys. 9, 064 (2020)

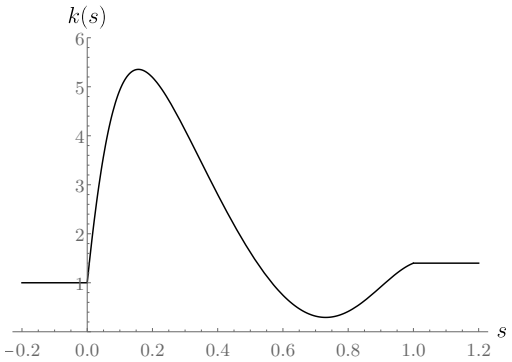

Figure 9: Stiffness profile for the symmetric coupled ESE treating particles distant by $d = 0.7\,\mu$m (coupling constant $\epsilon = 0.5$). Both potentials are controlled by the same protocol which is meant to drive the particles from K_i to $K_f = k_f \times K_i$ in the desired time t_f. The parameters of the ESE plotted here are: $t_f = 3$ ms, $K_i = 2.5 \times 10^{-6}$ N/m, $k_f = 1.4$ and $\Gamma = 2.5$

References

[1] D. S. Lobser, A. E. S. Barentine, E. A. Cornell and H. J. Lewandowski, *Observation of a persistent non-equilibrium state in cold atoms*, Nat. Phys. **11**, 1009 (2015), doi:10.1038/nphys3491.

[2] D. Guéry-Odelin and E. Trizac, *Boltzmann avenged*, Nat. Phys. **11**, 988 (2015), doi:10.1038/nphys3522.

[3] D. Guéry-Odelin, J. G. Muga, M. J. Ruiz-Montero and E. Trizac, *Nonequilibrium solutions of the Boltzmann equation under the action of an external force*, Phys. Rev. Lett. **112**, 180602 (2014), doi:10.1103/PhysRevLett.112.180602.

[4] D. Guéry-Odelin, A. Ruschhaupt, A. Kiely, E. Torrontegui, S. Martínez-Garaot and J. G. Muga, *Shortcuts to adiabaticity: Concepts, methods, and applications*, Rev. Mod. Phys. **91**, 045001 (2019), doi:10.1103/RevModPhys.91.045001.

[5] G. Li, H. T. Quan and Z. C. Tu, *Shortcuts to isothermality and nonequilibrium work relations*, Phys. Rev. E **96**, 012144 (2017), doi:10.1103/PhysRevE.96.012144.

[6] I. A. Martínez, A. Petrosyan, D. Guéry-Odelin, E. Trizac and S. Ciliberto, *Engineered swift equilibration of a Brownian particle*, Nat. Phys. **12**, 843 (2016), doi:10.1038/nphys3758.

[7] A. Bérut, A. Petrosyan and S. Ciliberto, *Energy flow between two hydrodynamically coupled particles kept at different effective temperatures*, Europhys. Lett. **107**, 60004 (2014), doi:10.1209/0295-5075/107/60004.

[8] A. Bérut, A. Imparato, A. Petrosyan and S. Ciliberto, *Theoretical description of effective heat transfer between two viscously coupled beads*, Phys. Rev. E **94**, 052148 (2016), doi:10.1103/PhysRevE.94.052148.

[9] J.-C. Meiners and S. R. Quake, *Direct measurement of hydrodynamic cross correlations between two particles in an external potential*, Phys. Rev. Lett. **82**, 2211 (1999), doi:10.1103/PhysRevLett.82.2211.

[10] S. E. M.Doi and S. F. Edwards, *The theory of polymer dynamics*, International Series of Monographs on Physics, Clarendon Press (1988).

[11] S. Herrera-Velarde, E. C. Euán-Díaz, F. Córdoba-Valdés and R. Castañeda-Priego, *Hydrodynamic correlations in three-particle colloidal systems in harmonic traps*, J. Phys.: Condens. Matter **25**, 325102 (2013), doi:10.1088/0953-8984/25/32/325102.

[12] J. A. C. Albay, P.-Y. Lai and Y. Jun, *Realization of finite-rate isothermal compression and expansion using optical feedback trap*, Appl. Phys. Lett. **116**, 103706 (2020), doi:10.1063/1.5143602.

[13] M. Chupeau, B. Besga, D. Guéry-Odelin, E. Trizac, A. Petrosyan and S. Ciliberto, *Thermal bath engineering for swift equilibration*, Phys. Rev. E **98**, 010104 (2018), doi:10.1103/PhysRevE.98.010104.

[14] A. Bérut, *Fluctuations and interactions of Brownian particles in multiple optical traps*, PhD Thesis, Ecole Normale Supérieure de Lyon - ENS LYON, (2015) https://tel.archives-ouvertes.fr/tel-01192759.

[15] J. Leach, H. Mushfique, S. Keen, R. Di Leonardo, G. Ruocco, J. M. Cooper and M. J. Padgett, *Comparison of Faxén's correction for a microsphere translating or rotating near a surface*, Phys. Rev. E **79**, 026301 (2009), doi:10.1103/PhysRevE.79.026301.

[16] C. A. Plata, D. Guéry-Odelin, E. Trizac and A. Prados, *Finite-time adiabatic processes: Derivation and speed limit*, Phys. Rev. E **101**, 032129 (2020), doi:10.1103/PhysRevE.101.032129.

Appendix B:

Experimental set-ups for ESE protocols on over-damped particles

The single particle ESE efficiency was experimentally demonstrated in Ref. 2, and we are able to reproduce these results using the set-up 1 of Fig. B.1. To test the ESE designed for coupled systems, set-up 1 has to be improved to create not only one but two harmonic traps that can be controlled independently. That is why we built set-up 2, successfully used in Ref. 1 to investigate the robustness of single particle ESE to coupling perturbation, and to validate our new families of ESE for coupled systems.

Set-up 1 and set-up 2 are sketched in Fig. B.1 and respectively create one or two tunable traps using optical tweezers. In set-up 1, the single trap is realized using a near-infrared single mode DPSS laser (Laser Quantum, $\lambda = 1064\,\mathrm{nm}$ used at power of 1W) expanded through a magnifying telescope and injected through an oil-immersed objective (Leica, 63× NA 1.40) into the fluid chamber. In the cell of miliQ water (to avoid trapping impurities) are immersed silica beads of radius $r = 1\,\mu\mathrm{m}$. The beads are trapped at $20\,\mu\mathrm{m}$ from the bottom plate of the cell thanks to the focusing lens L_1. We use a very small concentration of colloids in water and a specific design of the cell containing the particles in order to have very few beads in the measuring volume. This enables us to take long measurements without any spurious perturbation. Two Acousto-Optic Defectors (AOD X and AOD Y on Fig. B.1) controls the intensity and the 2D position of the trapping beam with the amplitude and frequency of the control signal, respectively. Let us point out that each AOD changes the polarisation (highlighted in red and green on the diagram) so that they compensates each other. We therefore create an harmonic potential whose center and stiffness are controlled respectively by the frequency and amplitude of the AODs' input signals.

Set-up 2 allows us to create two perfectly uncoupled traps separated by a tunable distance. To do so we split the initial beam in two and use a half-wave plate to change the polarisation of the second beam. Then we use two AODs (one for each

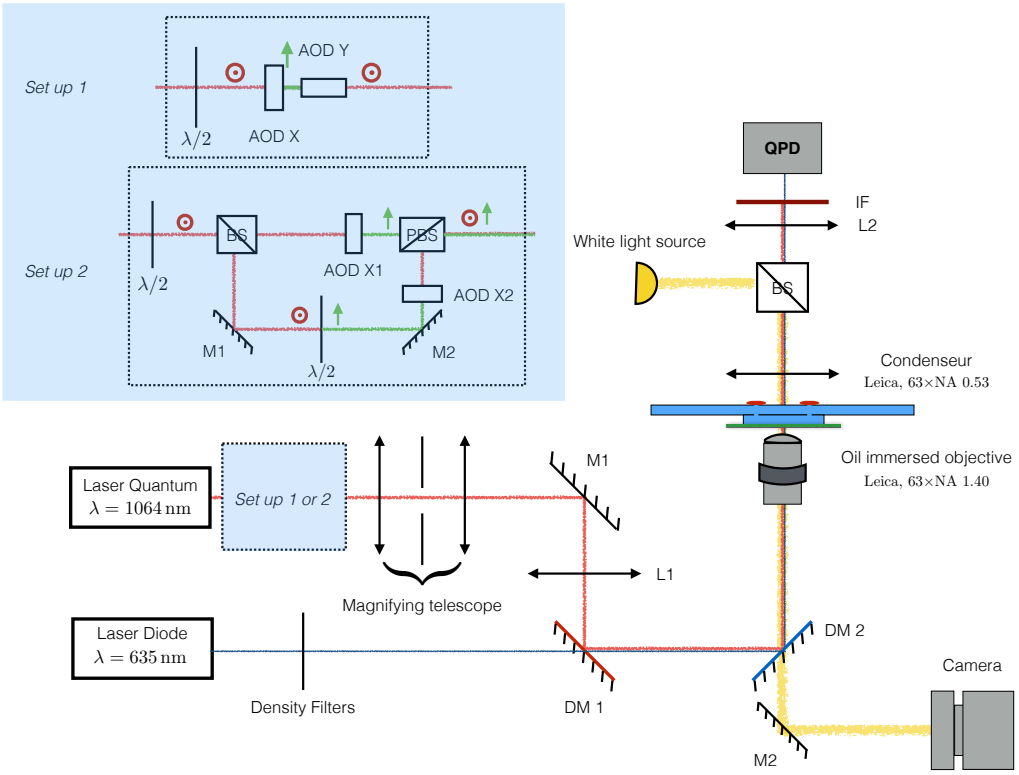

Figure B.1 – **Optical tweezers** Set-up 1 and set-up 2 are designed to create respectively one or two tunable harmonic potentials to trap silica micro-beads.

traps) to control the intensity and position of the two orthogonally polarized beams, recombined afterwards in the polarizing beam splitter without risk of interferences. The two superposed laser beams then follow the same path as for set-up 1 (through mirror M1, lens L1, dichroic mirrors DM1 and DM2 and the oil immersed objective) and create two harmonic traps whose stiffnesses and respective position on the x axis are fully tunable using the AODs input signals.

The detection of the particle position (only one can be measured in our set-up) is performed using a fiber coupled single mode laser (Thorlabs, $\lambda = 635\,\text{nm}$, power 1mW lowered to $100\,\mu\text{W}$ with a neutral density filter) which is collimated after the fiber and sent through the trapping objective through dichroic mirrors (DM 1 and DM 2). The forward -scattered detection beam is collected by a condenser (Leica, NA 0.53), and its back focal-place field distribution projected (with lens L2) onto a four quadrant detector (QPD from First Sensor with a bandpass of 1 MHz with custom made electronic) which gives a signal proportional to the particle position. The trapping infrared beam is filtred (IF) to ensure that only the detection beam can reach the QPD.

Besides we add a camera enlighten by a white light source, that helps positioning the cell to trap the beads. The camera could be used to detect the particles positions and allows to measure both positions, but it is much less accurate and slower than the detection laser method detailed above.

Appendix C:

Supplementary Material - Information and thermodynamics: fast and precise approach to Landauer's bound in an underdamped micromechanical oscillator

We attach in this section the Supplementary Material of our article in Ref. 3.

Supplemental material - Information and thermodynamics: fast and precise approach to Landauer's bound in an underdamped micro-mechanical oscillator

Salambô Dago, Jorge Pereda, Nicolas Barros, Sergio Ciliberto, and Ludovic Bellon*
Univ Lyon, ENS de Lyon, Univ Claude Bernard Lyon 1, CNRS, Laboratoire de Physique, F-69342 Lyon, France

FEEDBACK AND DOUBLE WELL POTENTIAL

To create the virtual double well potential energy $U(z, z_0, z_1)$, we use a feedback loop as sketched in Fig. 1 of the letter, which must meet two criteria: no hysteresis (z_0 is independent of z), and negligible delay $\tau_{\rm FB}$. The latter necessitates a loop response time much shorter than the natural response time of the system. This is achieved with a high-speed comparator ($\tau_{\rm FB} \sim 10\,$ns) and a slow cantilever (natural free oscillation period $f_0^{-1} \sim 0.8\,$ms). Implementing a comparator without any hysteresis is less straightforward, since we must prevent the detection noise of the system from causing the comparator to switch back-and-forth when the cantilever is near the threshold. Indeed, this fast switching could result in a mean voltage V actually stabilizing the cantilever around z_0 ! We solve this issue by implementing a temporal lock-up that prevents the comparator from switching back for $f_0^{-1}/4$: if the oscillator crosses the threshold, it will evolve in the new well for at least a quarter of its natural period. Consequently, the oscillator has time to reach the well center, far enough from z_0 that detection noise cannot cause subsequent switching. By the time the dynamics brings the cantilever back to the threshold, the comparator will be functional again.

The distance between the wells $2z_1$ is driven by the voltage V_1. When $V_1 \gg V_0$ we can consider that the electrostatic force F, and as a consequence z_1, is proportional to V_1. To confirm this linear behavior, we plot in Fig. S1 the half distance between the wells z_1 returned by the fit of the static distribution function of positions $P(z, z_0, z_1) \propto e^{-U(z,z_0,z_1)}$, as a function of the voltage V_1. The expected linearity is checked, and z_1 can be precisely set during the experiments.

One may wonder whether the feedback loop perturbs the system and impacts its exchange with the thermal bath, and therefore its kinetic energy $E_k = \frac{1}{2}\dot{z}^2/\omega_0^2$. Figure S2 aims at showing that the system behaves as in a real potential, whatever the strength of the feedback. A good indicator that this is the case is whether $\langle E_k \rangle$ remains equal to 1/2 according to the energy equipartition. The experimental results confirm that the velocity distribution remains gaussian and that $\langle E_k \rangle = 1/2$ for any z_1.

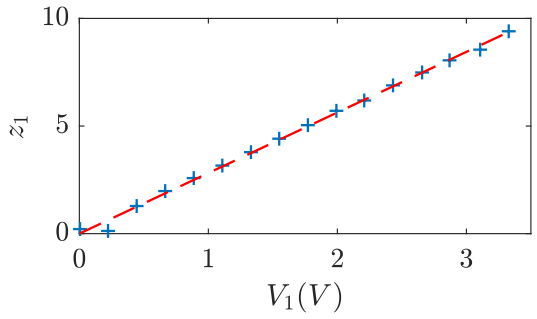

FIG. S1. Half distance between the wells z_1 returned by the fit of the static probability density function of the cantilever, as a function of the adjustable voltage V_1. The linear fit (dashed red) is in good agreement with the experimental points (blue).

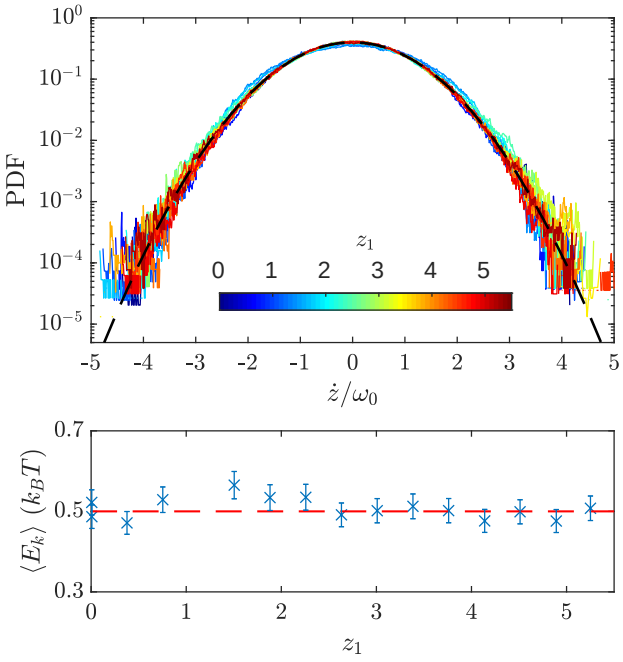

FIG. S2. (Top) PDF of the dimensionless velocity of the cantilever $\dot{z}/\omega_0$ for increasing values of z_1 (from 0 in blue to 5.5 in red) imposed by the feedback loop. The blue curve corresponds to $z_1 = 0$ (no feedback). The red line corresponds to very separated double wells: $z_1 = 5.5$. For each distance between the wells, the experimental PDF fits to the standard normal distribution expected (dashed black). (Bottom) Mean kinetic energy $\langle E_k \rangle = \frac{1}{2}\langle \dot{z}^2 \rangle/\omega_0^2$ for increasing distance between the wells. E_k is not influenced by the feedback loop, and it matches the value one would expect from the equipartition theorem.

STOCHASTIC WORK AND HEAT EXPRESSIONS

The underdamped system evolves in a potential $U(x, x_i(t))$, where $x_i(t)$ are the external control parameters of the potential. Noting that

$$\dot{U}(x, x_i) = \frac{\partial U}{\partial x}(x, x_i)\dot{x} + \sum_i \frac{\partial U}{\partial x_i}(x, x_i)\dot{x}_i, \tag{S1}$$

we obtain:

$$\dot{E}_k + \dot{U} = \sum_i \frac{\partial U}{\partial x_i}\dot{x}_i + \frac{\partial U}{\partial x}\dot{x} + \frac{dE_k}{dt} \tag{S2}$$

Integrating this equation leads to the energy balance of the system (with the positive exit heat flux convention)

$$\Delta U + \Delta E_k = \mathcal{W} - \mathcal{Q}, \tag{S3}$$

where the heat and the work have been defined as (following Refs. 1 and 2):

$$W = \int \sum_i \frac{\partial U}{\partial x_i}\dot{x}_i \mathrm{d}t \tag{S4}$$

$$Q = -\int \frac{\partial U}{\partial x}\dot{x}\mathrm{d}t - \Delta E_k \tag{S5}$$

In our experiment, the potential energy U is given by

$$U(z, z_0, z_1) = \frac{1}{2}\big(z - S(z - z_0)z_1\big)^2. \tag{S6}$$

The contribution of $(\partial U/\partial z_0)\dot{z}_0 \propto \delta(z - z_0)z_1\dot{z}_0$ disappears in the work expression: in our protocol $\dot{z}_0 = 0$, except at two particular times corresponding to the beginning and end of stage 2. The former corresponds to $z_1 = 0$, and the latter corresponds to the situation where z and z_0 cannot cross, which constrains this term to 0. In the heat expression, the contribution of the $\partial S/\partial z$ term in $(\partial U/\partial z)\dot{z}$ is proportional to $\delta(z - z_0)z_1 z\dot{z}$ and vanishing as well: assuming that $z(t)$ and $z_0(t)$ intersect at $t = t_0$, this contribution is

$$\int_{\sim t_0} \delta(z - z_0)z_1 z\dot{z}\mathrm{d}t = \frac{z_1(t_0)z(t_0)\dot{z}(t_0)}{\dot{z}(t_0) - \dot{z}_0(t_0)} = 0, \tag{S7}$$

since during our protocol z and z_0 only intersect during stage 1 where $\dot{z}_0 = 0$ at all times.

Eventually $\mathcal{W}$ and $\mathcal{Q}$ write:

$$\mathcal{W} = -\int_0^{\tau_f} \big(S(z - z_0)z - z_1\big)\dot{z}_1\mathrm{d}t \tag{S8}$$

$$\mathcal{Q} = \int_0^{\tau_f} \big(S(z - z_0)z_1 - z\big)\dot{z}\mathrm{d}t - \frac{1}{2\omega_0^2}\Big[\dot{z}^2\Big]_0^{\tau_f}. \tag{S9}$$

It should be noted that in the computation of the mean dissipated heat, we did not include the kinetic term which vanishes on average. These general expressions can be used to deduce work and heat during stage 1 or during stage 2, by adapting the integration bounds. It is straightforward to compute $\mathcal{W}$, since $\dot{z}_1 = 0$ outside the ramps. For $\mathcal{Q}$, we add at least 5 ms after reaching the final state, i.e. at least 2 relaxation times so that the system is very close to equilibrium.

During stage 1 we have $z_0 = 0$ and $z_1 = Z_1(1 - t/\tau)$, the potential energy is therefore simply

$$U_1(z, z_1) = \frac{1}{2}\big(|z| - z_1\big)^2. \tag{S10}$$

The work is then expressed:

$$\mathcal{W}_1 = -\int_0^{\tau} \big(|z| - z_1\big)\dot{z}_1\mathrm{d}t \tag{S11}$$

$$= \int_0^{Z_1} (|z| - z_1)\mathrm{d}z_1. \tag{S12}$$

For slow protocols ($\tau f_0 \gg Q$), we can assume that the PDF $P(z)$ satisfies at all times the static expression given by the Boltzmann distribution:

$$P(z) = \frac{1}{\mathcal{Z}}e^{-U_1(z,z_1)} = \frac{1}{\mathcal{Z}}e^{-\frac{1}{2}(|z|-z_1)^2}, \tag{S13}$$

where

$$\mathcal{Z} = \sqrt{2\pi}\left(1 + \mathrm{erf}(z_1/\sqrt{2})\right). \tag{S14}$$

$P(z)$ is even, so we can deduce that:

$$\langle|z|\rangle = \int_{-\infty}^{\infty} |z|P(z)\mathrm{d}z = 2\int_0^{\infty} zP(z)\mathrm{d}z \tag{S15}$$

$$= \frac{2}{\mathcal{Z}}\int_0^{\infty} ze^{-\frac{1}{2}(z-z_1)^2}\mathrm{d}z \tag{S16}$$

$$= \frac{2}{\mathcal{Z}}\left(z_1\int_0^{\infty} P(z)\mathrm{d}z - \Big[e^{-\frac{1}{2}(z-z_1)^2}\Big]_0^{\infty}\right) \tag{S17}$$

$$= z_1 + \sqrt{\frac{2}{\pi}}\frac{e^{-\frac{1}{2}z_1^2}}{1 + \mathrm{erf}(z_1/\sqrt{2})} \tag{S18}$$

All in all, we have the mean work in stage 1:

$$\langle\mathcal{W}_1\rangle = \langle\int_0^{Z_1} (|z| - z_1)\mathrm{d}z_1\rangle \tag{S19}$$

$$= \sqrt{\frac{2}{\pi}}\int_0^{Z_1} \frac{e^{-\frac{1}{2}z_1^2}}{1 + \mathrm{erf}(z_1/\sqrt{2})}\mathrm{d}z_1 \tag{S20}$$

$$= \ln\Big(1 + \mathrm{erf}(Z_1/\sqrt{2})\Big) \underset{Z_1 \gg 1}{\longrightarrow} \ln 2. \tag{S21}$$

For a robust 1-bit of information, and equivalently, for a complete and reliable erasure, we should take $Z_1 \gg 1$ in the initial state. As a result, for quasi-static erasure processes of 1 bit, $\langle\mathcal{W}_1\rangle = k_B T \ln 2$.

During the quasi-static merging of the wells, we can also compute the average instantaneous power:

$$\langle \frac{\partial U}{\partial z_1}\dot{z}_1\rangle = -\langle \big(|z|-z_1\big)\dot{z}_1\rangle \tag{S22}$$

$$= \sqrt{\frac{2}{\pi}}\frac{e^{-\frac{1}{2}z_1^2}}{1+\mathrm{erf}(z_1/\sqrt{2})}\frac{Z_1}{\tau}. \tag{S23}$$

This expression is plotted in Fig. 4 of the letter, and it closely follows the experimental data.

During stage 2, the cantilever no longer sees the second well and $S(z-z_0)=-1$, so that the potential simplifies into:

$$U_2(z,z_1) = \frac{1}{2}(z+z_1)^2. \tag{S24}$$

The mean work becomes

$$\langle \mathcal{W}_2\rangle = \langle -\int_0^\tau \big(z+z_1\big)\dot{z}_1 \mathrm{d}t\rangle \tag{S25}$$

$$= -\int_0^\tau \big(\langle z\rangle + z_1\big)\dot{z}_1 \mathrm{d}t. \tag{S26}$$

During the quasi-static translation, $\langle z\rangle = -z_1$, and so $\langle \mathcal{W}_2\rangle = 0$.

FAST ERASURE PROTOCOLS

In this section, we reproduce the results presented in Fig. 3 and Fig. 4 of the article, but for protocols that can no longer be considered as quasi-static. For fast protocols corresponding to a few oscillations of the cantilever such as the one in Fig. S3, the system can switch only once or twice between the wells. The work required is above the Landauer limit as pointed out in Fig. S4. Fig. S5 details the mean power required during the process: stage 1 power exceeds the quasi-static curve and the stage 2 contribution no longer vanishes.

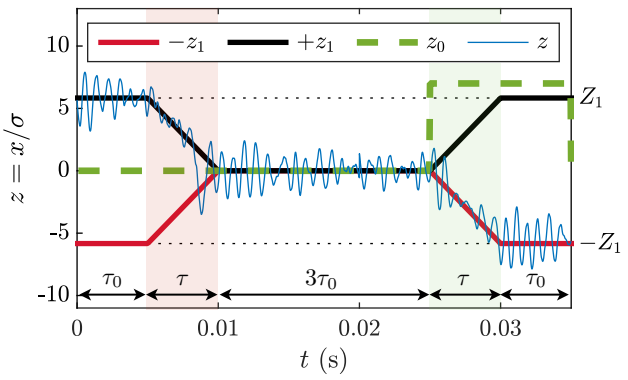

FIG. S3. Fast erasure protocol: the stage 1 and stage 2 duration is $\tau = 5\,\mathrm{ms}$, that is to say $f_0\tau = 6.4$.

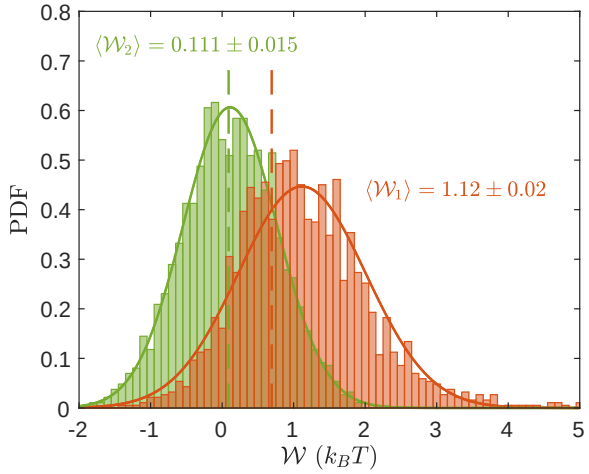

FIG. S4. Work distribution of 2000 iterations of the fast protocol of Fig. S3. For fast erasure, stage 2 contribution is no longer negligible: $\langle \mathcal{W}_2\rangle = 0.111 \pm 0.015$ is close to the expected asymptotic behavior $Z_1^2/(Q\omega_0\tau) = 0.091$, represented by the dashed green line. Stage 1 mean work $\langle \mathcal{W}_1\rangle = 1.12 \pm 0.02$ is now clearly above the LB represented by the red dashed line.

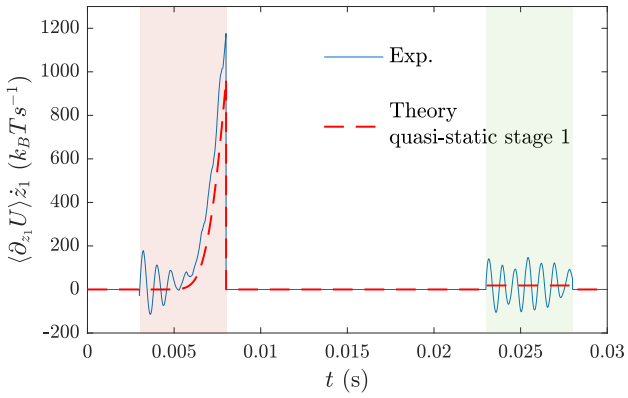

FIG. S5. Time evolution of the mean power over 2000 trajectories following the fast protocol of Fig. S3. The red dashed line corresponds to the quasi-static regime prediction for stage 1 (Eq. S21) and to the asymptotic mean power value for stage 2: $Z_1^2/(Q\omega_0\tau^2)$.

HEAT AND WORK DISTRIBUTION

We present in Fig. S6 the distribution of the work and the heat of 2000 iterations of the erasure with the slow protocol detailed in the letter Fig. 3. The work distribution is gaussian. Meanwhile, the heat distribution presents exponential tails. This observation is in agreement with the study of Ref. 3: $\mathcal{Q}$ is the convolution product of a gaussian and an exponential distribution. Besides, both distributions are centered on the LB because the protocol under study is close to the quasi-static regime.

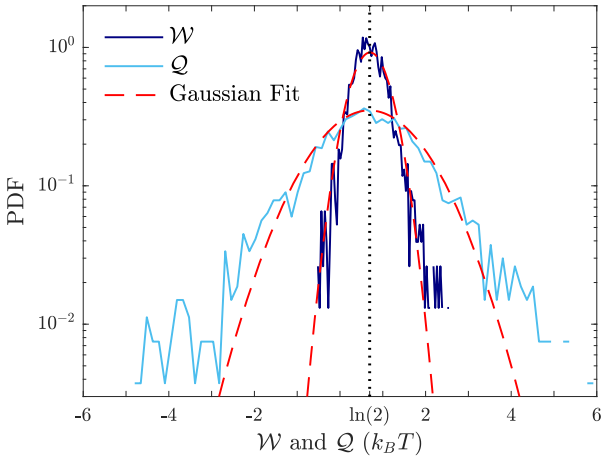

FIG. S6. Work (dark blue) and heat (light blue) distributions of 2000 erasure procedures of Fig. 3 of the letter. The gaussian shape of the work PDF is highlighted by the best fit to a gaussian distribution (dashed red line). The heat is far more dispersed than the work and presents exponential tails. Since it is a slow protocol, both are centered on the LB (dotted black vertical line).

* ludovic.bellon@ens-lyon.fr

[1] K. Sekimoto, *Stochastic Energetics*, Lecture Notes in Physics, Vol. 799 (Springer, 2010).
[2] K. Sekimoto and S. Sasa, Journal of the Physical Society of Japan **66**, 3326 (1997).
[3] S. Ciliberto, Phys. Rev. X **7**, 021051 (2017).

Appendix D:

Virtual double-well potential for an underdamped oscillator created by a feedback loop

We attach in this section our article in Ref. 4.

Virtual double-well potential for an underdamped oscillator created by a feedback loop

Salambô Dago, Jorge Pereda, Sergio Ciliberto, and Ludovic Bellon*
Univ Lyon, ENS de Lyon, CNRS, Laboratoire de Physique, F-69342 Lyon, France

Virtual potentials are a very elegant, precise and flexible tool to manipulate small systems and explore fundamental questions in stochastic thermodynamics. In particular double-well potentials have applications in information processing, such as the demonstration of Landauer's principle. Nevertheless, virtual double-well potentials had never been implemented in underdamped systems. In this article, we detail how to face the experimental challenge of creating a feedback loop for an underdamped system (exploring its potential energy landscape much faster than its over-damped counterpart), in order to build a tunable virtual double-well potential. To properly describe the system behavior in the feedback trap, we express the switching time in the double-well for all barrier heights, combining for the first time Kramer's description, valid at high barriers, with an adjusted model for lower ones. We show that a small hysteresis or delay of the feedback loop in the switches between the two wells results in a modified velocity distribution, interpreted as a cooling of the kinetic temperature of the system. We successfully address all issues to create experimentally a virtual potential that is statistically indistinguishable from a physical one, with a tunable barrier height and energy step between the two wells.

I. INTRODUCTION

Feedback traps are widely used to trap and manipulate Brownian particles in solution, and explore fundamental questions in non-equilibrium statistical mechanics of small systems [1–4]. Indeed, by controlling an external force acting on a colloidal particle as a function of its measured position, one can create a virtual potential. This is a very powerful tool, more flexible [5] than its physical counterparts consisting of localized potential forces created by optical or magnetic tweezers [6–10]. Feedback loops on the system's position are used in particular to study Landauer's principle, by creating double-well potentials and using the trapped particle as a memory [10, 11]. Within the information processing framework, lowering the dissipation seems a promising path to reduce energy costs [12–15]. Working with virtual potentials within underdamped dynamics thus appears as a natural endeavor. Moreover, the underdamped regime offers new insights on a wide variety of fundamental questions on the connections between feedback and thermodynamics [16–19].

Nevertheless, implementing virtual potentials in the underdamped regime is not an easy task, especially within the stochastic thermodynamics framework that requires a high measurement precision to resolve the k_BT scale. Indeed, at low damping, systems are resonant and very sensitive to perturbation, noise or drift. Moreover, the feedback update delay can have strong consequences on the coupling between the system and the thermal bath [4, 19].

We propose in this article an electrostatic feedback designed to create virtual double-well potentials acting on a micro-cantilever, which serves as an underdamped mechanical oscillator. The system offers a flexibility and a precision never achieved before, with excellent quality in terms of position measurement and force tuning. Thanks to the thorough study of the feedback effects detailed in this article, we are able to create clean, reliable and tunable double-well potentials which outperform those produced by optical and magnetic tweezers (either physical or virtual), and have the added advantage of being analytically tractable. Therefore, this experimental work presents an unprecedented experimental tool to explore information thermodynamics, and in particular Landauer's principle in the underdamped regime.

In the following, we detail the experimental challenges we faced to remove any bias introduced by the feedback loop. To put these challenges in context, we present a study of the response of underdamped systems to a feedback control. This study incorporates experimental and numerical simulation results, as well as a comprehensive theoretical model. The latter includes the unified and complete description of the switching time of the cantilever in the double-well potential: our expression tends towards Kramer's escape time in the high-energy barrier limit, but it also provides an adjusted model for barriers lower than the thermal energy, where Kramer's formula is no longer valid.

The article is organised as follows: we first present the experimental system and the principle of the feedback loop (section II), before exploring the non-idealities of a real-life implementation (section III). In particular, we analyse how an hysteresis in the switches between the wells, or, equivalently, a delay in the actuation, results in a bias of the energy exchanges with the thermal bath, effectively warming or cooling the oscillator Brownian noise. From this comprehensive analysis, we define in section IV the requirements that need to be met to mitigate imperfections. Lastly, section V describes the final implementation of the feedback loop, and shows that this loop creates a virtual potential indistinguishable from an equivalent physical one.

* ludovic.bellon@ens-lyon.fr

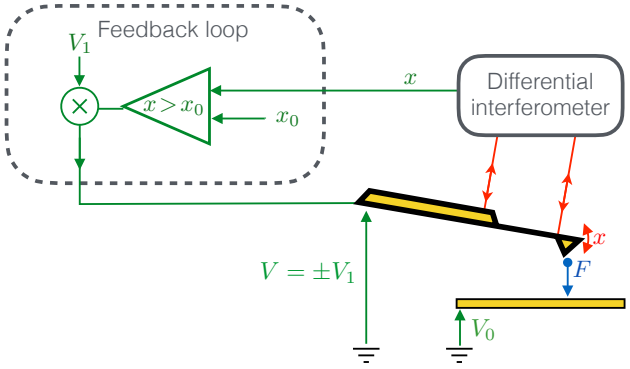

FIG. 1. **Experimental system.** The conductive cantilever is sketched in yellow. Its deflection x is measured with a differential interferometer [20], by two laser beams focused respectively on the cantilever and on its base. The cantilever at voltage $V = \pm V_1$ is facing an electrode at V_0. The voltage difference $V - V_0$ between them creates an attractive electrostatic force $F \propto (V - V_0)^2$. The dashed box encloses the feedback controller, consisting of a comparator and a multiplier, which create the double-well potential.

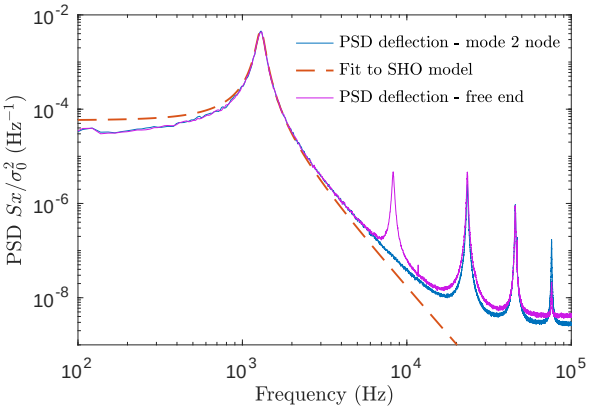

FIG. 2. **Power Spectral Density (PSD) of the cantilever deflection in a single well.** Measured PSD of the thermal noise driven deflection with no feedback ($V_1 = 0$, solid lines), and best fit by the theoretical spectrum of a Simple Harmonic Oscillator (SHO, dashed line). The second deflection mode, visible at 8 kHz when the laser beam is focused at the free end of the cantilever (magenta), is successfully hidden by focusing the laser beam on the node of this mode (blue). At frequencies up to 10 kHz, the cantilever behaves like a SHO at $f_0 = 1270$ Hz, with a quality factor $Q = 10$. We infer from this measurement the variance $\sigma_0^2 = \langle x^2 \rangle = k_B T_0/k$, used to normalize all measured quantities.

II. VIRTUAL DOUBLE-WELL POTENTIAL: PRINCIPLE

As sketched in Fig. 1, the underdamped oscillator is a conductive cantilever [21] mounted in a closed airtight chamber at room temperature T_0. The chamber minimises all air flows induced drifts in the measurement, and can also used as a vacuum chamber to modulate the pressure, thus the resonator quality factor, at will. The cantilever deflection x is measured with very high accuracy and signal-to-noise ratio by a differential interferometer [20]. The Power Spectral Density (PSD) of the thermal fluctuations of x is plotted in Fig. 2: the fundamental mode dominates by 3 orders of magnitude the higher-order deflection modes of the cantilever. The second deflection mode at 8 kHz is conveniently removed from the measured signal by focusing the sensing laser beam on its node, at around 0.78% of the cantilever length. This simple adjustment helps in having a physical system very close to an ideal Simple Harmonic Oscillator (SHO). The fit of this PSD with the theoretical thermal noise spectrum of a SHO leads to its resonance frequency $f_0 = \omega_0/2\pi = 1270$ Hz and quality factor $Q = m\omega_0/\gamma = 10$, where m, $k = m\omega_0^2$ and γ are respectively: the mass, stiffness and damping coefficient of the SHO. The slight difference between the measurement and the model is due to frequency dependency of the viscous damping of the cantilever in air [22]. From the PSD we compute the variance at equilibrium $\sigma_0^2 = \langle x^2 \rangle = k_B T_0/k \sim 1\,\text{nm}^2$, which is used as length scale.

Two time scales typically describe an underdamped system: its natural oscillation period $\mathcal{T}_0 = f_0^{-1} \sim 0.8$ ms (comparing the inertial and elastic terms), and its relaxation time $\tau_r = 2Q/\omega_0 \sim 2.5$ ms (comparing the inertial and damping terms). We add a third one, the time scale of position relaxation [23], which compares the damping and elastic terms: $\tau_\gamma = \gamma/k = 1/(Q\omega_0) \sim 13\,\mu$s. Due to its oscillating nature, the resonator explores the potential energy landscape typically every $\mathcal{T}_0$, and the dissipative part can be sensitive to changes in energy down to τ_γ. This position relaxation τ_γ is much faster than that of most over-damped systems used to create double wells in stochastic thermodynamics, namely colloidal particles optically trapped in water. Since inertia can be neglected in these systems, their response time is set by τ_γ, and typically amounts to 30 ms [24].

In order to use the cantilever as a one-bit memory, we need to confine its motion in an energy potential consisting of two wells separated by a barrier, whose shape can be tuned at will. This potential U is created by a feedback loop, which compares the cantilever deflection x to an adjustable threshold x_0. After having multiplied the output of the comparator by an adjustable voltage V_1, the result is a feedback signal V which is $+V_1$ if $x > x_0$ and $-V_1$ if $x < x_0$. The voltage V is applied to the cantilever which is at a distance d from an electrode kept at a voltage V_0. The cantilever-electrode voltage difference $V_0 \pm V_1$ creates an electrostatic attractive force $F = \frac{1}{2}\partial_d C(d)(V_0 \pm V_1)^2$ [25], where $C(d)$ is the cantilever-electrode capacitance. Since $d \gg \sigma_0$, $\partial_d C(d)$ can be assumed constant. We apply $V_0 \sim 100$ V and $V_1 \ll V_0$ so that, to a good approximation, $F \propto \pm V_1$ up to a static term. This feedback loop results in the

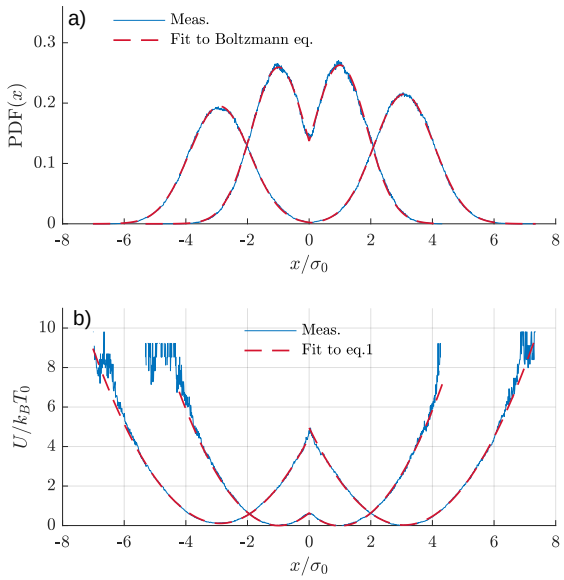

FIG. 3. **(a) Probability Density Function (PDF) of x.** The PDF of x (blue) measured during a 10 s acquisition with the feedback on, with $x_0 = 0$ and two values of V_1 adjusted to have respectively a $5\,k_BT_0$, and a $0.5\,k_BT_0$ energy barrier height. The fit using the Boltzmann equilibrium distribution with the potential shape in Eq. (1) (dashed red) is excellent. **(b) Double-well potential energy.** The measured potentials (blue) are inferred from the PDF of x in a) and the Boltzmann distribution. The high noise level for large values of U stems from the bad sampling of regions with low probability. We obtain as expected the $5\,k_BT_0$ and $0.5\,k_BT_0$ barriers corresponding to the two values of V_1. The fits using Eq. (1) are again excellent (dashed red).

application of an external force whose sign depends on whether the cantilever is above or below the threshold x_0. As long as the reaction time τ_d of the feedback loop is very fast (at most a few μs), the switching transient is negligible: $\tau_d \ll \tau_\gamma, \mathcal{T}_0, \tau_r$. As a consequence, the oscillator evolves in a virtual static double-well potential, whose features are controlled by the two parameters x_0 and V_1. Specifically, the barrier position is set by x_0 and its height is controlled indirectly by V_1, which sets the wells centers $\pm x_1 = \pm V_1 \partial_d C(d) V_0/k$. The potential energy constructed by this feedback is:

$$U(x, x_0, x_1) = \frac{1}{2} k x \big(x - S(x - x_0)x_1\big)^2, \qquad (1)$$

where S is the sign function: $S(x) = -1$ if $x < 0$ and $S(x) = 1$ if $x > 0$. In the following, unless we specify otherwise, we will always consider the case of a symmetric potential, corresponding to $x_0 = 0$.

The two degree of freedom of the underdamped system, the deflection x and the velocity $v = \dot{x}$, are considered as random variables of a stochastic process. They are ruled by a Langevin equation (Eq. (A2) in appendix A), or equivalently characterized by the Probability Density Function (PDF) $P(x, v, t)$ for finding the cantilever in position x, and velocity v at time t, whose dynamics is given by Kramer's equation [26]:

$$\partial_t P + v\partial_x P - \frac{\partial_x U}{m}\partial_v P = \frac{\gamma}{m}\partial_v(vP) + k_BT_0\frac{\gamma}{m^2}\partial_v^2 P, \qquad (2)$$

As the potential $U(x, x_0, x_1)$ does not depend on the speed, the equilibrium PDF of the velocity in the double-well is the same as the one in a single harmonic well and scales as a Gaussian of variance k_BT_0/m: $\mathrm{PDF}(v) \propto e^{-mv^2/(2k_BT_0)}$. The stationary Boltzmann distribution therefore factorizes the equilibrium x and v PDF:

$$P_{eq}(x, v) = \mathrm{PDF}(x) \times \mathrm{PDF}(v) \qquad (3)$$

$$\propto e^{-\frac{U(x)}{k_BT_0}} \times e^{-\frac{mv^2}{2k_BT_0}} \qquad (4)$$

The potential in Eq. (1) can be experimentally measured from the PDF of x and the Boltzmann equilibrium distribution: $U(x) = U_0 - k_BT_0 \ln[\mathrm{PDF}(x)]$, with U_0 an arbitrary constant. Fig. 3 presents two examples of an experimental symmetric double-well potential generated by the feedback loop, tuned to have a barrier of $\frac{1}{2}kx_1^2 = 5k_BT_0$ and $0.5k_BT_0$ (respectively $x_1 = \sqrt{10}\sigma_0$ and $x_1 = \sigma_0$). The dashed red line is the best fit with Eq. (1), demonstrating that the feedback-generated potential behaves as a static one, in terms of the position PDF.

The experimental challenge undertaken in this work is to build a proper virtual potential identical to a physical one: the feedback loop should have no noticeable effect on the position and velocity equilibrium distributions.

III. VIRTUAL DOUBLE-WELL POTENTIAL: PRACTICAL NON-IDEALITIES

Setup	Comparator	Filter bandpass	Defect	Main bias
1	TS3022	1 MHz	Hysteresis: $h = 0.15\sigma_0$	Cooling
2	LM219	No Filter	Early trigger: $h < 0$	Warming
Final	LM219	1 MHz	$h \sim 0$	No bias

TABLE I. Setup 1, setup 2, and final setup distinctive features.

An ideal feedback loop comparator satisfies three requirements: it presents no measurement noise, it is immediate, and it always switches exactly at the prescribed x_0 position. In real comparators, however, those three requirements compete with each other, and a tradeoff between them needs to be found. For example, a high-frequency measurement noise causes the comparator to switch at inexact positions. It is therefore common to low

pass filter the input signal to remove this noise, at the expense of introducing a delay in the switching time. Alternatively, one can reduce the effect of noise by introducing an artificial hysteresis around the threshold, larger than the noise amplitude, but in this case the switching between wells doesn't occur at the appropriate position. In the next subsections, we study the consequences of each of these non-idealities.

A. Hysteresis

1. *Experimental observation*

One major experimental challenge lies in the comparator hysteresis. To illustrate its consequences, we use the setup 1 whose circuit is detailed in section V (see Tab. I and Fig. 7). In this case we measure an average hysteresis of $h = 0.15\sigma_0$: the voltage switches upward from $-V_1$ to V_1 when the position crosses $x_0 + h$ from below, and downward when crossing $x_0 - h$ from above. This hysteresis is likely due to the use of the comparator outside its nominal regime in terms of voltage ranges.

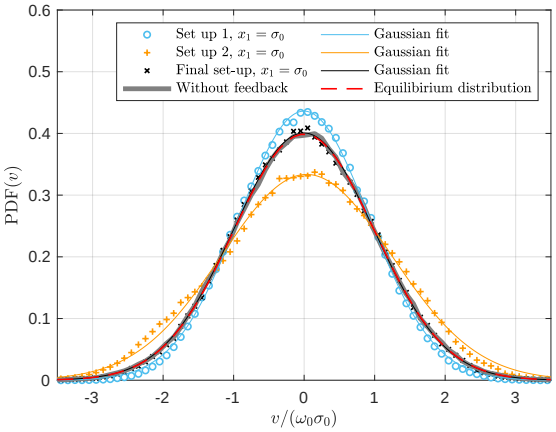

FIG. 4. **PDF of the oscillator speed.** Experimental PDF of v for $x_1 = \sigma_0$ inferred from a 10 s acquisition using setup 1, setup 2 and the final setup (see Tab. I), respectively in blue, orange and black markers. Each time, the best Gaussian fit is superimposed in plain line: the fit is excellent for the setups with positive or zero hysteresis (setup 1 and final setup). Regarding setup 2 (negative hysteresis), the Gaussian fit is not as good, but remains satisfactory, and the higher moments of the experimental PDF are close to the Gaussian vanishing values: respectively -0.08 and -0.3 for the skewness and the excess kurtosis. Finally, we superimpose in grey thick line the experimental PDF without feedback, which perfectly matches the equilibrium distribution (dashed red line). It is worth noticing that the final setup (black) also ideally reproduces the equilibrium distribution.

A comparator hysteresis has an effect on the velocity distribution of the system, as illustrated in Fig. 4. While the speed PDF keeps a satisfactorily Gaussian shape for the different setups, its variances are altered compared to the equilibrium distribution perfectly matched without feedback. Therefore, the velocity variance turns out to be an adequate observable to summarize the effect of the hysteresis on the velocity distribution. The hysteresis should also alter the PDF of position for nearby wells, in particular around the threshold cusp (rounding effect), but it is a tiny effect, hard to observe experimentally.

Let us introduce the kinetic temperature T of the system defined through the velocity variance: $\sigma_v^2 = \langle v^2 \rangle = k_B T/m$. At equilibrium in a bi-quadratic potential, the kinetic temperature should match the bath temperature T_0 as prescribed by the Boltzmann distribution. To facilitate the reading we introduce the ratio $\theta = T/T_0$, so that the velocity standard deviation simplifies into $\sigma_v = \sqrt{\theta}\omega_0\sigma_0$.

We measure the kinetic temperature evolution through the velocity variance for different distances between the wells. The experimental results plotted on Fig. 5 show a cooling of the system when the wells are close. We propose in the next paragraphs a theoretical model that supports this observation.

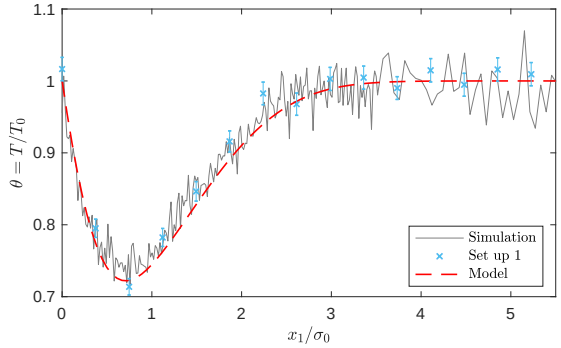

FIG. 5. **Kinetic temperature with hysteresis (setup 1).** The ratio $\theta = T/T_0$ is plotted as a function of the distance between the wells x_1. Blue markers: experimental data obtained from setup 1 with a typical hysteresis $h = 0.15\sigma_0$ at each switch. Grey line: simulation data from $N_{\text{sim}} = 200$ iterations of $30/f_0$ long trajectories of the cantilever evolving in a potential created with a $h = 0.15\sigma_0$ hysteresis on the threshold. Dashed red line: the numerical solution of Eq. (9) perfectly predicts the hysteresis consequences on the temperature.

2. *Theoretical model*

We model the consequences on the system temperature using the infinitesimal energy balance equation, with $K = \frac{1}{2}mv^2$ the kinetic energy, $\mathcal{W}$ the stochastic work and

$\mathcal{Q}$ the stochastic heat [12, 16, 27, 28]:

$$\frac{dU}{dt} + \frac{dK}{dt} = \frac{d\mathcal{W}}{dt} - \frac{d\mathcal{Q}}{dt} \tag{5}$$

This energy balance is the starting point of the model developed in this article to link the feedback hysteresis to the system temperature, similarly to the approach followed in the theoretical description of feedback cooling [14, 15].

In a stationary state when no external work is performed ($\langle \mathcal{W} \rangle = 0$) there is no kinetic energy evolution on average ($\langle dK/dt \rangle = 0$), so that using the heat expression (A7) derived in Appendix A, Eq. (5) reduces to:

$$\langle \frac{dU}{dt} \rangle = \frac{\omega_0}{Q} k_B T_0 (1 - \theta) \tag{6}$$

If there is a switching hysteresis, the comparator triggers only when $x = \pm h$ (sign depending on origin) instead of $x = x_0 = 0$. The cantilever overreaches the barrier at each crossing. This implies an extra distance travelled by the cantilever in the initial well (centred on $\pm x_1$) before the feedback makes it switch in the second well. This extra distance corresponds to a potential energy step:

$$\begin{aligned} \Delta U_h &= \frac{1}{2} k \left[(h + x_1)^2 - (h - x_1)^2 \right] \\ &= 2 k x_1 h \end{aligned} \tag{7}$$

This amount of potential energy is lost each time the cantilever crosses the barrier. Between the crossings, the system thermalizes in contact with the heat bath. Thus the system is always out-of-equilibrium and reaches a steady state characterized by the kinetic temperature T. The latter allows the warming heat influx from the thermostat to compensate on average the energetic losses caused by the hysteresis at each barrier crossing. It only remains to express the average heat flux corresponding to these discrete energetic losses: we need to quantify how often on average the cantilever crosses the threshold. In appendix B, we derive the crossing rate Γ of the potential barrier $\mathcal{B}$ for a system at temperature T:

$$\Gamma(\mathcal{B}, T) = \omega_0 \frac{\mathcal{B}}{k_B T} \int_1^\infty \frac{\exp(-\epsilon \frac{\mathcal{B}}{k_B T})}{\pi + 2 \sin^{-1}(\epsilon^{-1/2})} d\epsilon \tag{8}$$

Using Eq. (8) applied to the barrier energy $\mathcal{B} = \frac{1}{2} k (x_1 + h)^2$, we can express the potential contribution in Eq. (6) and derive:

$$\Gamma(\frac{1}{2} k (x_1 + h)^2, \theta T_0) \times \Delta U_h = \frac{\omega_0}{Q} k_B T_0 (1 - \theta) \tag{9}$$

The temperature solution of Eq. (9) allows the system to reach a steady state in which the average heat flux lost by the system ($\Gamma \Delta U_h$), and the heat influx from the heat bath (proportional to $T - T_0$) equilibrate. The numerical solution of Eq. (9) is plotted on Fig. 6: the kinetic temperature presents a minimum around $x_1 \lesssim \sigma_0$, which deepens as the hysteresis h increases. These trends can be easily understood: firstly, the larger the hysteresis, the greater the energy loss at each switch, and, therefore, the lower the system temperature. Secondly, the energy loss per switch is proportional to x_1, but the barrier crossing rate decreases with x_1: in the high barrier limit there are no more switches and $T = T_0$, and in the low barrier limit there is no more energy step at the switch, so that $T = T_0$ as well. The effect on the temperature is maximized for $x_1 \sim \sigma_0$ when the two opposing effects counteract each other most. The model, applied to the setup 1 measured hysteresis, is in perfect agreement with the experimental data as highlighted in Fig. 5. Let us also point out that the same description holds for negative hysteresis: early switches make the system warm up, as shown in red on Fig. 6. In conclusion, removing all hysteresis at the barrier crossing is mandatory to maintain a proper equilibrium in the double-well potential, instead of creating an out-of-equilibrium steady state characterized by a temperature $T \neq T_0$.

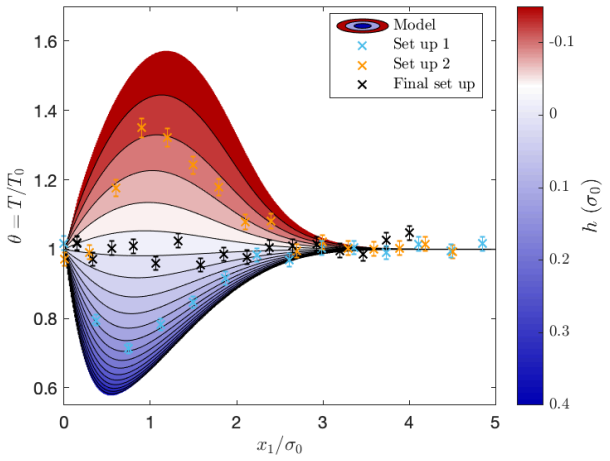

FIG. 6. **Consequences of an hysteresis on the kinetic temperature.** $\theta = T/T_0$ is plotted as a function of the distance x_1 between the wells. The colormap is drawn with the model prediction provided by Eq. (9): positive hysteresis h cools the system down, while negative hysteresis warms the system up. The dependance on x_1 comes from the balance between the barrier crossing rate and the energy step due to the hysteresis at each switch. The blue, black and orange points correspond respectively to the experimental results obtained with the three setups addressed in this paper: setup 1 ($h = 0.15\sigma_0$), final setup (tiny hysteresis), and setup 2 (early trigger).

3. *Simulation confirmation*

We complete the study by simulating $N_{\text{sim}} = 200$ trajectories of the cantilever evolving in a potential created with $h = 0.15\sigma_0$ hysteresis on the threshold. The numer-

ical simulation is in very good agreement with both the model and the experimental data (see Fig. 5).

B. Switching delay

A time delay between the cantilever crossing the barrier and the force switching is inevitable because real comparators have finite switching speed, but also due to the delay inherent to the low-pass filter applied to the position measurement. The effect of such a delay is similar to that of an hysteresis. Indeed, if there is a time delay τ_d, the cantilever overreaches the barrier of a distance h_d on average at each passage, that can be computed knowing the speed PDF:

$$h_d = \langle |v| \rangle \tau_d = \int_0^\infty |v| \frac{e^{-\frac{v^2}{2\sigma_v^2}}}{\sigma_v \sqrt{2\pi}} dv \tau_d \tag{10}$$

$$= \sqrt{\frac{2\theta}{\pi}} \sigma_0 \omega_0 \tau_d \tag{11}$$

The absolute value in the average of v comes from the fact that only the velocity sign that matches the barrier crossing is considered (for example positive velocity for upward crossing). The time delay can thus be treated as a mean hysteresis h_d, associated to an energy step $\Delta U_d = 2kx_1 h_d$, leading to an equation equivalent to Eq. (9) with an updated barrier height:

$$\Gamma(\frac{1}{2}kx_1^2, \theta T_0) \times \Delta U_d = \frac{\omega_0}{Q} k_B T_0 (1-\theta) \tag{12}$$

Thus, the temperature of the system trapped in a double-well potential with switching time delay τ_d is a solution of the following equation, derived from Eq. (12):

$$g\left(\frac{x_1}{\sigma_0\sqrt{2\theta}}\right) Q\omega_0\tau_d\,\theta = 1-\theta \tag{13}$$

where

$$g(z) = \frac{4}{\sqrt{\pi}} z^3 \int_1^\infty \frac{\exp(-\epsilon z^2)}{\pi + 2\sin^{-1}(\epsilon^{-1/2})} d\epsilon \tag{14}$$

The numerical solution of Eq. (13) has a profile similar to the solutions of Eq. (9) plotted on Fig. 6.

The function $g(z)$ presents a global maximum $g^* = 0.21$ in $z^* = 0.64$, allowing to compute the minimum temperature and corresponding well distance

$$\theta_{\min} = \frac{1}{1 + g^* Q \omega_0 \tau_d} = \frac{1}{1 + g^* \tau_d / \tau_\gamma} \tag{15}$$

$$x_{1,\min} = z^* \sigma_0 \sqrt{2\theta_{\min}} \tag{16}$$

The minimum temperature is thus a function of the ratio between the switch delay τ_d and the smallest intrinsic time of the resonator, τ_γ: no kinetic temperature change is expected if the former is much smaller than the latter.

C. Measurement noise

The PSD in Fig. 2 demonstrates that, in a single well, the thermal noise of the cantilever is very close to that of an ideal SHO, on a wide frequency range. Nevertheless, 2 sources of deviation can be noticed. First, higher-order deflection modes (from the third up) are clearly visible, and contribute to the measured signal by adding high frequency noise accounting for $0.05\sigma_0$. Second, some background noise remains, due to higher conditioning electronic noise and to the shot noise of the photodiodes of the interferometer. At high frequencies, this noise floor, around $3 \times 10^{-9}\,\sigma_0^2/\text{Hz}$, supersedes the signal from the first deflection mode. Integrated on the 1 MHz bandwidth of the final setup filtering (detailed later in section V C), this background noise contributes up to $0.05\sigma_0$. This measurement noise reaching in total $0.07\sigma_0$ has two unwanted consequences on the feedback generated potential: parasitic switches and early triggering.

1. *Parasitic swiches*

If the apparatus compares the raw deflection signal V_x from the interferometer directly to the threshold V_{x_0}, the noise in the input signals produces multiple transitions at the crossing. As a consequence, the feedback loop output voltage V oscillates rapidly between positive and negative values, so the mean voltage seen by the electrode vanishes. Because of these parasitic switches of the comparator, the cantilever ends up trapped at the threshold position $x_0 = 0$, in between the two desired equilibrium ones $\pm x_1$.

2. *Early triggering*

The high frequency noise triggers the switch before the signal of interest (the position of the first deflection mode) actually crosses the threshold, and therefore induces early switches. In setup 2 (whose circuit is detailed in Fig. 7, and summarized into Tab. I), the high frequency noise is not removed, so that a negative hysteresis appears due to the early triggers. Consequently the system temperature rises in accordance with the prediction of previous sections. The experimental evidence of the temperature rise in setup 2 is superimposed with orange crosses to the theoretical curves in Fig. 6.

IV. REQUIREMENTS

To mitigate the consequences of the experimental non-idealities listed above, we need to adapt the experimental setup. We detail in this section the essential experimental constraints to create a proper virtual potential.

A. Limiting the hysteresis

To maintain the velocity equilibrium distribution in the virtual potential, and to limit the cooling to 5%, from Fig. 6 we deduce that the hysteresis has to be lower than $0.02\sigma_0$. Note that this value, deduced from the model summarized in Eq. (9), is computed for a quality factor of 10, and higher values of Q would result in an even more stringent requirement. As regards the cooling effect, one would wish to suppress the hysteresis altogether, but a tiny hysteresis is nevertheless needed for stability purposes: the output of the comparator circuit is unstable if no reference to the input is introduced. All in all, the hysteresis of the comparator should remain between 0.5% and 2% of σ_0.

B. Removing parasitic switches: temporal lock-up

The common workaround to the issue of repeated fast-switches is to introduce an hysteresis through a positive feedback of the output on the comparator threshold. To be effective, this strategy requires an hysteresis wider than the measurement noise, hence larger than $0.07\sigma_0$ (see section III C). Such a large hysteresis is prohibitive in our case because of the cooling effect. As an alternative, we implement a temporal lock-up to freeze the comparator state after a switch, for roughly 1/4 of the oscillator's natural period $1/f_0$. By the time the comparator is active again, the cantilever has evolved in the new well –on average– long enough to reach the bottom of the well, and is therefore far enough from the threshold that an undue noise-induced switch is improbable. One drawback is that short excursions in the other well are forbidden as well. However, these events –indeed present in a real double-well potential– are unlikely enough that removing them has no noticeable effect of the statistical properties of the virtual potential.

C. Removing early triggering: low-pass filtering

To correct early switches (occurring in setup 2), we must filter the high-frequency noise. The second mode contribution is hidden by focusing the laser on the mode vibration node. The higher-order modes and the electronic shot noise are low-pass filtered. When designing this filter, the concern is the delay introduced, since it will induce an hysteresis, possibly cooling the system.

On the one hand the filter has to cut the high frequency noise over $1000f_0$ to limit the background noise contribution (increasing at high frequencies) to $0.05\sigma_0$. But on the other hand the filter response time τ_d has to remain much lower than τ_γ/g^* to limit the cooling effect: this bound corresponds to $1-\theta \ll 1$ using Eq.(15). To summarize, using the relation between the cutoff frequency f_c of a first order low-pass filter and its response time $\tau_d \sim \frac{5}{2\pi f_c}$ (the relation holds for higher-order filters in first approximation), f_c is bounded by:

$$5g^*Qf_0 \ll f_c < 1000f_0 \tag{17}$$

With a quality factor $Q = 10$ and a resonance frequency $f_0 = 1.2\,\text{kHz}$, the interval reads: $13\,\text{kHz} \ll f_c < 1.2\,\text{MHz}$.

D. Characteristics of the cantilever

The cantilever is chosen to meet the requirements of the filter cutoff frequency and the comparator hysteresis, expressed in Eq.(17): by selecting a low Q and low f_0, we minimize the cooling, and alleviate the constraints on the feedback characteristics. We thus choose $Q = 10$ and a relatively slow oscillator: $f_0 = 1.2\,\text{kHz}$. Furthermore, we choose a low stiffness $k \sim 5\times10^{-3}\,\text{N/m}$ to have a large thermal noise, thus a large signal (Brownian) to noise (background) ratio.

V. FINAL SETUP

We detail in this section the final experimental setup designed to meet all the requirements previously listed. The feedback circuit diagram is detailed in Fig. 7: it contains the basic components (comparator and multiplier) on which some elements are added to ensure its efficiency. The deflection signal from the interferometer V_x is filtered by a low-pass filter (green) before entering the comparator device (red). The tunable threshold V_{x_0} is biased by the voltage V_{lock} resulting from the lock-up feedback loop (blue components) before being compared to V_x. The comparator output voltage is then multiplied by the adjustable voltage V_1.

A. Stability

To ensure the stability of the comparator output, we introduce a tiny hysteresis corresponding to $R_i/R_h = 1.2\,\text{k}\Omega/3.2\,\text{M}\Omega$ fraction of the output fed on the positive input (see Fig. 7). As the position signal scales as σ_0 (in V) $= \sqrt{\langle V_x^2\rangle} \sim 50\,\text{mV}$, the hysteresis has to stay between $0.5\%\sigma_0 = 0.25\,\text{mV}$ and $2\%\sigma_0 = 1\,\text{mV}$ to meet the requirements of section IV A. With the $\pm1\,\text{V}$ power supply voltage of the comparator device, the hysteresis amplitude of our final design reaches 0.37 mV and therefore remains in the range specified.

B. Temporal lock up

The temporal lock-up feedback is implemented through a follower assembly and a capacitor (blue components on Fig. 7). The comparator (red device on

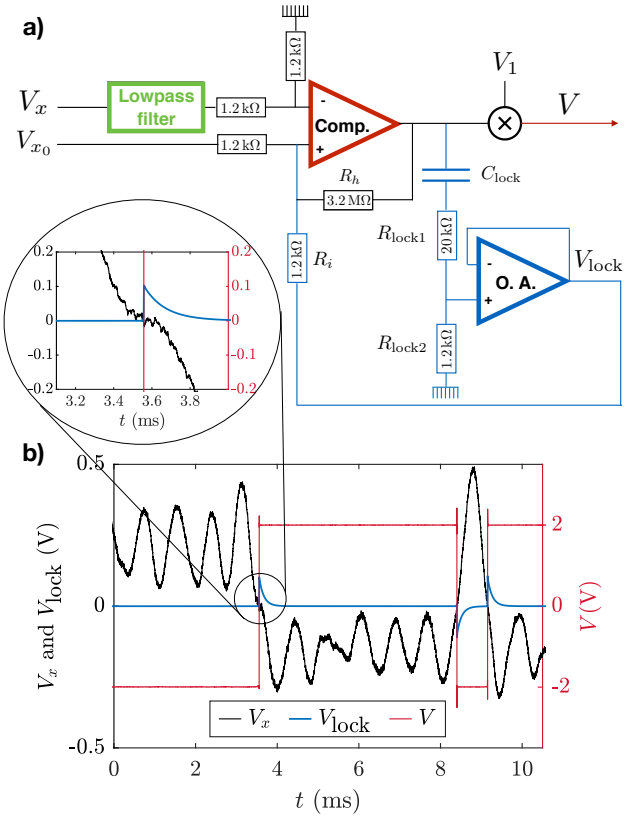

FIG. 7. **(a) Electrical diagram of the feedback loop.** The cantilever deflection signal V_x from the interferometer passes through a low pass filter ($f_c = 1\,$MHz, model SR560, green) before entering the LM219 comparator (red). The threshold signal V_{x_0} is momentarily modified by $V_{\rm lock}$ after each switching of the comparator. $V_{\rm lock}$ is the result of a lock-up feedback consisting in a follower assembly and a capacitive circuit built with the following components: operational amplifier LT131, capacity $C_{\rm lock} = 4.7\,$nF, resistances $R_{\rm lock1} = 20\,$kΩ and $R_{\rm lock2} = 1.2\,$kΩ. The output of the comparator is then multiplied by V_1 to modulate the final voltage V (using an AD633-EVALZ analog multiplier). With respect to this design (denoted as final setup), we call setup 1 the same circuit but with a TS3022 comparator leading to a switching hysteresis $h = 0.15\sigma_0$. Similarly we call setup 2 the final circuit without the low-pass filter leading to early triggers (negative hysteresis). The setups' distinctive characteristics are summarized in table I. **(b) Example of signals.** The cantilever deflection signal V_x is plotted in black, the lock-up voltage $V_{\rm lock}$ in blue and the output voltage V in red (with $V_1 = 2V$). The threshold V_{x_0} is set to 0.

Fig. 7) compares $V_x/2$ to $(V_{x_0} + V_{\rm lock})/2$, without being affected by the temporal lock-up components values thanks to the impedance conversion provided by the buffer. The purpose of this is to bias the threshold V_{x_0} during the discharge time of the capacitor $C_{\rm lock}$, in order to prevent the comparator switching back right after a switch. In the static regime without switches, the output is constant for example at $+V_{\rm sat} = 1\,$V, which corresponds to the charged capacity that acts as an open circuit so that $V_{lock} = 0$. Right after a switch of the output voltage, the capacity starts reversing its charge through $R_{\rm lock2} + R_{\rm lock1}$, and $V_{\rm lock}$ moves immediately to $2R_{\rm lock2}/(R_{\rm lock2} + R_{\rm lock1})V_{\rm sat} = 110\,$mV, before decreasing to 0. As long as V_{lock} remains large, it prevents any switch. The capacity $C_{\rm lock} = 4.7\,$nF rules the $V_{\rm lock}$ relaxation time $\tau_{\rm lock} = (R_{\rm lock1} + R_{\rm lock2})C_{\rm lock} = 0.1\,$ms. It is chosen to freeze the comparator during approximately a quarter of the cantilever period: $3 \times \tau_{\rm lock} = 0.3\,$ms $\sim 1/(4f_0)$. Indeed, we verify on Fig. 7 b) that when V_x (black line) crosses the threshold $V_{x_0} = 0$, the comparator properly switches only once from $V = -V_1$ to $V = +V_1$ (red line), as $V_{\rm lock}$ (blue line) becoming transiently positive significantly increases the threshold value for approximately 0.3 ms.

C. Devices characteristics

To maintain less than 5% cooling in the final setup, we use a LM219 comparator that has no hysteresis and a typical 80 ns response in the working conditions. A tiny hysteresis of 0.37 mV is added through feedback resistances to guarantee stability: $R_i/R_h = 1.2\,$kΩ$/3.2\,$MΩ. Finally, the low-pass filter added to remove early triggers has its cutoff frequency chosen within the prescribed range: $f_c = 1\,$MHz. A smaller cutoff frequency could be chosen (down to $\sim 500\,$kHz as prescribed by Eq.(17)), to lower the background noise contribution even more (reduced to $4\%\sigma_0$ for a 500 kHz bandwidth). In the final setup, we use a SR560 model containing two identical tunable cutoff frequencies 1st-order R-C filters, to provide first or second-order filtering at $f_c = 1\,$MHz.

D. Virtual potential characteristics

The position distribution of the cantilever trapped in the virtual potential produced with the final setup perfectly matches the expected equilibrium distribution in a double-well, as illustrated in Fig. 3. Moreover, we show in Fig. 4 that the velocity distribution in closely-spaced wells ($x_1 = \sigma_0$) is also in excellent agreement with the equilibrium expectation (without feedback), contrary to the two previous setups, for which the velocity PDF is clearly modified by the feedback. To complete the experimental verification, we measure the velocity variance for different distances between the wells. Fig. 6 (black markers) shows that the velocity distribution in the virtual double-well potential of the final setup is not biased.

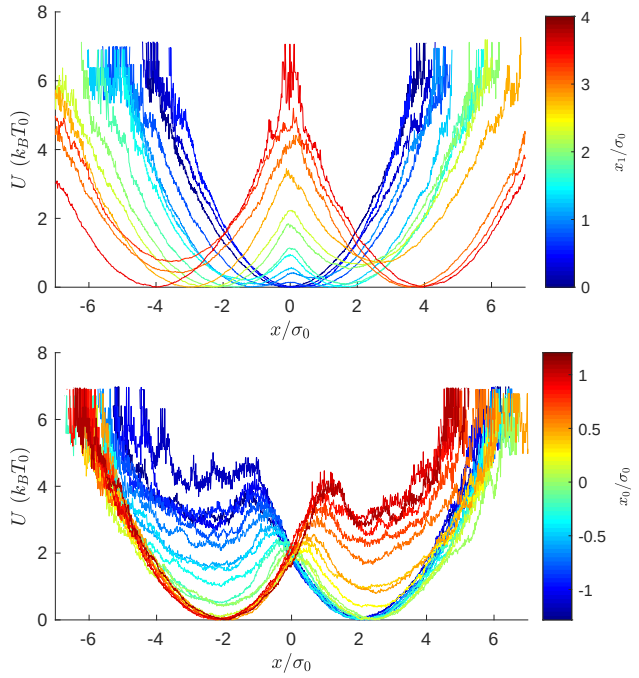

FIG. 8. **Double-well potential tuning**. $U(x_0, x_1, x)$ is computed through the measured PDF of x during 10 s acquisitions and the equilibrium Boltzmann distribution for different values of the controlled parameters x_0 and x_1. The top graph corresponds to $x_0 = 0$ and $x_1 \in [0, 4]\sigma_0$, the bottom one to $x_0 \in [-1.25, 1.25]\sigma_0$ and $x_1 = 2\sigma_0$. The two parameters allow to explore different barrier height and potential energy step between the two wells. The high noise level for large values of U stems from the low sampling of regions with low probability.

VI. CONCLUSION

This underdamped system has the strong merits of a short relaxation time and a highly precise deflection measurement, but controlling its virtual potential requires special caution on the feedback control. Namely, the underdamped regime makes the response much more sensitive to any noise or delay in the driving force. The thorough study of the effects of experimental non-idealities enables us to identify the key requirements needed to create a proper virtual potential. The experimental challenge that ensues is successfully addressed by the final setup. Ultimately, we demonstrate that the response of the system in the double-well potential built this way is statistically equivalent to the one expected at equilibrium in a physical potential.

Additionally, this virtual potential can be precisely controlled through the tuneable parameter x_0 which sets the barrier position, and the parameter x_1 which defines the distance between the wells. Fig. 8 shows the influence of the above mentioned parameters on the potential shape. The wells curvature is not tuneable as solely set by the cantilever stiffness, and the barrier height is enslaved to all other parameters.

The experimental work detailed in this article opens a wide range of possibilities in the field of underdamped system control, and allows high accuracy exploration of statistical physics in the underdamped regime (and in particular stochastic thermodynamics). The analysis presented holds at even lower damping $Q \gg 1$, achievable by placing the cantilever in vacuum. This configuration simply imposes more stringent constraints on the feedback time delay. Finally, this electrical circuit paves the way to the use of a field-programmable gate array (FPGA) configured to perform all the calibration and feedback operations, improving reliability and accuracy. Indeed, such a digital controller can readily give microsecond response (or even faster) and would meet easily the experimental requirements listed here, even in the highly underdamped regime. Besides, more complex configurations of the FPGA target (associating a specific output voltage to every position) would even allow to create any arbitrary non-linear potential shape, with several applications from optimal protocols for minimizing the work in finite-time operations [29, 30], to the exploration of non-equilibrium extensions of Landauer's theory [31, 32].

ACKNOWLEDGMENTS

Acknowledgments This work has been financially supported by the Agence Nationale de la Recherche through grant ANR-18-CE30-0013 and by the FQXi Foundation, Grant No. FQXi-IAF19-05, "Information as a fuel in colloids and super-conducting quantum circuits.".

Data availability The data that support the findings of this study are openly available in Zenodo [33].

Appendix A: Mean Heat

We derive in this section the very general expression of the average heat over an underdamped stochastic process following Ref. 27.

Applying to the underdamped regime the generic computations of stochastic energy exchanges [12, 16, 27, 30, 34], we have:

$$\frac{d\mathcal{Q}}{dt} = -\frac{\partial U}{\partial x}\dot{x} - \frac{dK}{dt}. \tag{A1}$$

The computation of the mean dissipated heat requires writing the general Langevin equation of an underdamped system in a potential U:

$$m\ddot{x} = -\frac{\partial U}{\partial x} - \gamma\dot{x} + F_{th}, \tag{A2}$$

where F_{th} is a delta correlated white Gaussian noise corresponding to the forcing due to the thermal bath:

$\langle F_{th}(t)F_{th}(t+t')\rangle = 2k_BT_0\gamma\delta(t')$. Multiplying Eq.(A2) by $\dot{x}$ leads to the dissipated heat defined by Eq. (A1):

$$\frac{d\mathcal{Q}}{dt} = m\ddot{x}\dot{x} - \frac{dK}{dt} + \gamma\dot{x}^2 - F_{th}\dot{x}. \tag{A3}$$

Some caution is required before taking the mean value of the above expression, because it involves products of stochastic quantities: in that respect, the Ito discretization prescribes for a stochastic function $K(v)$,

$$\frac{dK}{dt} = \frac{\partial K}{\partial v}\dot{v} + \frac{1}{2}\frac{\partial^2 K}{\partial v^2}\dot{v}^2 dt. \tag{A4}$$

We apply Eq. (A4) to $K = \frac{1}{2}mv^2$, and use Eq. (A2) to compute the $\dot{v}^2$ term:

$$\frac{dK}{dt} = mv\dot{v} + \frac{1}{2m}\left(-\frac{\partial U}{\partial x} - \gamma\dot{x} + F_{th}\right)^2 dt \tag{A5}$$

When taking the mean value and letting dt tend to 0, most terms simplify out. Indeed, only remain the terms that involve the thermal noise F_{th} scaling in $1/\sqrt{dt}$, some of which are cancelled by the Ito prescription: $\langle F_{th}v\rangle = \langle F_{th}x\rangle = 0$. Finally, we obtain the relation: $d\langle K\rangle/dt = m\langle\ddot{x}\dot{x}\rangle + k_BT_0\gamma/m$. Eq. (A3) then simplifies into:

$$\frac{d\langle\mathcal{Q}\rangle}{dt} = \frac{\gamma}{m}(2\langle K\rangle - k_BT_0). \tag{A6}$$

Using the definition of the kinetic temperature $T = 2\langle K\rangle/k_B$, and introducing the quality factor $Q = m\omega_0/\gamma$, Eq. (A6) becomes:

$$\frac{d\langle\mathcal{Q}\rangle}{dt} = \frac{\omega_0}{Q}k_B(T - T_0). \tag{A7}$$

This expression is completely general and highlights that the heat exchanges are reduced at high Q [13].

Appendix B: Switching rate

In the limit of weak damping, the total energy of the cantilever $E = U + K$ is conserved, and its motion is periodic in time. The period of oscillation $\mathcal{T}$ depends on the value of E with respect to the barrier height $\mathcal{B} = \frac{1}{2}kx_1^2$. If $E < \mathcal{B}$, then the motion is confined to a single well, there is no switches, and the period is $\mathcal{T}_0 = 1/f_0$. If $E > \mathcal{B}$, the cantilever visits both wells every period, so there are 2 switches every period, with

$$\mathcal{T}(E,\mathcal{B}) = 2\int_{-x_M}^{x_M}\sqrt{\frac{m}{2(E-U(x,x_1))}}dx \tag{B1}$$

$$= \frac{2}{\omega_0}\int_{-x_M}^{x_M}\frac{1}{\sqrt{(x_M-x_1)^2-(|x|-x_1)^2}}dx \tag{B2}$$

$$= \frac{2}{\omega_0}\left[\pi + 2\sin^{-1}\left(\sqrt{\frac{\mathcal{B}}{E}}\right)\right], \tag{B3}$$

where $x_M = x_1 + \sqrt{2E/k}$ is the maximum excursion of the cantilever. This period is twice $\mathcal{T}_0$ when $E \gtrsim \mathcal{B}$, and tends to $\mathcal{T}_0$ for $E \gg \mathcal{B}$.

In equilibrium, the statistics of the total energy E is ruled by the Boltzmann distribution: $P(E) = \exp(-E/k_BT)/k_BT$. We deduce the average switching rate Γ by weighting the 2 switches per period for $E > \mathcal{B}$ by this probability:

$$\Gamma(\mathcal{B},T) = \int_{\mathcal{B}}^{\infty}\frac{2}{\mathcal{T}(E,\mathcal{B})}\frac{\exp(-E/k_BT)}{k_BT}dE. \tag{B4}$$

For finite damping, the energy is not conserved along single trajectories, but still is in average thanks to the equilibrium with the thermostat. Eq. (B4) is therefore a good approximation of the switching rate between the wells for a given barrier height and system temperature.

In Fig. 9, we superimpose the switching rate computed with Eq. (B4) and the results of a simulation with or without hysteresis. The good agreement between the simulation and the model justifies the use of the $\Gamma(\mathcal{B},T)$ expression to derive the temperature evolution of the system in a double-well potential with switching delay. Besides, the dotted red line corresponds to Kramer's theory [26] prescribing the escape rate $\Gamma_K(\mathcal{B},T) = \frac{\omega_0}{2\pi}e^{-\mathcal{B}/k_BT}$ [35]. Hence, Fig. 9 highlights the fact that Kramer's simplest formula Γ_K doesn't work for low energy barriers.

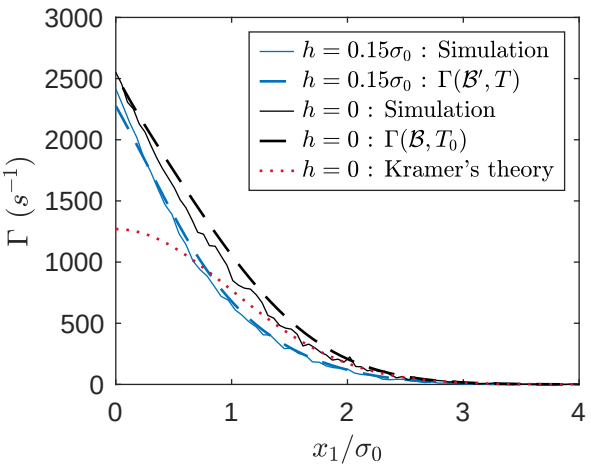

FIG. 9. **switching rate** Γ as a function of the distance x_1 between the wells without switching delay, for two hysteresis: $h = 0$ and $h = 0.15\sigma_0$. For $h = 0$ and high energy barriers $\mathcal{B} = \frac{1}{2}x_1^2$, Kramer's simplest model in dashed red line holds and perfectly matches the simulation data from $N = 100$ iterations of $30/f_0$ long trajectories in black line. However, for smaller barrier height the model $\Gamma(\mathcal{B},T_0)$ of Eq. (B4) in black dashed line provides a better prediction. For a $h = 0.15\sigma_0$ hysteresis, the simulation data from $N = 100$ iterations of $30/f_0$ long trajectories in blue line is in very good agreement with the model $\Gamma(\mathcal{B}',T)$ with parameters $T = \theta_hT_0$ solution of Eq. (9) and $\mathcal{B}' = \frac{1}{2}(x_1+h)^2$.

[1] M. Gavrilov, Y. Jun, and J. Bechhoefer, Real-time calibration of a feedback trap, Review of Scientific Instruments **85**, 095102 (2014).
[2] M. Gavrilov and J. Bechhoefer, Arbitrarily slow, nonquasistatic, isothermal transformations, EPL (Europhysics Letters) **114**, 50002 (2016).
[3] A. E. Cohen, Control of nanoparticles with arbitrary two-dimensional force fields, Phys. Rev. Lett. **94**, 118102 (2005).
[4] Y. Jun and J. Bechhoefer, Virtual potentials for feedback traps, Phys. Rev. E **86**, 061106 (2012).
[5] J. A. C. Albay, P.-Y. Lai, and Y. Jun, Realization of finite-rate isothermal compression and expansion using optical feedback trap, Appl. Phys. Lett. **116**, 103706 (2020).
[6] A. Bérut, A. Arakelyan, A. Petrosyan, S. Ciliberto, R. Dillenschneider, and E. Lutz, Experimental verification of landauer's principle linking information and thermodynamics, Nature **483**, 187 (2012).
[7] A. Bérut, A. Petrosyan, and S. Ciliberto, Information and thermodynamics: experimental verification of landauer's erasure principle, Journal of Statistical Mechanics: Theory and Experiment **2015**, P06015 (2015).
[8] J. Hong, B. Lambson, S. Dhuey, and J. Bokor, Experimental test of landauer's principle in single-bit operations on nanomagnetic memory bits, Sci. Adv. **2**, e1501492 (2016).
[9] L. Martini, M. Pancaldi, M. Madami, P. Vavassori, G. Gubbiotti, S. Tacchi, F. Hartmann, M. Emmerling, S. Höfling, L. Worschech, and G. Carlotti, Experimental and theoretical analysis of landauer erasure in nanomagnetic switches of different sizes, Nano Energy **19**, 108 (2016).
[10] K. Proesmans, J. Ehrich, and J. Bechhoefer, Finite-time landauer principle, Phys. Rev. Lett. **125**, 100602 (2020).
[11] Y. Jun, M. Gavrilov, and J. Bechhoefer, High-precision test of landauer's principle in a feedback trap, Phys. Rev. Lett. **113**, 190601 (2014).
[12] S. Dago, J. Pereda, N. Barros, S. Ciliberto, and L. Bellon, Information and thermodynamics: Fast and precise approach to landauer's bound in an underdamped micromechanical oscillator, Phys. Rev. Lett. **126**, 170601 (2021).
[13] S. Dago and L. Bellon, Dynamics of information erasure and extension of landauer's bound to fast processes, Phys. Rev. Lett. **128**, 070604 (2022).
[14] J. Gieseler and J. Millen, Levitated Nanoparticles for Microscopic Thermodynamics—A Review, Entropy **20**, 326 (2018).
[15] J. Gieseler, L. Novotny, C. Moritz, and C. Dellago, Nonequilibrium steady state of a driven levitated particle with feedback cooling, New J. Phys. **17**, 045011 (2015).
[16] U. Seifert, Stochastic thermodynamics, fluctuation theorems and molecular machines, Reports on Progress in Physics **75**, 126001 (2012).
[17] K. H. Kim and H. Qian, Entropy production of brownian macromolecules with inertia, Phys. Rev. Lett. **93**, 120602 (2004).
[18] L. Granger and H. Kantz, Thermodynamic cost of measurements, Phys. Rev. E **84**, 061110 (2011).
[19] M. L. Rosinberg, T. Munakata, and G. Tarjus, Stochastic thermodynamics of Langevin systems under time-delayed feedback control: Second-law-like inequalities, Phys. Rev. E **91**, 042114 (2015).
[20] P. Paolino, F. Aguilar Sandoval, and L. Bellon, Quadrature phase interferometer for high resolution force spectroscopy, Rev. Sci. Instrum. **84**, 095001 (2013).
[21] Doped silicon cantilever OCTO1000S from Micromotive Mikrotechnik, nominal length 950 μm, nominal mass 5×10^{-11} kg.
[22] L. Bellon, Thermal noise of microcantilevers in viscous fluids, Journal of Applied Physics **104**, 104906 (2008).
[23] M. Chupeau, S. Ciliberto, D. Guéry-Odelin, and E. Trizac, Engineered swift equilibration for Brownian objects: from underdamped to overdamped dynamics, New J. Phys. **20**, 075003 (2018).
[24] τ_γ is proportional to the power of the laser that creates the trap and can vary widely, ranging from $\sim$ 0.1 ms to 100 ms in the many optical tweezer setups that have been used to study stochastic thermodynamics. We retain 30 ms as the typical time scale of experiments tackling Landauer's bound [1, 2, 4, 6, 7, 10, 36].
[25] H.-J. Butt, B. Cappella, and M. Kappl, Force measurements with the atomic force microscope: Technique, interpretation and applications, Surface Science Reports **59**, 1 (2005).
[26] H. Kramers, Brownian motion in a field of force and the diffusion model of chemical reactions, Physica **7**, 284 (1940).
[27] K. Sekimoto, *Stochastic Energetics*, Lecture Notes in Physics, Vol. 799 (Springer, 2010).
[28] K. Sekimoto and S. Sasa, Complementarity relation for irreversible process derived from stochastic energetics, Journal of the Physical Society of Japan **66**, 3326 (1997).
[29] A. Gomez-Marin, T. Schmiedl, and U. Seifert, Optimal protocols for minimal work processes in underdamped stochastic thermodynamics, The Journal of Chemical Physics **129**, 024114 (2008).
[30] E. Aurell, K. Gawędzki, C. Mejía-Monasterio, R. Mohayaee, and P. Muratore-Ginanneschi, Refined second law of thermodynamics for fast random processes, Journal of Statistical Physics **147**, 487 (2012).
[31] T. Sagawa, Thermodynamic and logical reversibilities revisited, Journal of Statistical Mechanics: Theory and Experiment **2014**, P03025 (2014).
[32] M. Esposito and C. V. den Broeck, Second law and landauer principle far from equilibrium, EPL (Europhysics Letters) **95**, 40004 (2011).
[33] S. Dago, J. Pereda, S. Ciliberto, and L. Bellon, Dataset for J. Stat. Mech.: Virtual double-well potential for an underdamped oscillator created by a feedback loop, 10.5281/zenodo.6497247 (2022).
[34] C. Jarzynski, Equalities and inequalities: Irreversibility and the second law of thermodynamics at the nanoscale, Annual Review of Condensed Matter Physics **2**, 329 (2011).
[35] V. Mel'nikov, The Kramers problem: Fifty years of development, Physics Reports **209**, 1 (1991).
[36] A. Bérut, A. Petrosyan, and S. Ciliberto, Detailed jarzynski equality applied to a logically irreversible procedure, EPL (Europhysics Letters) **103**, 60002 (2013).

Appendix E:

Numerical simulation of the underdamped oscillator

The experimental results are supplemented by a numerical simulation providing a large number of trajectories ($N^{\text{sim}} = 5 \times 10^6$) without any calibration drift in the initial position X_1. The simulation is meant to mimic the experimental system during step 1, and therefore uses the experimental parameters ω_0, m, Q, X_1 and τ. The simulation code consists in integrating the Langevin equation that rules the cantilever position:

$$\ddot{x} + \frac{\omega_0}{Q}\dot{x} + \omega_0^2 x = \frac{F_\xi}{m} + \omega_0^2 S(x)(X_1 - \frac{X_1}{\tau}t), \tag{E.1}$$

where F_ξ the stochastic forcing from the bath defined in Eq. (1.4). F_ξ is implemented as a random number normally distributed around 0, with a standard deviation $\sqrt{2k_B T_0 m\omega_0/(Q\Delta t)}$, with Δt the simulation time step. We choose the symplectic Euler method [5], better suited to stochastic differential equation than the Runge-Kutta one [6], to solve numerically Eq. (E.1) and output the position and speed of the cantilever at every time step. We display in Listing E.1 the first steps of the symplectic Euler method with normalized quantities, $z = x/\sigma_0$, $s = \omega_0 t$ and $f = F_\xi/(k\sigma_0)$:

```
f=sqrt(2/(Q*ds))*randn(N)
for i in range(N-1)
  z[i+1]=z[i]+v[i]*ds
  dz=z[i+1]-sign(z[i+1])*z1[i+1]
  v[i+1]=v[i]-(dz+v[i]/Q+f[i])*ds
```

Listing E.1 – Symplectic Euler method

The initial position and speed are distributed according to the Boltzmann equilibrium distribution, corresponding to Eq. (4.8) with $\beta = 1/(k_B T_0)$ and $x_1 = X_1$.

Appendix F:

Fast Erasure model (FE model)

In all the following we no longer use the dimensionless positions $z = x/\sigma_0$, to better highlights that the position variance during the protocol can differ from the position variance at rest $\sigma_0^2 = k_B T_0/k$.

F.1 Mean work, potential and kinetic energy

Let us split the PDF $P^c(x,v)$ describing compression and its associated partition function Z^c of Eqs. (4.8) into their kinetic and potential contribution:

$$P_K^c(v) = \frac{e^{-\beta K^c}}{Z_K^c},\ Z_K^c = \int_{-\infty}^{+\infty} e^{-\beta K^c} dv = \sqrt{\frac{2\pi}{m\beta}} \tag{F.1a}$$

$$P_U^c(v) = \frac{e^{-\beta U^c}}{Z_U^c},\ Z_U^c = \int_{-\infty}^{+\infty} e^{-\beta U^c} dx = \sqrt{\frac{2\pi}{k\beta}} V. \tag{F.1b}$$

We now easily compute the mean values of K and U:

$$\langle K^c \rangle = \int_{-\infty}^{+\infty} K^c \frac{e^{-\beta K^c}}{Z_K^c} dv = -\frac{\partial \ln Z_K^c}{\partial \beta} = \frac{1}{2\beta}, \tag{F.2a}$$

$$\langle U^c \rangle = \int_{-\infty}^{+\infty} U^c \frac{e^{-\beta U^c}}{Z_U^c} dx = -\frac{\partial \ln Z_U^c}{\partial \beta} = \frac{1}{2\beta} - \frac{\partial \ln V}{\partial \beta}. \tag{F.2b}$$

Because there are no deterministic terms ($\langle x \rangle = 0$ and $\langle v \rangle = 0$) in the compression framework, those equations equivalently arise from Eqs. (4.10c-4.10d). The mean work time derivative is computed from Eq. 4.2:

$$\langle \frac{d\mathcal{W}^c}{dt} \rangle = \int_{-\infty}^{+\infty} \frac{\partial U^c}{\partial x_1} \frac{e^{-\beta U^c}}{Z_U^c} dx \dot{x}_1 = -\frac{1}{\beta} \frac{\partial \ln Z_U^c}{\partial x_1} \dot{x}_1, \tag{F.3}$$

which is again equivalent to Eq. (4.10b) in the absence of deterministic work.

The case of translation follows a similar pattern, except that we now need to include deterministic terms, since here $\langle x \rangle = x_D$ and $\langle v \rangle = \dot{x}_D$. We then rewrite the energies as:

$$\begin{aligned}
\langle K^t \rangle =& \langle \frac{1}{2} m v^2 \rangle \\
=& \langle \frac{1}{2} m (v - \dot{x}_D)^2 + m \dot{x}_D (v - \frac{1}{2} \dot{x}_D) \rangle \\
=& \langle \frac{1}{2} m (v - \dot{x}_D)^2 \rangle + \frac{1}{2} m \dot{x}_D^2 \qquad \text{(F.4)} \\
\langle U^t \rangle =& \langle \frac{1}{2} k (x - x_1)^2 \rangle \\
=& \langle \frac{1}{2} k (x - x_D)^2 + \frac{1}{2} k (x_D - x_1)^2 + k (x - x_D)(x_D - x_1) \rangle \\
=& \langle \frac{1}{2} k (x - x_D)^2 \rangle + \frac{1}{2} k (x_D - x_1)^2 \qquad \text{(F.5)}
\end{aligned}$$

The mean values of the energies are thus the sum of a deterministic and a stochastic term. The expressions of latter and of the PDF $P^t(x, v)$ in Eq. (4.9a) are those of an harmonic oscillator in the referential centered in x_D, which directly lead to the equipartition. Since $V = 1$ during a translation, we recover the mean values anticipated by Eqs. (4.10c-4.10d). The mean work time derivative is again computed from Eq. 4.2:

$$\langle \frac{d\mathcal{W}^t}{dt} \rangle = \langle \frac{\partial U^t}{\partial x_1} \rangle \dot{x}_1 = -k (x_D - x_1) \dot{x}_1 \qquad \text{(F.6)}$$

In this case, the mean work is purely deterministic, as expected in Eq. (4.10b) with $V = 1$. The ansatz for the PDF in the compression or translation stages thus lead to the Eqs. (4.10) describing all the energetic terms is any situation.

F.2 Deterministic terms

The trajectory $x(t)$ in a moving well decomposes into the stochastic response to the thermal fluctuations, which vanishes on average, and the response to the driving force ramp which is the solution of the following deterministic equation:

$$\ddot{x}_D + \frac{\omega_0}{Q} \dot{x}_D + \omega_0^2 x_D = \omega_0^2 x_1(t) \qquad \text{(F.7)}$$

with $x_1(t) = X_1(1 - t/\tau)$ decreasing from X_1 to 0 during step 1. We solve the above equation of motion, introducing $\Omega = \omega_0 \sqrt{1 - 1/(4Q^2)}$, and obtain the deterministic trajectory $\pm x_D(t)$ (the sign depending of which well is considered):

$$x_D(t) = x_1(t) + \frac{X_1}{\tau} \left[\frac{1}{Q\omega_0} \left(1 - e^{-\frac{t\omega_0}{2Q}} \cos \Omega t \right) - \frac{1 - 2Q^2}{2Q^2 \Omega} e^{-\frac{t\omega_0}{2Q}} \sin \Omega t \right] \qquad \text{(F.8)}$$

Therefore, using Eq. (F.6) the work required to move the system on a distance X_1 in a duration τ is:

$$\langle W^t \rangle = k \frac{X_1^2}{\tau^2 \omega_0^2} [\frac{\tau \omega_0}{Q} + (1 - \frac{1}{Q^2})(1 - e^{-\frac{\tau \omega_0}{2Q}} \cos \Omega \tau) + \frac{e^{-\frac{\tau \omega_0}{2Q}}}{2Q\Omega} (\frac{1}{Q^2} - 3) \sin \Omega \tau] \qquad \text{(F.9)}$$

In the small speed limit ($\mathbf{v}_1 \ll 1$), Eq. (F.9) becomes:

$$\langle W^t \rangle \sim k\frac{X_1}{\tau} \times \frac{X_1}{Q\omega_0} = (\frac{Z_1}{\tau} \times \frac{Z_1}{Q\omega_0})k_B T_0 \tag{F.10}$$

Those results can be applied for the translational motion during step 2, and at the beginning of step 1. Indeed, as long as the cantilever hasn't left its initial well, the above description holds during step 1. After the first switch, the cantilever switches frequently between the symmetric wells so that the deterministic terms can be neglected. We therefore introduce $\Pi(t)$ the probability that the cantilever remains in its initial well until time t, in order to modulate the deterministic contribution accordingly. The probability that a trajectories hasn't commuted at time t derives from the switching rate $\Gamma(t) = \Gamma(\mathcal{B}(t), T(t))$ in Eq. (1.38):

$$\Pi(t) = e^{-\int_0^t \Gamma(u)du}. \tag{F.11}$$

The deterministic work, kinetic and potential energies are then given by:

$$\frac{d\mathcal{W}_D}{dt} = -k(x_D - x_1)\dot{x}_1 \times \Pi(t) \tag{F.12a}$$

$$K_D(t) = \frac{1}{2}m\dot{x}_D \times \Pi(t) \tag{F.12b}$$

$$U_D(t) = \frac{1}{2}k(x_D - x_1)^2 \times \Pi(t) \tag{F.12c}$$

During step 2, $x_D(t)$ is still described by Eq. (F.8) with $x_1(t) = -X_1 t/\tau$, and the energetic terms correspond at all time to Eqs. (F.12) with $\Pi(t) = 1$ as the cantilever remains in the single well allowed.

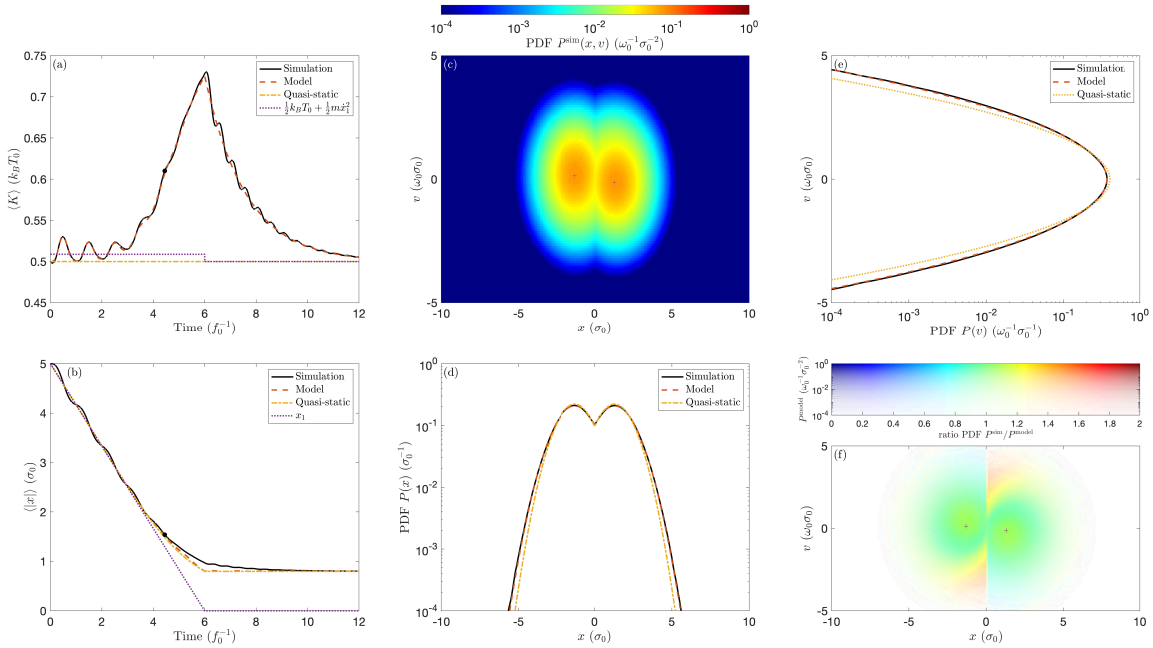

Figure F.1 – **Comparison of the PDFs $P^{\rm model}(x,v,t)$ from our ansatz and $P^{\rm sim}(x,v,t)$ from a numerical simulation.** This frame is captured from the movie `PDF_erasure_process.mov` available in Supplemental Materials of Ref. 7, corresponding to $t = 4.5 f_0^{-1}$. (a) Mean kinetic energy $\langle K\rangle$ vs time from the simulation and the model. The quasistatic case is shown for comparison. (b) Average absolute value of the position $\langle|x|\rangle$ vs time (c) 2D representation of the PDF $P^{\rm sim}(x,v,4.5f_0^{-1})$ with the color scale on top. (d) PDFs in position (obtained by integrating over all speeds the 2D PDF) from the simulation and the model. The quasistatic case is shown for comparison. (e) PDFs in speed (obtained by integrating over all positions the 2D PDF). (f) Ratio of the PDFs $P^{\rm sim}(x,v,4.5f_0^{-1})/P^{\rm model}(x,v,4.5f_0^{-1})$ in a 2D representation using the color scale on top.

F.3 Validation of the PDF ansatz

Using the PDFs of Eqs. (4.8) and (4.9) is based on some approximations: the dragging effect is assumed to vanish after the first switch of the system. We unavoidably leave aside some transients mixing position and speed during compression. In order to investigate on the validity of this approach we compare the numerical simulation data to the PDF models, using the following ansatz

$$P^{\rm model}(x,v,t) = \Pi(t)P^t(x,v) + [1-\Pi(t)]P^c(x,v) \tag{F.13}$$

$$P^c(x,v) = \frac{1}{Z^c} e^{-\frac{1}{2}\beta m v^2} e^{-\frac{1}{2}\beta k(|x|-x_1)^2} \tag{F.14}$$

$$P^t(x,v) = \frac{1}{Z^c} e^{-\frac{1}{2}\beta m(v-S(x)\dot{x}_D)^2} e^{-\frac{1}{2}\beta k(|x|-x_D)^2} \tag{F.15}$$

with $S(x)$ the sign of x. The PDF $P^{\rm sim}(x,v,t)$ is computed from 5×10^6 trajectories, half of them starting from each well, with $X_1 = 5\sigma_0$ and $\tau = 6f_0^{-1}$ corresponding to $\mathbf{v}_1 = 0.13$. We can then study the relevance of our model by comparing the PDFs. This is done in the movie `PDF_erasure_process.mov` available in Supplemental Materials of Ref. 7, a frame of which is shown as an example in Fig. F.1 corresponding to $t = 4.5f_0^{-1}$. It demonstrates how good is the model to estimate the position and velocity distribution: the oscillations due to the dragging force are replaced by the temperature

rise predicted by the compression model. The relaxation in temperature after step 1 predicted by the model also matches the simulation data, except for the transient relaxation oscillations which are not included in the model after the 1st switch of the system during step 1. The comparison of the PDFs by their ratio in panel (f) also demonstrates that for statistically relevant portion of the phase space, the agreement between the two is better than 20%. The main deviations occur in the middle of step 1 in the bottom left and top right corner areas. These areas corresponds to trajectories where the system has switched once and presents a mean velocity component from motion of the well it has switched to. The deviation is therefore explained by the fact that the model PDF doesn't includes the mean driving velocity after the first switch. But because the error made is symmetrical with the initial state, it doesn't impact the computation of average values such as the velocity variance.

F.4 T_{eff} approximation

To retrieve the gas analogy, we apply Eq. (4.10b) to the step 1 compression (no deterministic work), and reframe it to identify the volume total derivative:

$$\langle \frac{d\mathcal{W}_1^c}{dt} \rangle = -k_B T \frac{\partial \ln \mathcal{V}}{\partial x_1} \dot{x}_1 \tag{F.16}$$

$$= -k_B T \frac{d \ln \mathcal{V}}{dt} \left(1 + \frac{d \ln T}{d \ln(x_1^2/T)} \right) \tag{F.17}$$

The second term in the parenthesis on the right hand side can be evaluated from our model once the time evolution of the temperature has been numerically computed. After integration, it represents at most 10% of the final result (upper limit reached for the highest temperature rise in the adiabatic limit). The work required for a fast compression can therefore be approximated by $\langle \mathcal{W}_1^c \rangle \sim k_B T_{\text{eff}} \ln 2$, and meet the gas analogy with the effective temperature being worth

$$T_{\text{eff}} = \frac{1}{\ln 2} \int T d \ln \mathcal{V}. \tag{F.18}$$

For the erasure cycle in Fig. 4.4, we derive $T_{\text{eff}} = 1.35\, T_0$ which gives the compression work with a 6% error.

Appendix references

[1] S. Dago, B. Besga, R. Mothe, D. Guéry-Odelin, E. Trizac, A. Petrosyan, L. Bellon, and S. Ciliberto, SciPost Phys. **9**, 64 (2020).

[2] I. A. Martínez, A. Petrosyan, D. Guéry-Odelin, E. Trizac, and S. Ciliberto, Nature Physics **12**, 843 (2016).

[3] S. Dago, J. Pereda, N. Barros, S. Ciliberto, and L. Bellon, Phys. Rev. Lett. **126**, 170601 (2021).

[4] S. Dago, J. Pereda, S. Ciliberto, and L. Bellon, Virtual double well potential for an underdamped oscillator created by a feedback loop (2022), under review JSTAT. arXiv: 2201.09870.

[5] E. Hebestreit, *Thermal Properties of Levitated Nanoparticles*, Ph.D. thesis, ETH Zurich (2017), appendix A.

[6] K. Burrage, P. Burrage, D. J. Higham, P. E. Kloeden, and E. Platen, Phys. Rev. E **74**, 068701 (2006).

[7] S. Dago and L. Bellon, Phys. Rev. Lett. **128**, 070604 (2022).

THÈSE DE DOCTORAT DE L'UNIVERSITÉ DE LYON

opérée par

l'École Normale Supérieure de Lyon

Discipline : Physique

Soutenue publiquement par :

Salambô Dago

Directeur de thèse : **Ludovic Bellon**
Co-encadrant de thèse : **Sergio Ciliberto**

Devant le jury composé de :

Bechhoefer	John,	Professeur,	*Simon Fraser University,*	Rapporteur
Pekola	Jukka,	Professeur,	*Aalto University*,	Rapporteur
Jarzynski	Christopher,	Professeur,	*University of Maryland*,	Examinateur
Auffèves	Alexia,	DR,	*Institut Néel (CNRS)*,	Examinatrice
Bellon	Ludovic,	CR,	*ENS de Lyon (CNRS)*,	Directeur de thèse

Stochastic thermodynamics: driving of micro-oscillators applied to the study and the optimisation of information processing.

This thesis extends by theoretical and experimental studies our understanding of the dynamics of systems ruled by thermal fluctuations in order to better control them and, in particular, use them as 1-bit logic gates. This work falls within the framework of out-of-equilibrium statistical physics and of thermodynamics of information based on stochastic thermodynamics. In this respect, we study the minimal work required to perform irreversible operations on 1-bit of information ([RESET] to 0 or 1), or reversible ones ([NOT] operation), and we aim to optimise the energetic cost and the speed of these processes. Our strategy to enhance the processing efficiency and speed consists in using as 1-bit memory a low dissipation micro-mechanical oscillator, therefore evolving at much smaller time-scales than the over-damped test systems used to date (colloidal particles in solution). The feedback control designed to create a virtual energy potential in which evolves the micro-resonator is a major step forward in coding and handling the 1-bit information: it represents the fastest and most energy-efficient device among those which perform logic operations at the thermal energy scale. We furthermore provide a solid theoretical basis, validated by experimental and numerical simulation results, to model energy exchanges. Taken as a whole, this work results in the theoretical prediction of the energetic cost of any logical operation and opens perspectives for information processing optimisation in term of reliability, speed and energy saving.